ZnO Nanostructures: Low-Temperature Synthesis, Characterisation, Their Potential Application as Gene-Delivery Tools

Maryam Akhwater

November 2018

A thesis submitted to De Montfort University
in the partial fulfilment of the requirements for the degree of Doctor of Philosophy

Emerging Technologies Research Centre
De Montfort University, Leicester
United Kingdom

Author's declaration

I declare that the work in this thesis was carried out in accordance with the regulation of De Montfort University. No part of this thesis has been submitted for any other degree or qualification at De Montfort University, or any other academic institutions.

Permission to copy or use whole or part of the work contained herein must be solicited except for the purpose of private study or academic purposes in which case the author must be explicitly acknowledged. The work contained in this thesis is as a result of my own effort unless otherwise stated.

"Life is like riding a bicycle, to keep your balance you must keep moving."

... Albert Einstein

Acknowledgements

I would like to express my deepest appreciation to my supervisor Dr. Richard Cross for his guidance, help, encouragement and support during the entire duration of my research journey. His timely advice and suggestions have helped me to a great extent to accomplish my thesis.

I would like to express my gratitude to Prof. Shashi Paul, Head of Emerging Technologies Research Centre and Professor of Nanoscience and Nanotechnologies for his valuable advice and generous help.

Thanks also goes to Dr. Yong Sun for his role as second supervisor. My sincere appreciation goes to Dr. Neill Horley and Dr. Glen McCann for their assistance in the biological work.

I would like to thank my PhD colleagues and friends for their friendship and support and for creating a cordial studying environment.

I owe a deep sense of gratitude to my family for the faith, prayers and encouragement during the pursuit of this degree. Without their selfless love and endless support, I cannot be me today. Thank you for always being there!

Abstract

Among metal oxide nanomaterials, zinc oxide (ZnO) nanostructures are one of the most important nanomaterials in today's nanotechnology research.

Over the past several decades, ZnO nanostructures have been extensively investigated for their extraordinary physical and chemical characteristics and also for their prominent performance in various novel applications such as photonics, optics, electronics, drug delivery, cancer treatment, bio-imaging, etc. However, functionality of theses nanomaterials is eventually dictated by the capability to govern their properties including shape, size, position, and crystalline structure on the nanosized scale.

This thesis investigates the solution-based synthesis of ZnO nanostructures and their morphological and structural properties. Importantly, in order to achieve the promising structure of ZnO, a systematic investigation of the influence of processing parameters, including solution concentration, time and temperature of growth reaction on the resultant materials was addressed. The other main point for this work is not only to effectively control the morphology, size, uniformly distribution, and orientation of ZnO nanomaterials, but also to build a good comprehension of the mechanism of fabrication process to raise their performance in future nanoscale applications. Furthermore, the catalytic effect of RF sputtered gold (Au) thin layer on Si substrate prior to ZnO growth *was* investigated to demonstrate the contributory for the remarkable catalytic activity of Au nanoparticles in the formation of high quality ZnO nanostructures.

Furthermore, we introduce an effective, inexpensive lithographic patterning method to consistently control the position of solution-processed ZnO nanowires. Nanosphere lithography technique (NSL) utilizes a catalyst-assisted pattern generated by employing colloidal self-assembled crystal of polystyrene spheres (PS) on the substrate surface to guide the hydrothermal growth of ZnO nanowires. Further, we fabricate 3D NFs and branched NFs of ZnO on silicon substrate via simple and cost-effective solution growth method, incorporating with seed ZnO nanoparticles deposition. The synthesis of 3D branched ZnO nanostructure, could potentially exploit for applications in optoelectronics, catalysis, sensing and photovoltaics.

In addition to the synthesis of 1D and 3D ZnO nanostructures, their morphology and distribution have been analysed via scanning electron microscopy (SEM) while, the surface topography was analysed by atomic force microscopy (AFM). The crystalline structure, phase purity, and particle size of ZnO nanomaterials have been investigated using X-ray diffraction (XRD). The outcomes from all these efforts have been integrated for cellular investigation via fluorescence microscopy technique (FM) to demonstrate the potential application of ZnO nanostructures as a gene delivery/-tissue engineering tool in different expression systems.

Table of Contents

List of Figures

List of Tables

Chapter 1

Overview of Thesis

The main focus of the thesis is to synthesize nanostructured ZnO materials using a facile solution-based method and investigate the structural properties of these materials for their suitability in the cellular interfacing system of a novel healthcare application. From the application point of view, the diameter, length, morphology and consistent distribution of well- aligned 3D ZnO nanomaterials on a supporting substrate are highlight issues in this work, therefore initiating rational control with a better comprehension of the growth mechanism and physical characteristics of the as-synthesized ZnO nanostructures has been successfully addressed.

This thesis is divided into 10 chapters demonstrating the literature review, fabrication methods, characterisation techniques, experimental results and analysis and finally the conclusions and future scope of this work. These are as follows:

Chapter 2 gives an overview of ZnO nanostructures and their diverse application. It briefly demonstrates the fundamental physical properties of ZnO nanomaterials such as mechanical, structural, piezoelectric, optical and

electrical properties.

Chapter 3 describes a wide variety of chemical and physical methodologies to fabricate ZnO nanostructures. Particularly, it focuses on the solution- based method and the influence of different processing parameters on the resultant ZnO nanostructures.

Chapter 4 demonstrates characterisation methods utilised in this work.

Chapter 5 is focused on the hydrothermal growth of ZnO nanowires. In the first part, the fabrication process discussed to help elucidate control on dimension and morphology. The second part of the chapter described the results of ZnO nanowires synthesis and the use of design of experiments methodologies utilised therein.

Chapter 6 focuses on exploring the influence of a sputtered gold (Au) thin layer on solution processed ZnO nanowires and how thermal processing of nucleation/intermediary layers may aid in the fabrication of bespoke ZnO nanostructures.

In chapter 7, template-assisted synthesis of ZnO nanowire arrays based on a polystyrene sphere (PS) mask and a gold catalyst is discussed.

Chapter 8 is divided in two sections; the first section introduces a background review of recent developments of three-dimensional (3D) multibranched ZnO nanostructures processed via low temperature solution phase synthesis approaches. The second section details 3D nanostructures and their properties produced in the framework of this thesis.

In chapter 9 we investigate the potential within these optimizing ZnO nanostructures to serve as delivery agents/sensing elements for Nano-bio interfacial systems.

Chapter 10 highlights the overall conclusion of the work and gives an outlook for further studies based on the work undertaken in this thesis.

Chapter 2

ZnO nanomaterials and their physical property characterisations

2. 1. Introduction

This chapter gives an overview of ZnO nanostructure materials and their fundamental physical properties. Nanostructured ZnO materials have been the focus of intense research for a number of years due to their desirable properties suitable for exploitation in electronics, optical, electrochemical, electromechanical and photonics applications. ZnO is an n-type multifunctional material which has various applications in surface acoustic wave filters (Emanetoglu, Gorla et al. 1999), photonic crystals (Liang, Sheng et al. 2001) photo detectors (Liang, Sheng et al. 2001), light emitting diodes (LED) (Saito, Haneda et al. 2002), photo diodes (Lee, Choi et al. 2002), gas sensors (Mitra, Chatterjee et al. 1998), optical modulator waveguides (Koch, Timbrell et al. 1995), solar cells (Zhu, Pan et al. 2013) and varistors (Lin, Zhang et al. 1999). Further, because of its biocompatibility, antibacterial properties, chemical stability, high isoelectric point (IEP), electrochemical activity, high electron mobility, and large surface-to-volume ratio, ZnO nanostructures have been used in a wide range of applications, including medicine delivery system, cancer therapy, biological imaging techniques, medical devices, sunblock, skin moisturizers (Ma, Zhang 2009, Wang, Yang et al. 2007, Li, Mahendra et al. 2008, Joshi, Chakraborti et al. 2009).

Moreover, (1D) ZnO nanostructures with high aspect ratio have been used as photocatalysts to decompose organic environmental pollutants such as dyes and pesticides (Sapkota, Anceno et al. 2011).

In addition, ZnO nanowires could be used as an efficient intracellular platform to introduce different biomolecule into various types of cells due to their very small diameter size with a high aspect ratio. Importantly, comprehension of the remarkable physical properties of ZnO nanomaterials and their promising applications as an elementary unit of the functional nanodevices is the focus of the current research activities.

ZnO can be produced in a wide variety of nanoscale structures. Zero dimensional (0D) nanostructures such as quantum dots or nanoparticles which have near-unity an aspect ratio (Al-lami, Jaber 2014). One dimensional (1D) structures comprise the biggest group, including rods (Frade, Jorge et al. 2012), needles (Wahab, Ansari et al. 2007), helixes, springs and rings (Kong, Ding et al. 2004), ribbons (Pan, Dai et al. 2001), tubes (Chen, Liu et al. 2007) belts (Huang, He et al. 2006), wires (Nikoobakht, Wang et al. 2013) and combs (Xu, Ji et al. 2012). ZnO can be crystallized in (2D) geometries, such as nanoplate, nanosheet, and nanopellets (Chiu, Khiew et al. 2010, Jose-Yacaman, Gutierrez-Wing et al. 2005). The last group is (3D) structures such as flower, dandelion, snowflakes, etc (Polshettiwar, Baruwati et al. 2009, Xie, Dai et al. 2005, Liu, Huang et al. 2006, Bitenc, Orel 2009).

A group of different ZnO nanostructures synthesized in the framework of this thesis is presented in figure 1. 1.

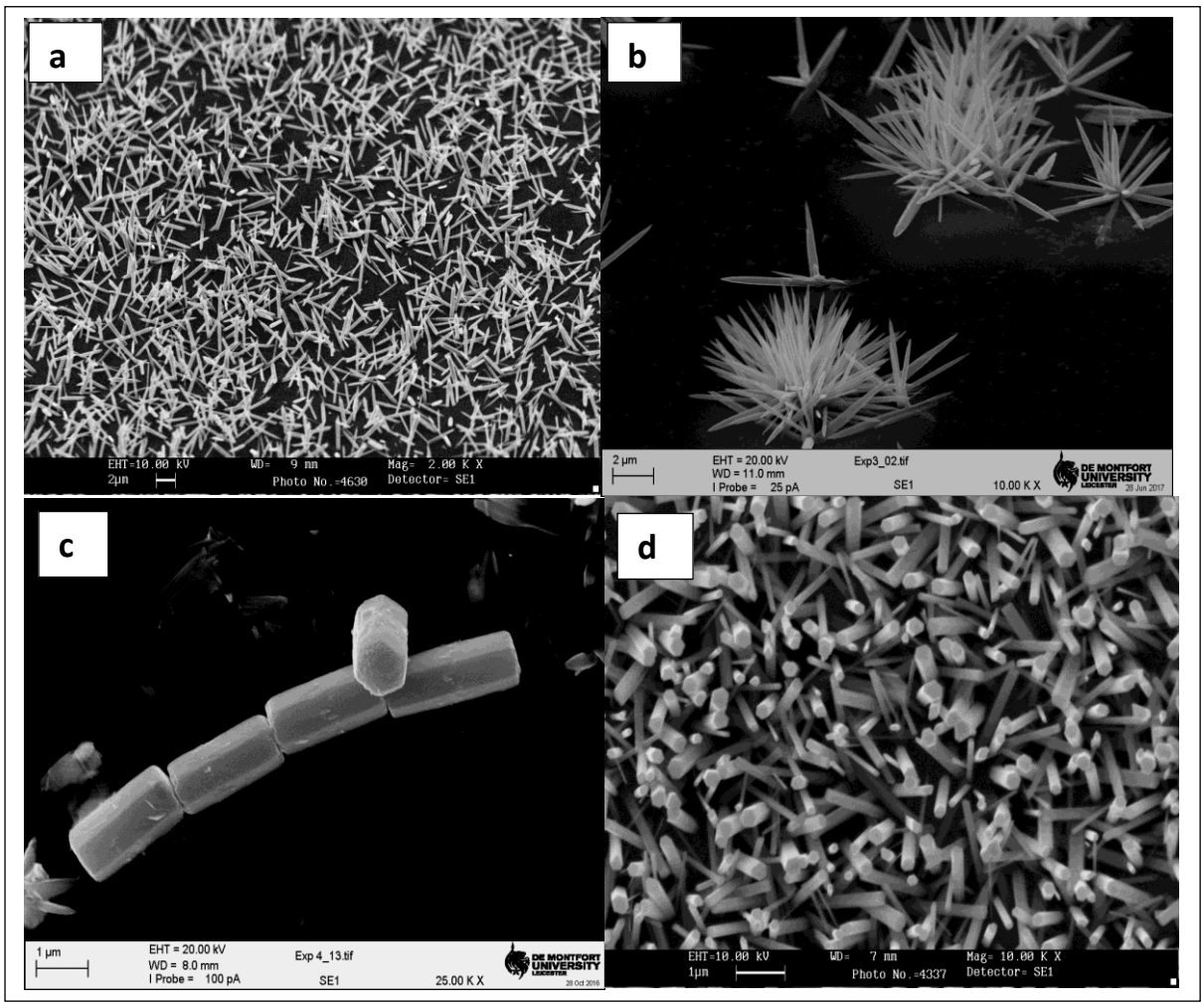

Figure 2. 1. A group of different ZnO nanostructures: (a) needle; (b) flower; (c) rods; (d) wires.

Here, the fundamental physical properties of ZnO are described below and summarised in table 2. 1 (Singh 2013).

Table 2. 1. Mechanical, vibrational, thermal, optical and electrical properties of ZnO (Singh 2013).

Physical properties	Values
1- Mechanical properties	
a) Bulk Young Modulus	11.2 ± 4.7 GPa
b) Bulk Hardness	5.0 ± 0.1 GPa
c) Epitax. Young Modulus	310 ± 40 GPa
d) Epitax. Hardness	5.75 ± 0.8 GPa
e) Bulk Modulus	142.4
2- Lattice vibrations	
a) TO(E_1)	591 cm^{-1}
b) LO(A_1)	574 cm^{-1}
c) TO(A_1)	380 cm^{-1}
d) E_2^{high}	437 cm^{-1}
e) E_2^{low}	101 cm^{-1}
3- Thermal properties	
a) Specific heat (C_P)	40.3 J mol^{-1} K^{-1}≈1.1 W cm^{-1} K^{-1}
b) Thermal conductivity	$\alpha_a = 4.31 \times 10^{-6}$ K^{-1}
c) Thermal exp. Coeff.	$\alpha_c = 2.49 \times 10^{-6}$ K^{-1}
4- Optical properties	
a) Refractive indices	n_w = 2.008
	n_e = 2.0029
b) Dielectric constants	
Static (E_0) E ⊥ C	7.46 (film), 7.77 (bulk)
E ‖ C	8.59 (film), 8.91 (bulk)
High freq. (ε_0) E ⊥ C	3.7 (film), 3.6 (bulk)
E ‖ C	3.78 (film), 3.66 (bulk)
5- Electrical properties	
a) Exciton band energy (RT)	60 me V
b) Band gap energy	3.44 eV
c) Effective masses	m_h =0.59 m_0, m_e =0.24 m_0
d) Hall mobility (RT)	μ_P = 5-50, μ_n = 200 cm^2 s^{-1} V^{-1}

2. 2. Mechanical properties

It is challenging to directly assess the mechanical performance of ZnO nanostructures as the conventional measurement approaches for bulk structures are inapplicable. Bai et al. (Bai, Gao et al. 2003) reported that ZnO nanobelt was a favourable candidate as nanoresonator and nanocantilever due

to its small dimensions which enhanced the cantilever sensitivity in contrast to typical cantilever. They investigated the flexural modulus of ZnO nanobelts by applying an oscillating electric field between a nanobelt and a constant electrode. Based on the classical theory of elasticity, flexural modulus of ZnO nanobelts was measured. Another report introduced by Hughes et al. (Hughes, Wang 2003) showed that control length and position of ZnO nanobelt potentially enables them to be applied as very sensitive cantilever for (AFM).

2. 3. Optical Properties

In material science, Luminescence yield of direct band gap materials is higher than those of indirect band gap materials which means the direct wide band gap energy lowers the leakage current of the systems and their temperature-dependent properties (Klingshirn, Waag et al. 2010). ZnO has a direct large band gap energy (3.40 eV) at room temperature that makes it transparent in the visible light region and highly photoactive in the UV region. Furthermore, ZnO has Higher exciton binding energy (~60 meV) which can increase its photo-activity and make it an attractive material for short wavelength optoelectronic devices (Jagadish, Pearton 2011). In addition, the high exciton binding energy in ZnO materials can enhance (UV) luminescence (~380 nm) at room temperature (Yang, Yan et al. 2002). Based on the photoluminescence (PL) spectroscopy of ZnO nanorods, it was observed that the quantum confinement effect is generally related to the small sizes of ZnO grains and can result in increasing the band gap energy and exciton binding energy (Gu, Kuskovsky et al. 2004). Strong luminescence peak at 380 nm was attributed to band-to band transitions and green-yellow emission was observed due to oxygen vacancy. Another red emission peak was also reported, which is explained as transitions caused by a doubly ionized oxygen vacancy (Fan, Chang et al. 2004).

ZnO is also considered as one of the most effective material to produce functional and efficient gas sensors, due to having oxygen vacancies on the surface that are active chemically and electrically (Zhao, Kim et al. 2009). Further, as ZnO nanowire/nanorod has nearly cylindrical shape and large refractive index (∼2.0), therefore, it is an attractive material for optical waveguide (Fan, Lu 2005).

2. 4. Structural and piezoelectric properties

ZnO materials can crystallize in three structures: hexagonal wurtzite, cubic zinc blended, and the infrequently noticed cubic rock salt (Figure 2. 1). The most common crystal is the hexagonal wurtzite structure which has lattice parameters a = 0.3296nm and c = 0.52065nm, schematically this form composes of zinc (Zn) and oxygen (O) atoms arranged layer by layer alternately along the c-axis direction. The zincblende structure crystalizes by fabricating ZnO on cubic crystal lattice substrates, while, rock salt form is only observed at comparably high pressure. Due to of the tetrahedral coordination nature of Zn^{2+} and O^{2-} (Figure 2. 2), the noncentralsymmetric structure of ZnO crystal is produced, resulting in impressive piezoelectric and pyroelectric characteristics (Vaseem et al. 2010).

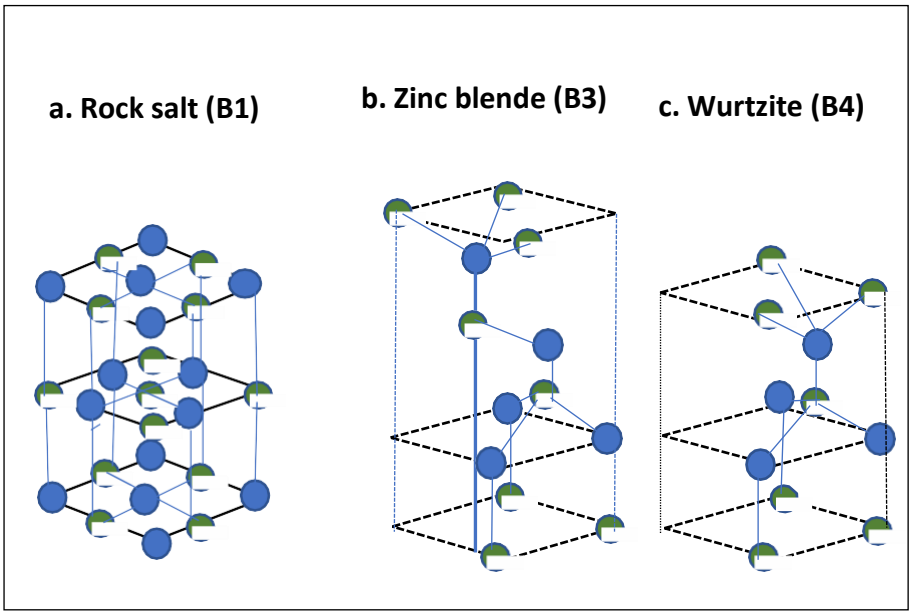

Figure 2.2. A demonstration of ZnO crystal forms: (a) cubic rock salt (B1), (b) cubic zinc blende (B3), and (c) hexagonal wurtzite (B4), the blue and green spheres refer Zinc and Oxygen atoms, respectively.

Additionally, in the wurtzite crystal structure of ZnO, each single negatively charged ion is encircled by four positively charged ions at the angles of the tetrahedron. What is more interesting about ZnO structures is that one end of the polar surface (0001) finishes with partially positive zinc lattice sites and the other end finishes with partially negative O lattice sites. Regularly, positively charged Zn (0001) and negatively charged O $(000\bar{1})$ surface are generated by differently charged ions, leading to induce a normal dipole moment, spontaneous electric polarization and various surface energy along the c-axis (Baruah, Dutta 2009).

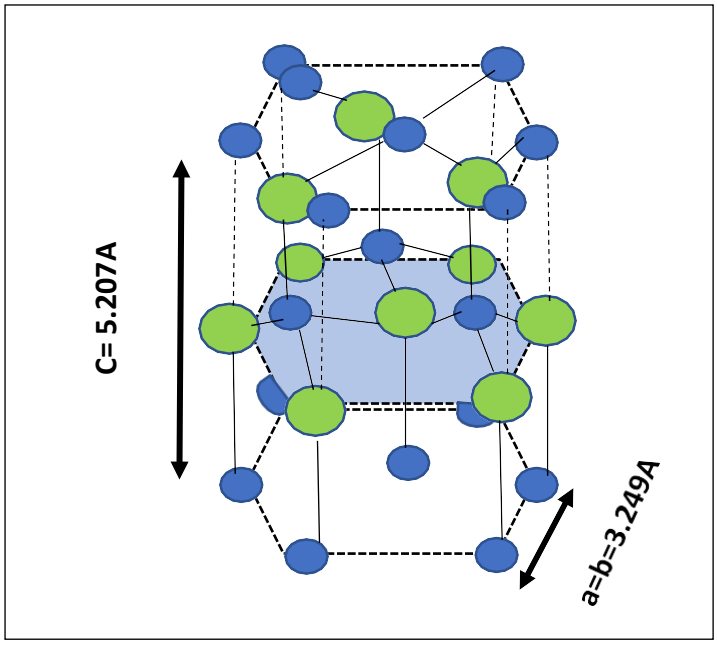

Figure 2. 3. The tetrahedral configuration of Zn-O. The bigger white spheres denote O atoms whilst the Zn atoms are smaller spheres.

In the wurtzite crystal form, the polar facets consist of the zinc and oxygen atoms which are organized alternately along the c-axis direction. The height plane facets are Zn-terminated (0001) which have high catalytic activity, whilst the bottom facets are O-terminated (000^{-}1) and they are inactive chemically (Gao, Wang 2004). Therefore, the polar plane surfaces (0001) have a fast growing-rate compared to other g plane facets (Li, Shi et al. 1998). The piezoelectricity is one of the most important properties of ZnO and has been widely investigated for potential applications in force sensor, acoustic wave resonator, acousto-optic modulator (Catti, Noel et al. 2003, Molarius, Kaitila et al. 2003, Wüthrich, Muller et al. 1998). As mentioned above, this property originates from the tetrahedrally bonded structure of zinc and oxygen atoms.

In such a noncentrosymmetric arrangement, the displacement of the centre of positive and negative charges under external pressure induced lattice distortion and local dipole moments. Generally, ZnO has the highest piezoelectric tensor and is extensively studied for its applications in nanoelectromechanical devices (Zhao, Wang et al. 2004). In most II-VI materials to sustain electrical neutrality and balanced structure, the polar plane surfaces reconstruct at the atomic level however, ZnO ± (0001) surfaces exhibit unusual phenomena, they are flat, stable and show no reconstruction which makes these two surfaces highly significant from a technical point of view and carry slightly various physical and chemical characteristics (Emanetoglu, Gorla et al. 1999, Chen, Bagnall et al. 2000). ZnO has also two non- polar facets, which are {2 $\bar{1}$ $\bar{1}$0} and {0 1 $\bar{1}$ 0} with lower energy compared to polar facet {0001}. These non-polar surfaces hold equal number of O and Zn ions whilst the polar facets are either O or Zn terminated.

2. 5. Electrical Properties

An investigation of the ZnO electrical properties is imperative for the evolution of future nanoelectronics devices. Electrical transport analysis has been conducted on the fabricated ZnO nanowire as field effect transistor (FET) (Liu, Yiu et al. 2003). ZnO nanowires were observed to show n-type semiconductor nature, due to the existence of the native defects like oxygen vacancies and zinc interstitials. Additionally, it was reported that the devices based on ZnO nanostructures can provide a faster device operation due to their high electron mobility which improves the performance of the device (Fan, Lu 2005).

Further, controlling a designed fabrication setup, the carrier density and mobility of the nanowires can be tuned therefore, the electrical characteristics of ZnO nanowires could be significantly adjusted (Chang, Fan et al. 2004). the obstruction of p-type doping for ZnO nanomaterials limits their eventual use in electronics and photonics. Prosperous synthesis of p-type doped ZnO nanostructure would strongly boost its potential applications in electronics and optoelectronics nanodevices (Fan, Lu 2005). P-type and n-type ZnO nanostructures may act as the light emission units in (LED) and p-n junction diodes (Fan, Lu 2005). In addition, the electric field emission measurements of aligned ZnO nanomaterials have been widely performed. ZnO nanoneedles with pointed end are promising candidate for electron field emission (Banerjee, Jo et al. 2004).

This chapter provides a brief review of ZnO nanostructure materials and their fundamental physical characteristics. The following chapter focuses on a variety of chemical and physical synthetic techniques that have been utilised to produce different structure of ZnO nanomaterials.

References

AL-LAMI, S. and JABER, H., 2014. Controlling ZnO Nanostructure Morphology on Seedless Substrate by Tuning Process Parameters and Additives. *Chemistry and Materials Research,* **6**(4), pp. 101-109.

BAI, X., GAO, P., WANG, Z.L. and WANG, E., 2003. Dual-mode mechanical resonance of individual ZnO nanobelts. *Applied Physics Letters,* **82**(26), pp. 4806-4808.

BANERJEE, D., JO, S.H. and REN, Z.F., 2004. Enhanced field emission of ZnO nanowires. *Advanced Materials,* **16**(22), pp. 2028-2032.

BARUAH, S. and DUTTA, J., 2009. Hydrothermal growth of ZnO nanostructures. *Science and Technology of Advanced Materials,* **10**(1), pp. 013001.

BITENC, M. and OREL, Z.C., 2009. Synthesis and characterization of crystalline hexagonal bipods of ZnO. *Materials Research Bulletin,* **44**(2), pp. 381-387.

CATTI, M., NOEL, Y. and DOVESI, R., 2003. Full piezoelectric tensors of wurtzite and zinc blende ZnO and ZnS by first-principles calculations. *Journal of Physics and Chemistry of Solids,* **64**(11), pp. 2183-2190.

CHANG, P., FAN, Z., WANG, D., TSENG, W., CHIOU, W., HONG, J. and LU, J.G., 2004. ZnO nanowires synthesized by vapor trapping CVD method. *Chemistry of materials,* **16**(24), pp. 5133-5137.

CHEN, W., LIU, W., HSIEH, S. and TSAI, T., 2007. Preparation of nanosized ZnO using α brass. *Applied Surface Science,* **253**(16), pp. 6749-6753.

CHIU, W., KHIEW, P., CLOKE, M., ISA, D., TAN, T., RADIMAN, S., ABD- SHUKOR, R., HAMID, M.A., HUANG, N. and LIM, H., 2010. Photocatalytic study of two-dimensional ZnO nanopellets in the decomposition of methylene blue. *Chemical Engineering Journal,* **158**(2), pp. 345-352.

EMANETOGLU, N., GORLA, C., LIU, Y., LIANG, S. and LU, Y., 1999. Epitaxial ZnO piezoelectric thin films for saw filters. *Materials Science in Semiconductor Processing,* **2**(3), pp. 247-252.

FAN, Z., CHANG, P., LU, J.G., WALTER, E.C., PENNER, R.M., LIN, C. and LEE, H.P., 2004. Photoluminescence and polarized photodetection of single ZnO nanowires. *Applied Physics Letters,* **85**(25), pp. 6128-6130.

FAN, Z. and LU, J.G., 2005. ZnO nanostructures: synthesis and properties. *Journal of nanoscience and nanotechnology,* **5**(10), pp. 1561- 1573.

FRADE, T., JORGE, M.M. and GOMES, A., 2012. One-dimensional ZnO nanostructured films: Effect of oxide nanoparticles. *Materials Letters,* **82**, pp. 13-15.

GAO, P.X. and WANG, Z.L., 2004. Substrate atomic-termination-induced anisotropic growth of ZnO nanowires/nanorods by the VLS process. *The Journal of Physical Chemistry B,* **108**(23), pp. 7534-7537.

GU, Y., KUSKOVSKY, I.L., YIN, M., O'BRIEN, S. and NEUMARK, G., 2004.Quantum confinement in ZnO nanorods. *Applied Physics Letters,* **85**(17), pp. 3833-3835.

HUANG, Y., HE, J., ZHANG, Y., DAI, Y., GU, Y., WANG, S. and ZHOU, C., 2006. Morphology, structures and properties of ZnO nanobelts fabricated by Zn- powder evaporation without catalyst at lower temperature. *Journal of Materials Science,* **41** (10), pp. 3057-3062.

HUGHES, W.L. and WANG, Z.L., 2003. Nanobelts as nanocantilevers. *Applied Physics Letters,* **82**(17), pp. 2886-2888.

JAGADISH, C. and PEARTON, S.J., 2011. *ZnO bulk, thin films and nanostructures: processing, properties, and applications.* Elsevier.

JOSE-YACAMAN, M., GUTIERREZ-WING, C., MIKI, M., YANG, D., PIYAKIS, K. and SACHER, E., 2005. Surface diffusion and coalescence of mobile metal nanoparticles. *The Journal of Physical Chemistry B,* **109**(19), pp. 9703-9711.

JOSHI, P., CHAKRABORTI, S., CHAKRABARTI, P., HARANATH, D., SHANKER, V., ANSARI, Z., SINGH, S.P. and GUPTA, V., 2009. Role of surface adsorbed anionic species in antibacterial activity of ZnO quantum dots against Escherichia coli. *Journal of nanoscience and nanotechnology,* **9**(11), pp. 6427-6433.

KLINGSHIRN, C.F., WAAG, A., HOFFMANN, A. and GEURTS, J., 2010. *Zinc oxide: from fundamental properties towards novel applications.* Springer Science & Business Media.

KOCH, M., TIMBRELL, P. and LAMB, R., 1995. The influence of film crystallinity on the coupling efficiency of ZnO optical modulator waveguides. *Semiconductor science and technology,* **10**(11), pp. 1523.

KONG, X.Y., DING, Y., YANG, R. and WANG, Z.L., 2004. Single crystal nanorings Formed by epitaxial self-coiling of polar nanobelts. *Science (New York, N.Y.),* **303** (5662), pp. 1348-1351.

LEE, J., CHOI, Y., KIM, J., PARK, M. and IM, S., 2002. Optimizing n-ZnO/p-Si heterojunctions for photodiode applications. *Thin Solid Films,* **403**, pp. 553- 557.

LI, Q., MAHENDRA, S., LYON, D.Y., BRUNET, L., LIGA, M.V., LI, D. and ALVAREZ, P.J., 2008. Antimicrobial nanomaterials for water disinfection and microbial control: potential applications and implications. *Water research,* **42**(18), pp. 4591-4602.

LI, W., SHI, E., TIAN, M. and ZHONG, W., 1998. Synthesis of ZnO fibers and nanometer powders by hydrothermal method. *Science in China Series E: Technological Sciences,* **41**(5), pp. 449-459.

LIANG, S., SHENG, H., LIU, Y., HUO, Z., LU, Y. and SHEN, H., 2001. ZnO Schottky ultraviolet photodetectors. *Journal of Crystal Growth,* **225**(2), pp. 110-113.

LIN, Y., ZHANG, Z., TANG, Z., YUAN, F. and LI, J., 1999. Characterisation of ZnO-based varistors prepared from nanometre Precursor powders. *Advanced Materials for Optics and Electronics,* **9**(5), pp. 205-209.

LIU, C., YIU, W., AU, F., DING, J., LEE, C. and LEE, S., 2003. Electrical properties Of zinc oxide nanowires and intramolecular p–n junctions. *Applied Physics Letters,* **83**(15), pp. 3168-3170.

LIU, J., HUANG, X., LI, Y., SULIEMAN, K., SUN, F. and HE, X., 2006. Selective growth and properties of zinc oxide nanostructures. *Scripta Materialia,* **55**(9), pp. 795-798.

MA, X. and ZHANG, W., 2009. Effects of flower-like ZnO nanowhiskers on the mechanical, thermal and antibacterial properties of waterborne polyurethane. *Polymer Degradation and Stability,* **94**(7), pp. 1103-1109.

MITRA, P., CHATTERJEE, A.P. and MAITI, H.S., 1998. ZnO thin film sensor. *Materials Letters,* **35**(1), pp. 33-38.

MOLARIUS, J., KAITILA, J., PENSALA, T. and YLILAMMI, M., 2003. Piezoelectric ZnO films by rf sputtering. *Journal of Materials Science: Materials in Electronics,* **14**(5), pp. 431-435.

NIKOOBAKHT, B., WANG, X., HERZING, A. and SHI, J., 2013. Scalable synthesis and device integration of self-registered one-dimensional ZnO nanostructures and related materials. *Chemical Society Reviews,* **42**(1), pp. 342-365.

PAN, Z.W., DAI, Z.R. and WANG, Z.L., 2001. Nanobelts of semiconducting oxides. *Science (New York, N.Y.),* **291**(5510), pp. 1947-1949.

POLSHETTIWAR, V., BARUWATI, B. and VARMA, R.S., 2009. Self-assembly of metal oxides into three-dimensional nanostructures: synthesis and application in catalysis. *Acs Nano,* **3**(3), pp. 728-736.

SAITO, N., HANEDA, H., SEKIGUCHI, T., OHASHI, N., SAKAGUCHI, I. and KOUMOTO, K., 2002. Low-temperature fabrication of light-emitting ZnO micropatterns using self-assembled monolayers. *Advanced Materials,* **14**(6), pp. 418-421.

SAPKOTA, A., ANCENO, A.J., BARUAH, S., SHIPIN, O.V. and DUTTA, J., 2011. ZnO Nanorod mediated visible light photoinactivation of model microbes in water. *Nanotechnology,* **22**(21), pp. 215703.

SINGH, S., 2013. ZnO Nanostructures; Synthesis, Characterizations and Device Applications. *Journal of Nanoengineering and Nanomanufacturing,* **3**(4), pp. 283-310.

WAHAB, R., ANSARI, S., KIM, Y., SEO, H. and SHIN, H., 2007. Room temperature Synthesis of needle shaped ZnO nanorods via sonochemical method. *Applied Surface Science,* **253**(18), pp. 7622-7626.

WANG, X., YANG, F., YANG, W. and YANG, X., 2007. A study on the antibacterial activity of one-dimensional ZnO nanowire arrays: effects of the orientation and plane surface. *Chemical communications,* (42), pp. 4419-4421.

WÜTHRICH, C.R., MULLER, C.A., FOX, G.R. and LIMBERGER, H.G., 1998. All-fibre acousto-optic modulator using ZnO piezoelectric actuators. *Sensors and Actuators A: Physical,* **66**(1-3), pp. 114-117.

XIE, Q., DAI, Z., LIANG, J., XU, L., YU, W. and QIAN, Y., 2005. Synthesis of ZnO three-dimensional architectures and their optical properties. *Solid State Communications,* **136**(5), pp. 304-307.

XU, T., JI, P., HE, M. and LI, J., 2012. Growth and structure of pure ZnO micro/nanocombs. *Journal of Nanomaterials,* **2012**, pp. 12.

YANG, P., YAN, H., MAO, S., RUSSO, R., JOHNSON, J., SAYKALLY, R., MORRIS, N., PHAM, J., HE, R. and CHOI, H., 2002. Controlled growth of ZnO nanowires and their optical properties. *Advanced Functional Materials,* **12**(5), pp. 323.

ZHAO, M., WANG, Z. and MAO, S.X., 2004. Piezoelectric characterization of individual ZnO nanobelt probed by piezoresponse force microscope. *Nano Letters,* **4**(4), pp. 587-590.

ZHAO, X., KIM, C., LEE, J., SHIN, C., HEO, J., LEEM, J., RYU, H., CHANG, J., LEE, H. and SON, C., 2009. Effects of thermal annealing temperature and duration on hydrothermally grown ZnO nanorod arrays. *Applied Surface Science,* **255**(11), pp. 5861-5865.

Chapter 3

Synthesis of Zinc Oxide (ZnO) Nanostructures

An assortment of ZnO nanostructures including particles, wires, needle, spiral, helical, flower, tetrapod etc. have been fabricated by employing several physical and chemical methods. Particularly, each synthesis method has its benefits and drawbacks, and in this chapter, different physical and chemical methods to fabricate several forms of ZnO nanomaterials are introduced and the relevance to this work highlighted.

3. 1. Solution phase synthesis

Solution phase synthesis is one of the most used techniques to fabricate ZnO nanostructures (Chandran, Mallik 2018). It is known as hydrothermal growth process and can be performed in liquid, such as aqueous or organic medium (Kim, Cho et al. 2011). Normally, it is driven by the interaction between a zinc precursor like zinc acetate, zinc nitrate, zinc chloride and a reductant agent like sodium or ammonium hydroxide/nitrates/carbonates. Various solution-processing routes such as precipitation, solvothermal, hydrothermal, sol–gel, electrochemical, sonochemical are presented in the following context. Appealing features including scalability and ease of handling, environment-friendly, low experimental budget, low- temperature growth (< 200^0 C), compatibility with flexible organic substrates, large scale deposition over heat-sensitive substrate enable such techniques to be the most common and suitable alternative for ZnO nanomaterials synthesis (Isik, Hilal et al.2019).

In addition, wet chemical processes provide a rational morphology control of ZnO nanostructures and its properties to achieve prominent level of the nanodevices performance.

3. 1. 1. Hydrothermal Method

The hydrothermal growth method is a versatile growth technique for ZnO nanowires fabrication (Eswar, Suhaimi et al. 2018), (Zhu, Li et al. 2018). The temperature and duration of the hydrothermal reaction are the crucial factors to generate diverse forms of ZnO nanomaterials (Mohd Fudzi, Zainal et al. 2018). A typical setup for the hydrothermal growth process of ZnO nanostructures is demonstrated in figure 3. 1.

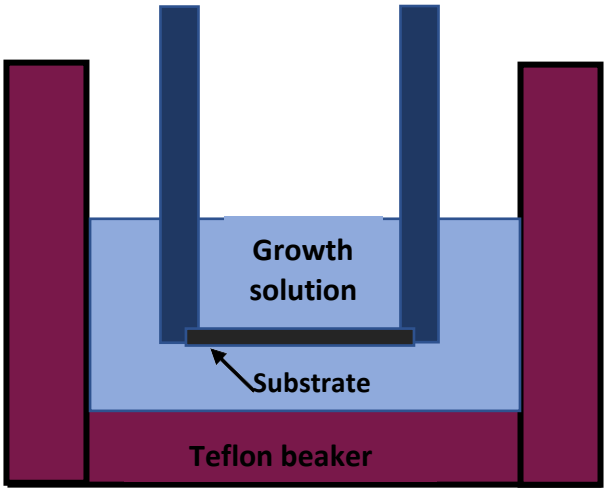

Figure 3. 1. A schematic diagram for the hydrothermal method of ZnO nanostructures.

In addition, Type and ratio of zinc precursor, solvent type, seeding layer, ratio of surfactant/polymers (auxiliary agent) utilised, and pH of the growth

solution is some of the factors to tailor dimension, geometry and crystallinity of nanostructures grown by solution-based methods. These solution-based growth parameters are separately discussed in the following subsections.

Generally, the formation of high quality and well-ordered ZnO nanowires by wet chemical techniques includes three main stages which are:

(1) Seeding a thin layer of ZnO nanoparticles on the surface of a specific substrate, this seed layer can be produced by several ways such as sputter deposition, spin-coating techniques, thermal decomposition, and physical vapor deposition (PVD). It plays a key role in promoting homogeneous nucleation sites due to the non-polar planes have lower energy barriers with more stability (Sugunan, Warad et al. 2006a).

(2) Preparing the growth solution by mixing an alkaline reagent such as sodium hydroxide (NaOH) or Hexamethylenetetramine (HMTA) and Zn^{2+} salt like Zinc nitrate hydrate ($Zn(NO_3)_2$), zinc chloride ($ZnCl_2$), etc.

(3) Pre-seeded ZnO substrate is immersed into the reaction solution for a particular time and temperature, and then the resultant ZnO substrate is cleaned with deionized water (DI) and dried.

It has been suggested that the position of the substrate inside the precursor solution is very critical, therefore, it is important to set the substrate in a floatable situation, facing down to prevent any bulk precipitates from the solution to drift and settle down on the substrate (Xu, Lao et al. 2008). One of the most important things to synthesize ZnO nanowires is that controlling the supersaturation levels of the growth solution.

Weintraub et al (Weintraub, Zhou et al. 2010) have supposed that high supersaturation levels of precursors prefer to promote nucleation sites of ZnO while low supersaturation levels are more likely to boost ZnO crystal growth. It is believed that if an abundant of hydroxide molecules are provided in a short duration of time, the pH value will be higher, as a result, the Zn^{2+} ions in growth solution will precipitate rapidly and contribute less to as-grown ZnO nanowires (Xu, Lao et al. 2008). In this way, it is preferable to keep the supersaturation of reactions at lower levels by governing the concentration of hydroxide molecules throughout the growth method (Zhang, Ram et al. 2012). The hydrothermal growth method is a series of chemical reactions that are mostly considered to be in a reversible equilibrium. The principal chemical reactions included in the ZnO fabrication are highlighted by following equations (Demianets, Kostomarov 2001):

$$Zn^{2+} + 2OH^- \leftrightarrow Zn(OH)_2 \quad (1)$$

$$Zn(OH)_2 + 2OH^- \leftrightarrow [Zn(OH)_4]^{2-} \quad (2)$$

$$[Zn(OH)_4]^{2-} \leftrightarrow ZnO_2^{2-} + 2H_2O \quad (3)$$

$$ZnO_2^{2-} + H_2O \leftrightarrow ZnO + 2OH^- \quad (4)$$

$$ZnO + OH^- \leftrightarrow ZnOOH^- \quad (5)$$

It is important to reduce the free energy during these reactions and this is an inherent nature of hydrothermal growth process (Xu, Shen et al. 2010). The growth mechanism of ZnO nanostructures is mainly correlated to the high energy polar surfaces of ZnO such as ± (0001). At the beginning of ZnO nucleation, the precursor molecules are more likely to be adsorbed on the polar facets $\pm\ (0001)$, specifically the surface energy of Zn-polar (0001) is larger compared to that of O-polar (0001). In such a crystal arrangement, the adsorption of arriving ions is more likely on the polar surfaces for the minimization of surface energy through the nucleation of ZnO crystals. It has been shown that the Zn-polar (0001) surface is more unstable and active than the O-polar (0001) surface (Yufei, Zhiyou et al. 2010). As a result, the polar surface changes into another polar surface with reversed polarity and a Zn^{2+} terminated surface alters into O^{2-} terminated surface or vice versa. Frequently, this procedure is repeated, resulting in a rapid growth of ZnO nanostructures along the c-axis directions (Xu, Wang 2011).

Generally, ZnO is an amphoteric oxide and has (IEP) value ~9.5 so, it crystallizes by the hydrolysis of zinc salts in a strong or weak alkaline environment (Xu, Wang 2011). Consequently, alkaline solutions play an essential role in crystallizing ZnO nanostructures (Demianets, Kostomarov et al. 2002), (Li, Chen et al. 2019). Mainly, the concentration of the alkaline solution and temperature influence the solubility of ZnO, as the rate of ZnO hydrolysis increases with alkaline concentration and temperature (Xu, Wang 2011). The most frequently basic compounds used to generate ZnO nanostructures are sodium hydroxide (NaOH) and potassium hydroxide (KOH). Favourably, (KOH) is used much more than (NaOH), because potassium ions have a larger radius and hence

is unlikely to integrate into the ZnO lattice (Demianets, Kostomarov et al. 2002). In addition, it has been reported that sodium cations are connected by hydroxide anions in closeness to the nanocrystal, leading to form a virtual capping layer that suppresses the nanocrystal growth (Viswanatha, Amenitsch et al. 2007).

For equation (2), the zinc compounds can take different intermediate forms including Zn $(OH)^{+}$, Zn $(OH)_2$, Zn $(OH)^{-}_3$ according to the concentration of Zn^{2+} and the PH value of reaction (shown in Figure 3. 2 (a)). The wet chemical method can be interpreted as follows (Kawska, Duchstein et al. 2008). Zinc cations and hydroxide ions correlate with each other at the initiation of the process, later they release protons in order to endure dehydration and then Zn^{2+}- O^{2-} - Zn^{2+} bonds are created, resulting in aggregating of octahedral formula of $[Zn_x\ (OH)_y]^{(2x-y)+}$. During dehydration, the H_2O molecules develop into solution, these agglomerations normally include less than 50 ions. The wurtzite form (tetrahedral coordination) of ZnO domains nucleate in the middle region of the agglomeration after the number of molecules increases to about 150 ions (Figure 3. 2 (b)).

The centre of agglomeration just consists of Zn^{2+} and O^{2-} ions, whereas the surface mostly involves Zn^{2+} and OH^{-} ions. Exceeding the number of ions to more than 200 ions via further supplementary, resulting in the development of wurtzite structured ZnO (Kawska, Duchstein et al. 2008). In such an aqueous method pH value of the precursor solutions determines the crystal phase of solution-processing nanostructures.

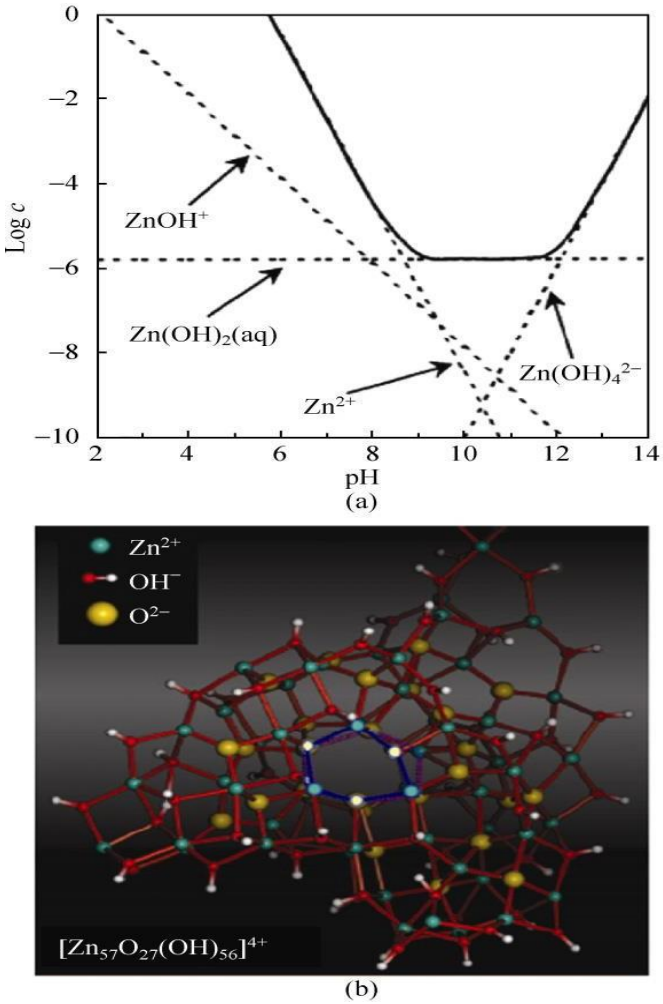

Figure 3. 2. (a) Variation in precursor concentration and PH of the ZnO(s)-H2O system at 25^0 C, the dashed lines refer to the thermodynamic stability between the Zn^{2+} collections and the equivalent solid phase. Reprinted with permission from (Yamabi, Imai 2002). (b) An agglomeration and nucleation of domains of the wurtzite structured ZnO, the centred-six rings highlighted in blue generate equilibrium and alignment of wurtzite structure. Reprinted with permission from (Kawska, Duchstein et al. 2008).

It is reported that both ZnO and Zn $(OH)_2$ are thermodynamically stable within a range of 7-14 of Ph value at a 0.01 M Zn concentration (Yamabi, Imai 2002). At pH value >9, the reaction is more likely to move forward because of the development of soluble Zn complexes in the form of Zn $(OH)_2$, $[Zn(OH)_4]^{2-}$ and etc in the solution with higher chemical potential of OH^- ion (Yamabi, Imai 2002).

By using an alkaline solution, the reactions may occur at room temperature via modifying the concentration of Zn^{2+} and OH^-. Cao et al (Cao, Qian et al. 2006) have revealed that it can be easily produced ZnO nanowires with different aspect ratios by tailoring hydroxide concentration and the duration of the reaction. It is worthwhile to mention here that $ZnOOH^-$ and ZnO^{2-} are the other two essential zinc species in the precursor solution where the predominance of one depends on the hydroxide concentration and reaction temperature (Demianets, Kostomarov 2001). Zhang et al have reported that producing ZnO nanostructures does not need the solvent to be water (H_2O), due to the O^{2-} ions in ZnO arises from alkaline solution not from (H_2O) (Zhang, Sun et al. 2002).

Typically, the above equations (1-5) illustrate agreeable reaction mechanism, however, the growth of ZnO nanostructures is probably much more complicated, e.g., oxygen ratio potentially influences the construction and growth of ZnO nanostructures. In addition, the comparative growth rates of polar and non-polar facets govern the aspect ratio of ZnO nanowires, as a result, it could be controlled by changing solvent polarity. Solvent molecules with high polarity have extremely energetic and strong interactions with ZnO polar surfaces, and thus inhibit precursor ions to be absorbed by the polar surface.

3. 1. 1. 1. Effect of seeded ZnO layer

The most advantageous thing about solution-processing approach is that, using ZnO seed layer, typically the structural properties of ZnO nanomaterials including its morphology, density, orientation, and facial distribution on the substrate, that mainly affect the performance of the subsequently grown nanostructures, are determined by the quality of the seeding layer (Baruah, Dutta 2009a).

A wide range of different substrates can be utilised for ZnO nanowires growth, such as Si wafers (Cheng, Yan et al. 2010), ITO coated glass (Mekhnache, Drici et al. 2011), polyethylene terephthalate (PET) (Yi, Choi et al. 2007), polydimethylsiloxane (PDMS) (Greene, Law et al. 2003), thermoplastic polyurethanes (TPU) (Liu, Liao et al. 2006), paper (Manekkathodi, Lu et al. 2010), fibres (Bae, Song et al. 2011), and carbon fibres (Na, Gong et al. 2009) (Figure 3. 3).

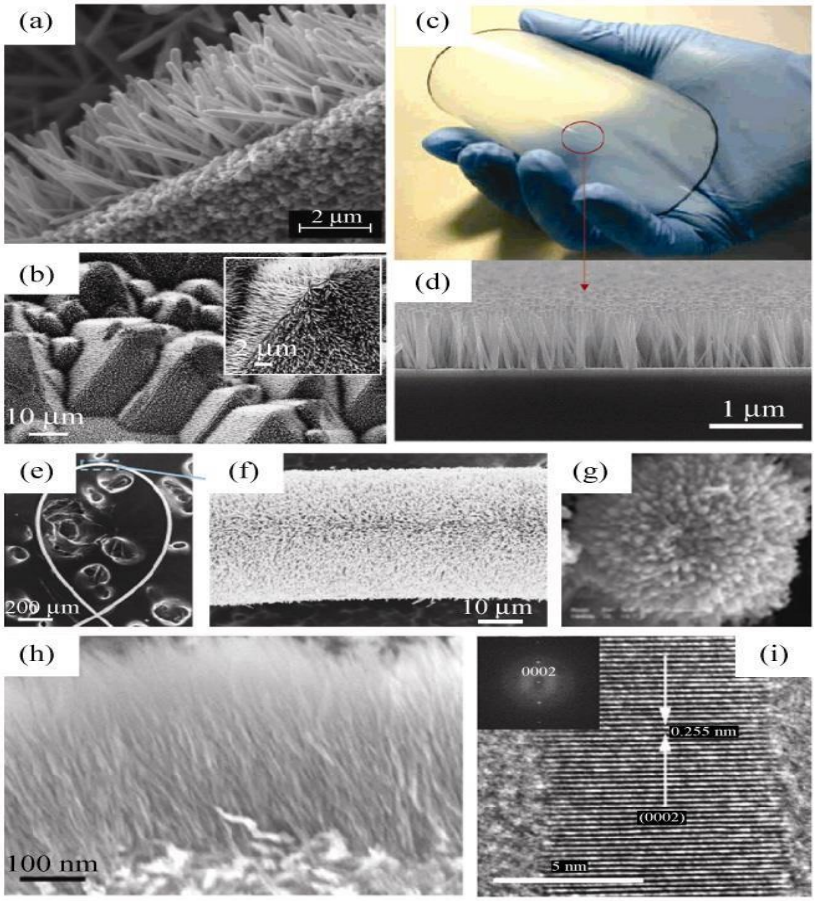

Figure 3. 3. SEM images of ZnO nanowires grew on a different ZnO seed layers (a) solid flat substrate. Reprinted with permission from (Vayssieres 2003), (b) etched Si wafer (inset displays a magnified view) Reprinted with permission from (Xu, Wang 2011). (c) A picture of a four- inch TPU substrate. Reprinted with permission from (Liu, Liao et al. 2006), (d) (SEM) image of well-ordered ZnO nanowires fabricated on the TPU substrate. Reprinted with permission from (Liu, Liao et al. 2006).

(e) (SEM) image of ZnO nanowires grew on a looped Kevlar fibre. Reprinted with permission from (Qin, Wang et al. 2008), (f) a magnified sector of (e). Reprinted with permission from (Qin, Wang et al. 2008). (g) (SEM) image of ZnO nanowires synthesized on a polystyrene sphere. Reprinted with permission from (Yang, Chu et al. 2006). (h) (SEM) Cross-section image of ultrathin ZnO nanofibres produced on a Zn metal substrate. Reprinted with permission from (Fang, Pang et al. 2006). (i) (TEM) image of a single ZnO nanofiber. Reprinted with permission from (Fang, Pang et al. 2006).

Furthermore, zinc metal could be used as a seed layer because of it can easily oxidize to ZnO in air and liquid mediums; Fang et al (Fang, Pang et al. 2006) used Zn metal as a substrate with growth solution that contained an ammonia and water or an alcohol and water to grow relatively high-density arrays of ultrathin ZnO nanofibres (Figure 3. 3). Kar et al (Kar, Dev et al. 2006) have shown that using NaOH with an ethanol as solution solvent could produce diverse species of ZnO morphologies on Zn foil, including nanosheets, nanonails, well-ordered nanorods. Wu et al (Wu, Bai et al. 2006) have used Zn $(NO_3)_2$ and KOH to fabricate well-oriented ZnO arrays on the zinc foil at room temperature. They have demonstrated that needle- like structures were produced by immediately oxidizing zinc foil in alkaline zincate ion mixture at low temperature while nanorod structure was formed at slightly elevated temperature. Maiti et al (Maiti, Maiti et al. 2014) has fabricated different morphology of ZnO nanostructures over zinc foil in alkaline supersaturated mixture including zinc salt.

The seed nanocrystals are assumed to create heterogeneous nucleation sites that are needed for the crystallization of the nanomaterials during the hydrothermal growth process. The seed layer in the form of thin film or nanoparticles could be coated previously on the substrate (Vayssieres

2003), (Boyle, Govender et al. 2002). Usually, it has been several ways to prepare ZnO seed layer such as, PVD, the thermal decomposition of zinc acetate, but the two most commonly used methods are sputtering deposition and spin coating of colloidal quantum dots (Sun, Luo et al. 2008). In addition, seeding layers have been produced by dip coating, whereby ZnO nanocrystallites were produced through in-situ oxidation on heated substrates in air. This has been shown to be effective compared to other ways involve dipping the substrate with pre-grown ZnO nanoparticles because these nanoparticles are agglomerated in small groups, so that, each particle could have many of polar facets oriented randomly. While, in the in-situ crystallization, each particle allows only one rod to grow from it because the single crystals are very tiny with uniform distribution over the surface (Baruah, Dutta 2009a). Baruah et al (Baruah, Thanachayanont et al. 2008) have adopted the dip coating approach to deposit a uniform layer of ZnO nanoparticles on a nonwoven polyethylene fibre. Zhao et al (Zhao, Jin et al. 2006) have followed the dip coating route to deposit ZnO seed layer by dissolving (0.75 mol/L) of Zn $(CH_3COO)_2 \cdot 2H_2O$ in (0.75 mol/L) of 2-methoxyethanol and monoethanolamine (MEA) solution with stirring at 60^0 C for 30 min. It was highlighted that the structure and thickness of the seed layer were influenced by dipping time, withdrawal speed, heating and cooling process.

It is essential that annealing ZnO seed at particular temperature in order to boost the adhesion of ZnO nanoparticles to the substrate and enhance the nanowires perpendicular alignment (Zhang, Ram et al. 2012), (Slimani, Justeau et al. 2018).

It could increase the adherence of the seed layer to substrate by fabricating an intermediate layer like Cr or Ti on inorganic substrates (Xu, Wei et al.

2008b), and by adding an interfacial bond layer such as tetraethoxysilane (TEOS) molecules on a polymer substrate (Qin, Wang et al. 2008). Greene et al (Greene, Law et al. 2005) have examined the impact of temperature on the seeding layer formed from zinc acetate on Si substrates; they suggested that producing well-ordered nanowires requires low temperature (150 - 200^0 C) while higher temperatures boost crystallinity growth. Baruah and Dutta (Baruah, Dutta 2009a) have shown that annealing the ZnO seed at a temperature of 350 ^{0}C can produce a well- aligned thin layer of ZnO nanoparticles. Ridhuan et al (Ridhuan, Razak et al. 2012) have prepared ZnO nanorod via using a facile hydrothermal approach on ZnO seeded n-type silicon substrate. It shown that the optimal thermal treatment temperature to generate uniform nanosized ZnO texture was 400°C. However, it has been noticed that elevating annealing temperature to 450^0 C could make ZnO crystallize into nanoparticles and nanorod-like structures, the researchers referred that the optimum annealing temperature of ZnO seed layer is about 350 ^{0}C (Zhang, Ram et al. 2012).

It has been many attempts to govern the thickness of the seed layer due to, thus, will help to tailor the density of ZnO nanoarrays. Liu et al (Liu, She et al. 2008) showed that when the thickness of the seed layer increased from 1.5 nm to 3.5 nm, the ZnO nanoarrays density rose from 6.8 $X10^4$ to 2.6 X 10^{10} nanowires/cm^2. Additional studies have shown the increase in nanowires diameter and decrease in their length and number of density as the result of the increase of the seed layer thickness (Ghayour, Rezaie et al. 2011). As it mentioned earlier, the seed layer can be formed by spin coating of colloidal dots, it is more likely to control the density of the colloidal dots by guiding the spin speed. In this case, adjusting the spin speed from 4000

to 8000 rpm, resulting in altering the density of dots from (1.8 ± 0.03) X 10^3 to (1.8 ± 0.03) X 10^2 dots/μm^2, therefore the density of ZnO nanowires arrays changed from (5.6 ± 0.01) X 10^2 to (1.2 ±0.01) X 10^2 nanowires/μm^2 (Sun, Luo et al. 2008). Ueno et al (Ueno, Maruo et al. 2010) have adopted spin coating approach to prepare a seed layer of zinc acetate dihydrate and sodium dodecyl sulfate (SDS) nanocomposite at spin speed (4000 rpm, 1min) for the nucleation of ZnO nanorods.

The crystallinity of the underlying seed layers not only affect the morphology of nanowires, but also their vertical alignment can be significantly dictated. The polycrystalline nature of the seed layer has been addressed as a reason behind the poor vertical alignment of ZnO nanowires arrays (Vayssieres 2003), (Boyle, Govender et al. 2002). It was reported that, the growth on a seeded substrate was comparatively influenced by heterogeneous and homogeneous nucleation, typically the energy barriers of heterogeneous nucleation were lower than that of homogeneous nucleation, and the surface free energy between crystal and substrate was normally less than that of crystal and solution (Vayssieres, Keis et al. 2001, Govender, Boyle et al. 2004). Therefore, heterogeneous growth takes place at low supersaturation levels than homogeneous growth (Boyle, Govender et al. 2002, Govender, Boyle et al. 2004).

Because of the large lattice mismatch (≈40%) between ZnO and Si, a lot of literature has used other materials that show less lattice mismatch with ZnO, such as Au (Shen, Bao et al. 2007), Pd (Lee, Yin et al. 2005),and Cu (Xu, Wei et al. 2006). Liu et al. (Liu, Vertegel et al. 2001) synthesized ZnO nanowires by electrodeposition route onto Au (111), Au (110), and Au (100) crystals, they produced well-aligned ZnO nanowires with high density along

c-axis. In addition, other materials have attracted researchers due to extremely little lattice mismatch between them and ZnO such as GaN (n- type) (Xu, Wei et al. 2008a) and (p-type) (Cole, Wang et al. 2008b), AIN, SiC, Al_2O_3, and $MgAl_2O_4$ substrates (Kim, Andeen et al. 2006). Because of GaN has very small lattice mismatch of 1.8% that is lower than that (12.7%) with Au (111) as well as the same wurtzite structure of ZnO (Pauporte, Lincot et al. 2006), approximately an ideal perpendicular alignment of ZnO nanowires arrays could be synthesized on n-type GaN (0001).

3. 1. 1. 2. Effect of an Ammonia and HMTA reagents

Weak basic solutions including ammonia solution and HMTA have been most likely adopted to grow ZnO nanostructures (Saranya, Devasena et al. 2019). Liu et al (Liu, Huang et al. 2007) fabricated ZnO nanowires in mild ammonia solutions at low temperature without using any catalysts and surfactants. Ammonium solution has a two- fold function in the synthesis method first, it supplies OH^- that is the source of oxygen. It also provides ammonium (NH^+4) which combines with Zn^+ ions to produce a complex as a buffering mechanism (Greene 2007). Further, ammonia aqueous solution not only generates an alkaline environment for solution-processing ZnO nanostructures, it also promotes the heterogeneous nucleation (Gao, Nagai et al. 2007). Commonly, HMTA has noteworthy benefits and its significant role in fabricating high-quality ZnO nanowires has been widely investigated (Govender, Boyle et al. 2004). HMTA is a highly water soluble, non-ionic tetradentate cyclic tertiary amine, despite a lot of literature has been examined the influence of HMTA during the

synthesis process, its role is still under debate. However, another review suggests that it functions as a bidentate Lewis base which can donate two pairs of electrons to the zinc ions to coordinate and bridge them to ZnO crystals (Xu, Wang 2011). When the HMTA ($(CH_2)_6N_4$) and Zn $(NO_3)_2$ are selected as precursors, the interaction mechanism can be demonstrated by the following equations (Xu, Wang 2011):

$$(CH_2)_6N_4 + 6H_2O \leftrightarrow 4NH_3 + 6HCHO \quad (6)$$

$$NH_3 + H_2O \leftrightarrow NH_4^+ + OH^- \quad (7)$$

$$Zn^{2+} + 4NH_3 \leftrightarrow [Z(NH_3)_4]^{2+} \quad (8)$$

$$Zn^{2+} + 2OH^- \leftrightarrow Zn(OH)_2 \quad (9)$$

$$Zn(OH)_2 \leftrightarrow ZnO + H_2O \quad (10)$$

HMTA provides hydroxide ions to the aqueous solution to push the precipitation reaction by thermal degradation (Ashfold, Doherty et al. 2007). Some studies have suggested that, HMTA could act as a weak base, PH buffer to adjust the pH value of the precursor medium and slow the contribution of hydroxide ions to control the growth rate of ZnO (Govender, Boyle et al. 2004). As presented in equations (6) and (7) HMTA hydrolyses in water, providing ammonia, and releasing the strain energy. Ammonia which further reacts with water and breaks down to hydroxide ion (OH^-) and forms $[Zn(NH_3)_4]^{2+}$. Typically, the synthesis process is crucially sensitive at this point due to the fast hydrolysis of HMTA would lead to yield a large quantity of hydroxide through a brief duration and increase PH value.

Such alkaline condition boosts the precipitation of zinc ions in the precursor solution therefore, these ions would rapidly precipitate and the aqueous growth solution would be quickly consumed, inhibiting supplemental synthesis of ZnO nanomaterials (Ashfold, Doherty et al. 2007). Govender et al have reported that the HMTA hydrolysis ratio declines with raising PH value and vice versa (Govender, Boyle et al. 2004). The decomposition of HMTA releases the Ammonia (NH_3) which creates a basic atmosphere that is essentially needed to produce Zn $(OH)_2$, additionally, it integrates with Zn^{2+} ions and stabilize them.

Further, compared to the ZnO precipitates Zn $(OH)_2$ is more dissoluble; therefore, the precipitates of Zn $(OH)_2$ are most likely to release Zn^{2+} and OH^- ions under elevated temperature. When utilizing microwave as heating source the reaction occurs quickly, increasing the growth rate of ZnO nanowires up to 100 $nm.min^{-1}$ (Unalan, Hiralal et al. 2008), while at the room temperature and solution concentration less than 10 mmol/L the growth solution can remain translucent for months (Xu, Wang 2011). The action of HMTA during ZnO nanowires growth has further been explained in entirely unlike way (Sugunan, Warad et al. 2006), it was suggested that because of (HMTA) is a long chain polymer and a non-polar chelating agent, it could be favourably intended to attach to the non-polar surfaces, resulting in blocking Zn^{2+} ions to get to them, exposing just the polar facets (001) for epitaxial growth along c-axis. Hence, it is more likely to act as a shape-inducing reactant instead as kinetic buffer to control the PH value in the solution (Figure 3. 4).

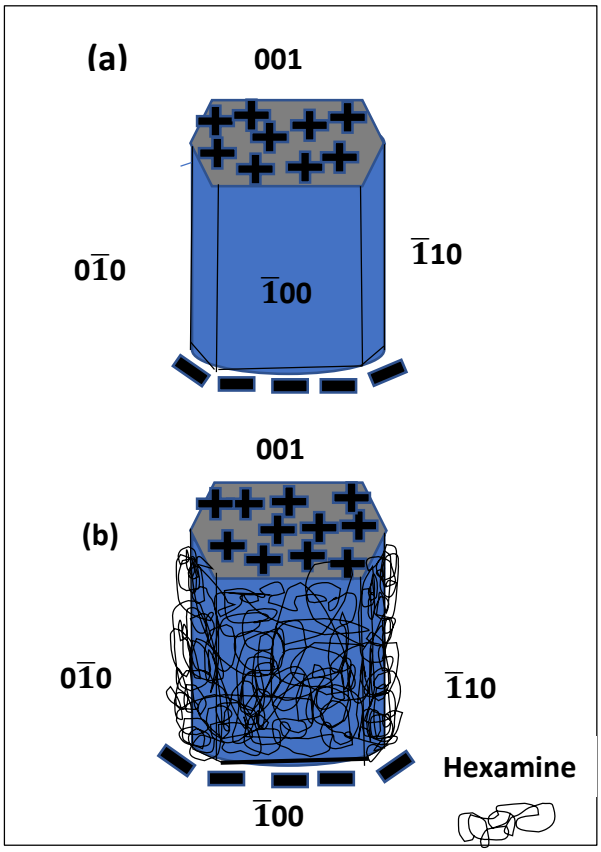

Figure 3. 4. (a) A wurtzite ZnO crystal. (b) potential connection of (HMTA) molecules with the non-polar side surfaces of the zincite crystal.

Recently, another attempt to understand the influence of HMTA on ZnO nanowires growth has been introduced by Parize et al (Parize, Garnier et al. 2016), it is found that HMTA significantly decreases the lateral growth of ZnO nanowires, by suppressing the growth evolution of their non-polar plane surfaces. In addition, their findings demonstrated diverse functions of HMTA in the synthesis of ZnO nanowires using chemical bath deposition, it is shown that a slight supply of HMTA compared to zinc nitrate is needed to attain the highest longitudinal growth rate of ZnO nanowires.

Additionally, HMTA is observed to serve as a pH buffer under a wide scale of bath concentration, except for high aqueous precursor ratios.

3. 1. 1. 3. Effect of solution concentration

There have been many reports that have attempted to discover the link between ZnO nanostructures synthesis and solution concentration (Rani, Zoolfakar et al. 2018). Xu et al carried out a number of examinations to find out the effect of precursor concentration on the nanowire's density (Xu, Lao et al. 2008). The empirical consequences indicated that when solution concentration changed from 0.1 to 5 mM, the density of ZnO nanowires rose from 55/100 μm^2 to 108/100μm^2. It gave a reason for that, increasing zinc concentration will lead to raising the chemical potential of zinc, to make equilibrium inside the growth reaction, more accommodation sites will create on the substrate surface, and hence an increase in the density of ZnO nanowires will be noticed. Nevertheless, if the density of nanowires was greater than the saturation density, any further increase in the precursor concentration will not raise the ZnO nanowires density. Wang et al investigated the impact of solution concentration at various ratios of [Zn $(NO_3)_2$] / [$C_6H_{12}N_4$] (Wang, Tseng et al. 2008). It observed that when the precursor concentration raised from 0.008 to 0.04 M the ZnO nanorods diameter approximately increased from 43 to 70 nm and the length from 65 to 320nm. The aspect ratio of ZnO nanorods increased from 1.8 to 5.8 and then slightly dropped to 4.6 (Figure 3. 5), however, it reached the highest point at 7.25 when the [Zn $(NO_3)_2$] / [$C_6H_{12}N_4$] ratio was set to unity (Figure 3. 6).

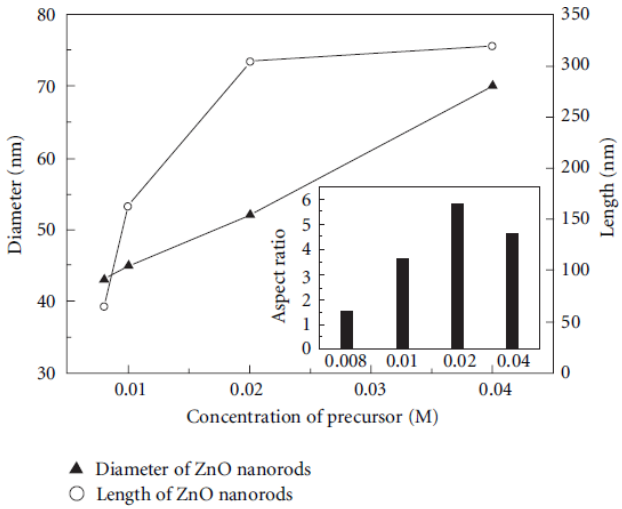

Figure 3. 5. Diameter, length, and aspect ratio of ZnO nanorods obtained at different solution concentration with a [Zn $(NO_3)_2$] / [$C_6H_{12}N_4$] ratio of 5. Reprinted with permission from (Wang, Tseng et al. 2008).

Another observation has shown that, an increase in the Zn^{2+} concentration from 0.01M to 0.033M results in raising of the length of ZnO nanorods from 400 nm to 1.5 μm, whilst their mean diameter was decreased from 160 to 100 nm (Le, Chua et al. 2006). Kim et al found that ZnO nanorods diameter and its density are broadly influenced by solution concentration (Kim, Lee et al. 2011). In addition, the structural transition of ZnO nanorods is affected by reactant concentration, when the concentration of Zn^{2+} was at lowest level ZnO nanorods crystallize in the form of a single crystal with low density, whereas the highest level of concentration resulting in polycrystalline growth of ZnO nanorods due to the supersaturated source of Zn^{2+}.

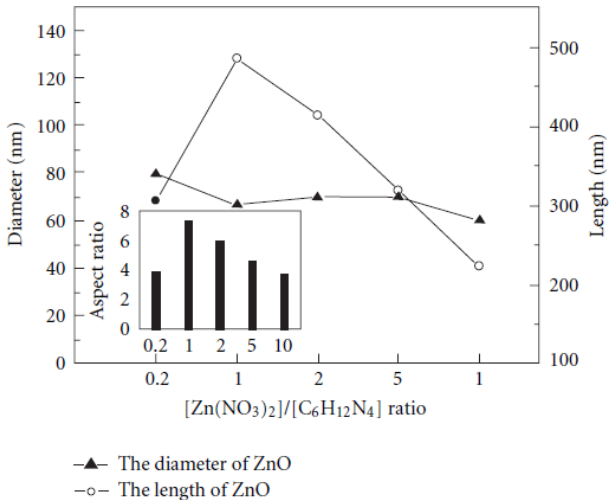

Figure 3. 6. Diameter, length, and aspect ratio of ZnO nanorods obtained in a 0.04 M precursor concentration at different [Zn $(NO_3)_2$] / [$C_6H_{12}N_4$] ratios. Reprinted with permission from (Wang, Tseng et al. 2008).

Heinonen et al (Heinonen, Nikkanen et al. 2016) have synthesized ZnO nanostructures on stainless steel plates by solution-based process, varying the aqueous precursor concentration from 0.029 M to 0.16 M and the growth temperature from 70˚C to 90 ˚C. It was shown that the nanostructures morphology was considerably temperature and precursor concentration dependent. Well-aligned nanoneedle structures were produced at lower base concentrations, while at higher concentrations, the needle-like structure changed to hexagonal columns.

3. 1. 1. 4. Effect of growth time

Synthesis ZnO nanowires is particularly sensitive to growth time (Mohd Fudzi, Zainal et al. 2018), Baruah and Dutta (Baruah, Dutta 2009a) synthesized ZnO nanowires on zinc acetate seeded substrate, they examined the growth at several durations(from 5 to 20 h). They have found that, during whole of 20 h

duration, the growth occurred at higher rate in the first 5 h afterward it decreased steadily due to the decline in the concentration of Zn^{2+} ions. Xu et al have introduced a similar finding and observed that in the beginning of the synthesis process, the growth rate along the lateral direction is faster (Xu, Lao et al. 2008). At the increase of time from 0.5 to 6 h, the growth mostly take place along c-axis direction [0001], whilst from 6 to 48 h the growth is significant along both radial and axial directions. Due to the synthesis rate of nanowires was low after a specific period of time, it has been a suggestion to refresh the precursor solution by frequently adding new solution into the bath to maintain the rate of growth (Sapkota, Anceno et al. 2011).

3. 1. 1. 5. Effect of the precursor's pH

The morphologies and synthesis rate of the as-deposited ZnO nanostructures have been shown to be strongly dependent on the pH value of precursor solution, as it dictates the concentration of the hydroxide ions in the nutrient solution. For instance, if the pH value was high the hydroxide concentration will be increased which can influence the growth rate (Amin et al. 2011). A diverse morphology and shape of ZnO nanostructures at variation of the pH value illustrated in Table 3. 1 (Baruah, Dutta 2009b).

Table 3. 1. Morphology and shape of ZnO nanostructures at variation of the precursor's pH (Baruah, Dutta 2009b).

pH	Morphology		Shape
9.0	Coalescence of Zno	Coalescence	Budding flower
9.5	Nano-particles	↑	
10.0	Zno nanorod		Blossom
10.5	Separation sharp rods	Separation	Chestnut but or echinoid
11.0	Separation of thick rods	↓	Dense chestnut bur
11.5	Coalescence of rods		Gingko leaves
11.8	Archetype of thick rods	Coalescence	Dendelion

Baruah and Dutta (Baruah, Dutta 2009c) have introduced detailed analysis on how varying the pH value could change the form and dimension of ZnO nanorods. The ZnO nanorods were synthesized on a seeded glass substrate by wet chemical approach and the growth solution was prepared by equal ratio of zinc nitrate and HTMA. During the growth process, the pH value had to change slowly from 6.4 to 7.3 over a time of 5 h, at the primary stage of growth with the basic environment of pH (8-12), ZnO NFs were produced. The authors showed that the variation of the reactant from acidic to alkaline takes place at the beginning phase of growth process subject to the concentration for example, the high precursor concentration fluctuates during the first hour of the synthesis procedure (Figure 3. 7). It also reported that the growth rate of the nanorods was faster in the alkaline condition than in the acidic one and the highest rate was observed at pH of 7.3, while the rods start decomposing at more than this value.

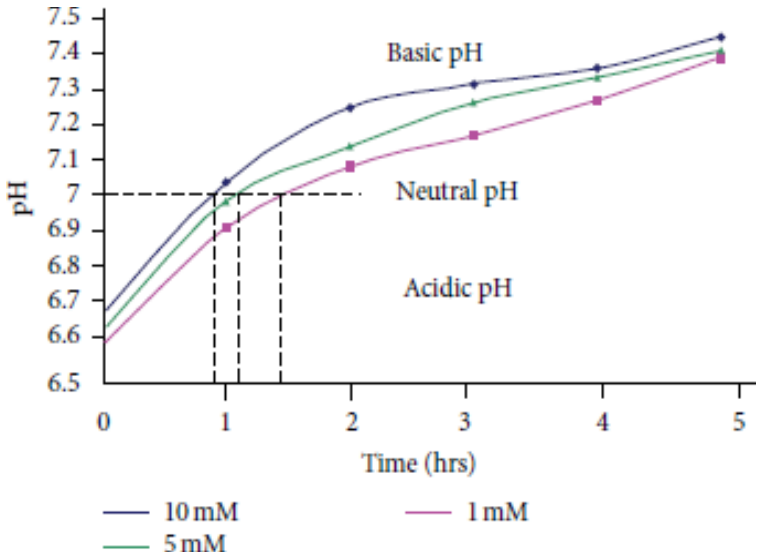

Figure 3. 7. Variation in the pH value over a time of 5 hrs during the ZnO nanorods growth. Reprinted with permission from (Baruah, Dutta 2009c).

Another analysis has offered by Akhavan et al to examine the effect of pH in the range from 7.5 to 11.44 on the morphology of ZnO nanorods, the precursor solution was prepared by Zinc nitrate and NaOH (Akhavan, Mehrabian et al. 2009). It has shown that an increase of nanorods diameter was noticed with increasing pH and then when pH came to 11.44, growing of a ZnO film was obtained. Furthermore, they reported that rapid growth of ZnO nanorods was identified at pH value of 11.33, causing a decrease in the optical band gap energy because of the formation of a lot of defects throughout this fast growth.

3. 1. 1. 6. Effect of growth temperature

Like other reaction parameters, the temperature of the growth could also significantly influence the dimension and morphology of ZnO nanostructures. Hou et al have fabricated various ZnO structures like multipods, tetrapods, nanoneedles, and nanowires by adapting the reaction temperatures at 620, 770, 840, and 900^0 C, respectively (Hou, Li et al. 2009). Tang et al have grown ZnO nanorods by using various reactants, like polyvinyl alcohol (PVA), polyethylene glycol (PEG), (SDS), or cetyltrimethylammonium bromide (CTAB) at higher growth temperatures for 5 h (Tang, Bao et al. 2008). Sondergaard et al have highlighted the impact of varied growth conditions on the hydrothermally synthesized ZnO nanoparticles (Søndergaard, Bøjesen et al. 2011). They found that the particle length and morphology are significantly temperature-dependent, cone-like particles of a maximal length of 1 µ were grown at a temperature of 122^0 C, whilst particles of 25 nm were formed at temperatures larger than 200^0 C.

3. 1. 1. 7. Effect of capping agent

Introducing capping agents into precursor solution could play a key role in adjusting the growth patterns of ZnO nanostructures (Zhang, Yang et al. 2005). In general, capping additives that can involve during the wet chemical growth of ZnO nanostructures may be categorized into two types: the first type accumulates on the side surface and promote the perpendicular growth, such as polyethyleneimine (PEI) (Wu, Hu et al. 2008) and ethylenediamine (EDA) (Shen, Bao et al. 2007), the other type covers onto the basal plane of ZnO nanostructures and then develops the lateral growth, like Chlorine (CI-) (Xu,

Guo et al. 2005) and citrate ions ($C_3H_5O(COO)^{3-}$) (Kim, Andeen et al. 2006). The charge of the surface sites of ZnO is governed by PH value, the (IEP) of ZnO powder is about PH =9.5 (Zang, Li et al. 2007), so at values of PH lower than the (IEP), ZnO surfaces will have positive charges while at values of PH higher of the (IEP) ZnO surfaces will have negative charges.

The function of PEI to dominate the growth of ZnO nanowires depends on an electrostatic relationship, and because of PEI contains a lot of amino groups it is easily protonated over a large scale of PH values (3-11) and make it positively charged. It is important to modify PH values in growth solution to be on the scale that allows PEI to be protonated, and then the high positively charged molecules of PEI actively adsorb on negatively charged surfaces (Figure 3. 8 (a)) (Wu, Hu et al. 2008).

Chen et al investigated the impact of PEI and ammonia on the ZnO nanowires formation, they observed that increasing the amount of PEI, causing a drop in the diameter and length of ZnO nanowires (Chen, Yin et al. 2011). Citrate ions are another capping agent that have been highlighted through a lot of literature due to possessing three negative charges in the usual growth environment. It reported that citrate ions could successfully accumulate to zinc ions on the polar surface (0001), and prevent growing nanowires along [0001] direction, therefore, the growth rate promotes along the $[01\bar{1}1]$ or $[2\bar{1}\bar{1}\,0]$ directions (Kim, Andeen et al. 2006), (Tian, Voigt et al. 2002), (Hidber, Graule et al. 1996) therefore, ZnO nanostructures like flat hexagonal nanoplates was synthesized (Figure 3. 8 (c)) (Kim, Andeen et al. 2006), (Tian, Voigt et al. 2002).

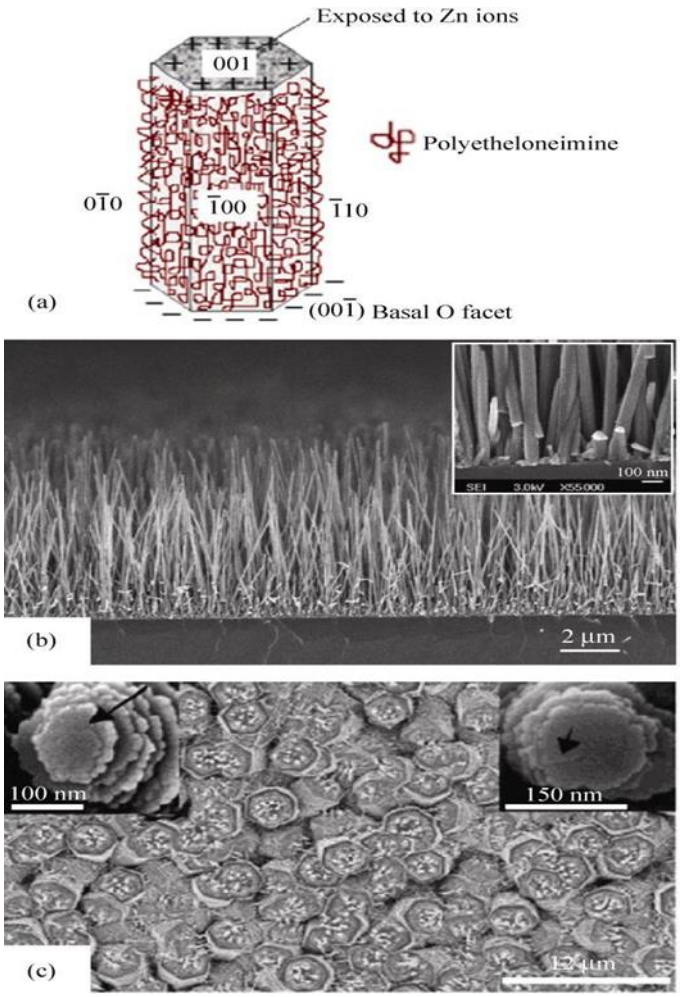

Figure 3. 8. (a) Attachment of PEI ions on the side facets of ZnO nanowires. Reprinted with permission from (Mclaren, Valdes-Solis et al. 2009). (b) SEM image of growing ZnO nanowires by adding PEI. Reprinted with permission from (Wu, Hu et al. 2008). (c) Well-ordered helical ZnO whiskers on top of ZnO rod base. Reprinted with permission from (Kim, Andeen et al. 2006).

3. 1. 2. Solvothermal Method

Conceptually, solvothermal method can be defined as the use of non- aqueous or combination of aqueous and non-aqueous as precursor solution in a reaction container (Figure 3. 9). By adjusting the growth processing parameters, like temperature, time, type of surfactant, precursor, and solvent, a precise control over the geometry and crystallinity of ZnO nanostructures might be achieved (Tiwari, Tiwari et al. 2012).

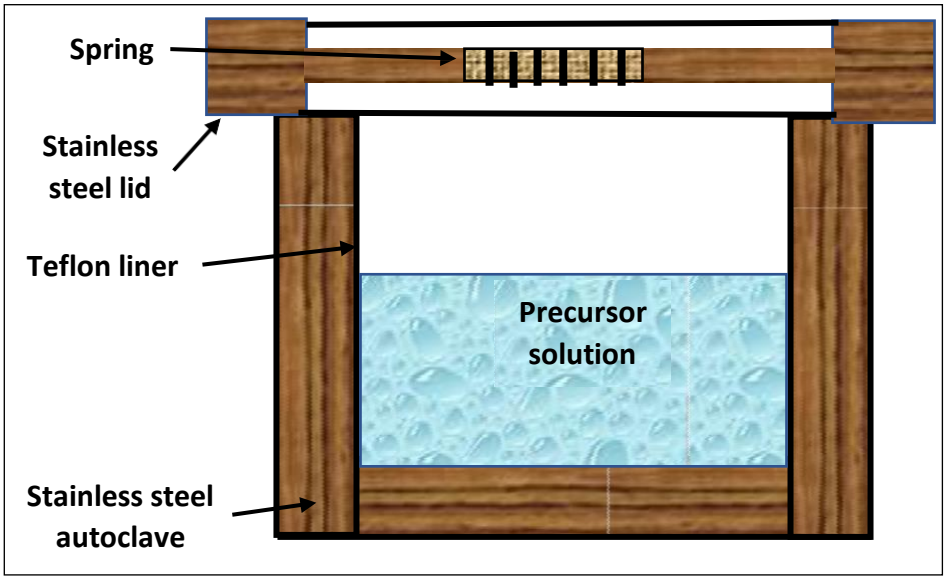

Figure 3. 9. A basic scheme of solvothermal system.

There is a lot of literatures on the fabrication of ZnO nanostructures by solvothermal approach under several reaction parameters (Dev, Kar et al. 2006, Tonto, Mekasuwandumrong et al. 2008). Tonto et al have produced solvothermal ZnO nanorods by using zinc acetate and different alcohols and have shown direct relationship of ZnO aspect ratio with the solvent boiling point and length of carbon chain in the alcohol (Tonto,

Mekasuwandumrong et al. 2008). Dev et al. have grown ZnO nanostructures on zinc foils by using different concentrations of water and (ENA) (Dev, Kar et al. 2006). It reported that with an increase of EN, a decrease in the diameter of ZnO nanorods was noticed while, their alignment was improved significantly. It also shown that the diameter and length of the ZnO nanorods increase with the growth time.

3. 1. 3. Precipitation Method

The precipitation method is another technique to fabricate ZnO nanostructures, during this process, concentration of zinc ions (nitrate or acetate or carbonate of zinc) is kept at a certain growth temperature (Bodke, Purushotham et al. 2018). At steady temperature, solvent of sodium or ammonium hydroxide is added under powerful stirring and heating for 3–4 hrs. Lastly, centrifugation is used to separate ZnO precipitate from the precursor medium and rinsed by DI water (Singh 2013). ZnO nanostructures have been produced by using different ratios of zinc acetate and Poly vinylpyrrolidone (PVP) as precursors solution. It was shown that the size of ZnO particles does not influence by the concentration of zinc acetate, but its morphology transforms from nanoplate to nanosphere at higher concentrations. In contrast, an increase in the PVP concentrations, causing a decline in the Crystallite size of ZnO particles (Suwanboon, Chukamnerd et al. 2007).

3. 1. 4. Sol–Gel Method

The sol–gel process is a very popular and widely used chemical solution deposition method for the fabrication of ZnO nanostructures by gelation, precipitation, and solution process (Kung, Ko 1996). A typical illustration of the sol–gel technique is shown in figure 3. 10. During such process, the synthesized materials are generated from a reaction solution (or sol) which services as the reactant for an integrated network (or gel).

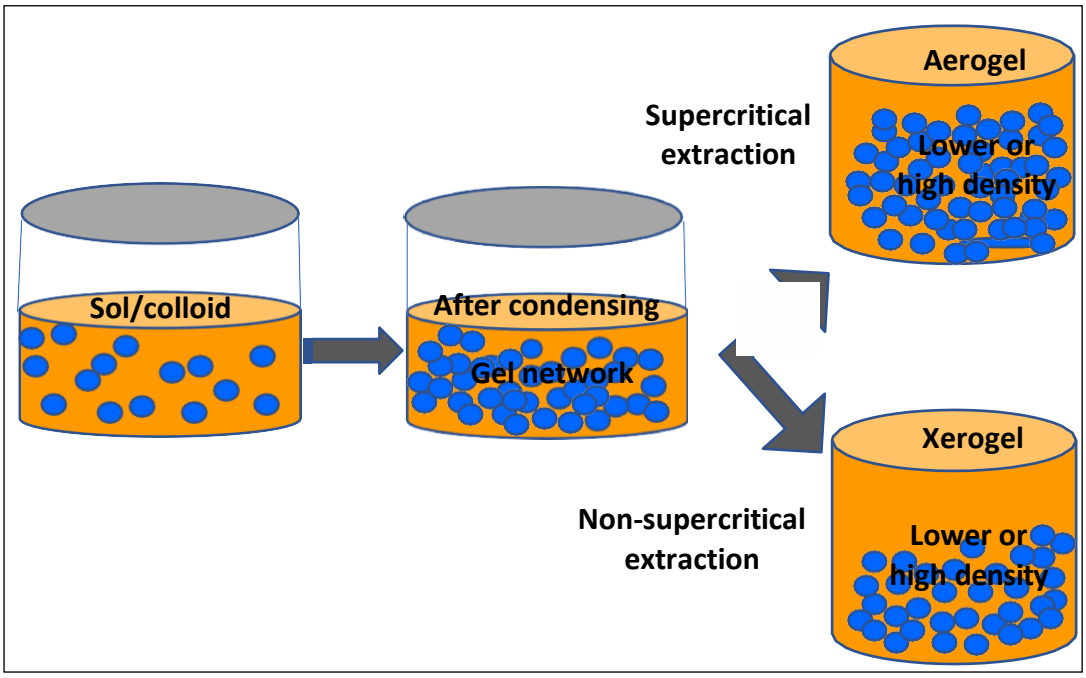

Figure 3. 10. Basic scheme for the sol–gel process.

Li et al have used sol–gel technique to synthesize ZnO nanostructures on silicon substrate, utilizing Zinc nitrate hexahydrate as zinc source, (HMTA) as stabilizing agent, and (DI) as solvent (Li, Srinivasan et al. 2008). By adding HNO_3 to precursor solution to produce neutral (pH = 7) and acidic medium (pH = 6),

different ZnO nanostructures were formed. It was shown that neutral solutions create ZnO nanorods, while acidic solutions generate rod or plate-like structures.The influence of solvents and stabilizer molar concentration on the structural and optical properties of the sol-gel-synthesized ZnO thin films were investigated to control their growth direction (Bekkari, Jaber et al. 2019).

Despite the noticeable progress in the investigations of the sol-gel mechanisms, the chemistry of reaction parameters and its influence on the material properties are still difficult to understand because of the various activities of the generation and modification of the network's elements and the large range of processing parameters (Schmidt 1988).

3. 1. 5. Electrochemical method

Electrochemical deposition is a method that employs electrical current for depositing a layer of metal/metal oxide nanostructure onto a desired conducting substrate (Izaki, Omi 1996). A lot of scientists have used the electrochemical deposition methods for the fabrication of nanostructures (Zhang, Zhou et al. 2010), (Sucharitakul, Panyathip et al. 2018). As shown in Figure 3. 11, the electrochemical deposition process is performed by using pulse electrodeposition (PE) which contains a three-electrode cell; thin Platinum wire, saturated calomel electrode (SCE) and counter (sample), reference and working electrodes, respectively. In the PE system, cathode potential, current density, deposition temperature, electrolyte structure and concentration are the main parameters influencing the morphology and dimension of nanostructured materials. The first electrochemically deposition of ZnO carried out by Izaki and Omi (Izaki, Omi 1996) using zinc nitrate as electrolyte, tin oxide as cathode and substrate, and zinc foil as anode.

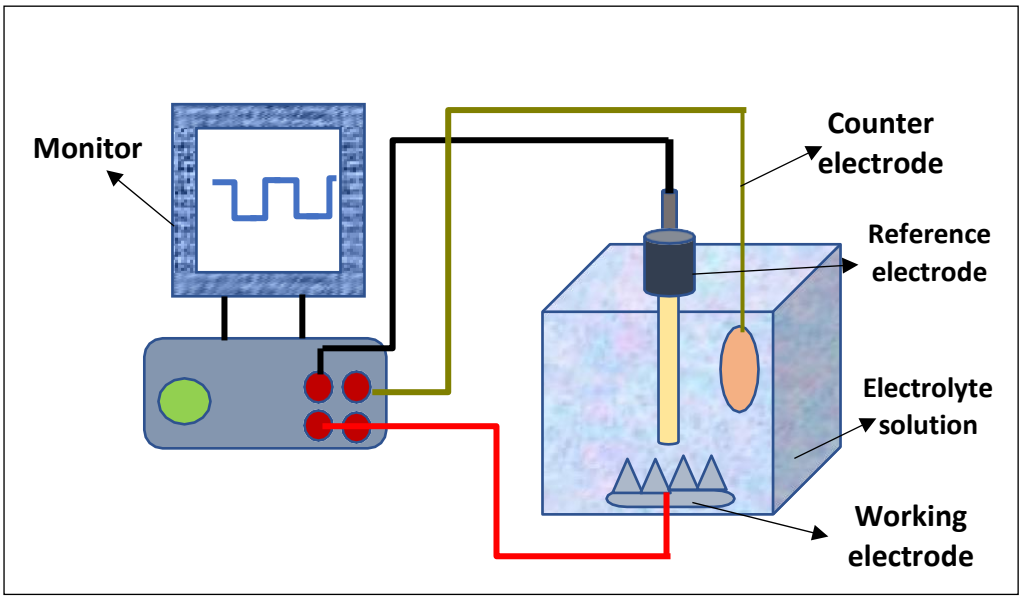

Figure 3. 11. A setup of an electrochemical deposition system.

By employing different cathode potential, several morphologies of the deposited ZnO nanomaterials were produced while, increasing the applied voltage lead to rise the deposition thickness.

3. 1. 6. Sonochemical Method

The sonochemical deposition is a simple and efficient solution-processing technique which has been used widely to synthesize novel nanostructures with unique properties (Isik, Hilal et al.2019). The most advantageous aspect of the sonochemical method is the fabrication of much smaller particles with higher surface area than those of other methods (Zhu, Koltypin et al. 2000). In the synthesis process of ZnO nanostructures, aqueous solution of zinc precursor and hydroxide source precursor like HMTA are placed in ultrasonochemical apparatus for various duration (Figure 3. 12).

The sonochemical process is based on breaking the chemical bonds by the ultrasound radiation. Nanostructures produced by the sonochemical reactions were various in dimension, morphology, structure, and in their crystal nature (amorphous or crystalline). Jung et al have obtained different morphologies of ZnO nanostructures such as nanorods, nanoflowers, nanocups, and nanodiscs with sonochemical method using equimolar solution of zinc nitrate hexahydrate and HMTA (Jung, Oh et al. 2007). Concentration and nature of precursors, power of the ultrasonic wave, and time of the ultrasonic treatments are main factors to tailor size, shape, composition, and geometry of nanostructured ZnO.

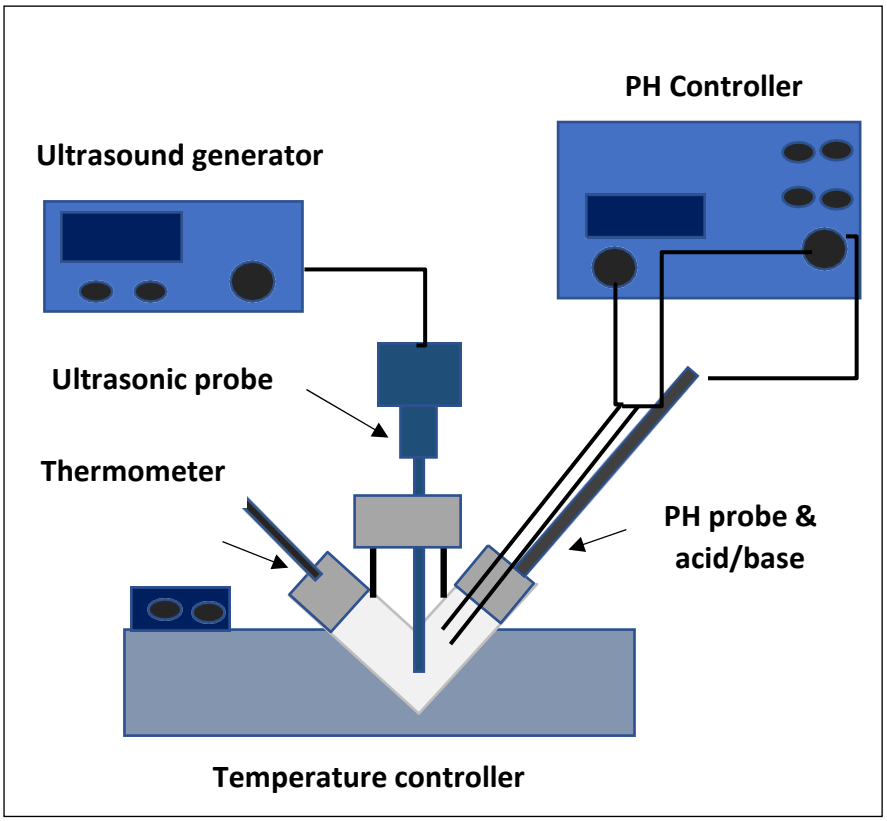

Figure 3. 12. An Illustration of the setup for the sonochemical reaction.

3. 1. 7. Spray pyrolysis method

Spray pyrolysis is a solution deposition technique in which a layer is directly fabricated by spraying a solution on a heated substrate, where the elements react to produce a chemical compound (Figure 3. 13). Such technique is a very straightforward, cost-efficient, requires no vacuum, superlative substrates, reactants, and costly gases (Emil, Alkan et al. 2018), (Ikhmayies 2019). In addition, it is applicable for synthesis of thin films on wide wafer-area and can be applied with Complementary metal–oxide–semiconductor technology (CMOS) (Mutinati, Brunet et al. 2012). Basically, a spray pyrolysis setup comprises of an atomizer, spray precursor, substrate heater, and temperature controller. The first step in this deposition process is the atomization procedure. The main function is to produce droplets from a precursor and then deliver them to the heated substrate. The solution droplets for the spraying process can be generated by a pneumatic system or an ultrasonic system. In a pneumatic system, a venturi nozzle is used to deliver the precursor solution through a fine inlet into a carrier gas jet flow. In an ultrasonic system, the droplets are formed by the ultrasonic waves generated with a piezoelectric disc in contact with the surface of the liquid solution (Falcony, Aguilar-Frutis et al. 2018). The atomizers vary in producing droplet volume, atomization rate, and the initial speed of the droplets. Several types of atomizers are utilised in spray pyrolysis approach, including air blast, ultrasonic, or electrostatic techniques (Perednis 2003).

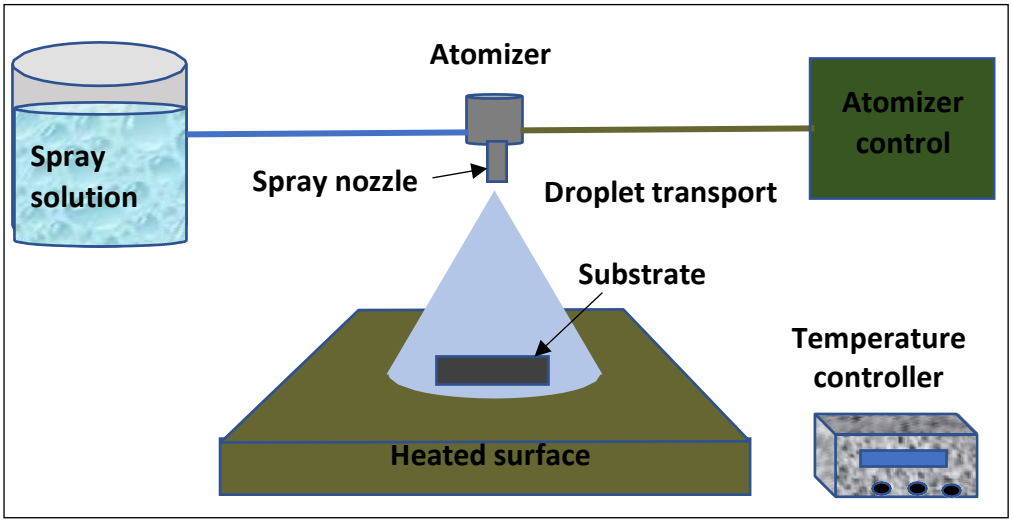

Figure 3. 13. A presentation of a spray pyrolysis deposition technique.

3. 1. 8 Spin coating deposition

Spin coating has been commonly used in the nanodevices manufacture to form a consistent thin film of photosensitive metal-organic systems with thickness ranging from nanometre to micrometre (Sahu, Parija et al. 2009). A nanodevice can be defined as a nanoscale tool that at least including nanosized elements. These nanosized components can be used in different applications e.g. to deliver drugs to an internal organism in the human body. However, the applicability of nanodevices depends significantly on their ability to be integrated with various electronic systems.

The physics of this process can be demonstrated through four main stages displayed in the figure 3. 14, which are drop of solution, spin-up, spin-off and solvent evaporation. It was reported that centrifugal force guides the solution radial, whereas the viscous force and surface tension leads a film residual to be condensed on the plane surface (Sahu, Parija et al. 2009). Stage 3 and stage 4 involve controlling fluid viscous flow and evaporation of solvent which have the most influence on the film thickness and quality such as uniformity. These two

stages have to be simultaneously happened during the whole process, but, at an engineering condition the viscous stream can first effectively governs the process while the evaporation dominates afterwards.

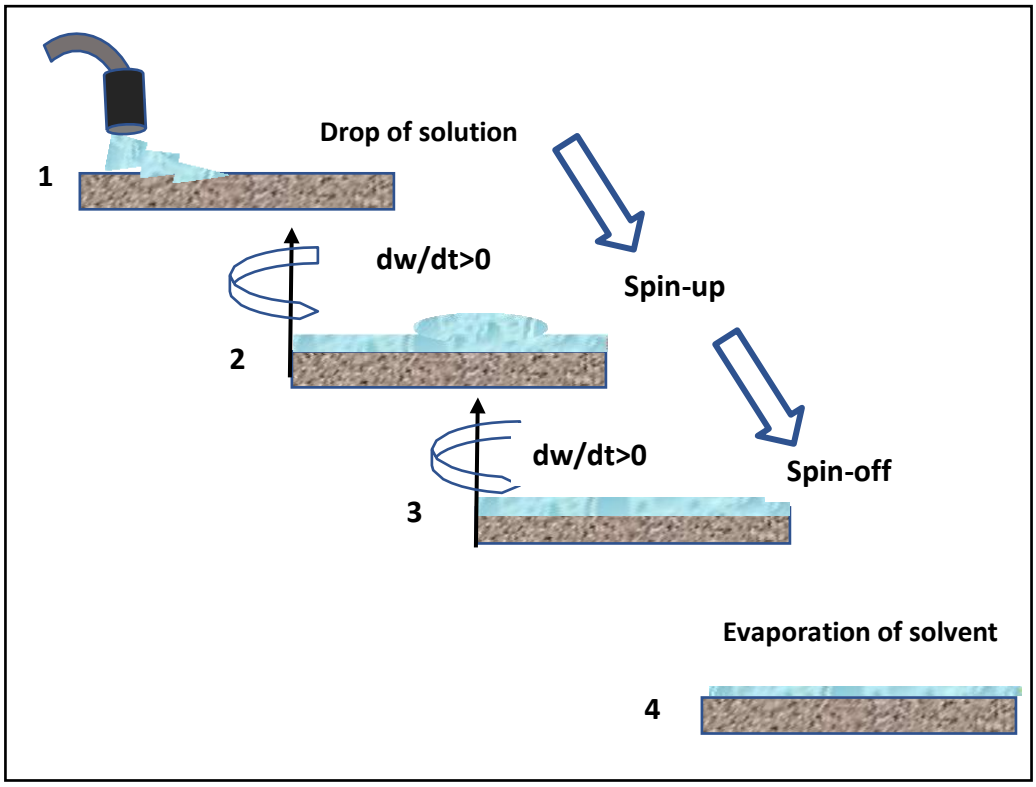

Figure 3. 14. Basic phases of spin coating procedure.

One of the essential physical interactions included in spin coating deposition is solution flow on a rotating substrate (Omar, Ray et al. 1997). Additionally, spin speed and time, solution viscosity and concentration and dispense volume are also important parameters strongly affect the deposition process.

3. 2. Gas phase synthesis

Gas phase methods have been broadly employed for the fabrication of high quality ZnO nanostructures on different substrates at elevated temperature (500^0 C-1500^0 C). Gaseous zinc species are first formed through many ways such as evaporating the zinc metal under oxygen atmosphere by thermal evaporation, laser ablation, electron, ion, and molecular beam. Then, these species react with oxygen to generate ZnO molecules, which lastly moves to condense on the surface of a solid substrate to produce ZnO nanostructures. According to the supplier of zinc vapor there are many vapour phase deposition processes including, vapour liquid solid (VLS) growth (Petersen, Likovich et al. 2009), metal organic chemical vapour deposition (MOCVD) (Ashraf, Jones et al. 2011), physical vapour deposition (PVD) (Wang, Zhang et al. 2005). These synthesis methods are separately discussed as follows.

3. 2. 1. Physical Vapour Deposition (PVD)

PVD techniques offers an environmentally friendly method to induce the source materials in vapour phase. It does not require a catalyst and contamination like, drain water, discharge gas, and waste slag cannot be released (Zhang, Zhou et al. 2009). It involves a variety of vacuum deposition techniques to fabricate thin films by the condensation of a vaporized material onto surface of the substrates (Figure 3. 15). An example of PVD methods for the synthesis of ZnO nanomaterials involve evaporation deposition, sputtering deposition techniques, and pulsed laser deposition. Some of these techniques to synthesize ZnO nanomaterials are briefly discussed in the next subsections.

PVD has been used to fabricate high crystal quality of ZnO nanowires arrays on silicon substrates (Zhang, Zhou et al. 2009), well-oriented ZnO nanowires with high aspect ratio and around 100 nm diameter produced in the chamber of the furnace at temperature of about 500^0 C under nitrogen flowing of 50 cm^3 /min.

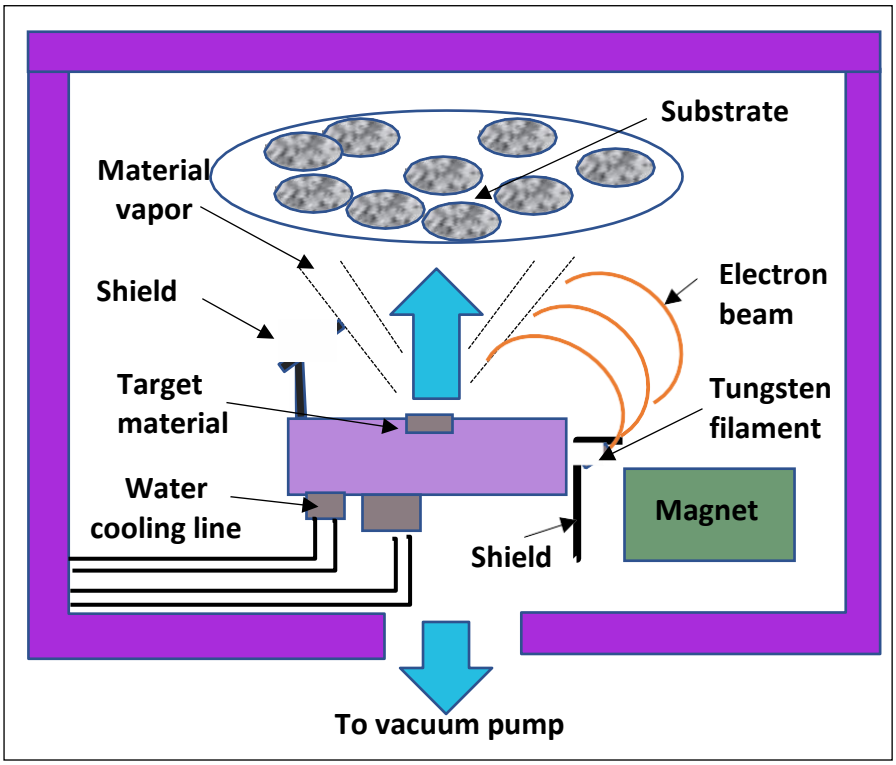

Figure 3. 15. A schematic diagram of an electron beam configuration of PVD.

Compared to chemical vapor method that mainly depends on the chemical reaction for coating the material on the surface, here, no chemicals react in the PVD technique and vacuum or low-pressure environment is required.

3. 2. 1. 1. Evaporation technique

Evaporation is a simple deposition process where the required target materials are evaporated at a high vapor pressure and an elevating temperature in “low” vacuum to be deposited at definite temperature, pressure onto the substrate surface (Tiwari, Tiwari et al. 2012).

Typical set up of the thermal evaporation equipment is illustrated in Figure 3. 16. The source material is placed into a suitable container such as a boat, a coil, a basket or a spiral wire. The container is typically made of a high melting temperature material such as tungsten, molybdenum or tantalum. The entire process occurs in vacuum, once the vacuum chamber is stabilized at the suitable pressure, a heating source is used for heating the source material within the container to high temperature to its boiling point. Vaporized atoms/molecules then travel toward the chosen substrate, where they can condense to produce a thin film onto the surface of the substrate (Venables 2000). Different structures of ZnO nanomaterials are grown by different evaporation methods, like thermal assisted evaporation techniques. The deposition conditions including temperature, time, pressure and type of substrate need to be adjusted and chosen accurately before starting the evaporation procedure. In addition, the thermal evaporation process is found to be highly affected by the oxygen ratio in the deposition chamber. Oxygen affects not only the evaporated material and the stoichiometry of the vapor phase, but also the growth of nanostructures (Singh 2013).

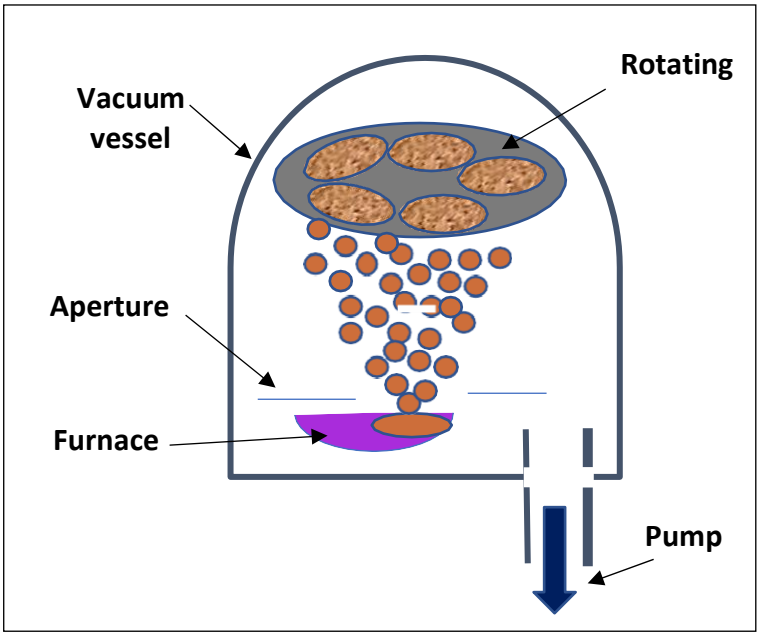

Figure 3. 16. An illustration of thermal evaporation setup.

The most used process to fabricate ZnO nanostructures is a vapor transport method in which zinc and oxygen are transported and react to generate ZnO nanostructures. There are many methods for creating Zn and oxygen vapor like ZnO decomposition, but it is restricted to a very high temperature (~1200 – 1400^0 C) (Park, Jung et al. 2005). Heating up zinc powder under oxygen flow is another direct process (Kim, Kawazoe et al. 2004) that offers low temperature (500~900^0 C), but the concentration of pressure of Zn vapor and oxygen has to be controlled to produce the desired stoichiometry component.

3. 2. 1. 2. Sputtering Deposition Techniques

Sputtering deposition is one of the most common methods for depositing thin films on substrate. In this process, the atoms of the designated materials are ejected by high-speed inert gas beam like helium or argon (Nalwa 2001a). A typical sputtering setup is presented in Figure 3. 17.

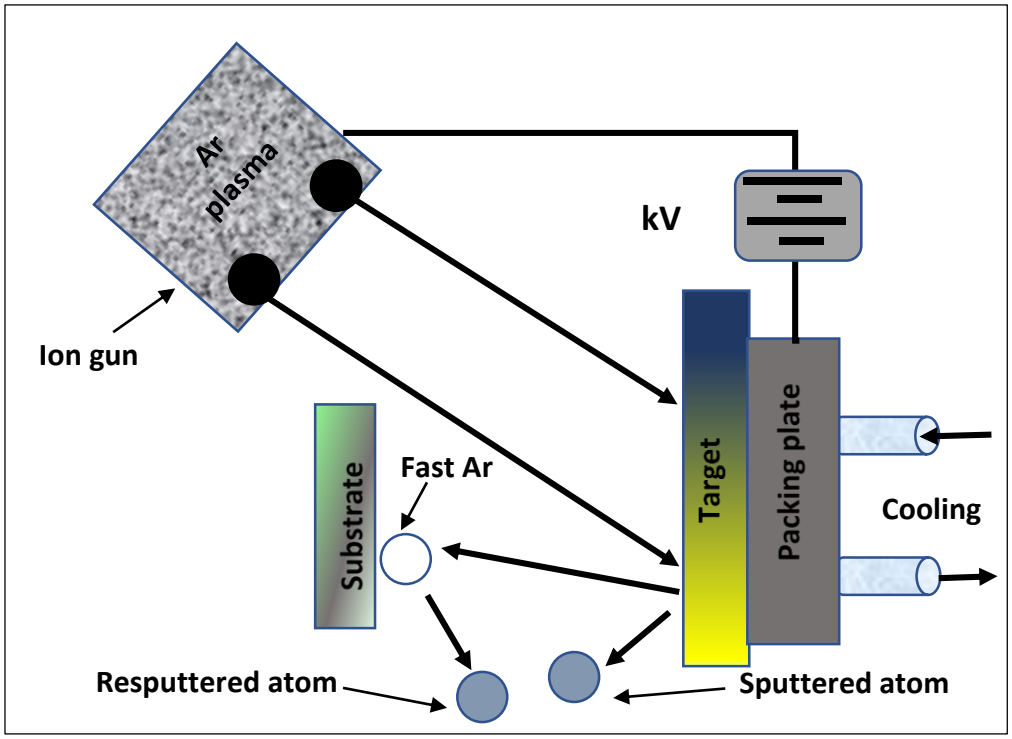

Figure 3. 17. An illustration of a typical sputtering system.

Once the inert gas atoms are ionized, they collide with the target atoms, therefore, these atoms are ejected toward the substrate to condense and form a thin film (Tiwari, Tiwari et al. 2012).

In general, sputtering is based on plasmas conditions which produce charged particles that can be accelerated towards a surface electrically. Sputtering takes place whenever those energetic particles hit a surface with sufficient energy to break bonds and dislodge atoms from the surface. The sputtering depends on the transformation of physical momentum and kinetic energy from the incident particle to the surface atoms, but this is independent of the particle's charge (Seshan 2002). The target material can be powered by several ways, including DC for conductive targets, RF for nonconductive targets and other different types of sputter depositions include ion-beam sputtering, reactive sputtering, ion-assisted sputtering, high-target utilization sputtering, gas flow sputtering, high power magnetron sputtering and facing target sputtering. DC sputtering deposition can be used for conductive materials, however, in case of insulator materials, this technique cannot be applied due to the development of surface charges created by striking ions. RF sputtering deposition can be used for semiconductor and insulator materials (Campbell 2012).

Saw el al have fabricated ZnO thin film on sapphire (0001) substrate by using a DC magnetron source to sputter a pure ZnO bulk in argon ambient (Saw, Lim et al. 2008). After annealing as-deposited thin film at 80^0 C temperature in nitrogen atmosphere for 2 h, ZnO nanotetrapods are produced. Choopun et al have used the radio frequency (RF) sputtering technique to grow ZnO nanobelts. ZnO polycrystalline was employed as a target under 1×10^{-5} torr vacuum for 60 minutes to fabricate ZnO thin film on the copper at room temperature (Choopun, Hongsith et al. 2005).

3. 2. 1. 3. Pulsed Laser Ablation Deposition (PLAD)

A pulsed laser ablation is a physical gas-phase method that can be used to generate high-purity and ultra-fine nanostructured materials. A typical PLAD setup is illustrated in Figure 3. 18. In the experimental procedure, the material is ablated using pulsed laser in the reaction chamber occupied by a definite quantity of a carrier gas at specific pressure. Vapor-phase materials is deposited onto seeded/unseeded, crystalline/non- crystalline substrate located vertical to the direction of the gas flow at certain distance from the target substrate.

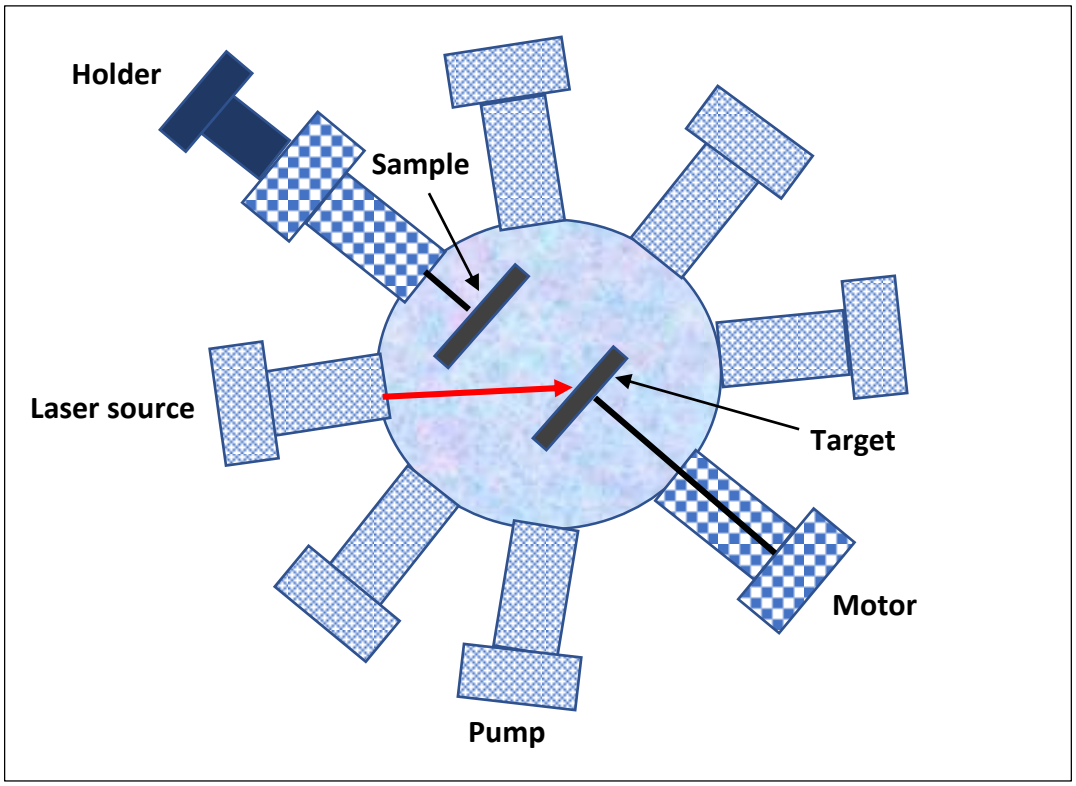

Figure 3. 18. A typical setup of the PLAD.

During the diffusion of the materials to settle down on the substrate, they bump with gas species to generate the mixed molecular composition (e.g., oxygen forms oxides, nitrogen or ammonia produces nitrides, methane

generates carbides, etc.) (Tiwari, Tiwari et al. 2012). The morphology, elemental structure, and size distribution of laser produced ZnO thin films or nanostructures can be tailored by some experimental parameters including, the composition and pressure of inert gas and the reagent gas, laser pulse power and wavelength, pressure and temperature inside the chamber, distance between substrate and target (Singh 2013).

3. 2. 1. 4. Electron Beam Lithography (EBL) Technique

In general, lithography techniques can be classified into two distinct categories, the first category duplicates the pattern information of the mask to a light-sensitive material, including optical lithography, X-ray lithography (XRL) (Madou2002), extreme ultraviolet lithography (EUVL) (Madou 2002) and nanoimprint lithography (NIL) (Yang, Jung et al. 2010). The second type is direct writing that generates the pattern, including (EBL) (Stepanova, Fito et al. 2010), ion beam lithography (IBL), scanning probes lithography (SPL) (Madou 2002), and electron-beam- induced deposition (EBID) (Abbas 2013).

Electron-beam lithography (EBL) is a high-resolution pattern generation method broadly utilised in many areas of modern research and technology with applications ranging from integrated circuit production (Pfeiffer, Groves et al. 1988), to photonic crystals (DeRose, Zhu et al. 2008) and channels for nanofluidics experimentations (Altissimo 2010). Figure 3. 21 presents a schematic diagram of the main steps of EBL technique. Due to EBL technique approximately resembles a SEM technique, its development began in the late 1960s (Chang 1967) by adapting the system of (SEMs). The main difference between them is that in an EBL system the beam is focused onto the surface based on the instructions delivering from the pattern generator, whilst in a SEM

system the beam is raster scanned through the sample surface to assemble secondary electrons to produce backscattered electrons and X-rays (Altissimo 2010). Compared to the wavelength of ultraviolet (UV) light used in photolithography, the shorter wavelength of accelerated electrons enabling such direct write systems to generate very small features less than 10 nm dimensions without a mask. Their drawback is the long times needed to generate large, complicated patterns results in limited mass production.

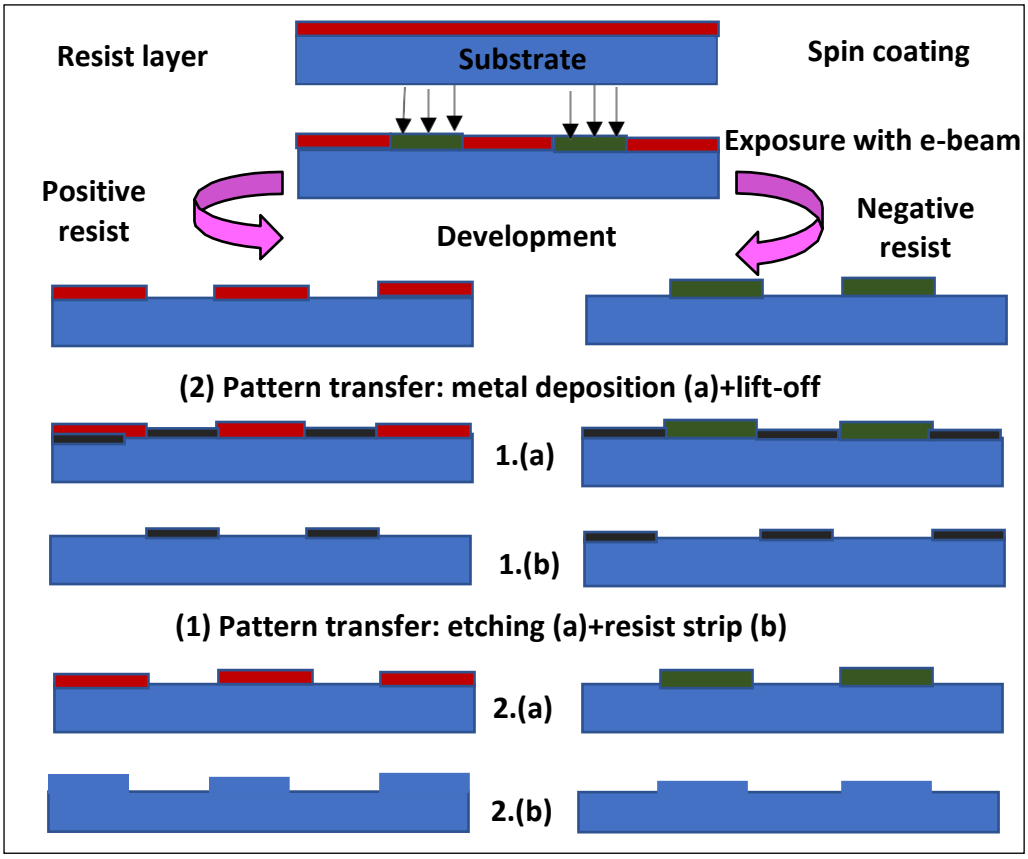

Figure 3. 21. Schematic of the main steps of EBL including deposition, exposure, development and pattern transfer.

Therefore, EBL has been employed to make photomasks for photolithography or produce low-volume patterns for academic use (Pala, Karabiyik 2012). EBL is a procedure by which a pattern is defined onto the surface of a film by first exposing a radiation sensitive resist to a precisely directed and strictly controlled electron beam and then selectively eliminating the exposed or nonexposed areas of the resist by a developer. After the development, the resist pattern can be used for pattern transfer processes such as lift-off or etching (Stepanova, Fito et al. 2010).

3. 2. 2. Chemical Vapor Deposition (CVD) methods

CVD is one of the most widely used technique for the nanostructure synthesis. Usually, in this method, the reacting gases pass over a heated substrate which is placed inside a reaction vessel where the pressure and gas flow can be controlled. The most common CVD techniques used for ZnO synthesis are low pressure CVD (LPCVD), plasma-enhanced CVD (PECVD), vapour liquid solid (VLS) catalyst-free metal-organic CVD (MOCVD), molecular beam epitaxy (MBE), and atomic layer deposition (ALD) (Venables 2000). Some of these methodologies are briefly described below.

3. 2. 2. 1. Vapour Liquid Solid (VLS)

Initially, the VLS technique was developed to grow micrometre-sized Si whiskers (Wagner, Ellis 1964), it has been extensively utilised for the epitaxial growth of ZnO semiconductors due to of their low cost, simplicity, and capability to synthesize ZnO on large wafers (Suh, Byeon et al. 2010), (Kong, Wei et al. 2018) . Figure 3. 19 demonstrates the mechanism of VLS fabrication method, nanosized liquid metal droplets such as Au, Cu, Ni, Sn can be used as a

metal catalyst that interacts with gaseous compounds to promote nucleation sites and crystalline growth for ZnO nanostructures. When the thermodynamic and supersaturation requirements are favourable, ZnO nanoparticles can nucleate homogeneously, allowing ZnO nanostructures to arrange in natural sequence (Udom, Ram et al. 2013).

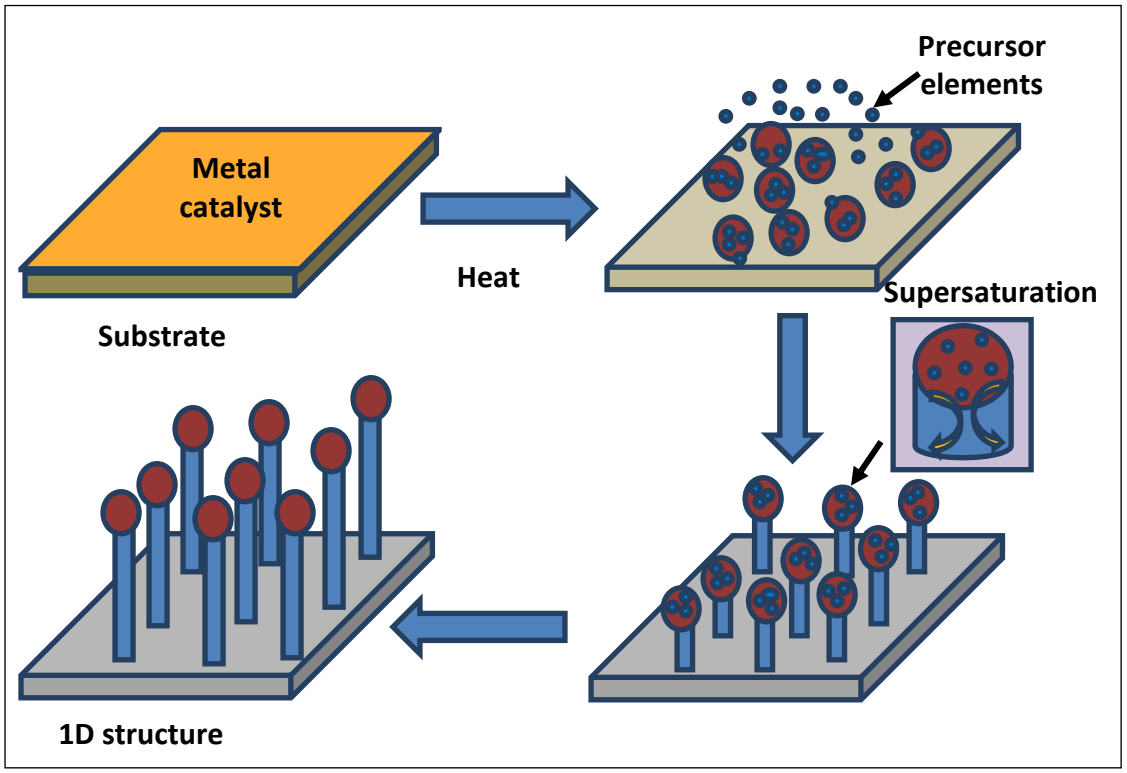

Figure 3. 19. Growth of 1D nanostructures by VLS mechanism.

Growth parameters like oxygen partial pressure, chamber pressure, and the catalyst layer thickness could extremely influence the quality of ZnO nanostructures. Well-ordered ZnO nanoarrays were successfully fabricated on a wide bandgap substrate such as sapphire, GaN, ALGaN, and ALN through the VLS route (Wang, Wang et al. 2005). It is highly appropriate to use conductive or semi-conductive substrates to create heterostructure platforms and perform an electronic analysis. It is known that GaN could electrically attach to the well-

oriented ZnO nanowires, because of the very similar band gaps of GaN (3.44 eV) and ZnO (3.37 eV). Additionally, due to small mismatch of the lattice constants (~1.8 %) of ZnO and GaN, a superb order of ZnO nanowires on GaN substrate can be achieved (Wang, Wang et al. 2005). The high crystallinity, stability at elevated temperature and transparency of the c-plane sapphire (0001), enable it to be widely used to grow ZnO nanowires, however a wide scale of defects at the interface is not avoidable, because of the large lattice mismatch between ZnO (a = 3.2495 Å, c=5.2069 Å) and sapphire (a =4.758 Å, c=12.990 Å) (Nikoobakht, Davydov et al. 2004).

3. 2. 2. 2. Catalyst-free Metal Organic Chemical Vapor Deposition (MOCVD)

Among different synthesis methods, catalyst-free (MOCVD) has been widely used for the epitaxial growth of semiconductors (Thompson 1997) especially, for growing ZnO thin films or/and ZnO nanowires. Compared to other growth processes, MOCVD provide many essential benefits, such as the capability to form high-quality ZnO nanowires at low temperature without the need of catalyst seed, hence exploiting this aspect could potentially scale up the versatility and performance for nanoscale photonic and electric platforms (Yi, Wang et al. 2005). An illustration of the MOCVD setup is presented in Figure 3. 20. Such reactor has a load-lock chamber to prevent exposing the chamber to the air and is evacuated to low pressure environment of 5×10^{-7} Torr before starting the fabrication process. A 3- in diameter nozzle can provide three types of gases through the chamber separately (Bang, Hwang et al. 2003).

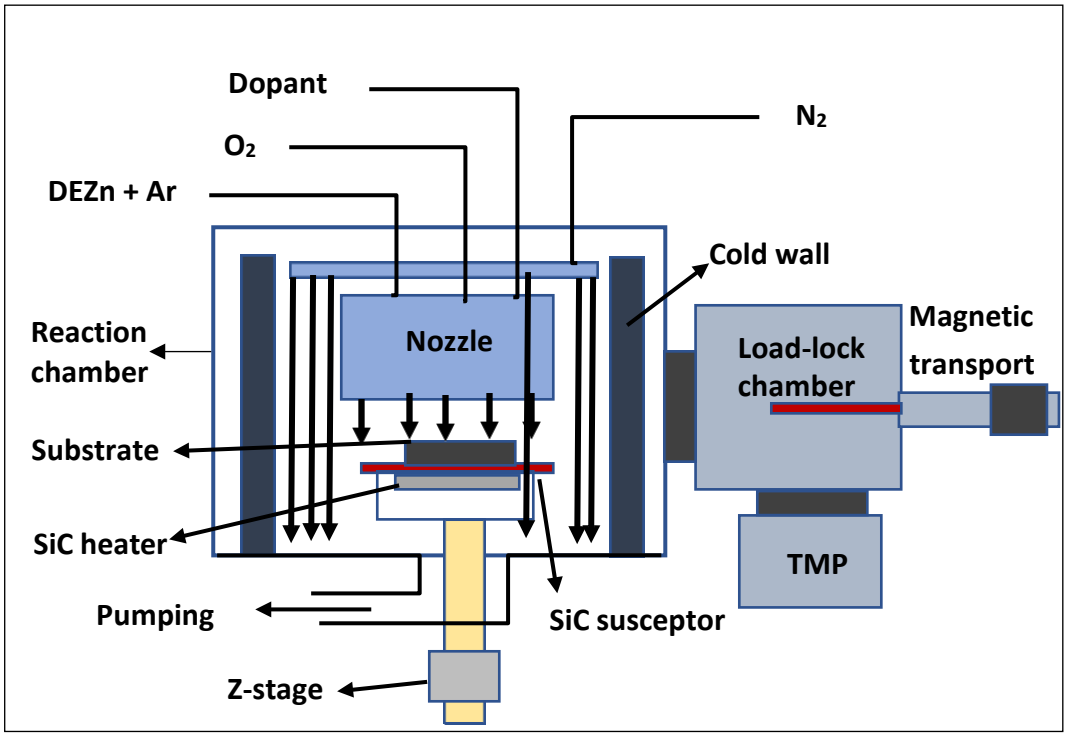

Figure 3. 20. A schematic illustration of a typical MOCVD system for ZnO fabrication.

To summaries, this chapter is demonstrated a detailed review on different fabrication techniques to grow ZnO nanostructure materials. The following chapter provides details on the characterization methods performed through this research to investigate the morphological, structural and functional properties of the ZnO nanostructures as well as their performance in Nano-bio platform.

References

ABBAS, A., 2013. Nanofabrication Using Electron Beam Lithography: Novel Resist and Applications.

AKHAVAN, O., MEHRABIAN, M., MIRABBASZADEH, K. And AZIMIRAD, R., 2009. Hydrothermal synthesis of ZnO nanorod arrays for photocatalytic inactivation of bacteria. Journal of Physics D: Applied Physics, 42(22), pp. 225305.

ALTISSIMO, M., 2010. E-beam lithography for micro-/nanofabrication. Biomicrofluidics, 4(2), pp. 026503.

ASHFOLD, M.N., DOHERTY, R.P., NDIFOR-ANGWAFOR, N.G., RILEY, D.J. and SUN, Y., 2007. The kinetics of the hydrothermal growth of ZnO nanostructures. Thin Solid Films, 515(24), pp. 8679-8683.

ASHRAF, S., JONES, A.C., BACSA, J., STEINER, A., CHALKER, P.R., BEAHAN, P., HINDLEY, S., ODEDRA, R., WILLIAMS, P.A. and HEYS, P.N., 2011. MOCVD of vertically aligned ZnO nanowires using bidentate ether adducts of dimethylzinc. Chemical Vapor Deposition, 17(1-3), pp. 45-53.

BAE, J., SONG, M.K., PARK, Y.J., KIM, J.M., LIU, M. and WANG, Z.L., 2011. Fiber Supercapacitors Made of Nanowire-Fiber Hybrid Structures for Wearable/Flexible Energy Storage. Angewandte Chemie International Edition, 50(7), pp. 1683-1687.

BANG, K., HWANG, D., LIM, S. and MYOUNG, J., 2003. Effects of growth temperature on the properties of ZnO/GaAs prepared by metalorganic chemical vapor deposition. Journal of Crystal Growth, 250(3), pp. 437-443.

BARUAH, S. and DUTTA, J., 2009a. Effect of seeded substrates on hydrothermally grown ZnO nanorods. Journal of Sol-Gel Science and Technology, 50(3), pp. 456-464.

BARUAH, S. and DUTTA, J., 2009b. Hydrothermal growth of ZnO nanostructures. Science and Technology of Advanced Materials, 10(1), pp. 013001.

BARUAH, S. and DUTTA, J., 2009c. pH-dependent growth of ZnO nanorods. Journal of Crystal Growth, 311(8), pp. 2549-2554.

BARUAH, S., THANACHAYANONT, C. and DUTTA, J., 2008. Growth of ZnO nanowires on nonwoven polyethylene fibers. Science and Technology of Advanced Materials, 9(2), pp. 025009.

Bekkari, R., Jaber, B., Labrim, H., Ouafi, M., Zayyoun, N. and Laânab, L., 2019. Effect of Solvents and Stabilizer Molar Ratio on the Growth Orientation of Sol-Gel-Derived ZnO Thin Films. International Journal of Photoenergy, 2019.

Bodke, M.R., Purushotham, Y. and Dole, B.N., 2018. Comparative study on ZnO nanocrystals synthesized by two precipitation methods. Cerâmica, 64(369), pp.91-96.

BOYLE, D.S., GOVENDER, K. and O'BRIEN, P., 2002. Novel low

temperature solution deposition of perpendicularly orientated rods of ZnO: substrate effects and evidence of the importance of
counter-ions in the control of crystallite growth. Chemical Communications, (1), pp. 80-81.

Campbell, S.A., 2012. Fabrication Engineering at the Micro-and Nanoscale (The Oxford Series in Electrical and Computer Engineering).

CAO, H., QIAN, X., GONG, Q., DU, W., MA, X. and ZHU, Z., 2006. Shape-and size-controlled synthesis of nanometre ZnO from a simple solution route at room temperature. Nanotechnology, 17(15), pp. 3632.

CHANDRAN, R. and MALLIK, A., 2018. Facile, seedless and surfactant-free synthesis of ZnO nanostructures by wet chemical bath method and their characterization. Applied Nanoscience, 8(7), pp. 1823-1830.

CHANG, T., 1967. Combined microminiature processing and microscopy using a scanning electron probe system, .

CHEN, L., YIN, Y., CHEN, C. and CHIOU, J., 2011. Influence of polyethyleneimine and ammonium on the growth of ZnO nanowires by hydrothermal method. The Journal of Physical Chemistry C, 115(43), pp. 20913-20919.

CHENG, C., YAN, B., WONG, S.M., LI, X., ZHOU, W., YU, T., SHEN,
Z., YU, H. and FAN, H.J., 2010. Fabrication and SERS performance of silver-nanoparticle-decorated Si/ZnO nanotrees in ordered arrays. ACS applied materials & interfaces, 2(7), pp. 1824-1828.

CHOOPUN, S., HONGSITH, N., TANUNCHAI, S., CHAIRUANGSRI, T., KRUA-IN, C., SINGKARAT, S., VILAITHONG, T., MANGKORNTONG,
P. and MANGKORNTONG, N., 2005. Single-crystalline ZnO nanobelts by RF sputtering. Journal of Crystal Growth, 282(3), pp. 365-369.

COLE, J.J., WANG, X., KNUESEL, R.J. and JACOBS, H.O., 2008b.
Patterned growth and transfer of ZnO Micro and nanocrystals with size and location control. Advanced Materials, 20(8), pp. 1474-1478.

DEMIANETS, L.N. and KOSTOMAROV, D.V., 2001. Mechanism of
ZnO single crystal growth under hydrothermal conditions, Annales de Chimie Science des Matériaux 2001, Elsevier, pp. 193- 198.

DEMIANETS, L., KOSTOMAROV, D., KUZ'MINA, I. and PUSHKO, S.,
2002. Mechanism of growth of ZnO single crystals from hydrothermal alkali solutions. Crystallography Reports, 47(1), pp. S86-S98.

DEROSE, G.A., ZHU, L., POON, J.K., YARIV, A. and SCHERER, A.,
2008. Periodic sub-wavelength electron beam lithography defined photonic crystals for mode control in semiconductor lasers. Microelectronic Engineering, 85(5), pp. 758-760.

DEV, A., KAR, S., CHAKRABARTI, S. and CHAUDHURI, S. , 2006. Optical and field emission properties of ZnO nanorod arrays synthesized on zinc foils by the solvothermalroute. Nanotechnology, 17(5), pp. 1533.

EMIL, E., ALKAN, G., GURMEN, S., RUDOLF, R., JENKO, D. and FRIEDRICH, B., 2018. Tuning the Morphology of ZnO Nanostructures with the Ultrasonic Spray Pyrolysis Process. Metals, 8(8), pp. 569.

ESWAR, K.A., SUHAIMI, M.H.F., GULILING, M., MOHAMAD, M., KHUSAIMI, Z., RUSOP, M. and ABDULLAH, S., 2018. The structural properties of flower–like ZnO nanostructures on porous silicon, AIP Conference Proceedings 2018, AIP Publishing, pp. 020032.

Falcony, C., Aguilar-Frutis, M. and García-Hipólito, M., 2018. Spray pyrolysis technique; High-K dielectric films and luminescent materials: A review. *Micromachines*, *9*(8), p.414.

FANG, Y., PANG, Q., WEN, X., WANG, J. and YANG, S., 2006. Synthesis of ultrathin ZnO nanofibers aligned on a zinc substrate. Small, 2(5), pp. 612-615.

GAO, Y., NAGAI, M., CHANG, T. and SHYUE, J., 2007. Solution-derived ZnO nanowire array film as photoelectrode in dye- sensitized solar cells. Crystal Growth and Design, 7(12), pp. 2467- 2471.

GHAYOUR, H., REZAIE, H., MIRDAMADI, S. and NOURBAKHSH, A., 2011. The effect of seed layer thickness on alignment and morphology of ZnO nanorods. Vacuum, 86(1), pp. 101-105.

GOVENDER, K., BOYLE, D.S., KENWAY, P.B. and O'BRIEN, P., 2004.

Understanding the factors that govern the deposition and morphology of thin films of ZnO from aqueous solution. Journal of Materials Chemistry, 14(16), pp. 2575-2591.

GREENE, L.E., LAW, M., GOLDBERGER, J., KIM, F., JOHNSON, J.C., ZHANG, Y., SAYKALLY, R.J. and YANG, P., 2003. Low-temperature wafer-scale production of ZnO nanowire arrays. Angewandte Chemie International Edition, 42(26), pp. 3031-3034.

GREENE, L.E., LAW, M., TAN, D.H., MONTANO, M., GOLDBERGER, J., SOMORJAI, G. and YANG, P., 2005. General route to vertical ZnO nanowire arrays using textured ZnO seeds. Nano Letters, 5(7), pp. 1231-1236.

GREENE, L.E., 2007. Next-generation photovoltaics using solution- grown ZnO nanowire arrays. ProQuest.

HEINONEN, S., NIKKANEN, J., HAKOLA, H., HUTTUNEN- SAARIVIRTA, E., KANNISTO, M., HYVÄRINEN, L., JÄRVELÄINEN, M. and LEVÄNEN, E., 2016. Effect of temperature and concentration of precursors on morphology and photocatalytic activity of ZnO thin films prepared by hydrothermal route, IOP Conference Series: Materials Science and Engineering 2016, IOP Publishing, pp. 012030.

HIDBER, P.C., GRAULE, T.J. and GAUCKLER, L.J., 1996. Citric acid—a dispersant for aqueous alumina suspensions. Journal of the American Ceramic Society, 79(7), pp. 1857-1867.

HOU, K., LI, C., LEI, W., ZHANG, X., YANG, X., QU, K., WANG, B., ZHAO, Z. and SUN, X., 2009. Influence of synthesis temperature on ZnO nanostructure morphologies and field emission properties. Physica E: Low-dimensional Systems and Nanostructures, 41(3), pp. 470-473.

Ikhmayies, S.J., 2019. Production of ZnO Cauliflowers Using the Spray Pyrolysis Method. In Sustainable Building for a Cleaner Environment (pp. 383-389). Springer, Cham.

Isık, T., Hilal, M.E. and Horzum, N., 2019. Green Synthesis of ZnO Nanostructures. In ZnO Based Nano Materials and Devices. IntechOpen.

IZAKI, M. and OMI, T., 1996. Transparent ZnO films prepared by electrochemical reaction. Applied Physics Letters, 68(17), pp. 2439-2440.

JUNG, S., OH, E., LEE, K., YANG, Y., PARK, C.G., PARK, W. and JEONG, S., 2007. Sonochemical preparation of shape-selective ZnO nanostructures. *Crystal growth and design,* **8**(1), pp. 265-269.

KAMATA, A., YOSHIDA, H., CHICHIBU, S. and NAKANISHI, H., 1997. Growth and doping characteristics of ZnSeTe epilayers by MOCVD. Journal of Crystal Growth, 170(1-4), pp. 518-522.

KAR, S., DEV, A. and CHAUDHURI, S., 2006. Simple solvothermal route to synthesize ZnO nanosheets, nanonails, and well-aligned nanorod arrays. The Journal of Physical Chemistry B, 110(36), pp. 17848-17853.

KAWSKA, A., DUCHSTEIN, P., HOCHREIN, O. and ZAHN, D., 2008.

Atomistic mechanisms of ZnO aggregation from ethanolic solution: Ion association, proton transfer, and self-organization. Nano letters, 8(8), pp. 2336-2340.

KIM, A.R., LEE, J., JANG, B.R., LEE, J.Y., KIM, H.S. and JANG, N.W., 2011. Effect of Zn2 source concentration on hydrothermally grown ZnO nanorods. Journal of nanoscience and nanotechnology, 11(7), pp. 6395-6399.

KIM, J.H., ANDEEN, D. and LANGE, F.F., 2006. Hydrothermal Growth of Periodic, Single-Crystal ZnO Microrods and Microtunnels. Advanced Materials, 18(18), pp. 2453-2457.

KIM, J., CHO, J.W. and KIM, S.H., 2011. The characteristic of the ZnO nanowire morphology grown by the hydrothermal method on various surface-treated seed layers. Materials Letters, 65(8), pp. 1161-1164.

KIM, T., KAWAZOE, T., YAMAZAKI, S., OHTSU, M. and SEKIGUCHI, T., 2004. Low-temperature orientation-selective growth and ultraviolet emission of single-crystal ZnO nanowires. Applied Physics Letters, 84(17), pp. 3358-3360.

Kong, X., Wei, C., Zhu, Y., Cohen, P. and Dong, J., 2018. Modeling of Catalyst-free Growth Process of ZnO Nanowires. Procedia Manufacturing, 26, pp.349-358.

KUNG, H.H. and KO, E.I., 1996. Preparation of oxide catalysts and catalyst supports—a review of recent advances. The Chemical Engineering Journal and the Biochemical Engineering Journal, 64(2), pp. 203-214.

LE, H., CHUA, S., KOH, Y., LOH, K. and FITZGERALD, E., 2006. Systematic studies of the epitaxial growth of single-crystal ZnO nanorods on GaN using hydrothermal synthesis. Journal of Crystal Growth, 293(1), pp. 36-42.

LEE, J., YIN, D. and HORIUCHI, S., 2005. Site and morphology controlled ZnO deposition on Pd catalyst prepared from Pd/PMMA thin film using UV lithography. Chemistry of materials, 17(22), pp. 5498-5503.

LI, J., SRINIVASAN, S., HE, G., KANG, J., WU, S. and PONCE, F., 2008. Synthesis and luminescence properties of ZnO nanostructures produced by the sol–gel method. Journal of Crystal Growth, 310(3), pp. 599-603.

Li, X., Chen, X., Yi, Z., Zhou, Z., Tang, Y. and Yi, Y., 2019. Fabrication of ZnO nanorods with strong UV absorption and different hydrophobicity on foamed nickel under different hydrothermal conditions. Micromachines, 10(3), p.164.

LIU, J., HUANG, X., LI, Y., JI, X., LI, Z., HE, X. and SUN, F., 2007. Vertically aligned 1D ZnO nanostructures on bulk alloy substrates: direct solution synthesis, photoluminescence, and field emission. The Journal of Physical Chemistry C, 111(13), pp. 4990-4997.

LIU, J., SHE, J., DENG, S., CHEN, J. and XU, N., 2008. Ultrathin seed-layer for tuning density of ZnO nanowire arrays and their field emission characteristics. The Journal of Physical Chemistry C, 112(31), pp. 11685-11690.

LIU, R., VERTEGEL, A.A., BOHANNAN, E.W., SORENSON, T.A. and SWITZER, J.A., 2001. Epitaxial electrodeposition of ZnO nanopillars on single-crystal gold. Chemistry of Materials, 13(2), pp. 508-512.

LIU, T., LIAO, H., LIN, C., HU, S. and CHEN, S., 2006. Biofunctional ZnO nanorod arrays grown on flexible substrates. Langmuir, 22(13), pp. 5804-5809.

MADOU, M.J., 2002. Fundamentals of microfabrication: the science of miniaturization. CRC press.

MAITI, S., MAITI, U.N., CHOWDHURY, A. and CHATTOPADHYAY, K.K., 2014. Ambient condition oxidation of zinc foil in supersaturated solution for shape tailored ZnO nanostructures: low cost candidates for efficient electron emitter and UV- detector. CrystEngComm, 16(9), pp. 1659-1668.

MANEKKATHODI, A., LU, M., WANG, C.W. and CHEN, L., 2010. Direct Growth of Aligned ZnO Nanorods on Paper Substrates for Low-Cost Flexible Electronics. Advanced Materials, 22(36), pp. 4059-4063.

MCLAREN, A., VALDES-SOLIS, T., LI, G. and TSANG, S.C., 2009. Shape and size effects of ZnO nanocrystals on photocatalytic activity. Journal of the American Chemical Society, 131(35), pp. 12540-12541.

MEKHNACHE, M., DRICI, A., HAMIDECHE, L.S., BENZAROUK, H., AMARA, A., CATTIN, L., BERNEDE, J. and GUERIOUNE, M., 2011. Properties of ZnO thin films deposited on (glass, ITO and ZnO: Al) substrates. Superlattices and Microstructures, 49(5), pp. 510-518.

MOHD FUDZI, L., ZAINAL, Z., LIM, H., CHANG, S. and HOLI, A., 2018. Effect of Temperature and Growth Time on Vertically Aligned ZnO Nanorods by Simplified Hydrothermal Technique for Photoelectro-chemical Cells. Materials, 11(5), pp. 704.

MUTINATI, G., BRUNET, E., STEINHAUER, S., KÖCK, A., TEVA, J., KRAFT, J., SIEGERT, J., SCHRANK, F. and BERTAGNOLLI, E., 2012. CMOS-integrable ultrathin SnO2 layer for smart gas sensor devices. Procedia Engineering, 47, pp. 490-493.

NA, J., GONG, B., SCAREL, G. and PARSONS, G.N., 2009. Surface polarity shielding and hierarchical ZnO nano-architectures produced using sequential hydrothermal crystal synthesis and thin film atomic layer deposition. Acs Nano, 3(10), pp. 3191-3199.

NALWA, H.S., 2001a. Handbook of advanced electronic and photonic materials and devices: semiconductors. Vol. 1. Academic Press.

NIKOOBAKHT, B., DAVYDOV, A. and STRANICK, S.J., 2004. Controlling the growth direction of ZnO nanowires on c-plane sapphire, MRS Proceedings 2004, Cambridge Univ Press, pp. M8. 25.1.

OMAR, O., RAY, A., HASSAN, A. and DAVIS, F., 1997. Resorcinol calixarenes (resorcarenes): Langmuir-Blodgett films and optical properties. Supramolecular Science, 4(3-4), pp. 417-421.

PALA, N. and KARABIYIK, M., 2012. Electron Beam Lithography (EBL). Encyclopedia of Nanotechnology. Springer, pp. 718-740.

PARIZE, R., GARNIER, J., CHAIX-PLUCHERY, O., VERRIER, C., APPERT, E. and CONSONNI, V., 2016. Effects of hexamethylenetetramine on the nucleation and radial growth of ZnO nanowires by chemical bath deposition. The Journal of Physical Chemistry C, 120(9), pp. 5242-5250.

PARK, J.Y., JUNG, I.O., MOON, J.H., LEE, B. and KIM, S.S., 2005. Temperature induced shape change of highly aligned ZnO nanocolumns. Journal of Crystal Growth, 282(3), pp. 353-358.

PAUPORTE, T., LINCOT, D., VIANA, B. and PELLÉ, F., 2006. Toward laser emission of epitaxial nanorod arrays of ZnO grown by electrodeposition. Applied Physics Letters, 89(23), pp. 233112- 233112.

PEREDNIS, D., 2003. Thin film deposition by spray pyrolysis and the application in solid oxide fuel cells, .

PETERSEN, E.W., LIKOVICH, E.M., RUSSELL, K.J. and NARAYANAMURTI, V., 2009. Growth of ZnO nanowires catalyzed by size-dependent melting of Au nanoparticles. Nanotechnology, 20(40), pp. 405603.

PFEIFFER, H., GROVES, T. and NEWMAN, T., 1988. High-throughput, high-resolution electron-beam lithography. IBM Journal of Research and Development, 32(4), pp. 494-501.

QIN, Y., WANG, X. and WANG, Z.L., 2008. Microfibre–nanowire hybrid structure for energy scavenging. Nature, 451(7180), pp. 809-813.

Rani, R.A., Zoolfakar, A.S., Sabri, W.S.W.M., Alrokayan, S., Khan, H.A. and Rusop, M., 2018, June. Influence of the precursor and annealing temperature on the hydrothermal growth of ZnO nanostructures. In IOP Conference Series: Materials Science and Engineering (Vol. 380, No. 1, p. 012018). IOP Publishing.

RIDHUAN, N.S., RAZAK, K.A., LOCKMAN, Z. and AZIZ, A.A., 2012. Structural and morphology of ZnO nanorods synthesized using ZnO seeded growth hydrothermal method and its properties as UV sensing. PloS one, 7(11), pp. e50405.

SAHU, N., PARIJA, B. and PANIGRAHI, S., 2009. Fundamental understanding and modeling of spin coating process: A review. Indian Journal of Physics, 83(4), pp. 493-502.

SAPKOTA, A., ANCENO, A.J., BARUAH, S., SHIPIN, O.V. and DUTTA, J., 2011. ZnO nanorod mediated visible light photoinactivation of model microbes in water. Nanotechnology, 22(21), pp. 215703.

Saranya, A., Devasena, T., Sivaram, H. and Jayavel, R., 2019. Role of hexamine in ZnO morphologies at different growth temperature with potential application in dye sensitized solar cell. Materials Science in Semiconductor Processing, 92, pp.108-115.

SAW, K., LIM, Y., TAN, G., HASSAN, Z., IBRAHIM, K., YAM, F. and NG, S., 2008. Effect of zinc on the growth mechanism of ZnO nanostructures in the nitrogen environment. Journal of Physics D: Applied Physics, 41(5), pp. 055506.

SCHMIDT, H., 1988. Chemistry of material preparation by the sol- gel process. Journal of Non-Crystalline Solids, 100(1-3), pp. 51-64.

SHEN, L., BAO, N., YANAGISAWA, K., ZHENG, Y., DOMEN, K., GUPTA, A. and GRIMES, C.A., 2007. Direct growth of comet-like superstructures of Au–ZnO submicron rod arrays by solvothermal soft chemistry process. Journal of Solid-State Chemistry, 180(1), pp. 213-220.

SINGH, S., 2013. ZnO Nanostructures; Synthesis, Characterizations and Device Applications. Journal of Nanoengineering and Nanomanufacturing, 3(4), pp. 283-310.

Slimani Tlemcani, T., Justeau, C., Nadaud, K., Poulin-Vittrant, G. and Alquier, D., 2019. Deposition Time and Annealing Effects of ZnO Seed Layer on Enhancing Vertical Alignment of Piezoelectric ZnO Nanowires. Chemosensors, 7(1), p.7.

SØNDERGAARD, M., BØJESEN, E.D., CHRISTENSEN, M. and IVERSEN, B.B., 2011. Size and morphology dependence of ZnO nanoparticles synthesized by a fast-continuous flow hydrothermal method. Crystal Growth & Design, 11(9), pp. 4027-4033.

STEPANOVA, M., FITO, T., SZABÓ, Z., ALTI, K., ADEYENUWO, A., KOSHELEV, K., AKTARY, M. and DEW, S., 2010. Simulation of electron beam lithography of nanostructures. Journal of Vacuum Science & Technology B, Nanotechnology and Microelectronics: Materials, Processing, Measurement, and Phenomena, 28(6), pp. C6C48-C6C57.

Sucharitakul, S., Panyathip, R. and Choopun, S., 2018. Effect of Annealing Temperature on ECD Grown Hexagonal-Plane ZnO. Materials, 11(8), p.1360.

SUGUNAN, A., WARAD, H.C., BOMAN, M. and DUTTA, J., 2006. ZnO nanowires in chemical bath on seeded substrates: role of hexamine. Journal of Sol-Gel Science and Technology, 39(1), pp. 49-56.

SUH, D., BYEON, C.C. and LEE, C., 2010. Synthesis and optical characterization of vertically grown ZnO nanowires in high crystallinity through vapor–liquid–solid growth mechanism. Applied Surface Science, 257(5), pp. 1454-1456.

SUN, H., LUO, M., WENG, W., CHENG, K., DU, P., SHEN, G. and HAN, G., 2008. Position and density control in hydrothermal growth of ZnO nanorod arrays through pre-formed micro/nanodots. Nanotechnology, 19(39), pp. 395602.

SUWANBOON, S., CHUKAMNERD, S. and ANGLONG, U., 2007. Morphological control and optical properties of nanocrystalline ZnO powder from precipitation method. Songklanakarin Journal of Science & Technology, 29(6).

TANG, L., BAO, X., ZHOU, H. and YUAN, A., 2008. Synthesis and characterization of ZnO nanorods by a simple single-source hydrothermal method. Physica E: Low-dimensional Systems and Nanostructures, 40(4), pp. 924-928.

THOMPSON, A.G., 1997. MOCVD technology for semiconductors. Materials Letters, 30(4), pp. 255-263.

TIAN, Z.R., VOIGT, J.A., LIU, J., MCKENZIE, B. and MCDERMOTT, M.J., 2002. Biomimetic arrays of oriented helical ZnO nanorods and columns. Journal of the American Chemical Society, 124(44), pp. 12954-12955.

TIWARI, J.N., TIWARI, R.N. and KIM, K.S., 2012. Zero-dimensional, one-dimensional, two-dimensional and three-dimensional nanostructured materials for advanced electrochemical energy devices. Progress in Materials Science, 57(4), pp. 724-803.

TONTO, P., MEKASUWANDUMRONG, O., PHATANASRI, S., PAVARAJARN, V. and PRASERTHDAM, P., 2008. Preparation of ZnO nanorod by solvothermal reaction of zinc acetate in various alcohols. Ceramics International, 34(1), pp. 57-62.

UDOM, I., RAM, M.K., STEFANAKOS, E.K., HEPP, A.F. and GOSWAMI, D.Y., 2013. One dimensional-ZnO nanostructures: synthesis, properties and environmental applications. Materials Science in Semiconductor Processing, 16(6), pp. 2070-2083.

UENO, N., MARUO, T., NISHIYAMA, N., EGASHIRA, Y. and UEYAMA, K., 2010. Low-temperature synthesis of ZnO nanorods using a seed layer of zinc acetate/sodium dodecyle sulfate nanocomposite. Materials Letters, 64(4), pp. 513-515.

UNALAN, H.E., HIRALAL, P., RUPESINGHE, N., DALAL, S., MILNE, W.I. and AMARATUNGA, G.A., 2008. Rapid synthesis of aligned ZnO nanowires. Nanotechnology, 19(25), pp. 255608.

VAYSSIERES, L., 2003. Growth of arrayed nanorods and nanowires of ZnO from aqueous solutions. Advanced Materials, 15(5), pp. 464-466.

VAYSSIERES, L., KEIS, K., LINDQUIST, S. and HAGFELDT, A., 2001. Purpose-built anisotropic metal oxide material: 3D highly oriented microrod array of ZnO. The Journal of Physical Chemistry B, 105(17), pp. 3350-3352.

Venables, J., 2000. Introduction to surface and thin film processes. Cambridge University Press.

VISWANATHA, R., AMENITSCH, H. and SARMA, D., 2007. Growth kinetics of ZnO nanocrystals: a few surprises. Journal of the American Chemical Society, 129(14), pp. 4470-4475.

WAGNER, R. and ELLIS, W., 1964. Vapor-liquid-solid mechanism of single crystal growth. Applied Physics Letters, , pp. 89-90.

WANG, L., ZHANG, X., ZHAO, S., ZHOU, G., ZHOU, Y. and QI, J., 2005. Synthesis of well-aligned ZnO nanowires by simple physical vapor deposition on c-oriented ZnO thin films without catalysts or additives. Applied Physics Letters, 86(2), pp. 24108.

WANG, S., TSENG, T., WANG, Y., WANG, C., LU, H. and SHIH, W., 2008. Effects of preparation conditions on the growth of ZnO nanorod arrays using aqueous solution method. International Journal of Applied Ceramic Technology, 5(5), pp. 419-429.

WANG, X., WANG, X., SONG, J., LI, P., RYOU, J.H., DUPUIS, R.D., SUMMERS, C.J. and WANG, Z.L., 2005. Growth of uniformly aligned ZnO nanowire heterojunction arrays on GaN, AlN, and Al0. 5Ga0. 5N substrates. Journal of the American Chemical Society, 127(21), pp. 7920-7923.

WEINTRAUB, B., ZHOU, Z., LI, Y. and DENG, Y., 2010. Solution synthesis of one-dimensional ZnO nanomaterials and their applications. Nanoscale, 2(9), pp. 1573-1587.

WU, W., HU, G., CUI, S., ZHOU, Y. and WU, H., 2008. Epitaxy of vertical ZnO nanorod arrays on highly (001)-oriented ZnO seed monolayer by a hydrothermal route. Crystal Growth and Design, 8(11), pp. 4014-4020.

WU, X., BAI, H., LI, C., LU, G. and SHI, G., 2006. Controlled one-step fabrication of highly oriented ZnO nanoneedle/nanorods arrays at near room temperature. Chemical Communications, (15), pp. 1655-1657.

XU, C., WEI, A., SUN, X.W. and DONG, Z.L., 2006. Aligned ZnO nanorods synthesized by a simple hydrothermal reaction. Journal of Physics D: Applied Physics, 39(8), pp. 1690.

XU, L., GUO, Y., LIAO, Q., ZHANG, J. and XU, D., 2005. Morphological control of ZnO nanostructures by electrodeposition. The Journal of Physical Chemistry B, 109(28), pp. 13519-13522.

XU, S., LAO, C., WEINTRAUB, B. and WANG, Z.L., 2008. Density- controlled growth of aligned ZnO nanowire arrays by seedless chemical approach on smooth surfaces. Journal of Materials Research, 23(08), pp. 2072-2077.

XU, S., SHEN, Y., DING, Y. and WANG, Z.L., 2010. Growth and transfer of monolithic horizontal ZnO nanowire superstructures onto flexible substrates. Advanced Functional Materials, 20(9), pp. 1493-1497.

XU, S. and WANG, Z.L., 2011. One-dimensional ZnO nanostructures: solution growth and functional properties. Nano Research, 4(11), pp. 1013-1098.

XU, S., WEI, Y., KIRKHAM, M., LIU, J., MAI, W., DAVIDOVIC, D., SNYDER, R.L. and WANG, Z.L., 2008a. Patterned growth of vertically aligned ZnO nanowire arrays on inorganic substrates at low temperature without catalyst. Journal of the American Chemical Society, 130(45), pp. 14958-14959.

XU, S., WEI, Y., LIU, J., YANG, R. and WANG, Z.L., 2008b. Integrated multilayer nanogenerator fabricated using paired nanotip-to- nanowire brushes. Nano letters, 8(11), pp. 4027-4032.

YAMABI, S. and IMAI, H., 2002. Growth conditions for wurtzite ZnO films in aqueous solutions. Journal of materials chemistry, 12(12), pp. 3773-3778.

YANG, J.K., JUNG, Y.S., CHANG, J., MICKIEWICZ, R., ALEXANDER- KATZ, A., ROSS, C. and BERGGREN, K.K., 2010. Complex self- assembled patterns using sparse commensurate templates with locally varying motifs. Nature nanotechnology, 5(4), pp. 256-260.

YANG, Y., CHU, Y., ZHANG, Y., YANG, F. and LIU, J., 2006. Polystyrene-ZnO core-shell microspheres and hollow ZnO structures synthesized with the sulfonated polystyrene templates. Journal of Solid-State Chemistry, 179(2), pp. 470-475.

YI, G., WANG, C. and PARK, W.I., 2005. ZnO nanorods: synthesis, characterization and applications. Semiconductor Science and Technology, 20(4), pp. S22.

YI, S., CHOI, S., JANG, J., KIM, J. and JUNG, W., 2007. Low- temperature growth of ZnO nanorods by chemical bath deposition. Journal of colloid and interface science, 313(2), pp. 705-710.

YUFEI, Z., ZHIYOU, G., XIAOQI, G., DONGXING, C., YUNXIAO, D. and HONGTAO, Z., 2010. First-principles of wurtzite ZnO (0001) and (0001) surface structures. Journal of Semiconductors, 31(8), pp. 082001.

ZANG, J., LI, C.M., CUI, X., WANG, J., SUN, X., DONG, H. and SUN, C.Q., 2007. Tailoring ZnO nanowires for high performance amperometric glucose sensor. Electroanalysis, 19(9), pp. 1008- 1014.

ZHANG, B., ZHOU, S., LIU, B., GONG, H. and ZHANG, X., 2009. Fabrication and green emission of ZnO nanowire arrays. Science in China Series E: Technological Sciences, 52(4), pp. 883-887.

ZHANG, H., ZHOU, W., DU, Y., YANG, P. and WANG, C., 2010. One- step electrodeposition of platinum nanoflowers and their high efficient catalytic activity for methanol electro-oxidation. Electrochemistry Communications, 12(7), pp. 882-885.

ZHANG, H., YANG, D., LI, D., MA, X., LI, S. and QUE, D., 2005. Controllable growth of ZnO microcrystals by a capping-molecule- assisted hydrothermal process. Crystal growth & design, 5(2), pp. 547-550.

ZHANG, J., SUN, L., YIN, J., SU, H., LIAO, C. and YAN, C., 2002. Control of ZnO morphology via a simple solution route. Chemistry of Materials, 14(10), pp. 4172-4177.

ZHANG, Y., RAM, M.K., STEFANAKOS, E.K. and GOSWAMI, D.Y., 2012. Synthesis, characterization, and applications of ZnO nanowires. Journal of Nanomaterials, 2012, pp. 20.

ZHAO, J., JIN, Z., LI, T. and LIU, X., 2006. Nucleation and growth of ZnO nanorods on the ZnO-coated seed surface by solution chemical method. Journal of the European Ceramic Society, 26(13), pp. 2769-2775.

ZHU, J., KOLTYPIN, Y. and GEDANKEN, A., 2000. General sonochemical method for the preparation of nanophasic selenides: synthesis of ZnSe nanoparticles. Chemistry of Materials, 12(1), pp. 73-78.

ZHU, L., LI, Y. and ZENG, W., 2018. Hydrothermal synthesis of Hierarchical flower-like ZnO nanostructure and its enhanced ethanol gas-sensing properties. Applied Surface Science, 427, pp. 281-28.

Chapter 4

Methods of Characterisation

The aim of this chapter is to summarise the characterization methods used within this thesis for the analysis of the morphological, structural and functional properties of the ZnO nanostructures and cellular studies.

4.1. SEM

SEM is a powerful tool that is frequently used to form high resolution images of nanomaterials and provide details on topographic properties of the sample surface. Electron Microscopes (EMs) utilises a high-energy electron beams instead of light to examine the surface of solid specimens and produce a variety of different signals (Voutou, Stefanaki 2008). The signals that collect from SEM exhibit an information about the morphology and crystalline composition of the specimen. The main steps involved in all EMs are the following: an electron beam is produced by electron source in a high vacuum environment (Voutou, Stefanaki 2008). This beam of high-energy electrons is accelerated and focused using magnetic lenses and apertures towards the specimen. When an incident electron beam interacts with the sample atoms, various signals can be detected. A variety of signals can be generated by SEM, which involves secondary electrons which form SEM images, backscattered electrons, and X-rays (Voutou, Stefanaki 2008). Figure 4. 1 illustrates the typical experimental setup of SEM.

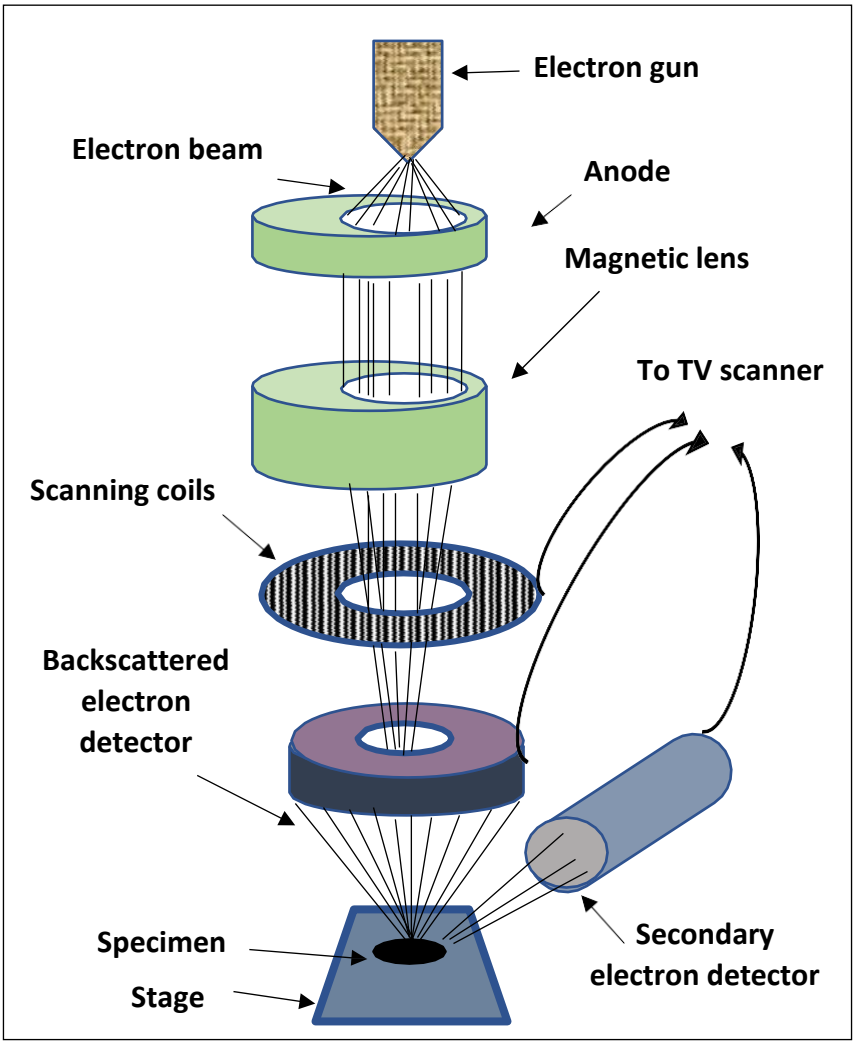

Figure 4. 1. A schematic diagram of SEM.

When the incident electron beam interacts with the specimen, elastic and inelastic collisions are noticed. Elastic collisions take place when the high energy electrons are ejected from the vicinity of the nucleus of the specimen's atom (e.g. backscattered). The generation of backscattered electrons differs directly with the sample's atomic number, therefore this varying generation rates results in larger atomic number samples to be brighter compared to lower atomic number samples. Inelastic collisions take place when the low energy of the electron beam (e.g. secondary electrons) is lost by scattering with the electrons in the sample (Flegler, Heckman et al,1993). Due to of their low

energy (~10-50 eV), Secondary electrons are only produced close to the surface, therefore topographic details can be obtained. Two different SEM models were used in this work; Carl-Zeiss EvoHD 15 and Leica S430. For cross sectional measurements of the samples, the stage was tilted to angles up to 60^0. The specimens were investigated in secondary electron modes.

3. 2. XRD

The discovery of X-rays in 1895 by Wilhelm Roentgen allowed physicists to study crystalline structure at the atomic scale (Jenkins 2000). XRD has been in use in two fundamental scopes, for the fingerprint characterisation of crystalline and amorphous materials and the identification of their composition. XRD is based on the elastic scattering of electrons that is the variation of direction of the electromagnetic waves without energy loss. Each crystal lattice contains a uniform, ordered an array of atoms with high atomic density planes which comprise of high electron density. When a monochromatic beam of X-ray photons falls onto crystal planes, scattering will take place and maximal diffraction may occur if the scattered photons interfere with each other, as well as one diffracted line will take place for each set of the crystal planes (Jenkins 2000). In the case of constructive interference, it is essential that the scattered beams generating from the individual atoms, be in phase with one another. A constructive interference will happen when the difference in the path lengths of the two scattered beams is equal to an integral number of wavelengths. Figure 4. 2 illustrates the principle of XRD.

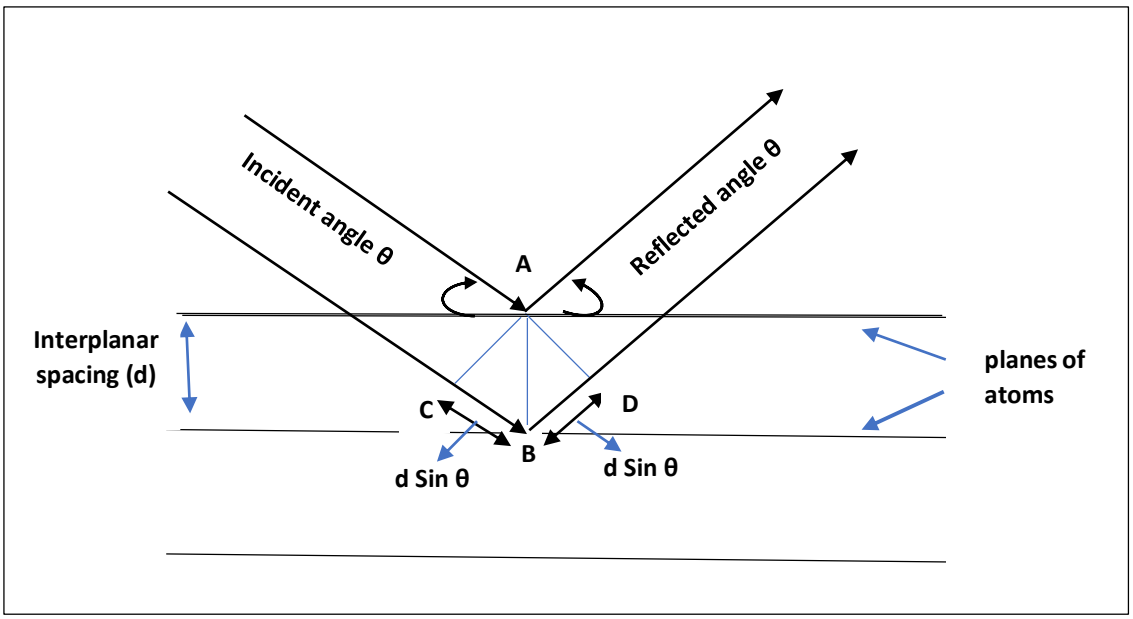

Figure 4. 2. Schematic representation of the XRD principle.

Hence, the condition of constructive interference will satisfy Bragg's law (Equation 11) (Jenkins 2000).

$$n\lambda = 2d \sin \Theta \qquad (11)$$

Where n is an integer, d is the inter-atomic spacing, and Θ is the diffraction angle. In general, XRD gives a plot of Intensity versus 2θ which exhibits a signature peak of the phases existing in the specimen. Comparison this signature peak with standard reference patterns, the needed characteristics can be addressed in the sample (Jenkins, 2000). The basic configuration of X-ray diffractometer is illustrated in figure 4. 3. In this work, different XRD models were utilized; Philips 1730 and Bruker D8 Advance with Da Vinci in the University of Leicester and Bruker D2 Phaser at De Montfort University.

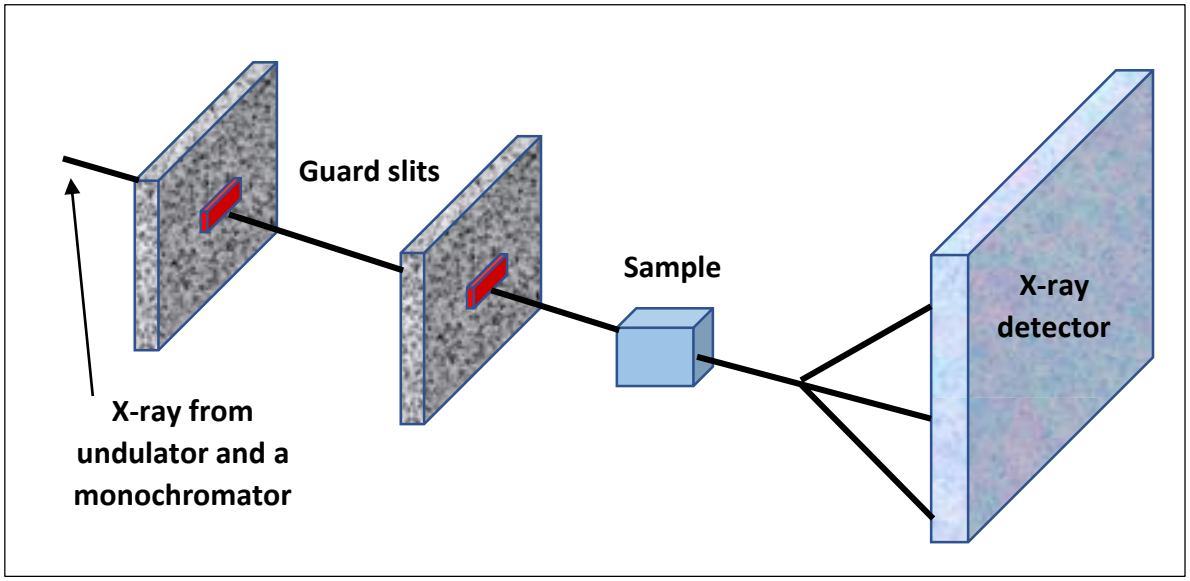

Figure 4. 3. The basic configuration of X-ray diffractometer.

4.3. AFM

AFM is one of the most high-resolution type of scanning probe microscope that utilizes to obtain three-dimensional topographic images of insulating and conducting samples. The AFM consists of a cantilever with a probe tip at its end. The tip radius of curvature on the order of nanometres is used to scan over the sample surface. The interactions between the sharp tip and the specimen are utilised to produce two or three-dimensional images. Whenever the pointed tip of cantilever goes through crosswise topographical details, van der Waals forces between the tip and the sample surface cause to deflect the cantilever. Then, this deflection is captured by a laser beam that reflects to change its angle. A detector is used to estimate the magnitude of the reflected beam of laser, which is corresponded to the surface topography of the specimen by software analysis. A schematic of AFM system is demonstrated in figure 4. 4 (Park systems).

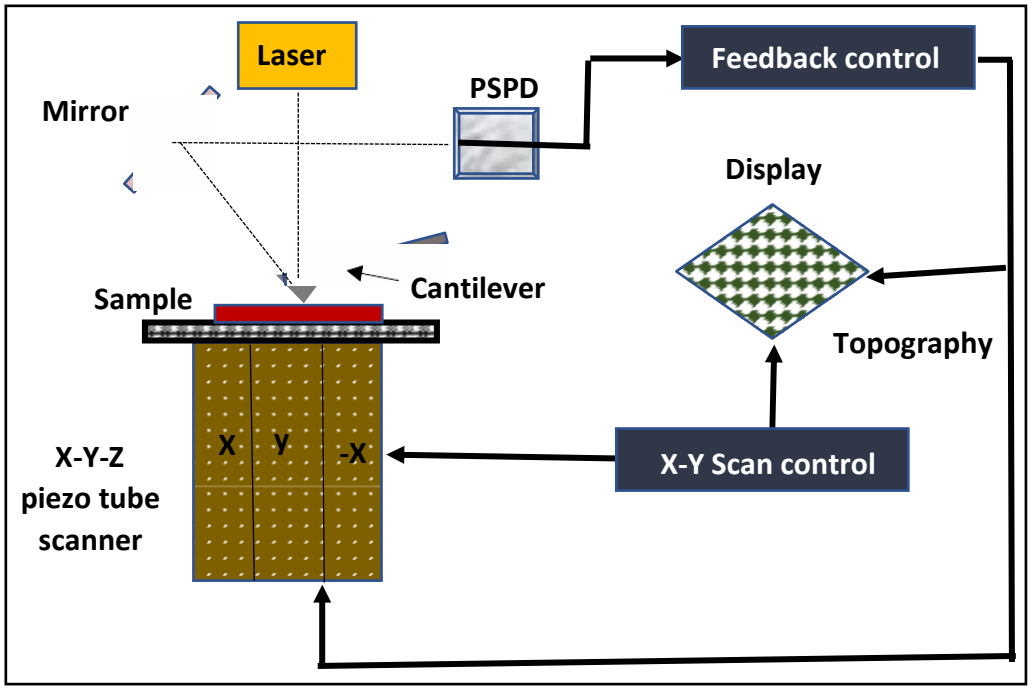

Figure 4. 4. A schematic diagram of AFM setup.

Figure 4. 5 demonstrates the distance dependency of the attractive and repulsive elements of the van der Waals force. The attractive force dominates when the tip is a few nanometres to the surface, however as the tip come nearer to the surface, the repulsion force creates a net repulsion.

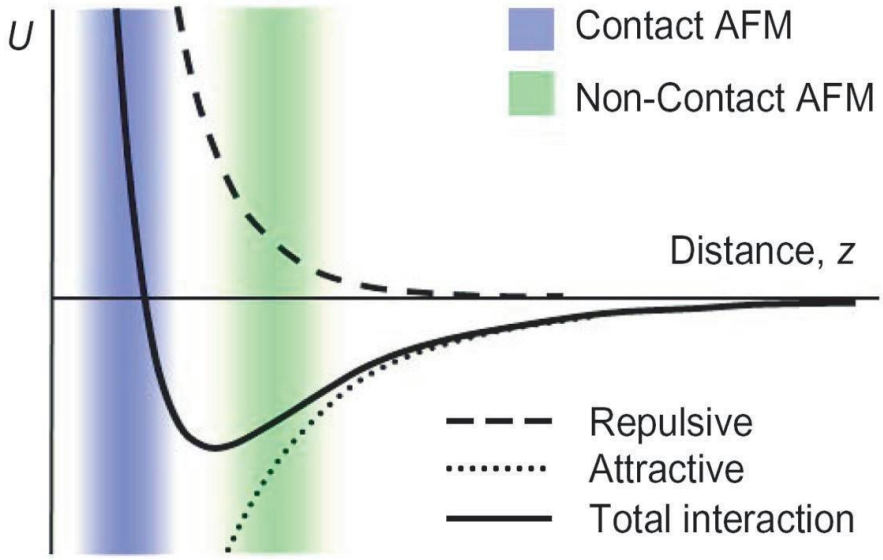

Figure 4. 5. the distance dependence of the interatomic force (Park systems).

Two different modes of AFM can be used; contact mode and non-contact mode. In contact mode, the tip is held in stable contact with the surface; hence, the surface topography is determined by shorter-scale repulsive deflections. In non-contact mode (NC-AFM), the tip is kept immediately above the surface; it probes surface features by deflections generated by larger-scale attractive interactions. In this mode, the tip is vibrated near the surface of a sample, the distance between the tip and the sample is on the order of 10-100 A^0. When the spacing between the atoms at the end of the probe tip and the atoms on the surface of the sample is much shorter, the repulsive forces between them are dominant, and the force varies due to the growing distance (Park systems). The AFM model used in this work is (Bruker DB) in NC-AFM mode (ParkAFM XE100).

4.3. Fluorescence Microscopy (FM)

Fluorescence is a type of photoluminescence, where a molecule absorbs light at a certain wavelength and subsequently emits light at a longer wavelength. The magnitude of the decay time between photon absorption and emission distinguish fluorescence phenomenon from its counterpart that known as phosphorescence (Spring 2003). Fluorescence usually takes less time; hence the corresponding decay time is shorter in the range of 10^{-8} seconds which causes in a negative frequency-shifted emission (Spring 2003). While the phosphorescence takes more time, therefore the decay time is longer in the range of milliseconds to seconds. Recently, FM has become a powerful technique in biology for study living material, including cells, tissues, and organisms (Spring 2003). It selectively enables testing of a specific element of a complicated biomolecular accumulation. The use of fluorochromes (fluorescent dyes) allows to determine cellular components and reveals the presence of a

single fluorescent molecule. Fluorochromes that are used to stain biological structures before examination, usually have significant quantum yield (the photon emission/absorption ratio) (Spring 2003). These special fluorescent reagents can absorb photon of a definite wavelength and emit another one at a longer wavelength slightly shifted to the red end of the spectrum from the absorbed light. For instance, if blue light is absorbed, green light will be emitted. So, green light is turned to yellow, yellow to red, and invisible UV light to visible blue light (Coling, Kachar 2001).

4. 4. 1. Principles of Fluorescence Spectroscopy

The main principle of the FM is to illuminate the sample with the desired wavelength and then to segregate the much weaker emitted light from the excitation light. The exciting light is typically 10^5 or 10^6 times brighter than the emitted light. Typically, light of a specific wavelength is passed through a wavelength selective exciter filter. The desired wavelength light reflects off a dichromatic mirror, through the objective lens to the sample. If the sample marked with the fluorescent molecule illuminates, the emitted light passes through the dichromatic mirror and then filtered by a barrier filter which obstructs the exciting wavelengths (Figure 4. 6). The emitted light irradiates in all directions, regardless of the direction of the excitation light and the objective must collect most of this radiation (Spring 2003). When the emission light is detected, the resulting fluorescent molecules will light up. Further details may be obtained from the optical and biochemical interactions shown by the fluorescent probe.

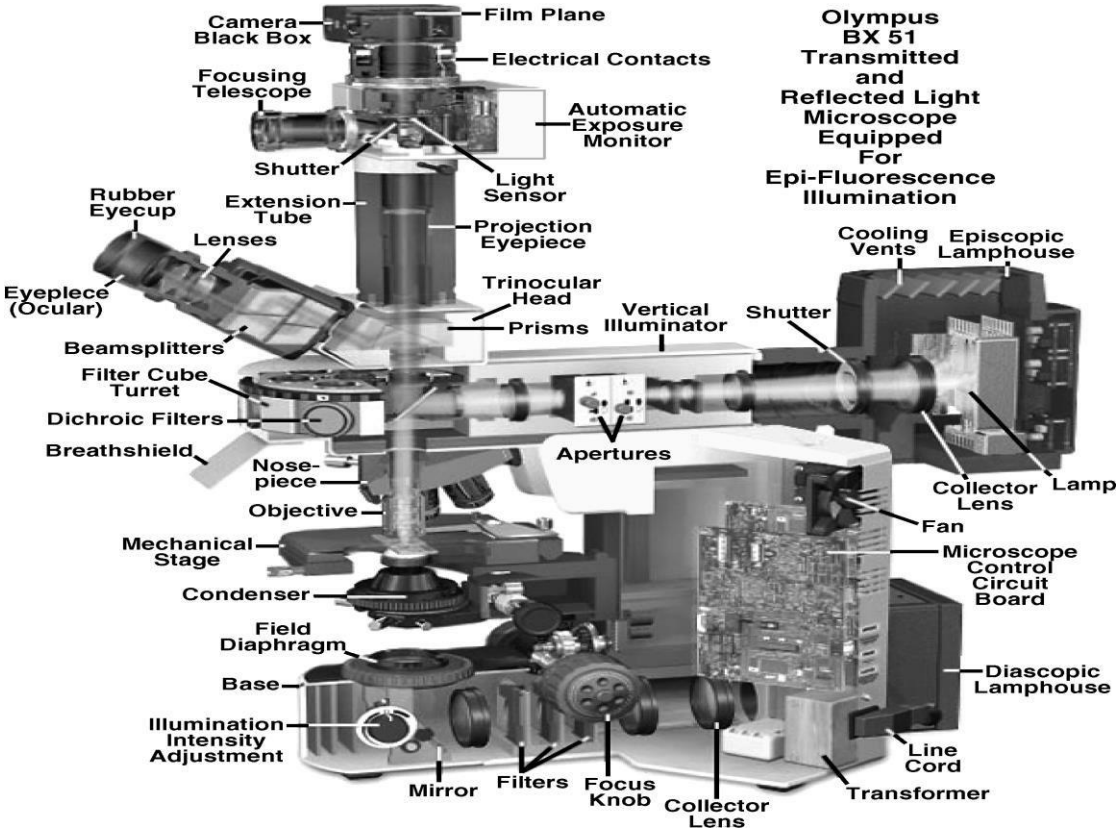

Figure 4. 6. The setup of FM. Reprinted with permission from (Spring 2003).

4. 4. 2. STOKES' Shift

When electrons transfer from the excited state to the ground state, they loss their radiation energy. As the radiation energy changes inversely to the wavelength, the emitted light is shifted to longer wavelengths than the excited light (Spring 2003). This phenomenon is known as Stokes' shift and the greater the Stokes' shift, the easier it is to separate excitation spectrum from emission spectrum usually, the intensity of emission peak is lower than the excitation peak (Figure 4. 7) (Spring 2003). The selection of excitation and emission wavelengths is mainly dependent on interference filters and the optical response of the system depends on such factors as glass transmission and detector responsivity (Spring 2003). A separation of the fluorescence emission

signal from the scattered excitation spectrum is assisted by selecting a fluorescent probe with a large Stokes shift.

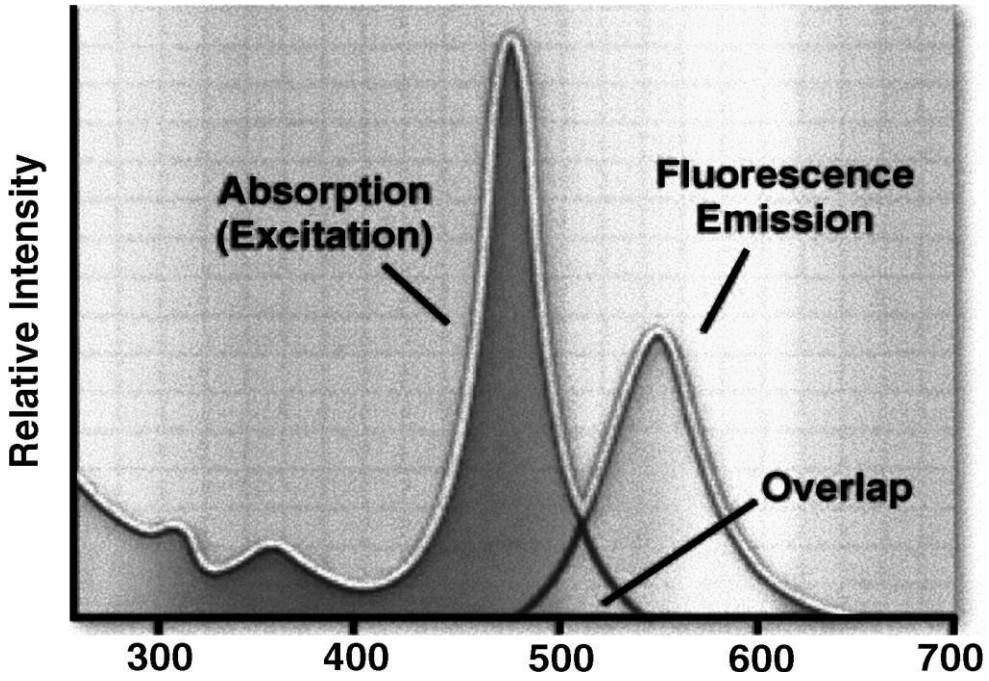

Figure 4. 7. A representation of the Stokes' shift. Reprinted with permission from (Spring 2003).

During excitation of a fluorescent molecules only some of the absorbed photons of the excitation light produce fluorescent emission. The quantum yield is a term that refers to the ratio of emitted to absorbed photons, usually it is between 0.1 and 1.0 (Spring 2003). Effective fluorescent reactants have a high quantum yield and many biological molecules fluoresce when they are illuminated with UV light. This effect is known as auto fluorescence. For example, the fluorescent amino acid tryptophan takes place in many proteins. Such molecules are limited in cell biology due to the lack of selectivity. Satisfyingly, auto fluorescence of cells and biological tissues and fluids can be reduced by utilizing probes that can be excited at >500 nm (Coling, Kachar 2001).

Here, the microscope is an Olympus CKX41. The samples were characterised using the “B” filter which allows excitation of GFP. A mercury vapour Short-arc bulb controlled by an Olympus U-RFLT50 power supply was used to produce light.

To summaries, the current chapter presents a variety of the characterization techniques used through this thesis. The next chapter demonstrates an optimizing statistical method to control the hydrothermal growth process of ZnO nanostructures.

References

COLING, D. and KACHAR, B., 2001. Principles and application of fluorescence microscopy. *Current Protocols in Molecular Biology,* , pp. 14.10. 1-14.10. 11.

Flegler, S.L., Heckman Jr, J.W. and Klomparens, K.L., 1993. Scanning and transmission electron microscopy: an introduction. *Oxford University Press(UK), 1993,*, p.225.

JENKINS, R., 2000. X-Ray Techniques: Overview. *Encyclopedia of analytical chemistry,* .

SPRING, K.R., 2003. Fluorescence microscopy. *Encyclopedia of Optical Engineering,* , pp. 548-555.

VOUTOU, B. and STEFANAKI, E., 2008. Electron microscopy: the basics. Physics of advanced materials winter school. *Aristotle University of Thessaloniki, Greece,* .

Park systems. (n. d) *True Non-Contact mode: Ultimate resolution of atomic force microscopy* [WWW] Park systems. Available from: http://www.parkafm.com/index.php/applications/nanotechnology. [Accessed 07/03/16].

Chapter 5

The hydrothermal growth of ZnO nanostructures

5. 1. Introduction

The main objective of this chapter is to introduce an optimizing approach based on statistical methods for designing and analyzing experiments to guide the synthesis process and perform high quality and reproducible hydrothermally synthesized ZnO nanostructures. In particular, the statistical analysis depends on the design of experiment technique which is a systematic method of changing process inputs and analyzing the resulting process outputs in order to quantify the cause and effect relationship between them. Importantly, it is possible to detect interaction effects among the input parameters which is considered the key to understanding and assess a process and that is not feasible by other statistical methods like one factor at a time approach. In this study, we use factorial design to sequentially plan the experiments and identify optimum response settings via tailoring the hydrothermal reaction parameters such as reaction temperature, time, and solution concentration. Anderson and Whitcomb provide a simple description of the analysis strategies of the design of experiments (Anderson, Whitcomb 2015), it allows the effects of a parameter to be estimated at several levels of the other parameters as well as a fewer number of runs is needed for the same precision in effect estimation (Anderson, Whitcomb 2015).

5. 2. Experimental details

P-type silicon (100) substrates with a surface of 1 × 1 cm^2 were utilized to synthesize ZnO nanowires. Before the growth process, the silicon samples were first ultrasonically cleaned by acetone and isopropanol for 15 min each to remove dust and surface contamination, then they were kept in ultrasonic deionized water bath for 10 min. Later, substrates were dried with nitrogen gas and baked on a hotplate at 150 ^0C for 10 min to eliminate any adsorbed moisture. The next step was deposition a thin layer of Au (5 nm) on the surface of the substrate by RF sputtering technique which acts as an intermediate layer to facilitate ZnO nanowires growth. For the hydrothermal growth of ZnO nanowires, an equimolar aqueous solution was prepared by using Zinc Nitrate Hexahydrate ($Zn(NO_3)_2.6H_2O$) and HexamethylTetramine (HMTA) ($C_6H_{12}N_4$). All precursors/solvents were purchased from Sigma-Aldrich with purity of 99%. Each precursor was dissolved in 100 ml of (DI), then the nutrient solution was transferred to sealable glass beaker that contains the Au-coated Si substrate and the nanowires were grown in a conventional oven. Here, the area of interest is to understand the growth mechanism of hydrothermally grown ZnO nanostructures and achieve the promising morphology which is required later to incorporate with cellular interface. Before proceeding to design the experiment and select the experimental parameters, literature search was conducted to know about previous studies, instruments used, procedures and the findings. Based on this search it was decided to choose the reaction parameters which are more likely to satisfy the need of producing the desired shape with a few numbers of experiments, hence, it is feasible to reduce time and the budget of experiments.

To investigate the effects of the hydrothermal reaction parameters on the morphology and aspect ratio of ZnO nanowires, the nutrient solution was

modified to high and low levels of growth parameters. So, based on tow- level factorial design the reactant concentration was adjusted to 3 mM and 30 mM to investigate at two various times (12hrs, 24hrs) and two different temperature (70 ^{0}C, 90 ^{0}C). Lastly, the resultant ZnO nanowires were washed with (DI) and dried by nitrogen gas. The morphology of the nanowires was examined using scanning electron microscopy (SEM) and their structure were analyzed by XRD. The length and diameter of ZnO nanostructures were determined with the aid of the Image J software.

5. 3. Results and discussion of the controlled synthesis of ZnO nanostructures by the reaction parameters

In the nutrient solution, Zn $(NO_3)_2{\cdot}6H_2O$ supplies zinc ions, water produces oxygen ions, and HMTA releases hydroxyl ions by the thermal decomposition process. The hydroxyl ions will react with zinc ions to form $Zn(OH)_2$ which then undergoes a dehydration reaction to form ZnO nanowires. These chemical reactions can be controlled by tailoring the growth parameters, such as precursor concentration, time, and temperature of the growth. In the following sections, the influence of each parameter on the crystal morphology, aspect ratio, and number of densities of ZnO nanowires is investigated.

5. 3. 1. Temperature

The effect of growth temperature on the as-synthesized ZnO nanowires was investigated. According to the design of experiments separate growth runs were carried out at 70 ^{0}C and 90 ^{0}C and the corresponding SEM images of the growth structures are presented in Figures 5. 1 and 5. 3. It was found that the temperature significantly affects the aspect ratio of the nanowires, as at low temperature (70 ^{0}C) the nanowires of an average length of 2.28 µm were

obtained. A further increase in the processing temperature up to 90 ^{0}C leads to a great reduction in the nanowire's length to about 384.86 nm. It was not a considerable dissimilarity in the diameter of nanowires at the processing temperatures 70 and 90^0 C.

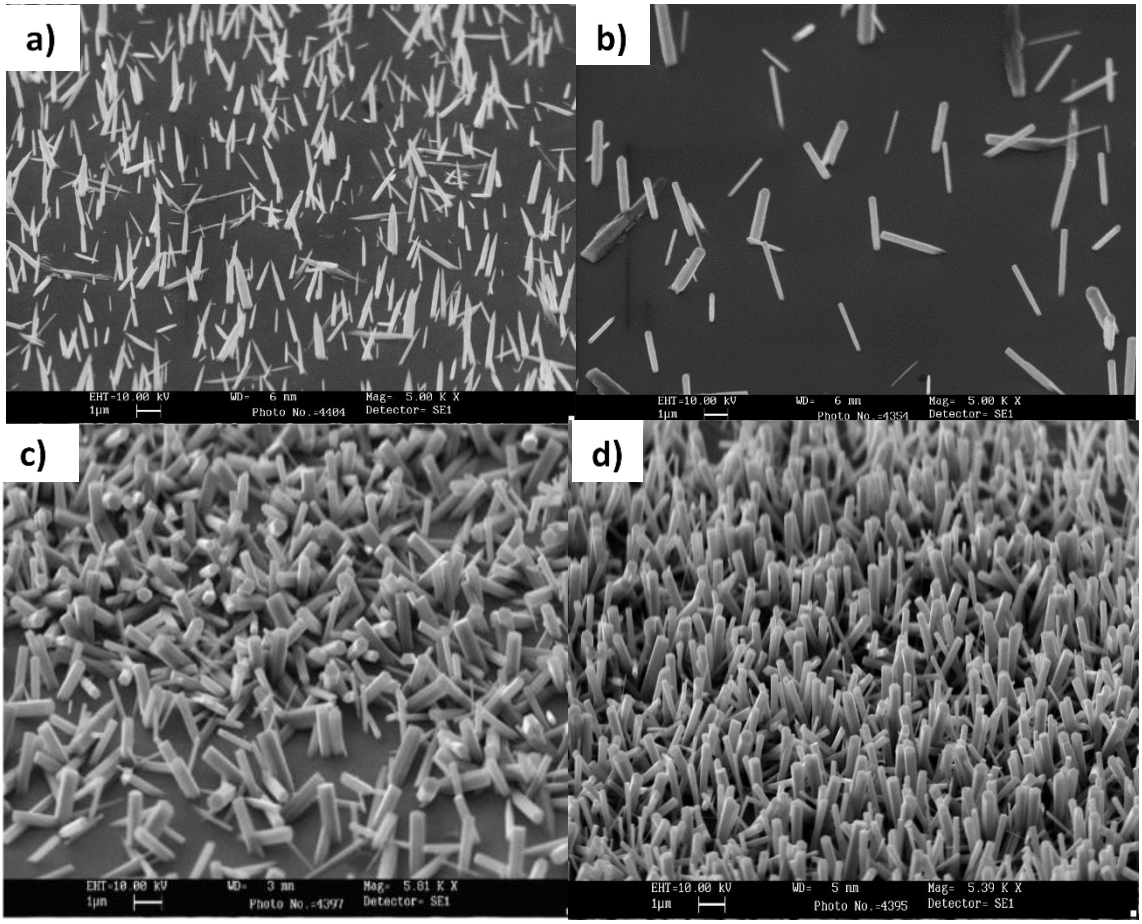

Figure 5. 1. Tilted-view SEM images of ZnO nanostructures. They are grown (a) at 3mM, 70 ^{0}C, 24h. (b) at 3 mM, 70 ^{0}C, 12hrs. (c) at 3o mM, 70 ^{0}C, 12hrs. (d) at 30 mM, 70 ^{0}C, 24h.

The influence of the reaction temperature can be attributed to a number of reasons: first is the role that of HMTA plays in NW growth (Sun, Riley et al. 2006). As we can see from equations (1-4), HMAT is used as the alkali source to supply OH^- anions which react with Zn^{2+} cations to produce zinc species. These species consider as growth units which decompose at a suitable supersaturation condition through the growth process to form ZnO crystals.

Accordingly, at high temperature associated with high precursor concentration, the thermal decomposition rate of HMTA will be significant leading to faster breaking down of the chemical bonds and releasing OH^- ions, so at this stage growing thicker and shorter hexagonal like shape will be preferred (Figure 5. 1c, d). This observation indicates that the length of ZnO NWs is directly influenced by the solution supersaturation, which is determined by the precursor's concentrations.

Independent modification of these two processing parameters is uncontrollable with HMTA due to the mechanism of OH^- production that is intrinsically related to temperature through the thermal decomposition kinetics of HMTA (McPeak, Le et al. 2011). Additionally, the solution supersaturation is still important certainly in the early stage of the nucleation growth, as it was found that the heterogeneous growth of ZnO just take place at critical (metastable) supersaturation level where the critical radius or nucleus size can be initiated (Cubillas, Anderson 2010). However, elevating reaction temperature causes a decline of the critical radius which means the likelihood of creating nucleation sites will be higher. It is essential to use the main effect and interaction effect in order to identify the relationship between the reaction parameters and measured responses. According to the interaction's plots, the greater the variation in slope between the lines (nonparallel lines), the stronger the degree of interaction. The main effect plot of the length (Figure 5. 2 a) illustrates that the length of the nanowires is considerably increased at low temperature (70 ^{0}C) while at temperature of 90 ^{0}C producing shorter hexagonal nanostructures is significantly high. In the interaction effect (Figure 5. 2 b), it seems that the length of nanowires is greatly affected by the interactions of the all other growth parameters.

However, some reaction settings are not good e.g. the combination of high levels of the nutrient concentration and processing temperature is unsuitable in terms of producing good uniformity, and controllable sizes of ZnO nanostructures.

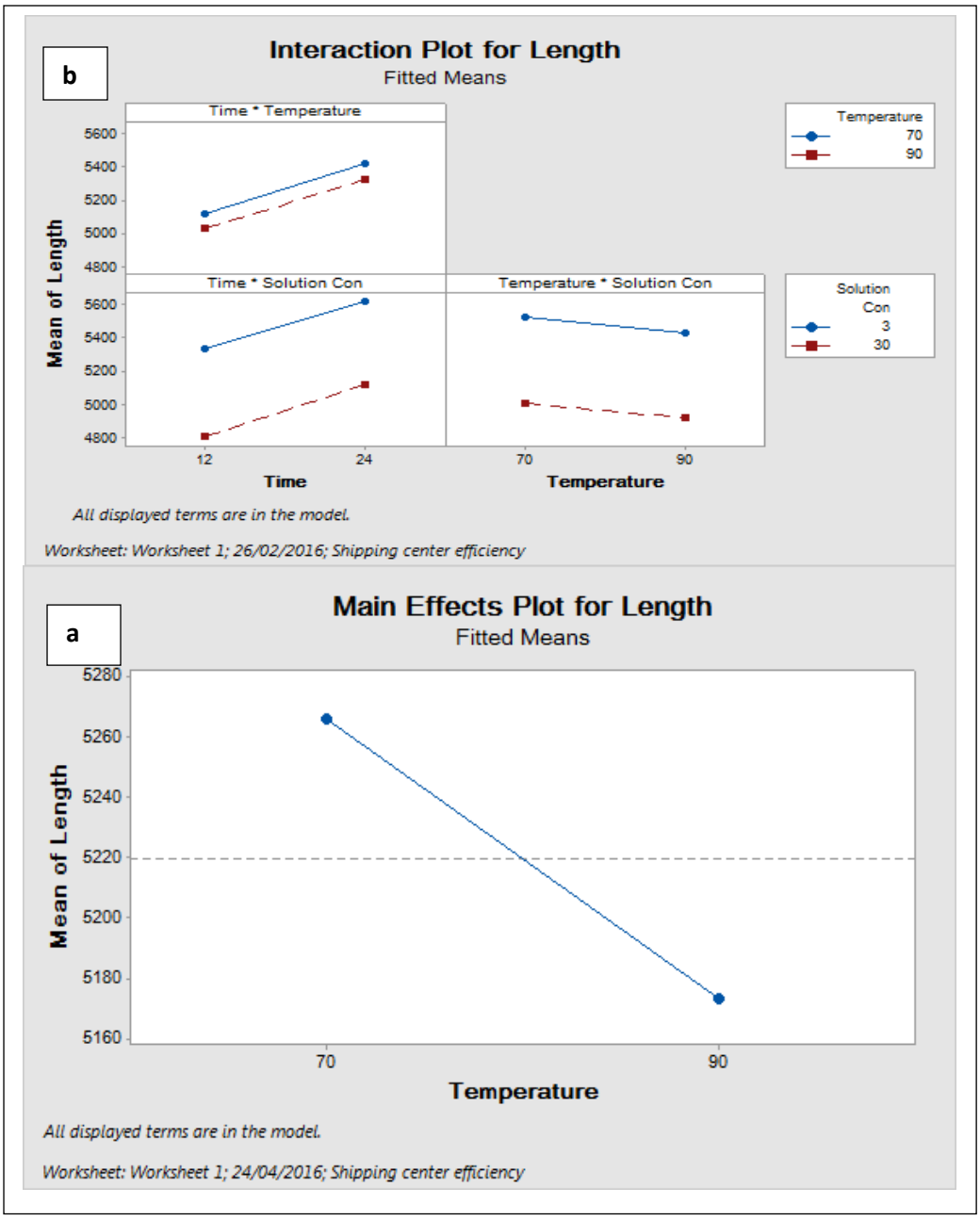

Figure 5. 2. (a) the main effect of the length. (b) The interaction effects for the length.

5. 3. 2 Precursors concentration

A series of experimental settings was conducted to explore the connection between the precursor concentration and the number density of ZnO nanowires. It is worth mention here that the measured data of the nanowire's density was calculated as a number of nanowires per 64 μm^2. We choose to carry out the runs at high and low concentration of an aqueous solution and It was observed that the density of nanowires strongly depended on the precursor concentration. At precursor concentration of 30 mM, the number of densities increases dramatically which could be attributed to the following reason.

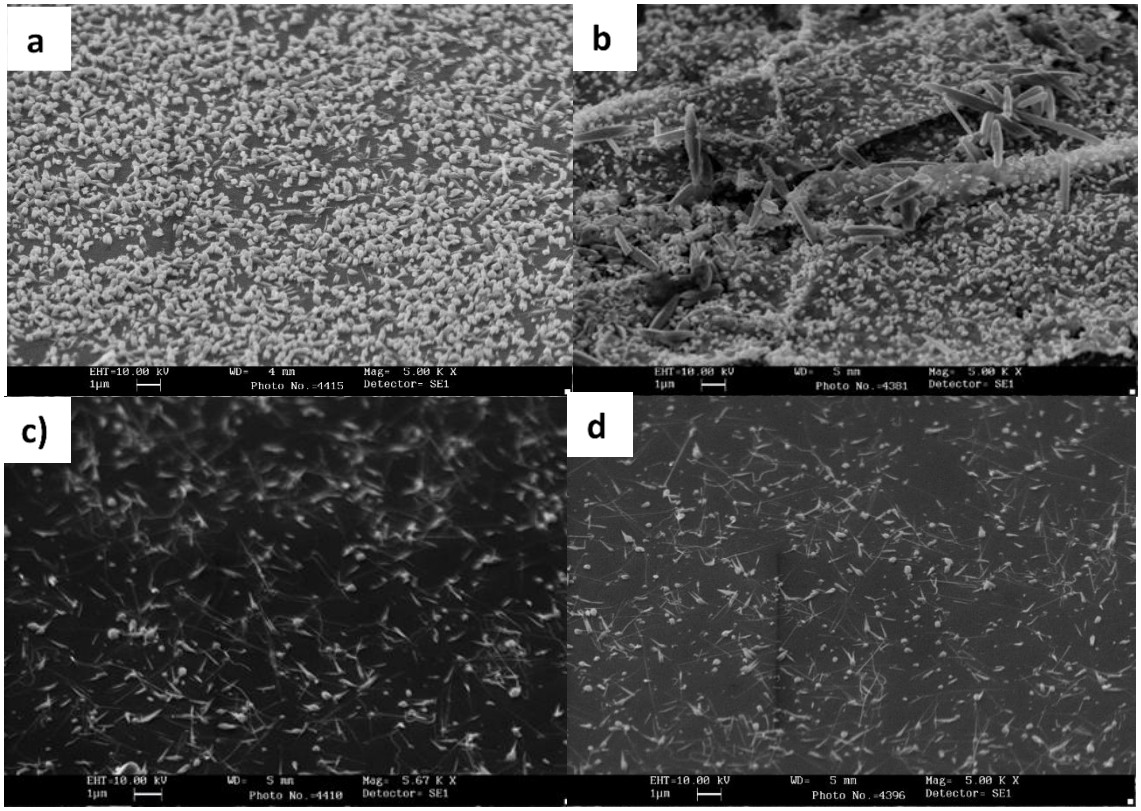

Figure 5. 3. Plan-view SEM images of ZnO nanostructures. They are grown (a) at 30 mM, 90 ^{0}C, 12hrs. (b) at 30 mM, 90 ^{0}C, 24hrs. (c) at 3 mM, 90 ^{0}C ,12hrs. (d) at 3 mM, 90 ^{0}C ,24hrs.

At the initial stage of the growth with a high concentration of Zn^{2+} ions, the chemical potential of zinc and the surface free energy increase. To minimize the zinc chemical potential and maintain an equilibrium environment that needed to initiate the growth, the formation of more nucleation sites is required, resulting in the number density of the nanowires increasing (Xu, Lao et al. 2008) (Figure 5. 3 a, b). It was also noticed that the concentration of HTMA and Zn $(NO_3)_2$ is in close relationship with the nucleation rate of ZnO facets which considerably influences ZnO morphology. Such strong link could be explained by the crystal growth and nucleation theory (Cubillas, Anderson 2010), as reaction procced, adsorption of precursor ions from the nutrient solution on the firstly formed accommodation site/ZnO nucleus is needed to generate ZnO crystal therefore If the concentration of Zn^{2+} precursor is low, the contribution from Zn $(NO_3)_2$ will be very limited which explain why at a concentration of 3 mM and temperature of 90^0 C very sparse and poor uniformity of ZnO NWs was obtained. Over the course of time, Zn^{2+} ions will be nearly consumed at the root of nanowires and the remnant precursor could not approach the top surface. So, the growth rate is comparatively limited at tops of nanowires which leads to the production of shaped needle-like structures (Figure 5. 1 a).

However, an increase of the precursor concentration result in further supply from nutrient solution to crystal growth, and, therefore, Zn^{2+} precursor can contribute regularly to root and top areas, resulting in the formation the ZnO hexagonal wurtzite structures (Figure 5. 1 c, d). Based on these observations, it was found that high values of precursor concentration and processing temperature lead to form more accommodation sites rather than supporting the nanowire growth to get longer. The cause behind that is the degree of solution saturation whether is under- saturated or supersaturated that decides

the probability of nucleus that has settled down onto the surface of the substrate remaining on it or eventually incorporating and proceeding nanowires crystal growth forward. As mentioned above, the significant impact of the precursor concentration on the morphology and density of ZnO nanowires is demonstrated in figure 5. 4.

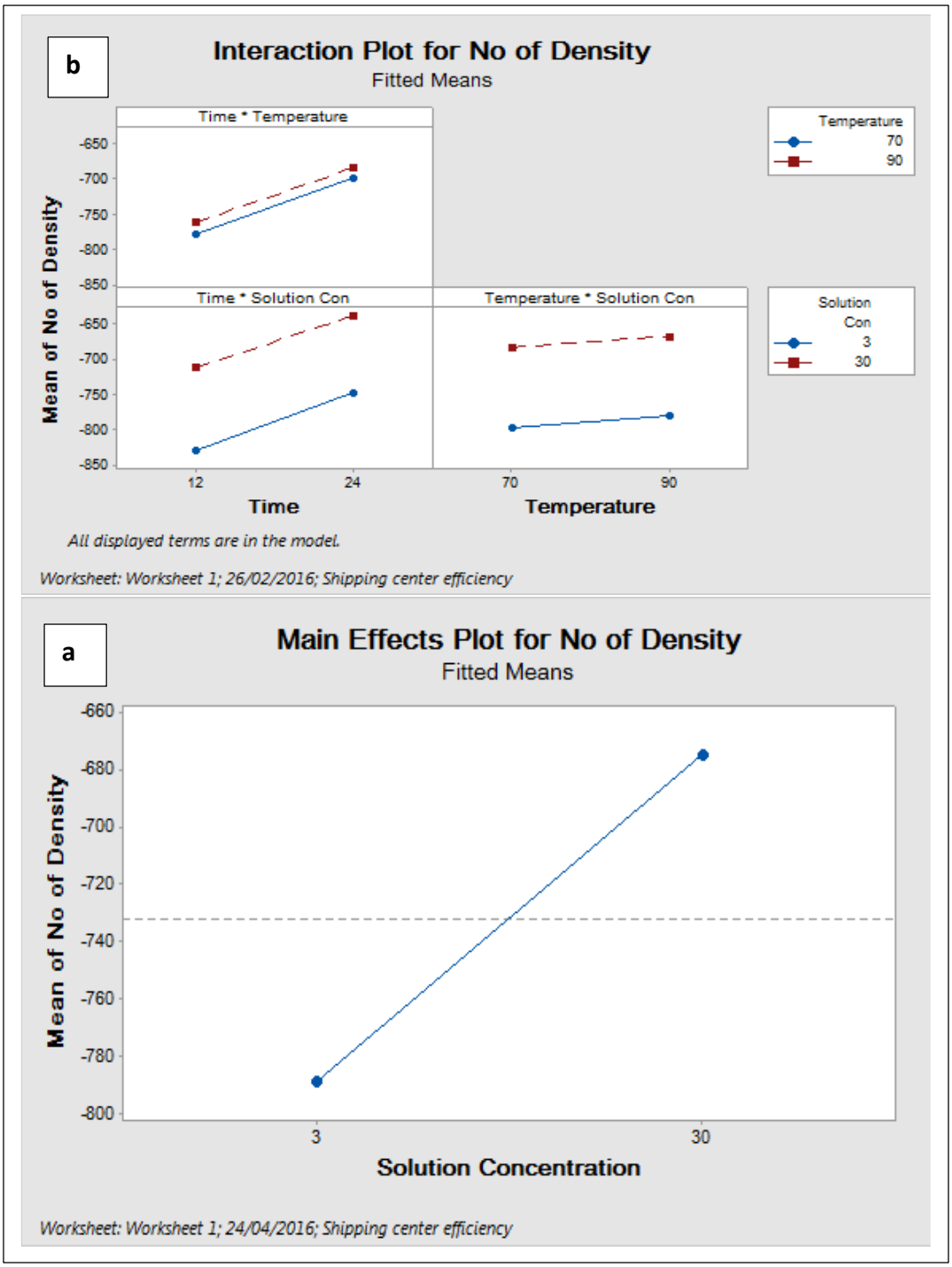

Figure 5. 4. (a) the main effect of number of densities. (b) The interaction effects for number of densities.

It can be seen that the density of nanowires is significantly decreased at low concentration, whereas dense and thick ZnO nanowires is observed at high solution concentration. Based on the interaction effects of reaction parameters (Figure 5. 4), it was noticed that the experimental runs with low levels of precursor concentration result in the promised structure of the nanowires (needle-like structure).

5. 3. 3. Time

It was found that time plays a key role in a formation of homogenous, well-oriented ZnO nanowires with high aspect ratio. Figures 5. 1a, b shows the tilted-view SEM images of ZnO nanowires prepared at tow various times of 24 and 12 h, respectively while maintaining precursor concentration (3mM) and reaction temperature (70 ^{0}C) constant. Different morphology of nanowires obtained at different growth duration, like-needle structures formed at 24 h whereas reducing reaction time to 12 h produces hexagonal- column nanostructures. The aspect ratio of the nanowires was strongly dependent on the reaction time, as double of the reaction duration from 12 to 24 h, resulting in an increase of the average length and diameter of ZnO nanowires from 1.48 µm to 2.27µm and from 267.9 nm to 445.7 nm respectively (see appendix A). The variation of nanowires shape from hexagonal to needle-like structures at different growth duration can be probably associated to the electrostatic interaction between charged precursor ions and oppositely charged crystal surfaces that can promote or suppress the crystal growth into particular facets at specific growth time. In addition, ZnO polar surfaces are much more energetic than non-olar surfaces (Qiu, Li et al. 2009), that means the adsorption of precursor ions will be higher along c-axis while the non-polar facets will have low incorporation rates into the growth of ZnO crystals, resulting in long nanowires. We also

suggest that carrying out experiments with low precursor concentration for an extended period could lead to depleting the nutrient supply and slow down the growth rate. In accordance to the main and interaction effects for the aspect ratio of ZnO nanowires (Figure 5. 5), it is obvious that the growth duration is a critical parameter which influences the morphology and aspect ratio of the nanowires.

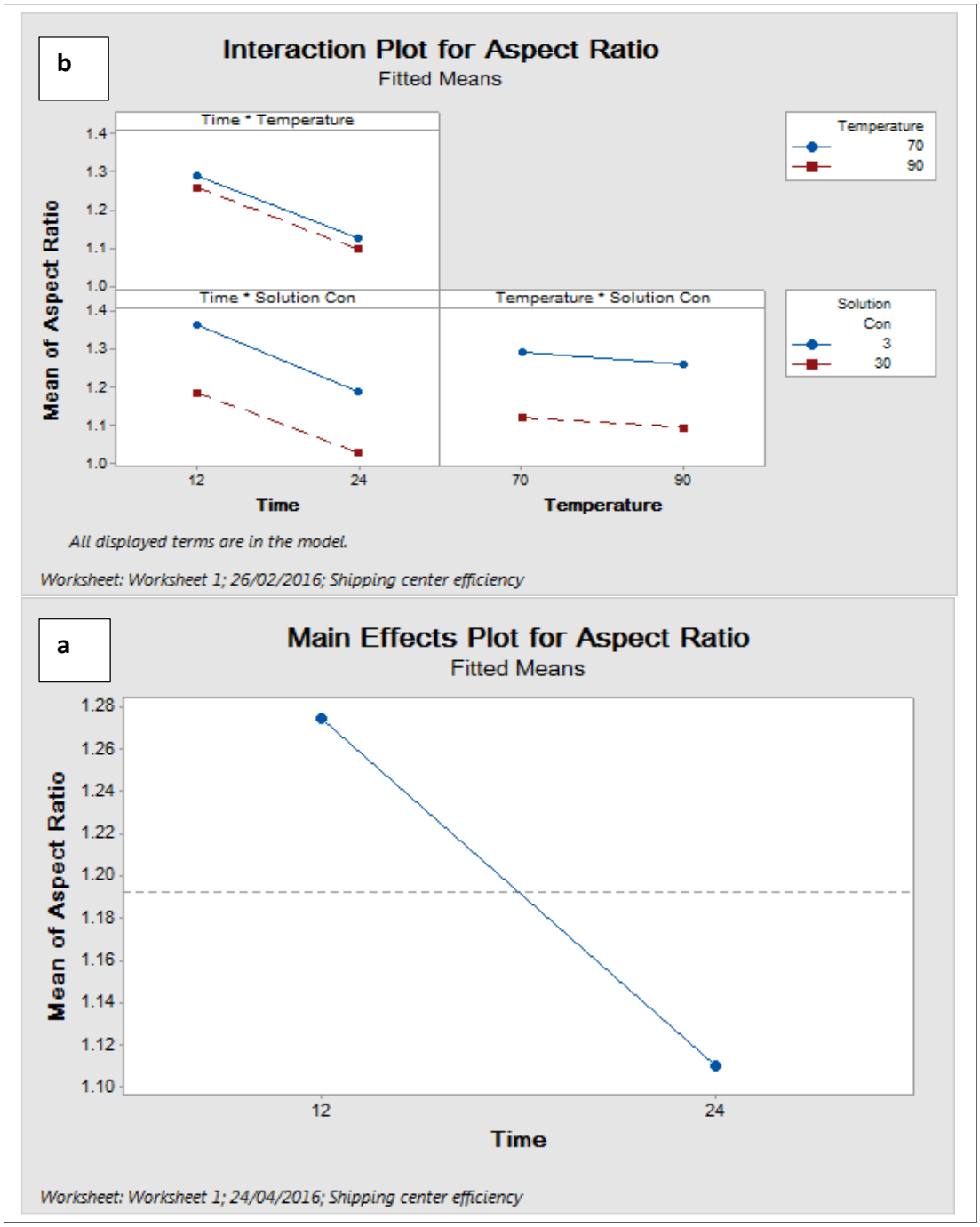

Figure 5. 5. (a) the main effect of aspect ratio. (b) The interaction effects for aspect ratio.

The different morphology of ZnO NWs was analysed by XRD to investigate its crystal structure and phase purity (Figure 5. 6). The ZnO diffraction peaks showed high crystallinity for both hexagonal wire and needle wire shapes. All the observed peaks were indexed to the wurtzite hexagonal structure of ZnO according to JCPDS-file 36-1451 which is given in Table 5. 1. Apart from Si (211), no other diffraction peaks were found, which proves that there were no impurities existent. The strong, prominent diffraction peaks corresponding to (002) planes confirm that the product was well crystalline with a preferential growth orientation along c-axis in both morphologies.

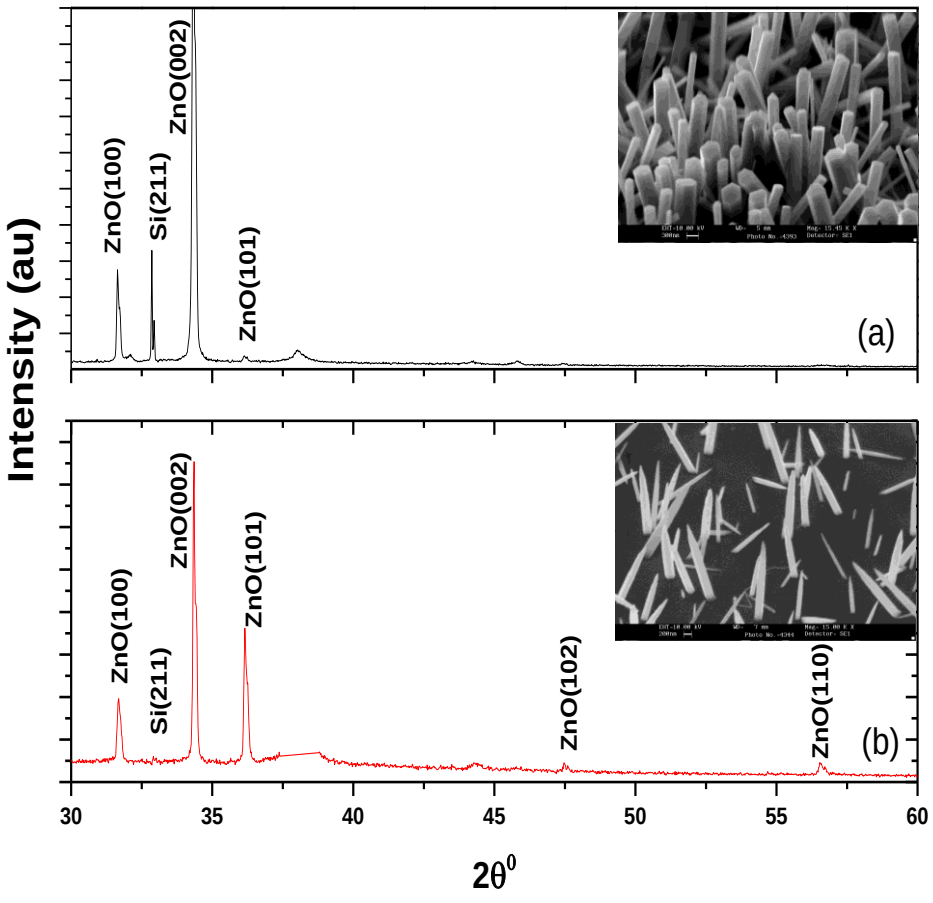

Figure 5. 6. XRD pattern of (a) Hexagonal ZnO nanowires grown at 3o mM, 70 ^{0}C, 24h.(b) ZnO nanoneedles grown at 3 mM, 70 ^{0}C, 24h.

It was found that Si (211) was less evident in XRD diffractogram of ZnO nanoneedles which can be attributed to variations in the scattering cross section intensity of the sample. In addition, a different state of the particles aggregation in the crystal plane may certainly produce differences in the intensity of diffractions of the same crystal plane.

Table 5. 1. XRD reference data for ZnO wurtzite hexagonal structure (McMurdie, Morris et al. 1986).

2θ	Peak number	d(Å)	Normalized Intensity	h	k	l
31.7694	1	2.814300	57	1	0	0
34.4211	2	2.603320	44	0	0	2
36.2521	3	2.475920	100	1	0	1
47.5376	4	1.911140	23	1	0	2
56.6015	5	1.624720	32	1	1	0
62.8626	6	1.477120	29	1	0	3
66.3783	7	1.407150	4	2	0	0
67.9608	8	1.378180	23	1	1	2
69.0981	9	1.358250	11	2	0	1

5. 4. Statistical design of experiments

In this investigation, systematic condition-dependent design was applied to comprehensively compare the dependency among the processing parameters to realize their effect on the morphology and aspect ratio of solution-synthesized ZnO nanostructures. Thus, a two-level factorial design analysis was used to identify optimal reaction settings of the process parameters, such design is necessary when main interactions between parameters may be existent and it is hard to separate. In doing so, the relative effects of the various parameters on specific properties can be elucidated. The experiments were conducted in two main stages, the experimental settings and their measured responses for the first and second stage are listed in Tables 5. 2 and 5. 3 respectively.

Table 5. 2. Design and experimental results of the first stage.

Run order	Time (h)	Temperature (C^0)	Solution Con(mM)	Length (nm)	Diameter (nm)	Aspect Ratio	No of Density
1	12	70	3	2130	268	0.12	44
2	24	70	3	2163	357	0.17	183
3	12	90	3	371	200	0.53	130
4	24	90	3	330	200	0.60	125
5	12	70	30	1482	353	0.23	244
6	24	70	30	2278	446	0.19	199
7	12	90	30	385	291	0.75	375
8	24	90	30	259	218	0.84	350

In the first stage, it was tried two various levels of the reaction parameters to explore which combination of setting produces a desirable shape of

nanostructures. Once the desirable nanostructures (like-needle shape) were achieved, we focus on exploring the optimum reaction combination for increasing the aspect ratio of ZnO nanowires. Systematically, we conducted eight experiments in the first stage, we noticed that few of settings provided a consistent consequence. In contrast, some of the combinations resulted in the inconsistent growth of nanowire, the results of these setting are shown in figures (5. 7, 5. 8).

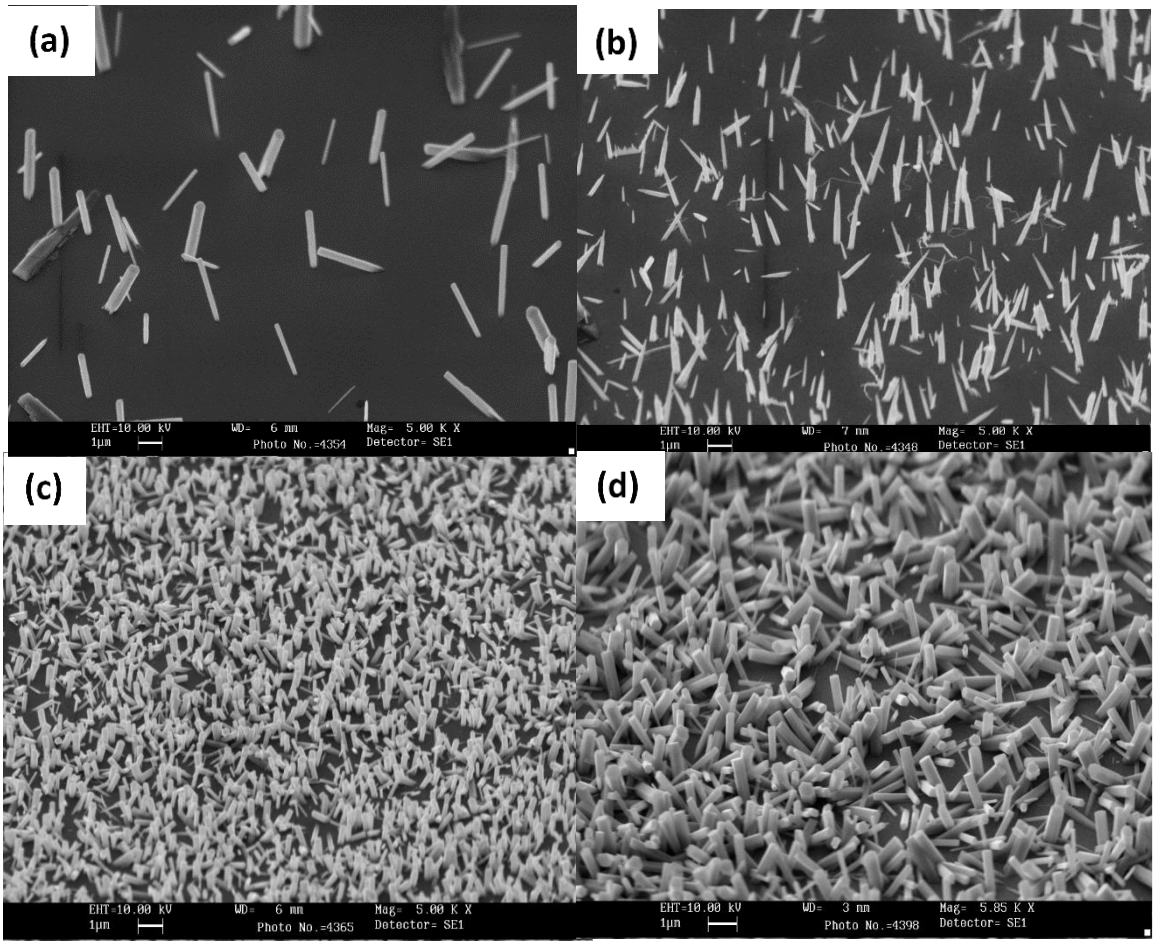

Figure 5. 7. SEM images of ZnO nanowires and the growth conditions are listed in table 1 based on the run order; (a) at 3 mM, 70 ^{0}C, 12hrs. (b) at 3 mM, 70 ^{0}C, 24hrs. (c) at 30 mM, 70 ^{0}C ,12hrs. (d) at 30 mM, 70 ^{0}C ,24hrs.

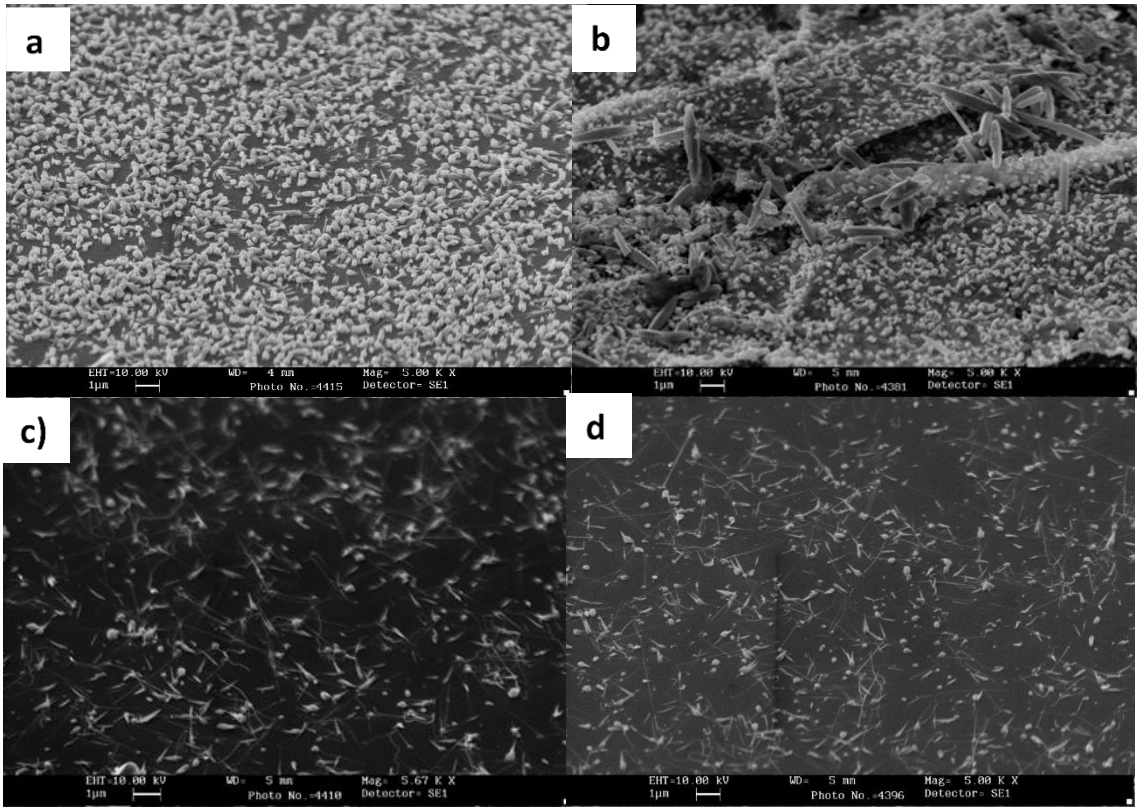

Figure 5. 8. SEM images of ZnO nanowires and the growth conditions are listed in table 1 based on the run order; (a) at 30 mM, 90 ^{0}C, 12hrs. (b) at 30 mM, 90 ^{0}C, 24hrs. (c) at 3 mM, 90 ^{0}C ,12hrs. (d) at 3 mM, 90 ^{0}C ,24hrs.

A statistical interaction occurs when the effect of one reaction parameter on the one measured response changes depending on the level of another reaction parameter while the main effect is just related to the dependency of measured variable on one reaction parameter. For example, we can see from the two lines presented the time and temperature in figure 5. 9 that they are far from parallel which means a strong interaction between the time and temperature of the reaction that could significantly affect the diameter of the nanowires.

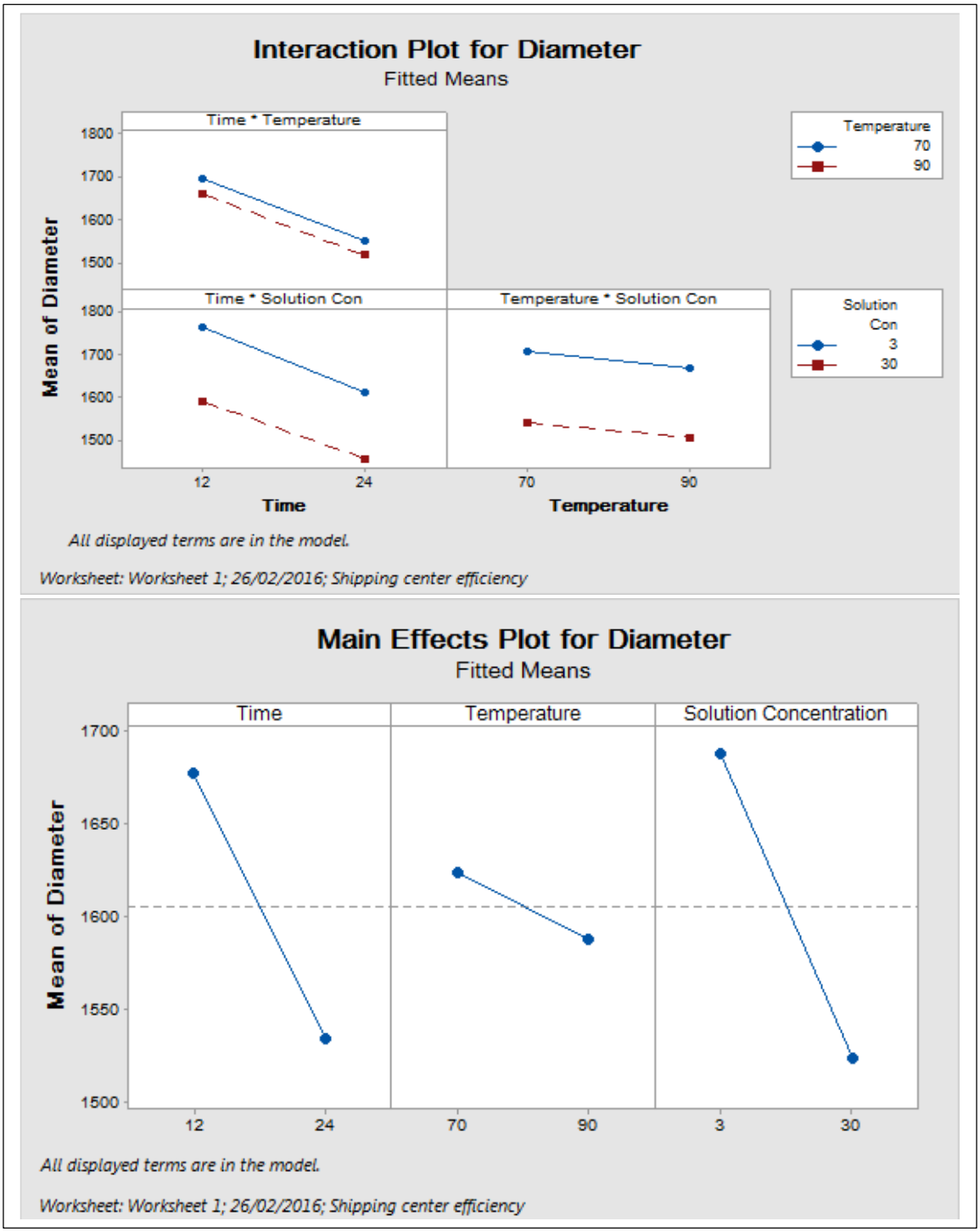

Figure 5. 9. The main and interaction effects plots of the diameter of ZnO nanowires (stage 1).

In contrast, they are nearly parallel in the second stage (Figure 5. 10) which indicates that there is no significant difference in the diameter of the nanowires at these levels of reaction parameters.

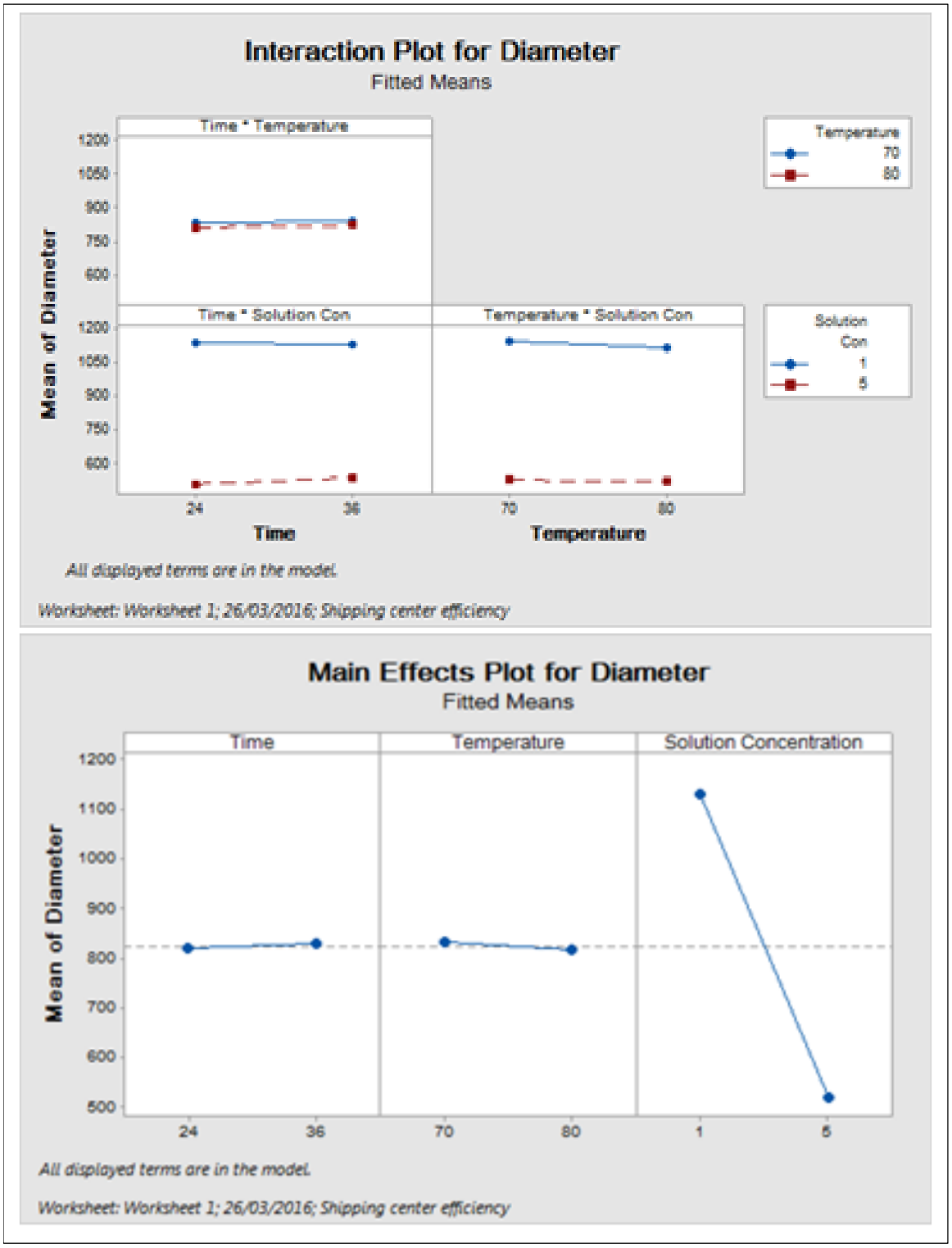

Figure 5. 10. The main and interaction effects plots of the diameter of ZnO nanowires (stage 2).

Detailed information about the correlation between the processing parameters are drawn based on their main effects and interaction effects, further, a prediction of a potential link among these parameters and the measured responses is deduced from 3D surface representations (see appendix. A). Stand on the observed statistical data, we noticed that a combination setting of precursor concentration and growth temperature at 30 mM and 90 ^{0}C results in a poor growth of nanowires. The possibility of acceptable growth was higher at low levels of solution concentration and reaction temperature (3 mM, 70 ^{0}C). On account of these observations, we neglected the levels of temperature at 90 ^{0}C and precursor concentration at 30 mM. It was clear that the growth duration affects the aspect ratio of the nanowire. Therefore, our next goal in the second stage to concentrate on the vicinity of parameters setting that leads to the consistent and uniform morphology of ZnO nanowires.

In the second stage, we performed eight experiments to optimize nanowires morphology. SEM images of the grown nanowires are shown in figures (5. 11, 5. 12), and It was obvious that most of the experimental collections provided a reasonable growth of ZnO nanowires. Importantly, the aspect ratio of nanowires was greatly enhanced when compared to the earlier stage. In the first stage, precursor concentration and growth duration were found to be the most significant parameters that greatly affect all resulted responses. As low precursor concentration at 3 mM was good than that at 30 mM, we tried a further combination around 1 and 5 mM in the second stage. Since the growth duration of 24 h was better than that of 12 h, we decided to set time at 24 and 36 h to find out if there will be any enhancement at 36 h. Lastly, because of the high level of temperature at 90 ^{0}C did not perform better than that at 70 ^{0}C, we replaced it by temperature of 80 ^{0}C.

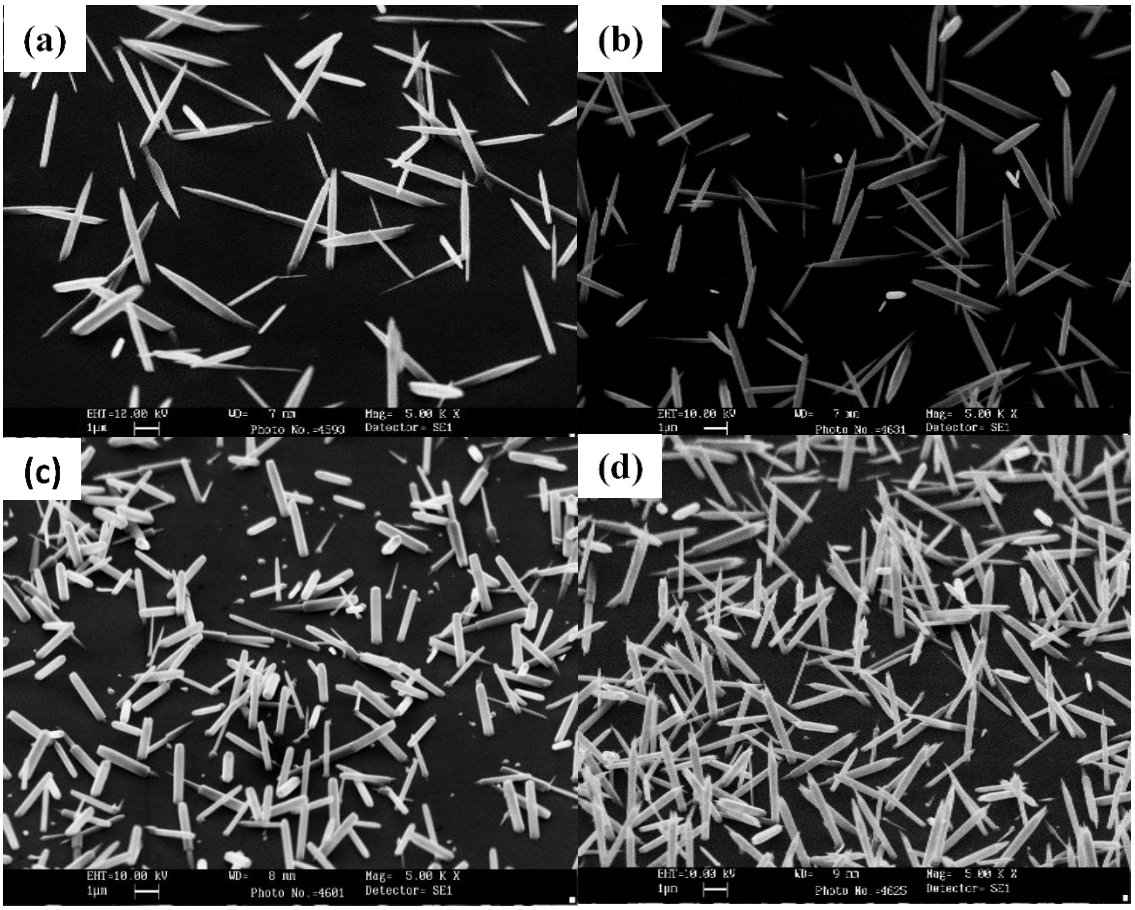

Figure 5. 11. SEM images of ZnO nanowires and the growth conditions are listed in table 2 based on the run order; (a) at 1 mM, 70 ^{0}C, 24h. (b) at 1 mM, 70 ^{0}C, 36h. (c) at 5 mM, 70 ^{0}C ,24h. (d) at 5 mM, 70 ^{0}C ,36h.

Table 5. 3. Design and experimental results of the second stage.

Run order	Time (h)	Temperature (C^0)	Solution Con(mM)	Length (nm)	Diameter (nm)	Aspect Ratio	No of Density
1	24	70	1	3024	429	0.14	56
2	36	70	1	3633	398	0.11	51
3	24	80	1	1630	336	0.20	76
4	36	80	1	872	327	0.37	20
5	24	70	5	2194	356	0.16	105
6	36	70	5	3221	348	0.11	125
7	24	80	5	839	307	0.36	100
8	36	80	5	1479	332	0.22	120

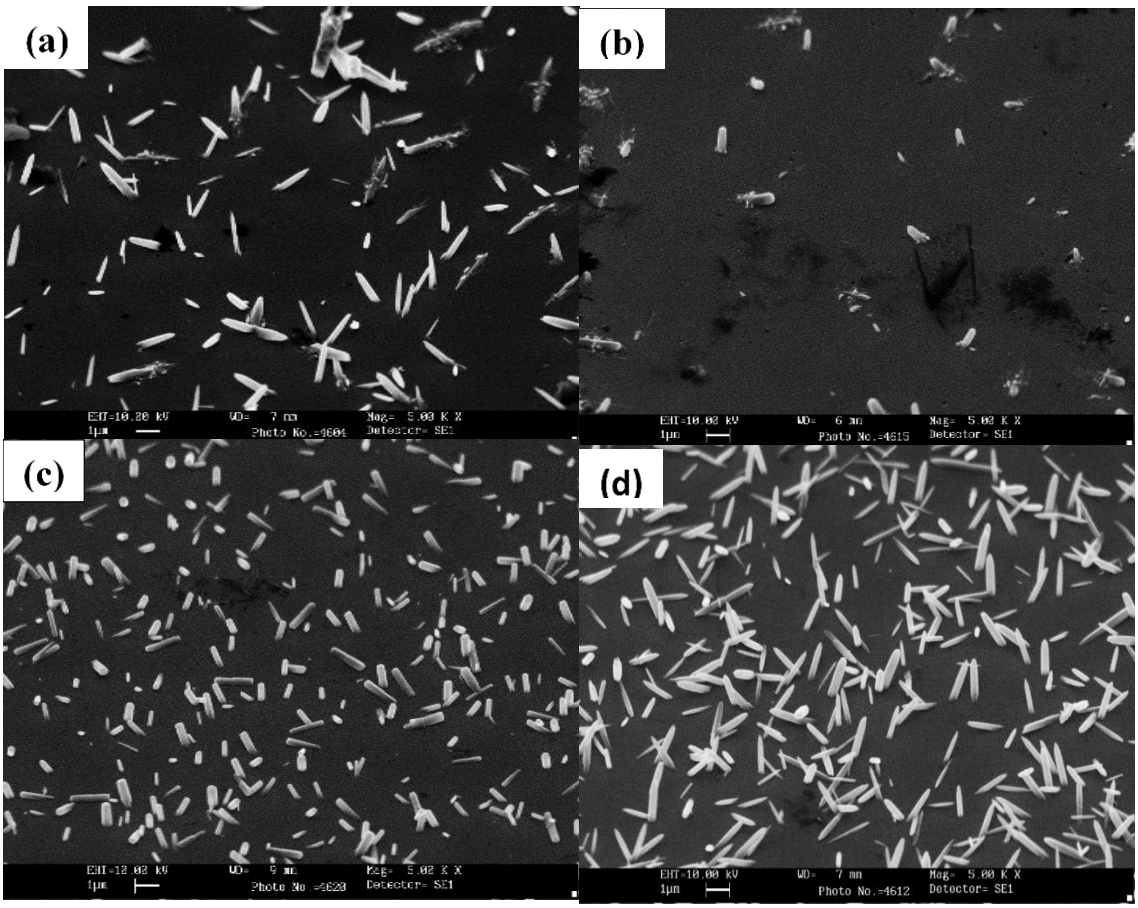

Figure 5. 12. SEM images of ZnO nanowires and the growth conditions are listed in table 2 based on the run order; (a) at 1 mM, 80 ^{0}C, 24h. (b) at 1 mM, 80 ^{0}C, 36h. (c) at 5 mM, 80 ^{0}C ,24h. (d) at 5 mM, 80 ^{0}C ,36h.

By performing the runs with these new selected values of reaction parameters, it was seen that all measured responses were significantly influenced by precursor concentration (see appendix. A). However, the length of nanowires was considerably affected by all reaction parameters especially solution concentration and growth duration and their interactions. As a result of this stage, the average length and diameter of ZnO nanoneedles was greatly enhanced. At the first runs, the average length and diameter was 2.16 µm and 357 nm respectively. After carrying out the second runs, the average length and diameter was increased to 3.63 µm and 429 nm respectively.

In addition, acceptable quality, good homogeneity, and controllable sizes of ZnO nanostructure was successfully achieved.

5. 5. Conclusion

It was reported here a systematic optimization analysis of the influence of different processing parameters on the crystal morphology of hydrothermally synthesized ZnO nanostructures. Initially, the effect of precursor concentration, growth time, and temperature on the aspect ratio of nanowires was investigated. It was found that to obtain well-aligned ZnO nanoneedles, a low concentration of solution of 3 mM associated with low processing temperature of 70 ^{0}C and interaction time of 24h are preferential. While, uniformly distributed hexagonal nanowires were produced at high ratio of Zn $(NO_3)_2$ and HMTA of 30 mM combined with low growth temperature of 70 ^{0}C and growth time of 24h. XRD pattern confirmed that the crystal structure of ZnO was the Wurtzite crystal structure. Essentially, the statistical experiment design was efficient in determining the optimal growth setting as well as achieving the desired result with a few numbers of runs.

In the current chapter, sputtered gold intermediary layers were used as nucleation layer to assist the hydrothermal synthesis of ZnO nanostructures however, the physical mechanism of these underlying layers in the formation of ZnO nanostructures still needs further investigations. Therefore, the following chapter focuses on the role of gold thin layer on the hydrothermally grown ZnO nanostructures.

References

ANDERSON, M.J. and WHITCOMB, P.J., 2015. *DOE simplified: practical tools for effective experimentation.* CRC Press.

CUBILLAS, P. and ANDERSON, M.W., 2010. Synthesis mechanism: crystal growth and nucleation. *Zeolites and Catalysis: Synthesis, Reactions and Applications,* , pp. 1-55.

MCMURDIE, H.F., MORRIS, M.C., EVANS, E.H., PARETZKIN, B., WONG-NG, W., ETTLINGER, L. and HUBBARD, C.R., 1986. Standard X-ray diffraction powder patterns from the JCPDS research associateship. *Powder Diffraction,* **1**(2), pp. 64-77.

MCPEAK, K.M., LE, T.P., BRITTON, N.G., NICKOLOV, Z.S., ELABD, Y.A. and BAXTER, J.B., 2011. Chemical bath deposition of ZnO nanowires at near- neutral pH conditions without hexamethylenetetramine (HMTA): understanding the role of HMTA in ZnO nanowire growth. *Langmuir,* **27**(7), pp. 3672-3677.

QIU, J., LI, X., HE, W., PARK, S., KIM, H., HWANG, Y., LEE, J. and KIM, Y., 2009. The growth mechanism and optical properties of ultralong ZnO nanorod arrays with a high aspect ratio by a preheating hydrothermal method. *Nanotechnology,* **20**(15), pp. 155603.

SUN, Y., RILEY, D.J. and ASHFOLD, M.N., 2006. Mechanism of ZnO nanotube growth by hydrothermal methods on ZnO film-coated Si substrates. *The Journal of Physical Chemistry B,* **110**(31), pp. 15186-15192.

XU, S., LAO, C., WEINTRAUB, B. and WANG, Z.L., 2008. Density-controlled growth of aligned ZnO nanowire arrays by seedless chemical approach on smooth surfaces. *Journal of Materials Research,* **23**(08), pp. 2072-2077.

Chapter 6

The effects of annealing a gold intermediary layer on the hydrothermally grown ZnO nanowires

6. 1 Introduction

As the properties of ZnO are crucially influenced by its morphology, size, and orientation, therefore, control over the morphology and functional properties of theses nanostructures has been a long-standing ambition in the evolution of nanodevices fabrication (Tian, Voigt et al. 2003). Nano- sized gold particles have intensively drawn considerable attention in the large-scale of industrial and academic applications due to their extraordinary physical and chemical properties (Wallace, Whetten 2002, Hagen, Socaciu et al. 2002, Häkkinen, Landman 2001, Molina, Hammer 2003). Bulk gold has been considered as an ‘‘inert’’ metal in catalysis however, when its dimensions are reduced to the nanometre scale gold acts as an excellent catalyst (Meyer, Lemire et al. 2004). These small gold particles show unique catalytic activity which could be employed in different applications ranging from nanocatalysis to bio-detectors and advanced drug delivery systems (Choudhary, Goodman 2002). It has reported that the catalytic activity of gold nanoparticles can be tuned by their particle size, composition, morphology, substrate materials (Bernhardt, Heiz et al. 2007, Lyalin, Gao et al. 2016). The catalytic activity of Au nanoparticles of 3-5 nm dimension is mainly associated to their large catalytic surface area which allows to more interactions with various small molecules (Liu, Tsunoyama et al. 2010, Haruta 2003, Daniel, Astruc 2004).

On the macroscopic scale, gold does not react with molecular oxygen (Daniel, Astruc 2004) however, nano-sized Au nanoparticles activate oxygen molecules efficiently.

Here, gold is used as a catalyst for ZnO nanostructures synthesis. The motivation behind choosing this noble metal is to explore the influence of gold catalyst in the growth mechanism of ZnO nanostructures synthesized via a low-temperature hydrothermal approach. In particular, it is aimed to investigate the outstanding catalytic activity of gold nanoparticles which can be shown even at room temperature. The most interesting reaction of the gold catalytic activity is the oxidation reaction therefore, to shed light on this interaction, it is necessary to study the physical characteristics of gold thin layer under different annealing atmospheres, temperature and time prior to its use for the hydrothermal growth of ZnO nanostructures. Subsequently, the morphological and structural properties of synthesized ZnO nanostructures were investigated as well.

Overall, post-growth thermal treatment has been used previously with solution processed nanomaterials in order to lower the defect density and impurity concentration, increase crystallite sizes and release strain energy (Lin, Fu et al. 2001). The annealing can enable the catalyst and substrate to alloy and form the primary interfaces which will be the nanowire growth front. However, the main drawback of the thermal annealing process is that enlarging the grain-growth and agglomeration of nanostructures, resulting in the production of larger and extended particles that show bulk properties (López, García et al. 2016). In addition, the annealing atmosphere, temperature, and duration could produce new defects into the ZnO crystal (Knutsen, Galeckas et al. 2012). Here, the Au-coated Si substrates were subjected to several annealing conditions prior to the hydrothermal growth of ZnO nanostructures onto these substrates.

6. 2. Materials and Methods

Silicon (p-type, (100)) substrates with a surface of 1 × 1 cm^2 were ultrasonically cleaned by acetone and isopropanol for 15 min each to remove surface contamination and were then kept in ultrasonic DI water bath for 10 min. Substrates were blown dry with nitrogen gas and baked on a hotplate at 150 ^{0}C for 10 min to eliminate any adsorbed moisture. A thin layer of Au (5 nm) was then deposited by RF sputtering technique onto the substrates to act as an intermediary layer to facilitate ZnO nanowires growth. Au films were annealed at various temperatures and duration using different annealing atmospheres (air, oxygen (O_2) and nitrogen (N_2)).

All precursors/solvents were purchased from Sigma-Aldrich with purity of 99%. For the hydrothermal growth of the ZnO nanowires, equimolar (30 mM) aqueous solutions of Zinc Nitrate Hexahydrate ($Zn(NO_3)_2.6H_2O$) and HexamethylTetramine (HMTA) ($C_6H_{12}N_4$) were utilized. The nutrient solution was transferred to a sealable glass beaker and the growth substrates were placed upside down in the solution and the beaker was then transferred to a convection oven at 70 ^{0}C for 24 hrs. To investigate the influence of annealing conditions on the Au film, XRD with Cu-Kα X-ray radiation having a characteristic wavelength of 1.5418 Å with a 2^0/min scanning speed and (Bruker DB) (AFM) in noncontact mode (Park AFM XE100) were used. In addition, the morphological characteristics of ZnO nanostructures were studied using (SEM Leo S430) and XRD.

6. 3 Result and discussion

6. 3. 1. XRD and AFM analysis of the gold thin layer

Figure 6. 1 (a, b & c) shows the XRD pattern of gold thin films annealed at different temperatures (350 ^{0}C – 650 ^{0}C) and atmospheres (oxygen (O_2), nitrogen (N_2) and air respectively).

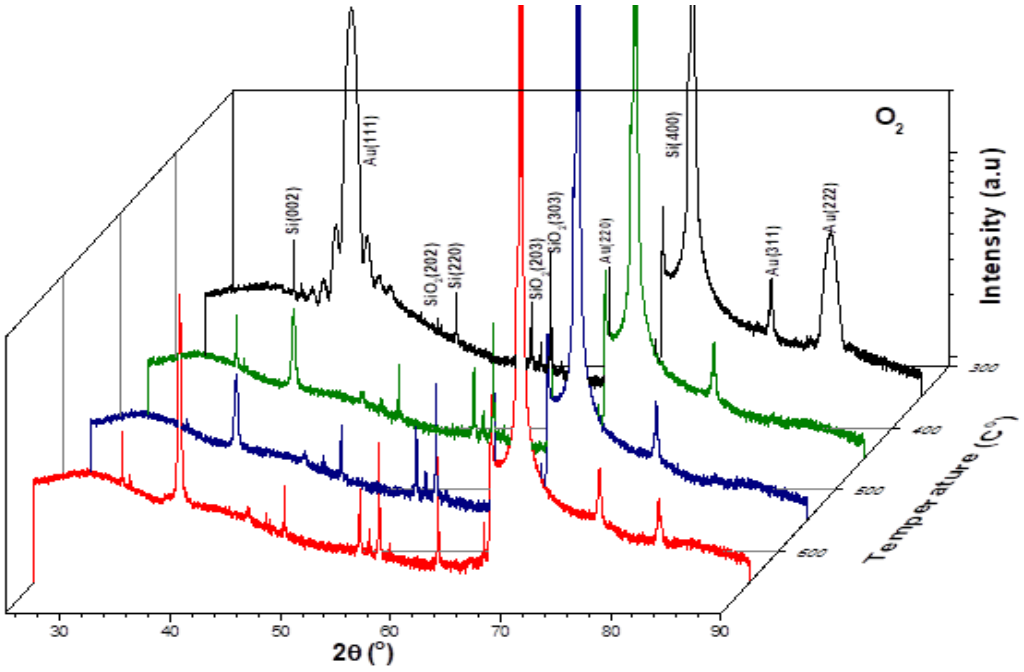

Figure 6. 1. (a) The XRD pattern of an Au layer annealed at 350 ^{0}C, 450 ^{0}C, 550 ^{0}C and 650 ^{0}C in O_2 ambient.

Diffraction peaks belonging to (111), (200), (220), (311) and (222) planes were observed in all the gold thin films for each annealing condition. All evident peaks confirmed the fcc structure of Au according to the standard data of the JCPDS file (JCPDS no.04-0784) (Swarthmore 1991) and (American Mineralogist Crystal structure database, Codes No. 0013108) (Suh, Ohta et al. 1988).

The (111) plane, which has the lowest surface energy and the highest population of the gold particle (Amran, Hashim et al. 2013), was barley evident in the as-grown sample, but became the dominant Au peak once an annealing step had taken place other than the major contribution from the substrate (Si (400)); this was the case for all annealing environments studied.

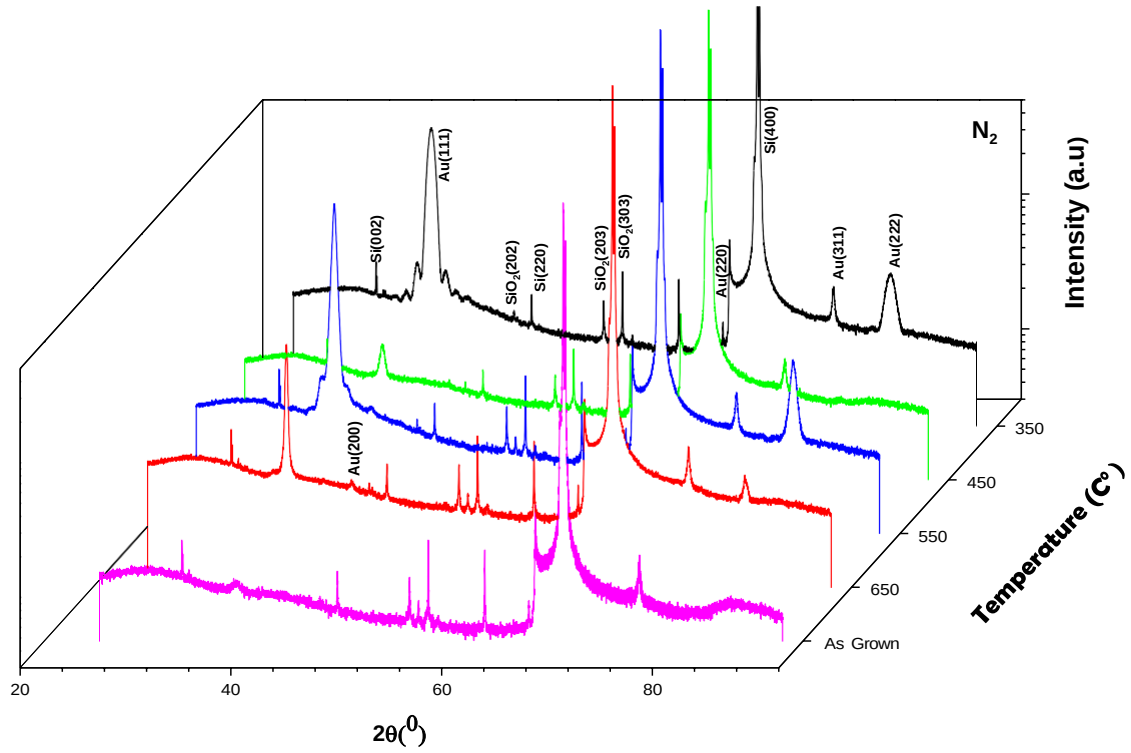

Figure 6. 1. (b) The XRD pattern of an Au layer annealed at 350 ^{0}C, 450 ^{0}C, 550 ^{0}C and 650 ^{0}C in N_2 ambient.

In addition, whilst annealing improved the crystallinity of the as-deposited film, as evidenced by the decrease in full-width-half-maximum (FWHM) of the (111) plane with temperature, the relative intensity of this peak for the different atmospheres was not the same suggesting that both ambient and temperature was affecting the structure of the deposited film.

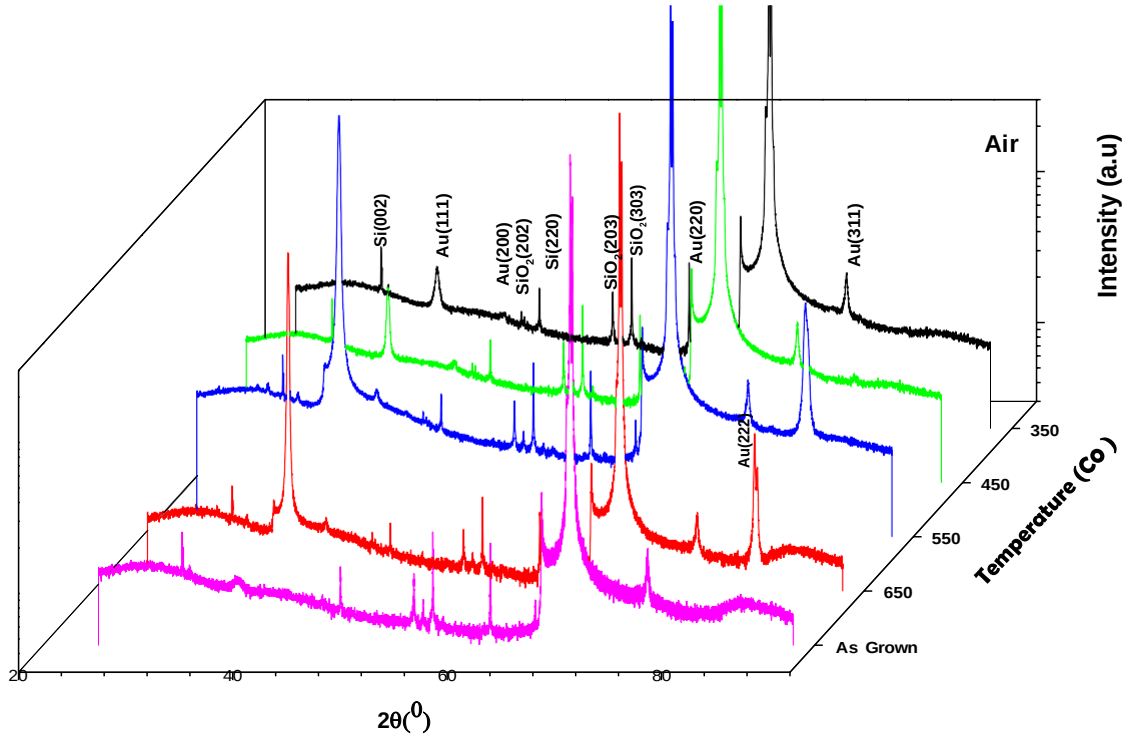

Figure 6. 1. (c) The XRD pattern of an Au layer annealed at 350 ^{0}C, 450 ^{0}C, 550 ^{0}C and 650 ^{0}C in Air ambient.

According to the shape of the obtained peaks all samples showed high crystallinity. The increase in the XRD intensity supports the increasing and the enhancement of material's crystallization or the order of the material.

Interestingly, it was observed that all sample, annealed from 350 ^{0}C to 650 ^{0}C under a flowing stream of nitrogen, oxygen, and air show phases of silicon dioxide in XRD profile. The most intensive diffraction peak corresponds to SiO_2 (303) plane was at the 2θ of 56.44° which means that coated gold catalysts could promote silicon crystallization during the thermal treatment (Cros, Derrien et al. 1981). It is reported that broadening of diffraction peaks is influenced by lattice imperfections of nanocrystallites. The two main properties that can be extracted from XRD profile are the crystallite size and lattice strain, which further affects the intensity and shift in the peak position (Prabhu, Rao et al. 2014). Lattice strain is released as a result of crystal imperfections, such as

lattice dislocations, grain boundary, triple junction, contact or sinter stresses, stacking faults and coherency stresses (Zhang, Zhang et al. 2006).

The average size of gold crystallites was determined by using *Debye-Scherrer* formula as follows:

$$D = k\lambda/\beta_D \cos\theta \qquad (1)$$

where k is the Scherrer constant (≈ 0.90), λ the wavelength of the X-rays used (0.1541 nm), θ the diffraction angle and β_D is the full width at half maximum (FWHM; in radians). The broadening of diffraction peaks is a combination of both instrument and sample contributions. For a precise evaluation for crystallite size and strain contributions, the instrumental broadening (β_D) must be accounted therefore, it is needed to assemble a diffraction pattern from the line broadening of a standard material such as silicon (Zak, Majid et al. 2011). The instrument corrected broadening corresponding to the diffraction peaks was estimated using following equations:

$$\beta_D^2 = [\beta^2_{measures} + \beta^2_{instrumental}] \qquad (2)$$

At high annealing temperature, it is observed that an increase in the crystallite size of Au nanoparticles which can be attributed to the adjacent Au particles which start restructuring to form Au island structures (Rosli, Yusof et al. 2014). An air anneals at ≥550 ^{0}C resulted in the highest intensity of (111) and the largest crystallite sizes of 30 nm and 70 nm for 550 ^{0}C and 650 ^{0}C respectively (Figure 6. 2 (a)).

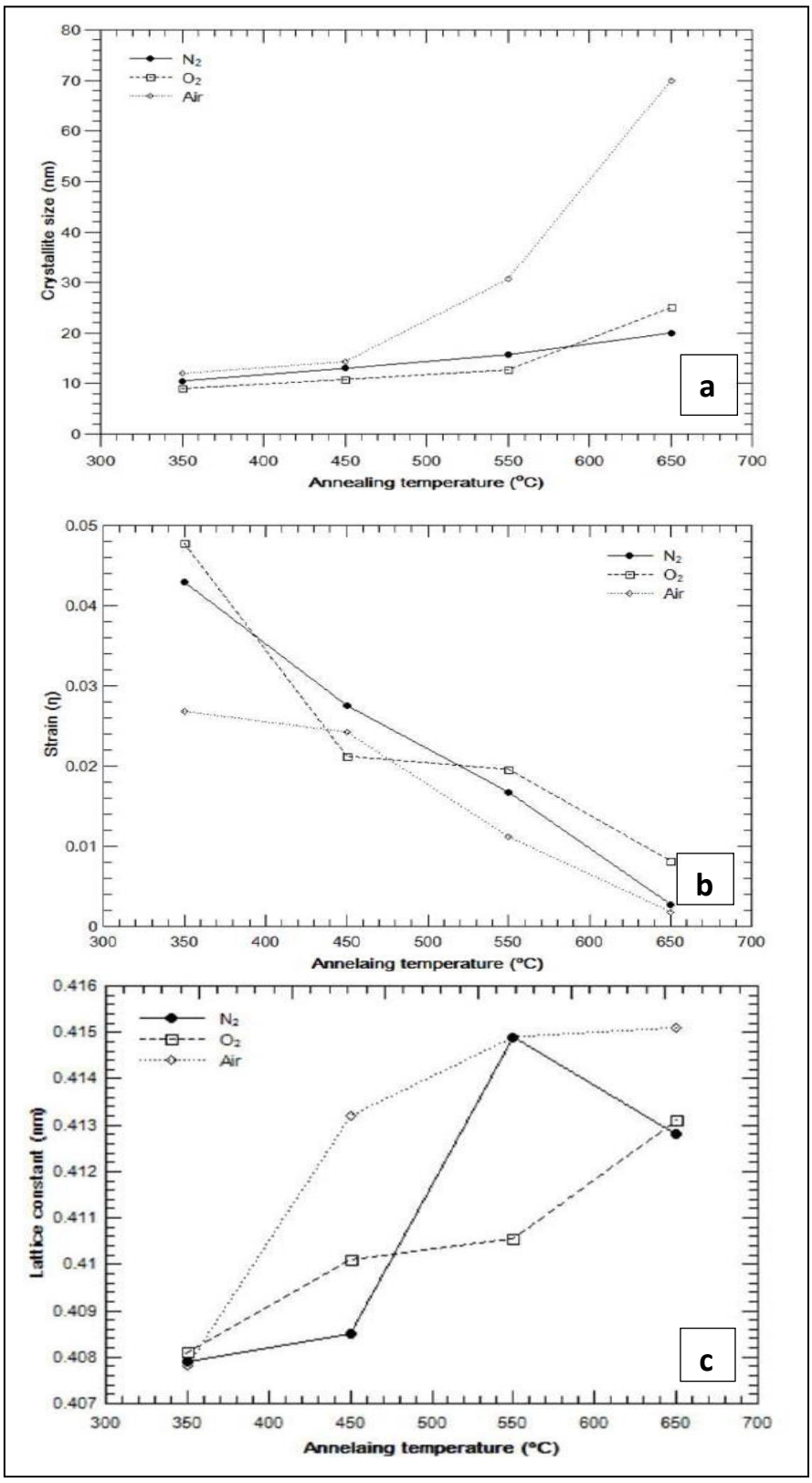

Figure 6. 2. Plots of (a) crystallite size, (b) strain, and (c) lattice constant versus annealing temperature for the Au thin films at N_2, O_2 and air ambient.

This compares to maximum sizes of 20 nm for N_2 and 25 nm O_2 respectively (see Table 6. 1). The increase in grain size with temperature is to be expected, as elevated temperatures lead to an enhancement of the crystallization process, a reduction in residual stress and long-range atomic rearrangements.

According to Williamson and Hall approach, the broadening of X-ray peaks is due to crystallite size and lattice strain effects thus, lattice strain-induced peak broadening is related by $\eta \approx \beta_{strain}/\tan\vartheta$. *Debye-Scherrer* formula (1) has a $1/\cos\vartheta$ dependency, while the Williamson-Hall (W-H) relation has $\tan\vartheta$ dependency (Prabhu, Rao et al. 2014); the latter of which facilitates the segregation of crystallite size and strain broadening. So, the total peak breadth is described by the sum of the crystallite size and strain contributions and can be represented as:

$$\beta_{hkl} = (k\lambda / D\cos\theta) + \eta\tan\theta \qquad (3)$$

Where η is a strain. From the example W–H plot using the XRD data for the sample annealed in air at 550 ^{0}C (Figure 6. 3), The crystallite size and lattice strain are obtained from the intercept of the *y*-axis and the slope of the fitted line respectively.

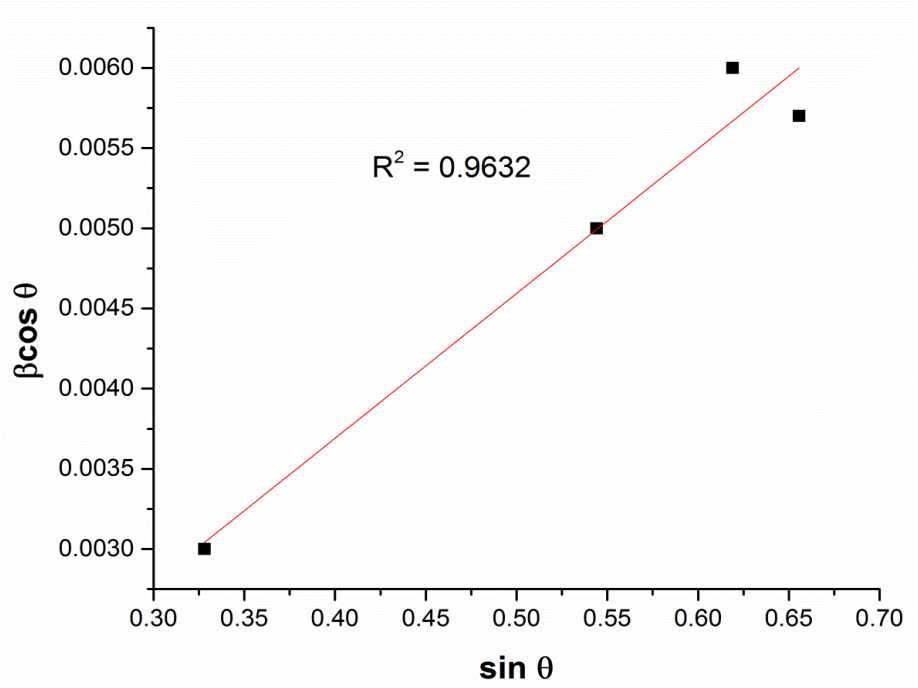

Figure 6. 3. The W-H plot of an Au thin film annealed at 550 ^{0}C for 30 minutes in Air.

It was observed that the lattice strain increased in all samples when the crystallite size decreased (see Table 6. 1). As it might be expected that, the most lattice strain was extant in the as-deposited film (0.2535) and decreased to its lowest level at an annealing temperature of 650 ^{0}C for all atmospheres, with an air anneal producing the lowest value 0.00182 (Figure 6. 2 (b)). This could attribute to the effect of the thermal treatment in reducing the concentration of lattice defects and dislocation.

To know more about lattice strain, it is essential to precisely measure the correct value of lattice constant which is free from all systematic errors such as inaccuracy in the measurement of θ and hence in the estimation of the lattice spacing d.

Table 6. 1. The Crystallite size, Strain, and Lattice constant of the Au nucleation layer at different annealing temperature and ambient.

Atmosphere	Temperature (^{0}C)	Lattice constant(nm)	Crystallite size D(nm)	Strain (η)
As- grown	RT	0.4086	8	0.2535
N_2	350	0.4079	10.5	0.04293
	450	0.4085	13	0.02756
	550	0.4149	15.7	0.01674
	650	0.4128	20	0.00273
O_2	350	0.4081	9	0.04772
	450	0.4101	10.8	0.02123
	550	0.41056	12.7	0.01958
	650	0.4131	25	0.00816
Air	350	0.4078	12	0.02681
	450	0.4132	14.31	0.02424
	550	0.4149	30.7	0.01117
	650	0.4151	70	0.00182

The lattice constant was determined by plotting the calculated lattice parameters via Bragg's law against the Nelson-Riley function (Begum, Hussain et al. 2012), constructing a linear regression, and determining the y-intercept (Figure 6. 4).

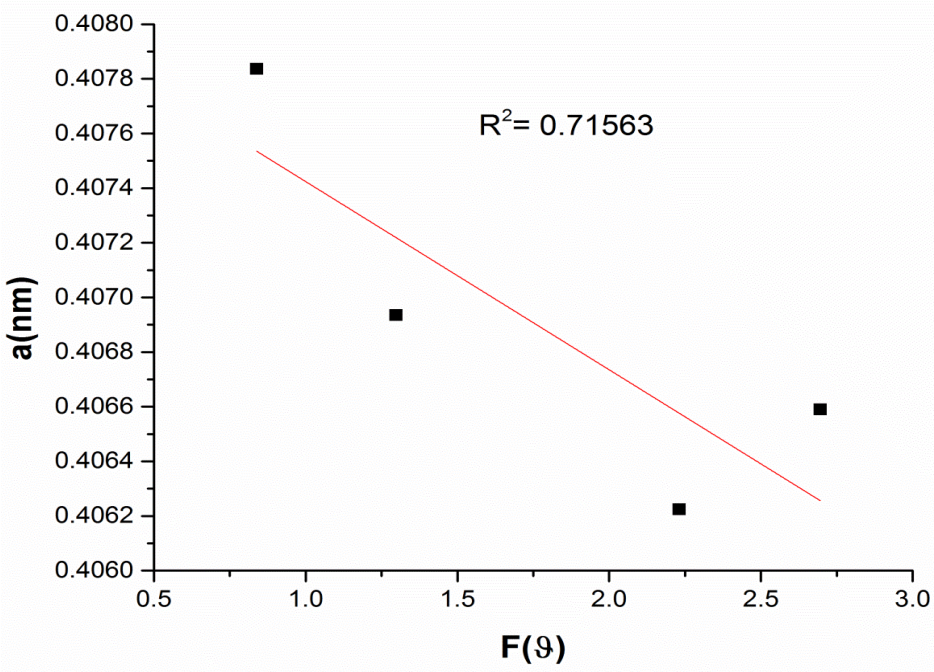

Figure 6. 4. Determination of the lattice constant by the Nelson-Riley function F(θ).

the Nelson-Riley Function F(θ) (Nelson, Riley 1945) is given as:

$$F(\theta) = [(cos^2\theta/sin\theta) + (cos^2\theta/\theta)]/2 \qquad (4)$$

where θ is the Bragg's angle. The experimental lattice constant '*a*' was in the range of 0.4078 - 0.4151 nm, which is in reasonable agreement with the literature report (Suh, Ohta et al. 1988). However, it is noticed slight differences in some orientations of Au thin layer, which can be attributed to the divergence of the X-ray beams and the refraction and absorption of X-rays by the specimens. In addition, the lattice shrinkage depends implicitly on the grain size, so in our case, the lattice constant was increased marginally at high annealing temperature due to thermal expansion (Figure6. 2 (c)). The structural changes within the deposited film were mirrored in AFM studies undertaken of the surface morphology (Figure 6. 5 (a-d)).

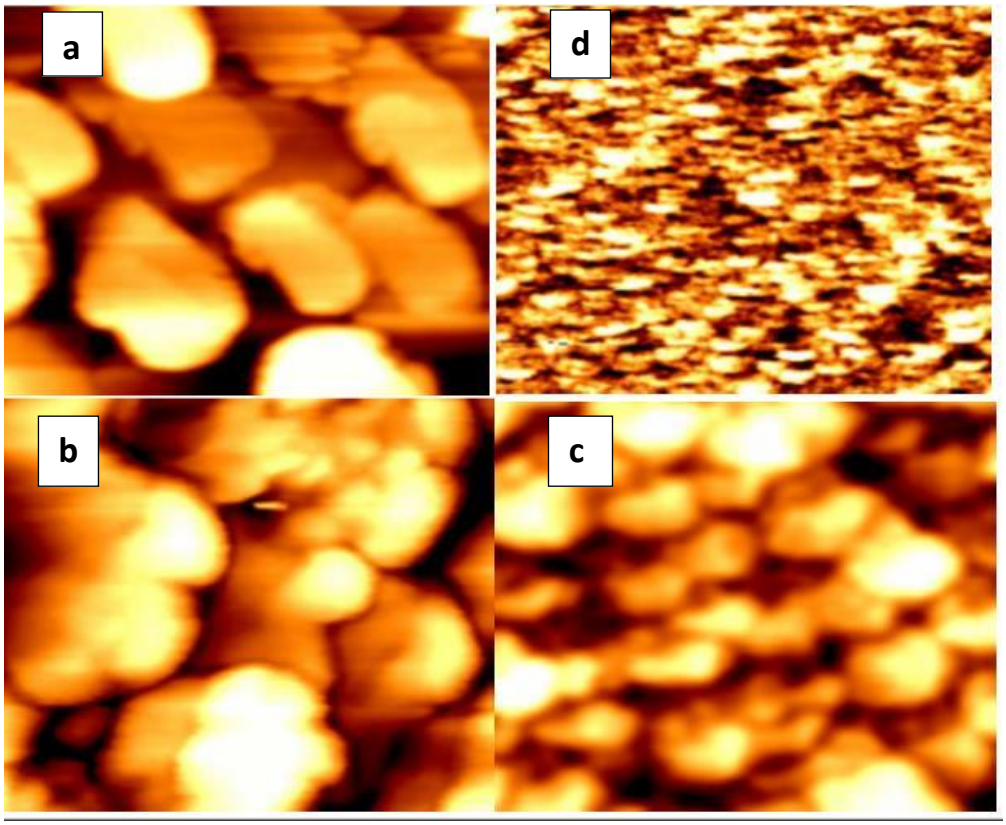

Figure 6. 5. NC-AFM data of the Au nucleation layer (a) O2 ambient anneal at 650 ^{0}C for 2hrs; (b) N_2 ambient anneal at 650 ^{0}C for 2hrs; (c) Air ambient anneal at 650 ^{0}C for 2hrs; (d) as- deposited. All scans 1 µm.

The annealing had a dramatic effect on the topology and feature size of the deposited layer for all temperatures but was most evident at the highest temperature of 650 ^{0}C for each ambient. From an average feature size of ≈ 30-50nm for the as-deposited film (Figure 6. 5 (d)), this then increased to ≈ 200-500nm as the thin film began to coalesce into irregularly shaped large islands or regions across the surface. While, at all lower temperatures, the contiguous film resulting from the initial deposition, broke-up into Au islands of <100nm in diameter. It seemed that annealing temperature affected the final crystallographic structure of the Au film in all atmospheres.

It was found that, crystallite size of Au nanoparticle extracted by XRD data (Table 6. 1) was not in agreement with AFM images shown in figure (6. 5). It could be owed to the fact that XRD data based on Scherrer formula is an estimation method in addition, Scherrer formula does not work when the crystallites are larger than 100 nm due to the peak broadening would be so small to estimate based on the inversely proportional of crystal size and FWHM.

6. 3. 2. XRD and SEM analysis of ZnO nanowires

The gold samples from all annealing experiments were used for the ZnO nanowires growth process together with an as-deposited film. The XRD diffractograms for the ZnO nanowires synthesized from equimolar (30mM) aqueous solutions of Zinc Nitrate Hexahydrate and (HMTA) are shown in Figures 6. 6 and 6. 7.

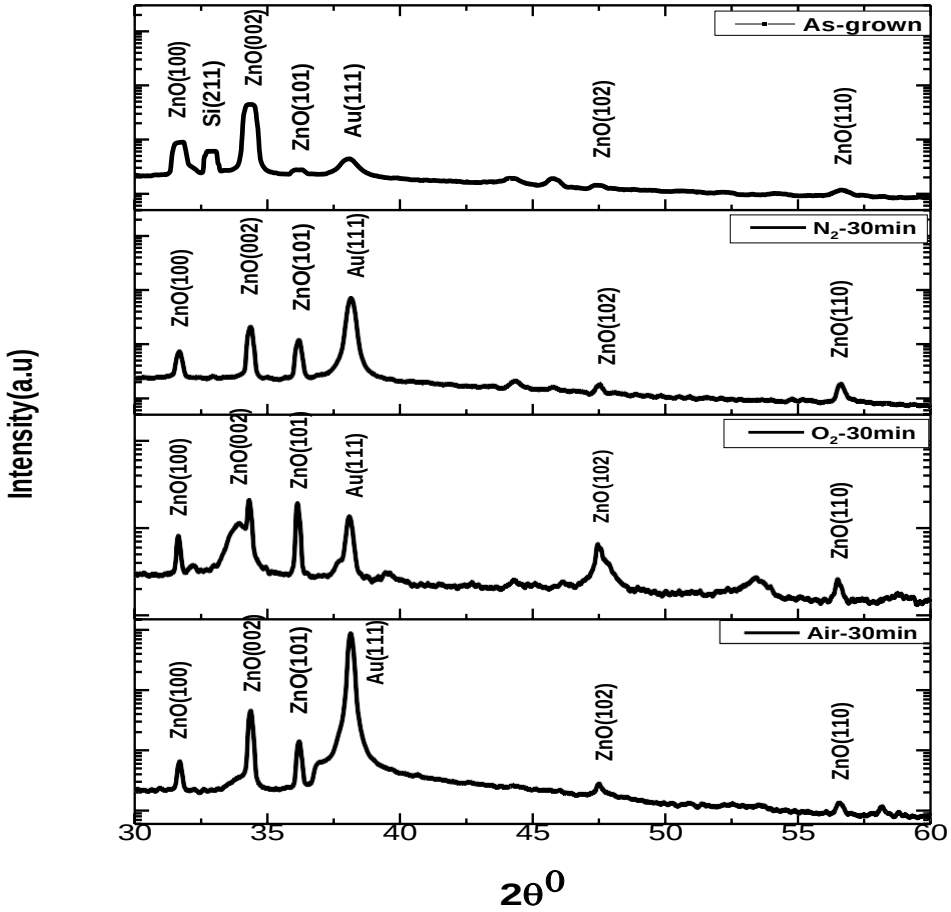

Figure 6. 6. The XRD pattern of ZnO nanowires grown on Au-coated silicon substrates annealed at 650 ^{0}C for half of hour in (a) Air, (b) O_2, (c) N_2, (d) As-grown samples.

All diffraction peaks were perfectly indexed to the hexagonal wurtzite structure of ZnO according to JCPDS-file 36-1451 (McMurdie, Morris et al. 1986) and American Mineralogist Crystal Structure database codes no. 0005206 (Kihara, Donnay 1985). The intensity of the (002) peak is found to be the most intense compared to those of the (100) and the (101) peaks, which indicates the growth rate of ZnO crystals is much faster along the [002] direction than along the lateral directions [100] and [101]. In contrast, (100) and (101) reflection have low intensities which confirm the well crystallographic orientation of ZnO crystals (according to JCPDS-file 36- 1451).

It is also known that the surface free energy of the (002) plane is the lowest, therefore, crystal orientation of ZnO is a result of a self-ordering effect caused

by the minimization of the crystal surface free energy (Jiang, Jia et al. 2006). In addition, XRD diffractograms have smooth base lines with sharp and well-defined peaks which reflect the highly crystalline phases.

The shoulder of the ZnO (002) diffraction peak was clearly observed in O_2 annealing atmosphere. One reason could be because of the disorientation due to the large lattice mismatches between the Au (111) and the ZnO (002) planes (9.4%); lattice mismatch refers to the condition where two materials showing different lattice constants are deposited one on a top of another, therefore these large lattice mismatches across crystals usually do not favour epitaxial growth (Liu, Qiao et al. 2015). In addition, peak deformation could be due to the structural distortion of the unit cell.

Another reason could be extracted from Bragg's law, the Bragg angle should either decrease or increase if the d-spacing of the crystallographic planes changes. Hence, the tensile stress increases the d-spacing which causes a shifting of peak towards lower 2θ values whereas compression stress decreases the d-spacing which result in shifting of peaks towards higher 2θ values in the XRD pattern (Kumar, Asokan et al. 2014). In addition, the growth conditions and thermal treatment could cause the tensile and compressive stress. At low annealing temperature stress of the as-grown ZnO is compressive however, due to the variation in the thermal expansion coefficients under the high annealing temperature the compressive stress converts to tensile stress.

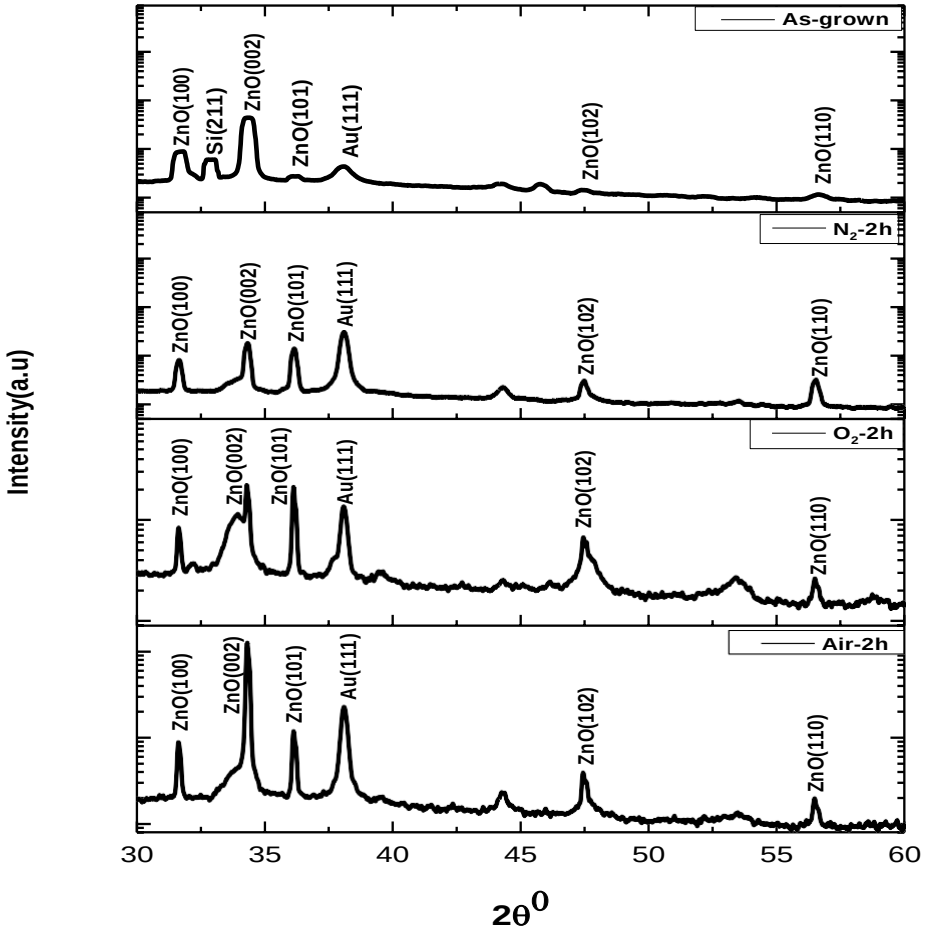

Figure 6. 7. The XRD pattern of ZnO nanowires grown on Au-coated silicon substrates annealed at 650 ^{0}C for 2hrs in (a) Air, (b) O_2, (c) N_2, (d) As-grown samples.

At 2θ = 34.31^0 peak profiles take asymmetric shapes "*shoulders*" and the peak start to splitting and shifting at 2θ = 33.90^0 which could be attributed to changes in the interplanar spacing and easily explained based on the Bragg's law:

$$\theta = \sin^{-1}(\lambda/2d) \qquad (5)$$

Lastly, this behaviour may be due to the presence of impurity or secondary phase in the sample that has a diffraction peak close to the main peak. The average crystallite sizes of ZnO nanowires were determined by using *Debye-Scherrer* formula (equation 1). It was observed that samples annealed at 650 ^{0}C for 2hrs in O_2 and air atmospheres showed better crystallinity and their peak breadth decreases in association with a significant increase of intensities (Table 6. 2).

Table 6. 2. The crystallite size of ZnO nanowires at different annealing time and atmospheres.

Atmosphere	Annealing Time (min)	Crystallite size D(nm)
N_2	30	12
	120	13
O_2	30	18
	120	23
Air	30	20
	120	32
As-grown		7

This observation was in good agreement with SEM micrographs of ZnO nanowires shown in Figure 6. 8 as it can be seen the enhancement in distribution, the surface to volume ratio and crystal orientation of ZnO NWs after annealing for two hrs.

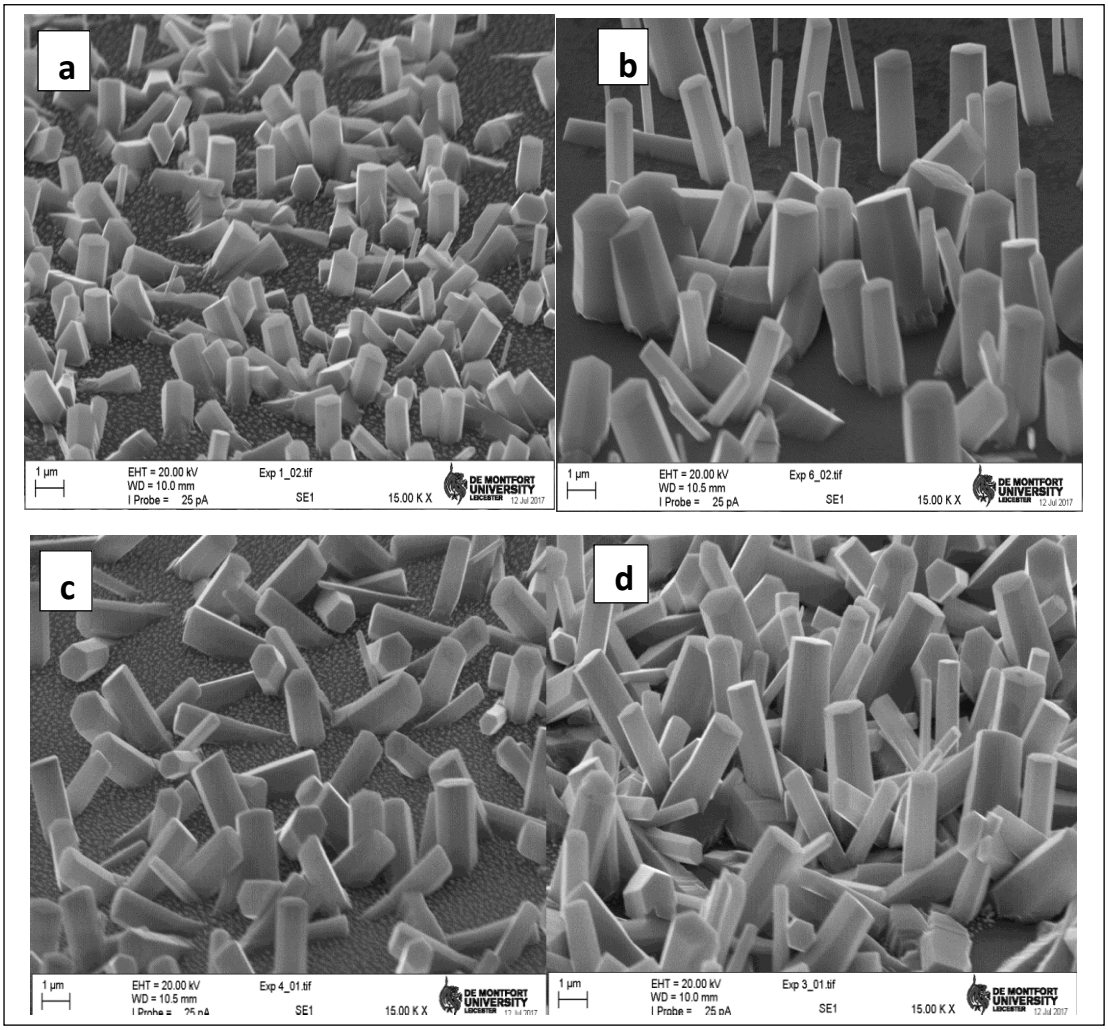

Figure 6. 8. SEM images of the hydrothermally grown ZnO NWs with an Au thin layer annealed at 650 ^{0}C in Air ambient for (a) half of hour, (b) 2hrs, and O_2 ambient for (c) half of hour, (d) 2hrs.

This can be attributed to the reason that during thermal treatment oxygen from the ambient diffuses through the gold layer and accumulates at the gold/silicon interface. Such, a physical process takes place according to the general law of gas diffusion through a metal of thickness x that is given by:

$$x = \sqrt{(6D\tau)} \qquad (6)$$

where D is the diffusion constant and τ represents the time necessary for oxygen ions to pass through the gold layer. These interfacial reactions could be room temperature oxidation of silicon catalysed by the existence of gold layer. (Ponpon, Grob et al. 1978). After the adsorption on the gold surface, the O−O bond is elongated because of electron density transfer from the Au nanoparticle to the oxygen molecule (Staykov, Nishimi et al. 2012).

We suggest that these active oxygen molecules could incorporate with zinc molecules from the nutrient solution and induce the formation of Zn-O-Zn bonds under suitable growth condition. The most experimental data of oxidation reactions of molecular oxygen and nano-sized gold nanoparticles were related to their catalytic activity (Gao, Horita et al. 2017), (Coquet, Howard et al. 2008). It was demonstrated such catalytical activity is not exclusive to Au nanoparticles as a thin layer gold films can show the same activity toward CO oxidation (Chen, Goodman 2006). The adsorption and activation of O_2 on the gold layer are the key factor to understand the role of gold layer in hydrothermally grown ZnO nanowires. On the other hand, samples annealed in the same ambient for 30 minutes results in low-quality nanowires that might be understood from equation (6) as oxygen diffusion is a time-dependent process, so, no oxygen adsorption at the gold surface up to reach a steady state of time (τ).

In contrast, for the nanowires annealed in the N_2 atmosphere, it was no differences in their crystallite size determined by the Scherrer equation (Table 6. 2). However, it appears that the surface to volume ratio of ZnO NWs was enhanced during annealing for a brief time, while the size or the aspect ratio of those annealed for long duration was diminished (Figure 6. 9). it seems that nitrogen-rich annealing association with elevated thermal treatment suppress

grain growth of Au nanoparticles due to nitrogen diffuses through grain boundaries and may inhibit grain boundary motions and decrease the gold atom mobility and diffusion over the surface of the substrate. So, such phenomena may affect the growth of ZnO crystals on gold thin layer as it was reported nitrogen atmosphere partially prevents agglomeration of ZnO nanograins and reduces their participation in grain growth (Jang, Cho et al. 2012, López, García et al. 2016).

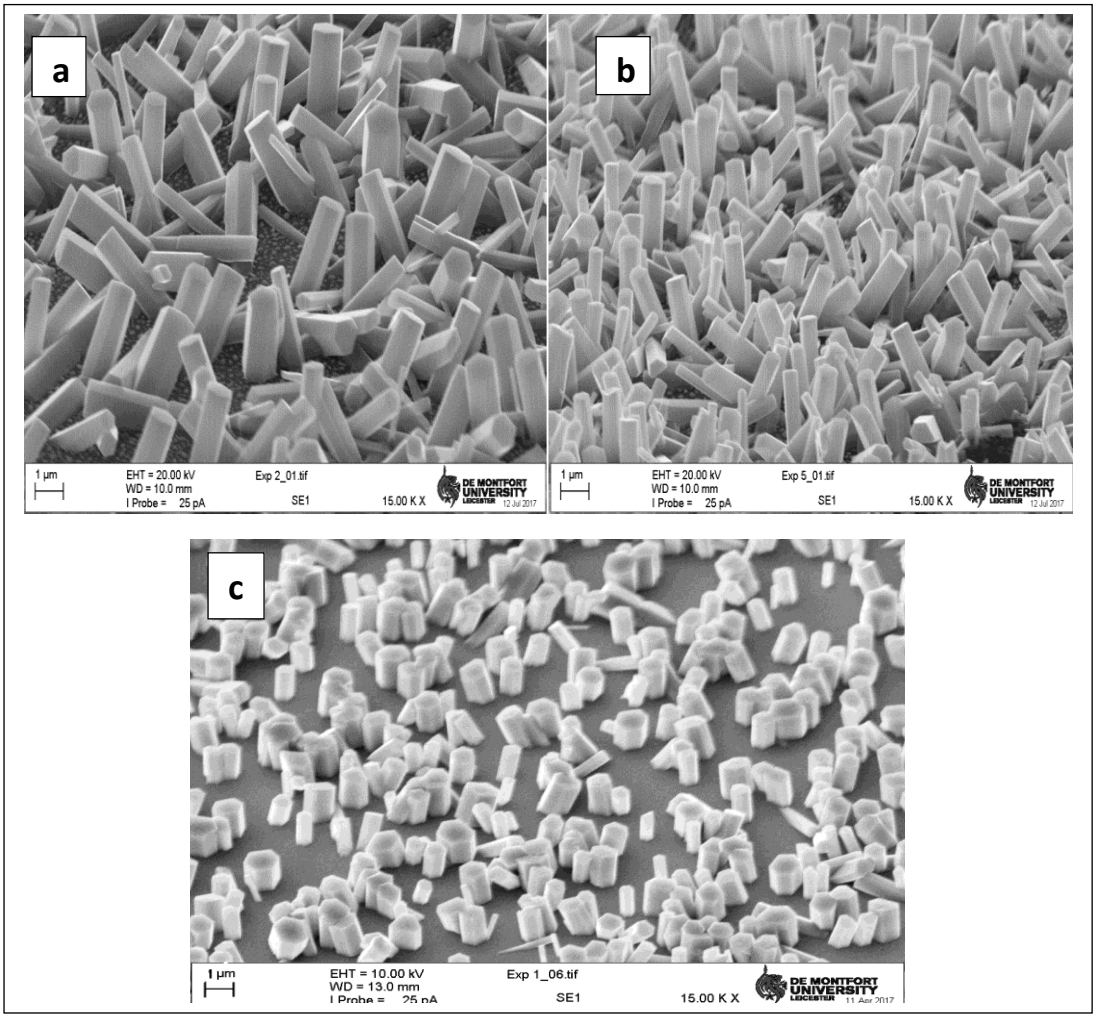

Figure 6. 9. SEM images of the hydrothermally grown ZnO NWs with an Au thin layer annealed at 650 ^{0}C in N_2 ambient for (a) half of hour, (b) 2hrs, and (c) As-deposited.

Another group of Au-coated samples have been subjected to the similar annealing condition, but they have been used to grow the nanowires at low precursor concentration. It was observed that the nanostructures from the as-deposited film were needle-like in structure and grew individually from the substrate without any clustering (Figure 6. 10 (d)). Conversely, at high temperature (650 ^{0}C) for all annealing atmospheres groups, ZnO nanostructures were formed from the surface in flower-like forms without any individual nanowires evident. However, it was found under a rich oxidation conditions (O_2 and air) a large cluster/flower with many branches/wires was produced (Figure 6. 10 (a, b)), while nanoflowers grown on samples annealed in N_2 environment were quite small (Figure 6. 10 (c)). These observations could be attributed to the same reason mentioned earlier about the adsorption and activation of O_2 on Au catalyst surface and their contribution in assisting the following hydrothermal growth of ZnO nanowires.

In addition, we suggest a second cause of the mismatch between the gold film and underlying silicon lattice (24.9%) (Switzer, Hill et al. 2016) which could lead to Au particles to be strained by the interfacial free energy, causing a decrease in their binding energy. So, this will reduce the strength of Au–Au bonds and induce Au particles to be involved in the reactions with an oxidation environment as well as clarify the remarkable catalytic properties of Au nanoparticles (Coquet, Howard et al. 2008).

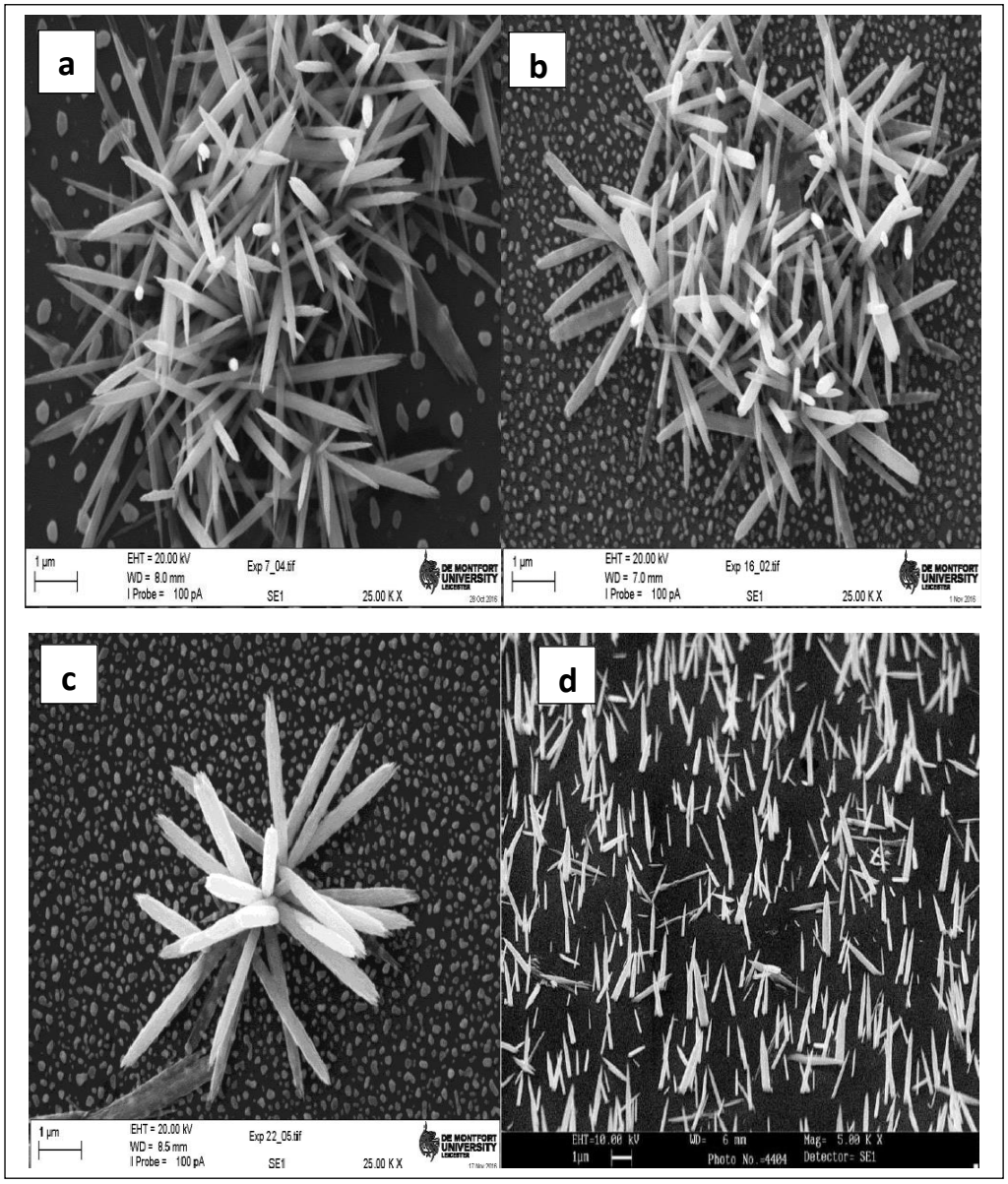

Figure 6. 10. SEM images of the hydrothermally grown ZnO NWs with an Au thin layer annealed at 650 ^{0}C in (a) O_2, (b) air (c) N_2, and (d) As-deposited.

It was found that Au nanoparticles appeared in sparse area on the substrate surface (Fig. 6.10). this observation could be attributed to the low precursor concentration (3 mM) used to grow this group , over the course of time, the precursor ions from the nutrient solution will adsorb by the newly formed ZnO nucleus to participate in the growth of ZnO wires rather than generating nucleation sites on Au nanoparticles. Therefore, the influence of Au

nanoparticles may become less significant and the growth can be only guided by ZnO nucleus on the substrate.

6. 4. Conclusion

The physical properties of RF sputtered Au thin films after annealing in different atmospheres at a wide temperature range of 350–650 ^{0}C have been studied. Subsequently, the structural properties of hydrothermally grown ZnO nanowires on these films have been investigated as well. The morphology evolutions and crystal structures were characterized by SEM, XRD, and AFM in an effort to explore the influence of thermal treatment on the gold layer and nanostructures growth. Based on the measurement of XRD lattice constant and FWHM data, it was found the crystallographic nature of the Au thin layer was considerably dependent on annealing temperature, where higher temperatures resulted in larger crystallite size, reduced lattice strain and improved crystallinity. Furthermore, the annealing atmospheres significantly influence the agglomeration and coalescence of gold grains.

In addition, we demonstrate how the type of adsorbate gases used for annealing process could influence the growth behaviour of ZnO nanostructures and how this effect can enhance the contributory for the remarkable catalytic activity of Au nanoparticles. As It is found that reasonable-quality nanostructures obtained from the rich-oxidation annealed samples in terms of well-aligned ZnO nanostructures with high aspect ratio. These practical measurements suggest that not only the annealing temperature but also the type of the gas atmosphere influence both of Au thin layer and the structural characteristics of hydrothermally grown ZnO nanostructures. However, the

role of the Au catalyst in the guidance of the ZnO nanostructures growth still requires further attention.

In the current chapter, the role of gold catalyst in the growth mechanism of ZnO nanostructures grown by a solution-based method was investigated. Even though the ZnO nanostructures were well distributed over the substrate surface it was still a lack of control over their location. Therefore, the following chapter introduces template-assisted synthesis method as an effective approach to control the ZnO nanostructures sites using self-assembled close-packed crystals of polystyrene spheres.

References

AMRAN, T.S.T., HASHIM, M.R., AL-OBAIDI, N.K.A., YAZID, H. and ADNAN, R., 2013. Optical absorption and photoluminescence studies of gold nanoparticles deposited on porous silicon. *Nanoscale research letters,* **8**(1), pp. 1.

BEGUM, A., HUSSAIN, A. and RAHMAN, A., 2012. Effect of deposition temperature on the structural and optical properties of chemically prepared nanocrystalline lead selenide thin films. *Beilstein journal of nanotechnology,* **3**(1), pp. 438-443.

BERNHARDT, T., HEIZ, U. and LANDMAN, U., 2007. Chemical and catalytic properties of size-selected free and supported clusters. *Nanocatalysis.* Springer, pp. 1-191.

CHEN, M. and GOODMAN, D.W., 2006. Catalytically active gold: from nanoparticles to ultrathin films. *Accounts of Chemical Research,* **39**(10), pp. 739-746.

CHOUDHARY, T. and GOODMAN, D., 2002. Oxidation catalysis by supported gold nano-clusters. *Topics in Catalysis,* **21**(1), pp. 25-34.

COQUET, R., HOWARD, K.L. and WILLOCK, D.J., 2008. Theory and simulation in heterogeneous gold catalysis. *Chemical Society Reviews,* **37**(9), pp. 2046- 2076.

CROS, A., DERRIEN, J. and SALVAN, F., 1981. Catalytic action of gold atoms on the oxidation of Si (111) surfaces. *Surface Science,* **110**(2), pp. 471-490.

DANIEL, M. and ASTRUC, D., 2004. Gold nanoparticles: assembly, supramolecular chemistry, quantum-size-related properties, and applications toward biology, catalysis, and nanotechnology. *Chemical reviews,* **104**(1), pp. 293-346.

GAO, M., HORITA, D., ONO, Y., LYALIN, A., MAEDA, S. and TAKETSUGU, T., 2017. Isomerization in Gold Clusters upon O2 Adsorption. *The Journal of Physical Chemistry C,* **121**(5), pp. 2661-2668.

HAGEN, J., SOCACIU, L.D., ELIJAZYFER, M., HEIZ, U., BERNHARDT, T.M. and WÖSTE, L., 2002. Coadsorption of CO and O 2 on small free gold cluster anions at cryogenic temperatures: model complexes for catalytic CO oxidation. *Physical Chemistry Chemical Physics,* **4**(10), pp. 1707-1709.

HÄKKINEN, H. and LANDMAN, U., 2001. Gas-phase catalytic oxidation of CO by Au2. *Journal of the American Chemical Society,* **123**(39), pp. 9704-9705.

HARUTA, M., 2003. When gold is not noble: catalysis by nanoparticles. *The chemical record,* **3**(2), pp. 75-87.

JANG, S., CHO, H., LEE, Y. and KIM, D., 2012. Atmospheric effects on the thermally induced sintering of nanoparticulate gold films. *Journal of Materials Science,* **47**(13), pp. 5134-5140.

JIANG, X., JIA, C. and HONG, R., 2006. Microstructure dependence of ZnO: Al films on the deposition conditions and the surface morphology of silicon substrate. *Journal of Crystal Growth,* **289**(2), pp. 464-471.

KIHARA, K. and DONNAY, G., 1985. Anharmonic thermal vibrations in ZnO. *The Canadian Mineralogist,* **23**(4), pp. 647-654.

KNUTSEN, K., GALECKAS, A., ZUBIAGA, A., TUOMISTO, F., FARLOW, G., SVENSSON, B. and KUZNETSOV, A.Y., 2012. Zinc vacancy and oxygen interstitial in ZnO revealed by sequential annealing and electron irradiation. *Physical Review B,* **86**(12), pp. 121203.

KUMAR, S., ASOKAN, K., SINGH, R.K., CHATTERJEE, S., KANJILAL, D. and GHOSH, A.K., 2014. Investigations on structural and optical properties of ZnO and ZnO: Co nanoparticles under dense electronic excitations. *RSC Advances,* **4**(107), pp. 62123-62131.

LIN, B., FU, Z. and JIA, Y., 2001. Green luminescent center in undoped ZnO films deposited on silicon substrates. *Applied Physics Letters,* **79**(7), pp. 943-945.

LIU, J., QIAO, B., SONG, Y., HUANG, Y. and LIU, J.J., 2015. Hetero-epitaxially anchoring Au nanoparticles onto ZnO nanowires for CO oxidation. *Chemical Communications,* **51**(83), pp. 15332-15335.

LIU, Y., TSUNOYAMA, H., AKITA, T., XIE, S. and TSUKUDA, T., 2010. Aerobic oxidation of cyclohexane catalyzed by size-controlled Au clusters on hydroxyapatite: size effect in the sub-2 nm regime. *ACS Catalysis,* **1**(1), pp. 2-6.

LÓPEZ, R., GARCÍA, G., COYOPOL, A., DÍAZ, T. and ROSENDO, E., 2016. Effect of nitrogen gas in the agglomeration and photoluminescence of Zn-ZnO

nanowires after high-temperature annealing. *Revista Mexicana de Física,* **62**(1), pp. 1-4.

LYALIN, A., GAO, M. and TAKETSUGU, T., 2016. When inert becomes active: a fascinating route for catalyst design. *The Chemical Record,* **16**(5), pp. 2324-2337.

MCMURDIE, H.F., MORRIS, M.C., EVANS, E.H., PARETZKIN, B., WONG-NG, W., ETTLINGER, L. and HUBBARD, C.R., 1986. Standard X-ray diffraction powder patterns from the JCPDS research associateship. *Powder Diffraction,* **1**(2), pp. 64-77.

MEYER, R., LEMIRE, C., SHAIKHUTDINOV, S.K. and FREUND, H., 2004. Surface chemistry of catalysis by gold. *Gold Bulletin,* **37**(1-2), pp. 72-124.

MOLINA, L. and HAMMER, B., 2003. Active Role of Oxide Support during CO Oxidation at A u/M g O. *Physical Review Letters,* **90**(20), pp. 206102.

NELSON, J.B. and RILEY, D., 1945. An experimental investigation of extrapolation methods in the derivation of accurate unit-cell dimensions of crystals. *Proceedings of the Physical Society,* **57**(3), pp. 160.

PONPON, J., GROB, J., GROB, A., STUCK, R. and SIFFERT, P., 1978. Interface studies of metal-semiconductor contacts by means of SIMS, nuclear reaction and RBS. *Nuclear Instruments and Methods,* **149**(1-3), pp. 647-651.

PRABHU, Y.T., RAO, K.V., KUMAR, V.S.S. and KUMARI, B.S., 2014. X-ray analysis by Williamson-Hall and size-strain plot methods of ZnO

nanoparticles with fuel variation. *World Journal of Nano Science and Engineering,* **4**(01), pp. 21.

ROSLI, A.B., YUSOF, K.A., HERMAN, S.H., JOHARI, M.H., SHARIFFUDIN, S.S. and ANI, M., 2014. Effect of Metal Catalysts Type and Annealing Time on the Growth of ZnO Nanostructures by Thermal Vapor Deposition Method, *Advanced Materials Research* 2014, Trans Tech Publ, pp. 60-63.

STAYKOV, A., NISHIMI, T., YOSHIZAWA, K. and ISHIHARA, T., 2012. Oxygen activation on nanometer-size gold nanoparticles. *The Journal of Physical Chemistry C,* **116**(30), pp. 15992-16000.

SUH, I., OHTA, H. and WASEDA, Y., 1988. High-temperature thermal expansion of six metallic elements measured by dilatation method and X- ray diffraction. *Journal of Materials Science,* **23**(2), pp. 757-760.

SWARTHMORE, P., 1991. Joint Committee on Powder Diffraction Standards Diffraction Data File. *JCPDS International Center for Diffraction Data,* .

SWITZER, J.A., HILL, J.C., MAHENDERKAR, N.K. and LIU, Y., 2016. Nanometer-thick gold on silicon as a proxy for single-crystal gold for the electrodeposition of epitaxial cuprous oxide thin films. *ACS applied materials & interfaces,* **8**(24), pp. 15828-15837.

TIAN, Z.R., VOIGT, J.A., LIU, J., MCKENZIE, B., MCDERMOTT, M.J., RODRIGUEZ, M.A., KONISHI, H. and XU, H., 2003. Complex and oriented ZnO nanostructures.

Nature materials, **2**(12), pp. 821-826.

WALLACE, W.T. and WHETTEN, R.L., 2002. Coadsorption of CO and O2 on selected gold clusters: Evidence for efficient room-temperature CO2 generation. *Journal of the American Chemical Society,* **124**(25), pp. 7499- 7505.

ZAK, A.K., MAJID, W.A., ABRISHAMI, M.E. and YOUSEFI, R., 2011. X-ray analysis of ZnO nanoparticles by Williamson–Hall and size–strain plot methods. *Solid State Sciences,* **13**(1), pp. 251-256.

ZHANG, J., ZHANG, Y., XU, K. and JI, V., 2006. General compliance transformation relation and applications for anisotropic hexagonal metals. *Solid State Communications,* **139**(3), pp. 87-91.

Chapter 7

Nanosphere Lithography for the Controlled Synthesis of ZnO Nanostructures

7. 1. Introduction

Since the nanomaterials have become an essential units for several nanotechnology applications include health and medicine, photonics, electronics, etc. The entire promising outcome of potential applications can be achieved only when the fabrication process of nanostructures integrated with a consistent control on their position by organizing them in the form of controlled patterns of well-ordered nanoarrays on different substrates. For example, in biology and life-sciences application, the pitch between the nanowires may affect cell adhesion (Li, Zhai et al. 2011), therefore it has generally been a high demand for accomplishing well-ordered nanopattern structures so that their functional properties can be enhanced. Lithographic and nanopatterning methods including photolithography (Martin 2003), (EBL) (Haynes, McFarland et al. 2003), focused (FIB) (Tong, Jansen et al. 2004), self-assembly and template assisted processes (Li, Zhai et al. 2011) have been widely applied to synthesize size-tunable metal nanoparticle patterns on substrate. Optical lithography techniques are limited as their resolution are restricted by the wavelength of the light used to expose the photoresist (Martin 2003). EBL and FIB can sequentially produce shaped nanopattern with extremely high resolution (e.g., 2 and 6 nm for EBL (Marshall, McDonald et al.

1998) and FIB, (Brambley, Martin et al. 1994) respectively) by controlling the dimension, spacing and structure, orientation of nanomaterials. However, the complexity of the procedures associated with excessive cost, low patterning areas leads to limit their applications in many research areas (Li, Zhai et al. 2011). Template-based patterning method is one of the most common techniques to synthesize highly ordered nanoarrays. One type of templates are hard templates which are able to generate complicated nanostructures with well control over size, spacing and morphology of the nanodots. An obstacle combined with hard templates is the capability to clear away templates after fabrication and maintain a homogenous structure of the nanopatterns. The other type is soft templates that comprise of organic surfactants, polymers, and even flexible biological viruses. In such templates, the nanostructures may accumulate into polycrystalline clusters which lead to an irregular shape (Li, Zhai et al. 2011).

7. 2. Nanosphere Lithography (NSL)

Nanosphere lithography is an advanced technique that employ template directed colloidal self-assembled crystal monolayers of polystyrene spheres on a large scale of the substrate surface to generate a long sequence of periodic nanopatterns. Compared to complex and expensive lithography techniques, NSL is now being widely used in nanofabrication as an alternative route because of its flexibility, low cost, controllable parameters, and high throughput (Hulteen, Van Duyne 1995, Deckman, Dunsmuir 1982). A colloid can generate a spontaneous structure of sequentially periodic colloidal crystal patterns called colloidal self-assembly.

Under specific conditions, colloidal crystals are organized frequently in the form of hexagonal close-packed (HCP) structures. Polystyrene, polymethyl methacrylate (PMMA) or silica colloidal spheres have been mostly used for well-ordered colloidal crystal lattices that can be used as lithographic masks (Oshima 2012). Other modified polystyrenes, such as poly-(diallyl dimethyl ammonium chloride) (DADMAC)/poly (sodium 4-styrenesulfonate) (PSS) thin shell, have been employed to synthesize NSL templates (Han, Shi et al. 2002, Han, Briseno et al. 2002).

Figure 7. 1 schematically describes the process of the synthesis of well- ordered nanoarrays by NSL. The process first involves the fabrication of nanosphere mask by applying the spherical colloidal mixture (e.g., polystyrene) on flat substrates which are chemically pre-treated to improve their surface hydrophilicity. After the evaporation of the colloidal suspension, the mask of self-assembled hexagonal-close-packed (HCP) nanospheres is obtained which can be used to sequentially pattern the surface. The material of interest is then deposited on the substrate through the interstices of the ordered beads. In the last step, a designed pattern of nanodots is produced after removing the nanospheres monolayers or bilayers by sonication in an organic solution or by tape stripping.

Many techniques have been applied to deposit colloidal suspension onto a substrate and produce high quality colloidal crystal mask such as dip coating, spin coating, electrophoretic deposition and Langmuir Blodgett method (Li, Zhai et al. 2011).

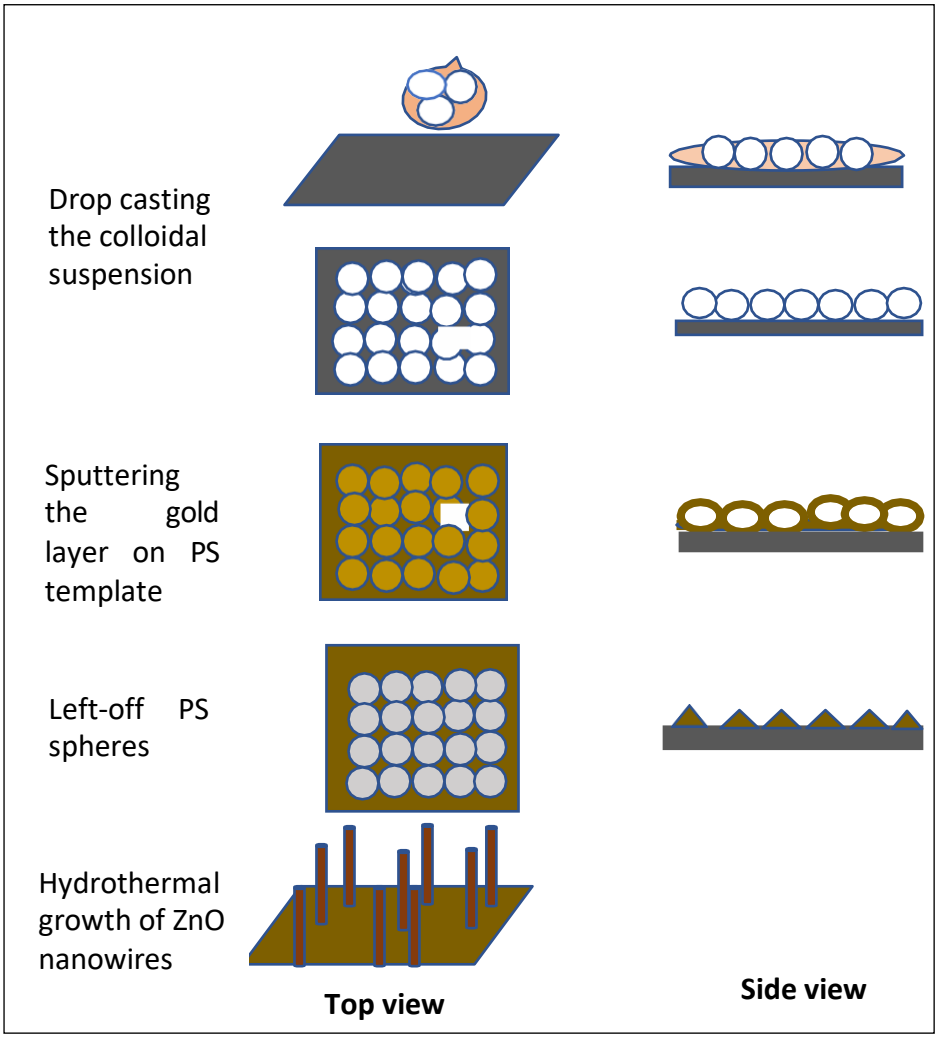

Figure 7. 1. A schematic diagram of NSL procedure combined with solution-based technique.

The structure of nanopatterns can be controlled by changing the nanospheres diameter (e.g., polystyrene), which are commercially available with different sizes/diameters as well as the processing conditions. However, Self-assembly nanospheres are more likely to suffer from structural defects, and imperfection of their periodic patterns (Gates, Xu et al. 2005) as it lacks precise control on their dimensional arrangement to generate large area ordered nanopatterns.

In this work, we introduced NSL which is an effective, inexpensive process to produce a well-ordered honeycomb like hexagonal gold pattern. Then, this catalyst gold pattern was applied to guide the hydrothermal growth of ZnO nanostructures onto silicon substrates. Here, the main role of self-assembled polystyrene spheres (PS) is to produce (HCP) monolayers which are then applied as a mask/template to pattern the deposition of gold onto the underlying substrate. After the deposition of gold, the PS is removed from the substrate, leaving behind gold patterns in the areas corresponding to the voids between the PS.

Briefly, PS suspension was dropped on the pre-treated silicon wafer. Gold was then deposited on the PS-templated substrate by RF sputtering technique. The PS template was then etched away, leading to form honeycomb patterns of gold nanodots. Finally, the growth of ZnO was successfully performed on silicon substrates via a solution-based process, with the use of a gold catalyst pattern produced from the PS mask.

7. 3. Materials and Methods

Silicon (p-type, (100)) was cut into 1cmx1cm of substrate area using a diamond scriber. The silicon pieces were initially cleaned by acetone and isopropanol for 15 min each to remove suspended contamination and then kept in (DI) bath for 10 min. Silicon substrates were blown dry with nitrogen gas and baked on a hotplate at 150 ^{0}C for 10 min to eliminate any adsorbed moisture. Because of surface chemistry and hydrophilicity of the substrate affect self-assembly organization of PS spheres, silicon substrate was treated with Oxygen plasma etching to enhance its hydrophilicity and surface wetting properties. The drop-casting route was applied to generate monolayer Self-Assembled Arrays of PS nanospheres. PS nanospheres (1% solid content) with 500 nm and 1µm

diameters were used. Tow group of samples were differently processed by drop coating procedure. In the first group, it was referred to as samples A, a small amount of PS suspension was dropped onto the surface of the substrate and kept immobile for nearly 1 min to ensure well dispersion of the PS suspension. Then the substrate was gently immersed into (DI). To adjust the surface tension of water, a small drop of SDS solution was added. Then the substrate was slowly lifted in plain area, to avoid further deposition of PS spheres on the monolayer during its removal from the water. In another group, it was referred to as samples B, the PS spheres of 1 µm diameter were pipetted and dispersed onto the surface of substrates which were tilted at roughly 45^0 angles. The substrates were left to allow the colloidal suspension to be evaporated without immersing in (DI) or adding SDS. After drying, the PS mask was used to pattern ZnO growth onto the substrate by depositing a thin layer of gold onto the PS-templated substrate by RF sputtering technique. For the last step, the PS spheres were removed by ultrasonication in Isopropyl Alcohol (IPA) for 5 min. well-ordered honeycomb like hexagonal gold pattern was formed.

7. 4. Result and discussion

The SEM images of the PS spheres in samples A are shown in Figure 7. 2. It was observed that two-dimensional monolayers of self-assembled spheres on Si substrate were obtained for 500 nm PS. The arrangement was sensibly acceptable as PS spheres were compressed in one-layer with some line deformity and emptiness in some regions.

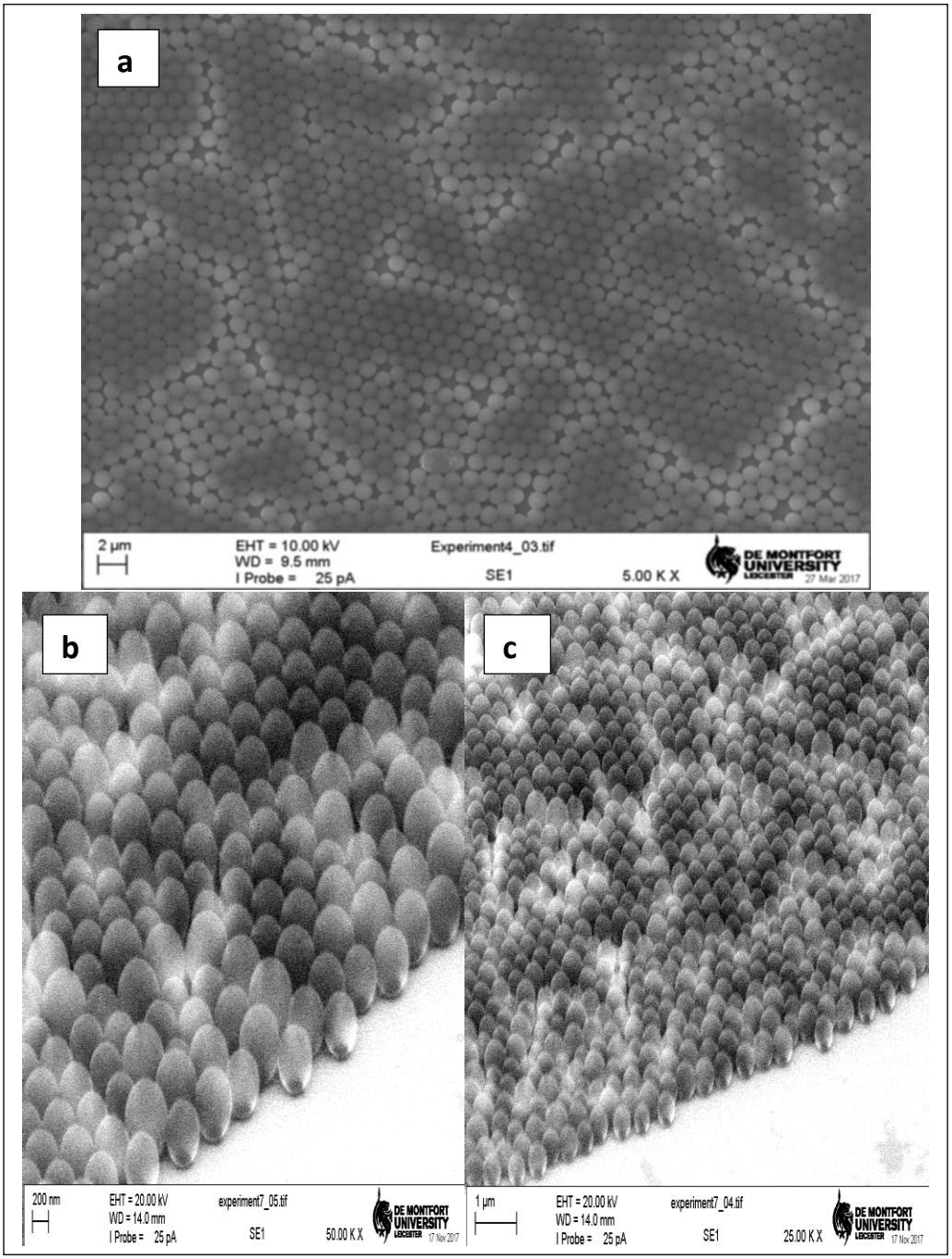

Figure 7. 2. Top-view (a) and tilted-view (b, c) SEM images of a monolayer of self-assembled PS spheres of 500 nm diameter.

In these group of samples, the PS colloids were distributed onto the surface of substrate, which is slowly immersed into water, releasing the colloidal suspension from substrate, leading to form PS monolayer on the surface of water which can be seen by necked eye. When a substrate is then gently clear away the variation in surface tension between the substrate and the surface of water results in transferring the PS colloidal crystal to the substrate to generate ordered arrays of PS monolayers. However, some defects and cracks of PS sphere were observed which could be attributed to the variation of sphericity and diameter of polystyrene spheres.

Even though drop-casting method is one of the easiest methods of obtaining a monolayer, the chance of forming a double layer is very high. In particular, with samples B where gaps and multi-layered regions of the self-assembled PS spheres were continually formed (Figure 7. 3). The formation of multi-layered regions on these samples may attribute to the high concentration of PS suspension, as once a colloidal suspension was dropped, the colloidal crystals were dispersed over the surface and because of not imbedding in (DI) they had high concentration therefore, they were compressed to form double layers on the surface. In addition, during flowing the colloidal suspension, it is more likely large quantity of crystals settles nearby the edge especially with the tilted position of the substrate, so It is difficult to have a homogenous distribution of PS colloids which result in creating disorderly multilayers of PS spheres.

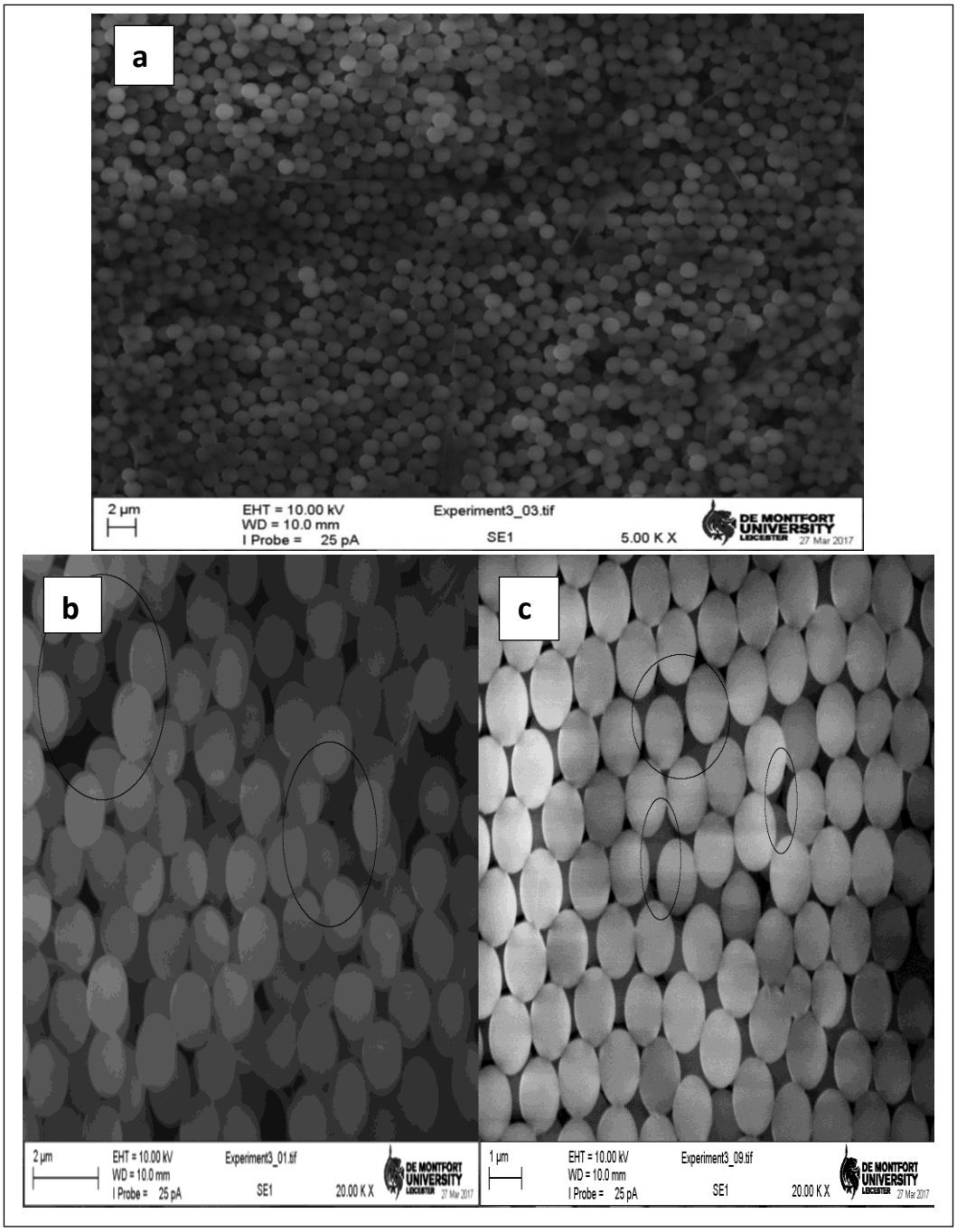

Figure 7. 3. Low magnification (a), high magnification (b, c) SEM images of a multilayers of self-assembled PS spheres of 1 µm diameter.

While samples A that were gently immersed into (DI) with adding SDS produced monolayered areas. So, PS colloidal crystals were loosely floated on the water surface which can prevent clustering of PS colloidal crystals onto Si slides when they were left up and promote a formation of monolayers regions on the surface. Further, the change of the water surface tension provided by SDS can drive the colloids to organize into self-assembly of monolayered pattern on the surface of substrate. In general, the driving forces of the solution techniques depend on the interactions between the colloidal crystals and the solvent. Therefore, surface tension, evaporation, capillary forces or a combination of those forces significantly affect the formation of colloidal crystals (van Dommelen, Fanzio et al. 2017).

Based on these observations, it seems that the drop-casting technique was efficient in producing well-order monolayer colloidal crystals of PS spheres. Sputtered gold particles were covered the interstices between the PS spheres, so removing the PS spheres away result in a honeycomb like hexagonal gold pattern (Figure 7. 4) on Si substrate which were used in the subsequent experiments to guide the growth of ZnO nanowire arrays. Combining PS pattern- guided gold arrays and the hydrothermal growth is a very efficient method to produce 1D ZnO nanoarrays due to the low temperature during the growth process.

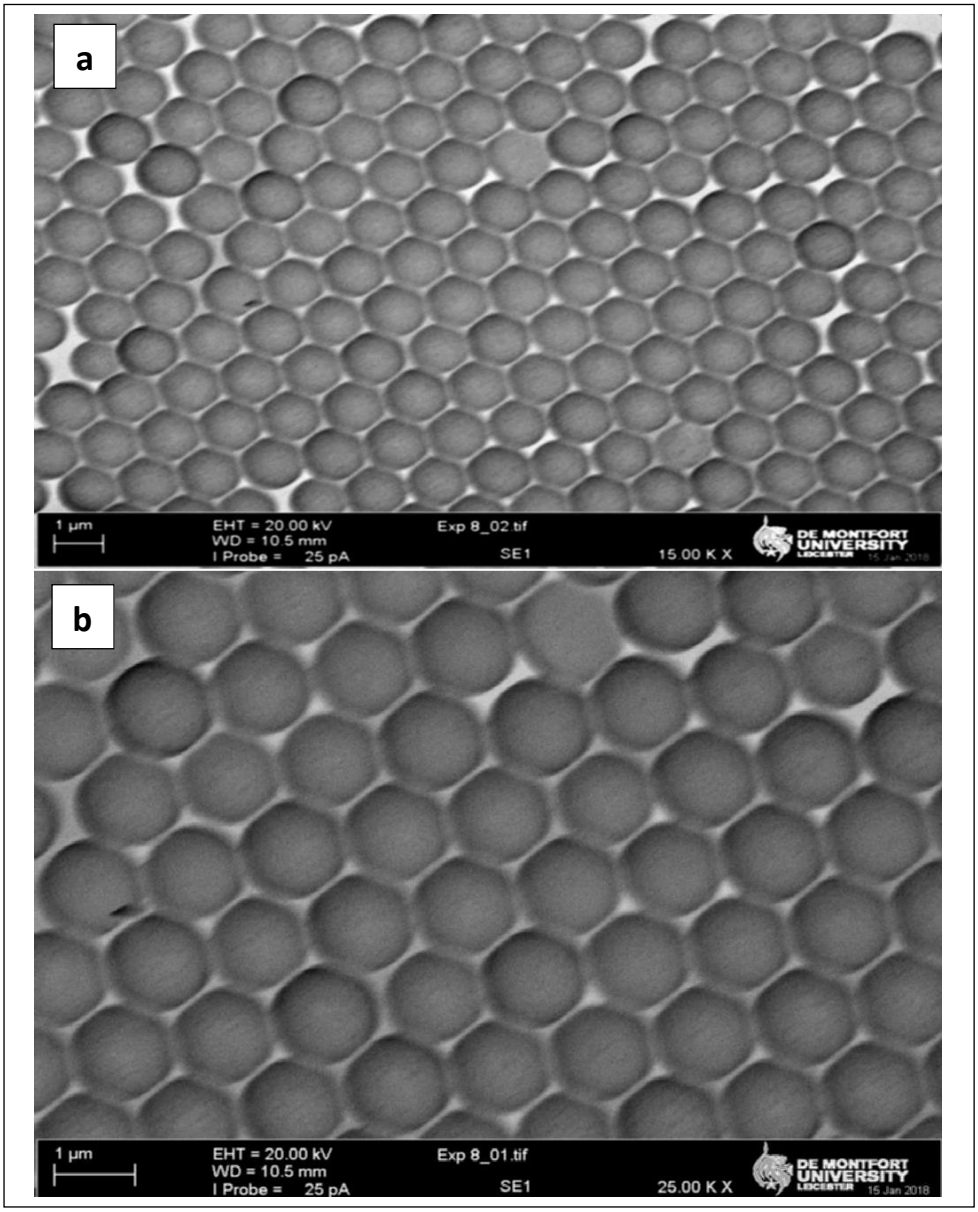

Figure 7. 4. Low magnification (a), high magnification (b) SEM images of the honeycomb gold pattern produced by a sputtering technique.

Using the gold honeycomb pattern, ZnO nanowire arrays were grown by a solution- based process at 70 ^{0}C. Figure 7. 5 shows the low magnification SEM image of well distributed ZnO arrays grown from these Au patterns on a large scale using this method.

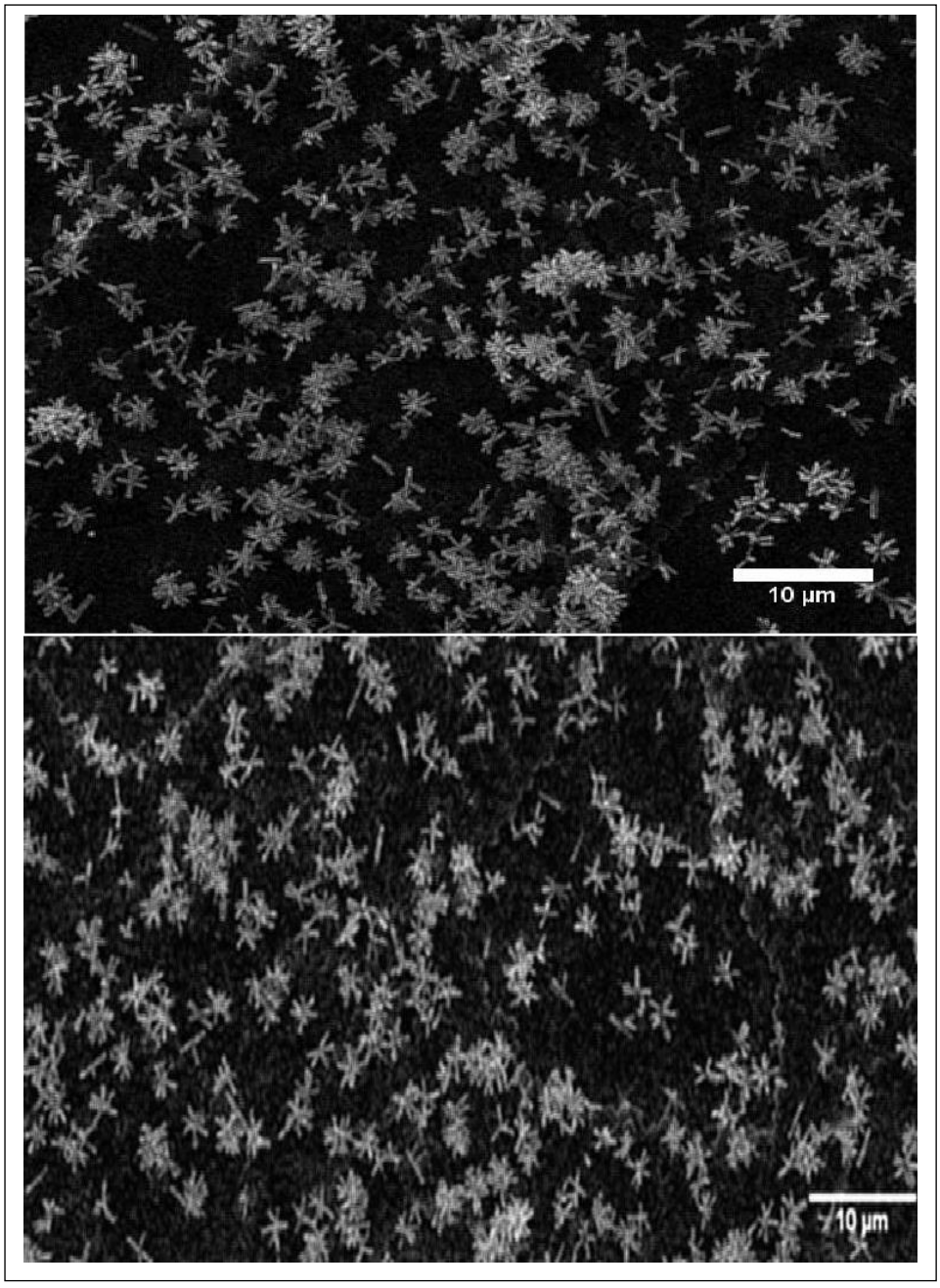

Figure 7. 5. Low magnification of top view SEM images of hydrothermal ZnO nanowire arrays grown from gold honeycomb structured pattern.

A magnified SEM images of the top and tilted views are shown in figure (7.6) nearly, All the ZnO nanowires have an average height in the range of 1 to 1.5 µm and their average diameters are between 50 and 100 nm. The dimension of the ZnO nanowires could be modified by changing the growth conditions as was discussed earlier.

The distribution and uniformity of the obtained ZnO nanoarrays were affected by the shape and pattern vacancies within the template. Since, defects in some sites of the template were not avoidable, resulting in much less ordered nanoarrays on these sites or even absence of the grown nanowires. Another explanation could be linked to the deposition of sputtered gold layer through PS mask, as during the sputtering procedure the energetic and high mobility of the gold atoms allowed the gold to cover the whole surface even underneath the PS spheres especially if the PS spheres are not well adhered to the Si substrates (Wang, Summers et al. 2004) therefore, the growth of nanowires in these areas of the template would be less ordered and unsystematic.

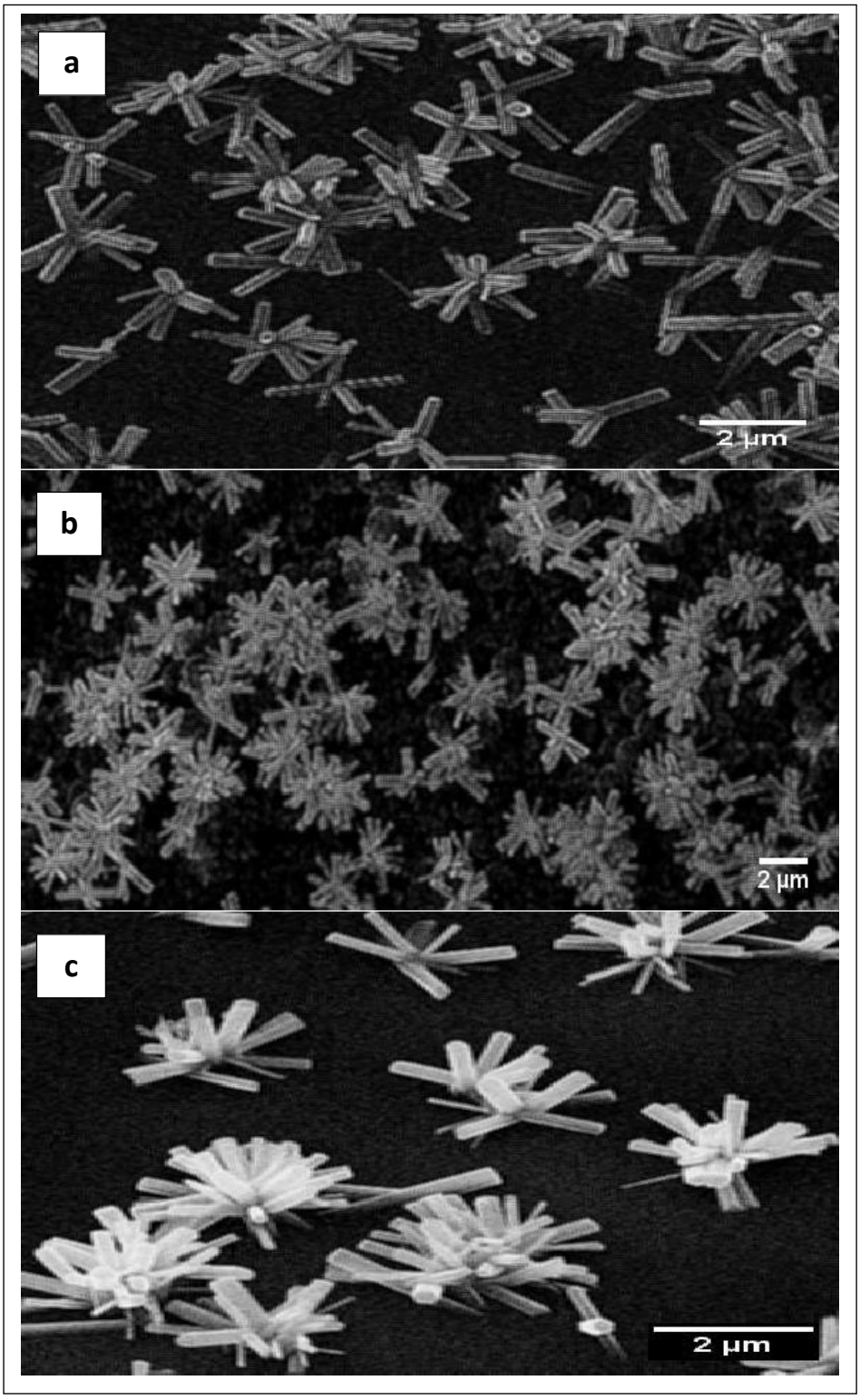

Figure 7. 6. High magnification of top view SEM images (a and b) and tilted view (c) of hydrothermal ZnO nanowire arrays grown from gold honeycomb structured pattern.

7. 5. Conclusion

Template-assisted synthesis of ZnO nanowire arrays based on PS sphere mask, employing gold catalyst pattern and solution-based process was discussed. Drop-casting method was straightforward and efficient technique for the formation of well-ordered colloidal crystal of self- assembled PS spheres with less deformation. Despite variation of interparticle spacing of PS mask, the close packing of colloidal monolayer was agreeable and the probability of production of multi-layered area was low. Such lithographic patterning method allows good control on the site of nanowires.

However, it was observed that the formed ZnO nanoarrays showed irregularity and randomness in some areas over the substrate surface which could be attributed to the imperfection of PS template. Even though, an effort to control the position of ZnO nanoarrays was performed, additional optimizations are still required to produce well-aligned ZnO nanoarrays over the substrate surface.

In terms of application point of view, (3D) branched ZnO nanostructure platforms show more capability and higher performance for intracellular delivery owing to their high surface to volume ratio. Therefore, the following chapter focuses on the fabrication of (3D) NFs and branched NFs of ZnO using solution-based method.

References

BRAMBLEY, D., MARTIN, B. and PREWETT, P., 1994. Microlithography: an overview. *Advanced Functional Materials,* **4**(2), pp. 55-74.

DECKMAN, H. and DUNSMUIR, J., 1982. Natural lithography. *Applied Physics Letters,* **41**(4), pp. 377-379.

GATES, B.D., XU, Q., STEWART, M., RYAN, D., WILLSON, C.G. and WHITESIDES, G.M., 2005. New approaches to nanofabrication: molding, printing, and other techniques. *Chemical reviews,* **105**(4), pp. 1171-1196.

HAN, S., BRISENO, A.L., SHI, X., MAH, D.A. and ZHOU, F., 2002. Polyelectrolyte-coated nanosphere lithographic patterning of surfaces: fabrication and characterization of electropolymerized thin polyaniline honeycomb films. *The Journal of Physical Chemistry B,* **106**(25), pp. 6465-6472.

HAN, S., SHI, X. and ZHOU, F., 2002. Polyelectrolyte hollow sphere lithographic patterning of surfaces: Construction of 2-dimensional well-ordered metal arrays. Nano Letters, 2(2), pp. 97-100.

HAYNES, C.L., MCFARLAND, A.D., ZHAO, L., VAN DUYNE, R.P., SCHATZ, G.C., GUNNARSSON, L., PRIKULIS, J., KASEMO, B. and KÄLL, M., 2003. Nanoparticle optics: the importance of radiative dipole coupling in two-dimensional nanoparticle arrays. The Journal of Physical Chemistry B, 107(30), pp. 7337-7342.

HULTEEN, J.C. and VAN DUYNE, R.P., 1995. Nanosphere lithography: A materials general fabrication process for periodic particle array surfaces. Journal of Vacuum Science & Technology A: Vacuum, Surfaces, and Films, 13(3), pp. 1553-1558.

LI, L., ZHAI, T., ZENG, H., FANG, X., BANDO, Y. and GOLBERG, D., 2011. Polystyrene sphere-assisted one-dimensional nanostructure arrays: synthesis and applications. *Journal of Materials Chemistry,* **21**(1), pp. 40-56.

MARSHALL, M.T., MCDONALD, M., TONG, X., YEADON, M. and GIBSON, J., 1998. A new surface science in situ transmission and reflection electron microscope. *Review of scientific instruments,* **69**(2), pp. 440-447.

MARTIN, O.J., 2003. Surface plasmon illumination scheme for contact lithography beyond the diffraction limit. Microelectronic engineering, 67, pp. 24-30.

OSHIMA, H., 2012. Nanosphere Lithography for High-Density Nanopatterning. *Vistas in Nanofabrication,* , pp. 1.

TONG, H.D., JANSEN, H.V., GADGIL, V.J., BOSTAN, C.G., BERENSCHOT, E., VAN RIJN, C.J. and ELWENSPOEK, M., 2004. Silicon nitride nanosieve membrane. *Nano letters,* **4**(2), pp. 283- 287.

VAN DOMMELEN, R., FANZIO, P. and SASSO, L., 2017. Surface self-assembly of colloidal crystals for micro-and nano-patterning. *Advances in Colloid and Interface Science,* .

WANG, X., SUMMERS, C.J. and WANG, Z.L., 2004. Large-scale hexagonal patterned growth of aligned ZnO nanorods for nano- optoelectronics and nanosensor arrays. *Nano letters,* **4**(3), pp. 423-426.

Chapter 8

Synthesis of 3D branched ZnO nanostructures

8. 1. Introduction

The formation of uniformly nanostructured zero-, one-, and two-dimensional nanocrystals into three- dimensional multifunctional systems is imperative and highly challenging in materials science and nanoscale devices. 1D nanocomponents have been reported to be most frequently used either as backbones, grafting materials, or fundamental building blocks for assembly synthesis process. 2D and 3D nanocrystals have been used for further growths and assembly methods to help constructing nanostructured 3D complexes with higher orders of topological complex architectures.

In comparison to simple nanorods, nanopillars, nanowires, nanobars, nanoneedles, nanobelts and other relative 1D nanostructures, a three-dimensional (3D) complex nanostructures with a precisely controlled size and morphology can provide us with newer and/or better physical and chemical properties (Wang, Zhou 2011) because of their unique complication in morphology, structural hierarchy, high surface areas and direct electron transport pathways for charge carriers (Wang, Lieber 2003). It has been demonstrated that 3D-multibranched ZnO nanostructures with a large surface area exhibit better photocatalytic performance than those of Low dimensional ZnO nanostructures (Cheng, Le et al. 2011). photocatalytic properties are largely tailored by the nanostructure morphology thereby its overall surface area and defect constitution.

With a large accessible surface area of the catalyst that provides plentiful active adsorption sites, the probability of electrons/holes to come across with water/oxygen is highly enhanced which further leads to improve the radical formation efficiency. That is to say, if much more atoms settle on the surface, it enhances the adsorption ability of the photocatalysts towards dye (Maiti, Pal et al. 2015). Photocatalytic reaction occurs when the metal oxide catalyst absorbs a light of energy higher or equal to the band gap energy of it, which can promote an electron (e^-) from the valence band to the conduction band, forming a positive hole (h^+) in the valence band. Then, these electrons in conduction band on the catalyst surface reduce the molecular oxygen to superoxide anion which, in presence of organic scavengers, could form organic peroxides or hydrogen peroxide. In some case, a high surface to volume ratio could also cause surface defects, which may act as active photocatalytic reaction sites.

Compared to high temperature synthesis methods such as chemical vapor deposition(CVD) (Hata, Futaba et al. 2004), PVD (Lao, Wen et al. 2002), and vapor–liquid–solid (VLS) growths (Hannon, Kodambaka et al. 2006), solution-based techniques offer two main benefits:(1) the reaction conditions provide an easy handling, wider selections of substrates and maintain a good control over their composition ;(2) reactions could be scaled up easily at low cost. Herein, we mainly highlight an overview over recent development of multi- dimensional ZnO nanoarchitectures processed via low temperature solution phase synthesis approaches. Those various synthetic methods and growth mechanisms of the nanostructured 3D ZnO complexes, including multistep sequential growth techniques, template-based synthesis, template-free self- assembly and precursor or self-templating approaches.

8. 2. Synthetic Strategies of 3D-multibranched ZnO Nanostructures

8. 2. 1. Multistep Sequential Growth Methods

The multi-step sequential growth methods can be employed in the fabrication of heterostructures or hybrid nanostructures in a cost-effective way (Maiti, Pal et al. 2015). A multistep self-assembly approach can be classified into two main categories, namely multistep self-assembly with multi-discontinuous processes and multi-step self-assembly completed in one-pot solution syntheses. Multistep self-assembly with multi-discontinuous processes includes the formation of underlying low dimensional structures, followed by the fabrication of 3D- multi-structures via sequential adjustment of firstly prepared structures. Zhang et al. (Zhang, Dong et al. 2006) fabricated an organized construction of a complex ZnO nanostructure based on 1D ZnO nanorods by a low temperature solution-based route (Figure 8. 1).

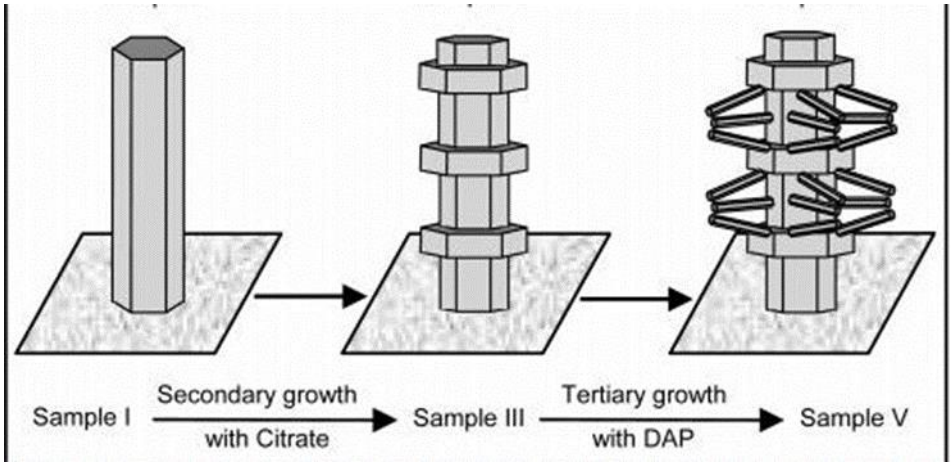

Figure 8. 1. A schematic illustration of the formation of ZnO complex crystals. Reprinted with permission from (Zhang, Dong et al. 2006).

Seung et al. (Ko, Lee et al. 2011) have demonstrated nanoforest of high density, long branched tree-like complex hierarchical ZnO nanowire photoanodes via a simple solution processed hydrothermal approach that could enhance the Dye-Sensitized Solar Cell (DSSC) power conversion efficiency. As shown in Figure 8. 2, first generation (backbone) ZnO nanowires were produced from ZnO quantum dot seeds deposited on a substrate immersed in an aqueous precursor solution.

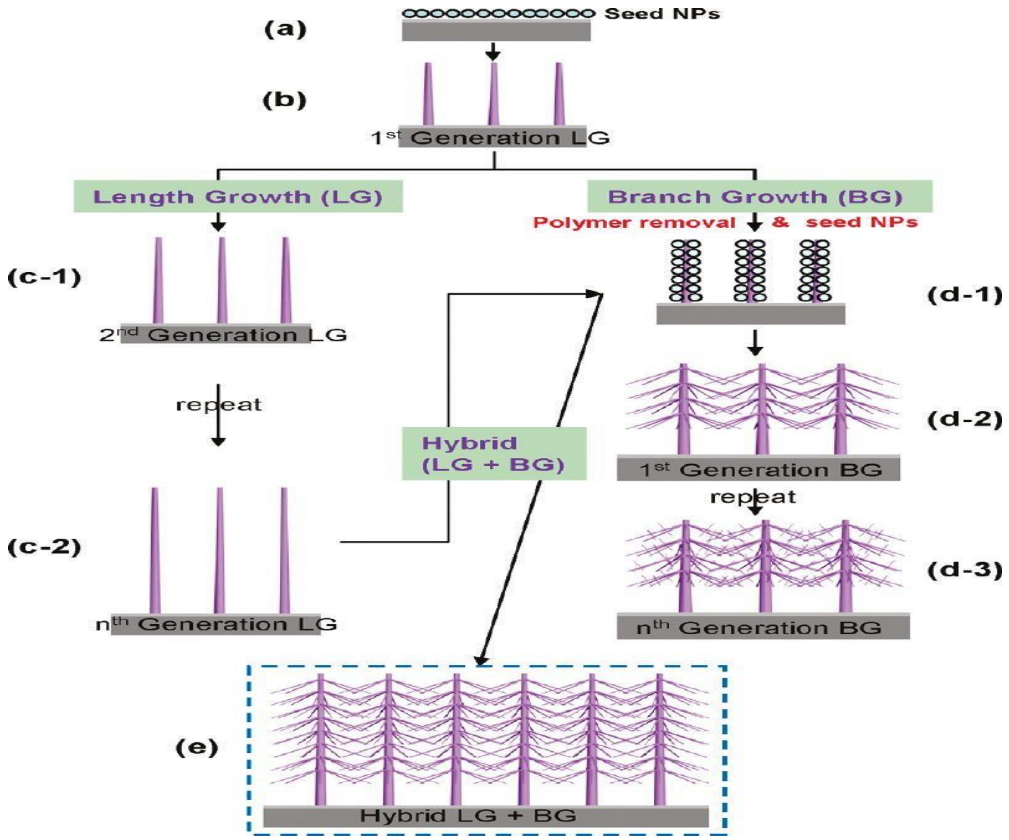

Figure 8. 2. Two routes for hierarchical ZnO NW hydrothermal growth. Length growth (LG) (a-b-c), branched growth (BG) (a-b-d), and hybrid (a-b-c-d-e). Reprinted with permission from (Ko, Lee et al. 2011).

To increase the length of ZnO nanowires, the hydrothermal growth process was repeated in a fresh aqueous precursor solution. Xu et al. (Xu, Dai et al. 2010) carried out a two-step growth process to produce complex ZnO nanowire-nanosheet arrays by preparing of ZnO nanosheet arrays on glass substrates and then growing ZnO nanowires by the hydrothermal growth (Figure 8. 3).

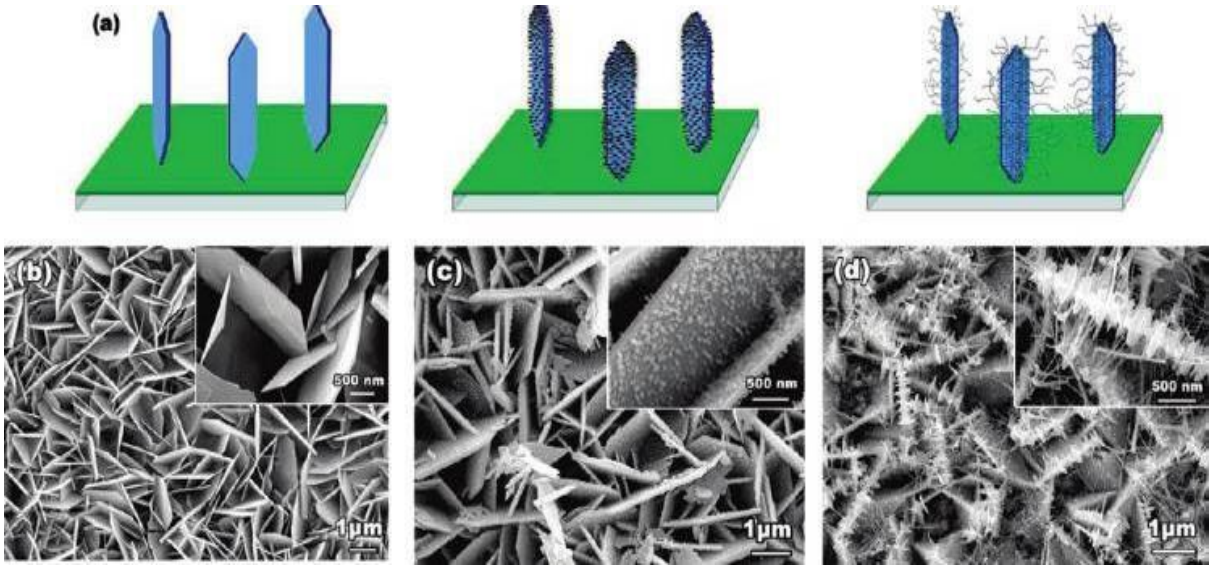

Figure 8. 3. (a) The schematic growth procedure of the hierarchical ZnO nanoarchitectures and (b–d) top-view SEM images of the complex ZnO nanowire-nanosheet architectures at different growth stages. Reprinted with permission from (Xu, Dai et al. 2010).

Cheng et al. (Cheng, Chiu et al. 2008) fabricated branched ZnO nanowires on FTO substrates using a solvothermal method for (DSCs) (Figure 8. 4).

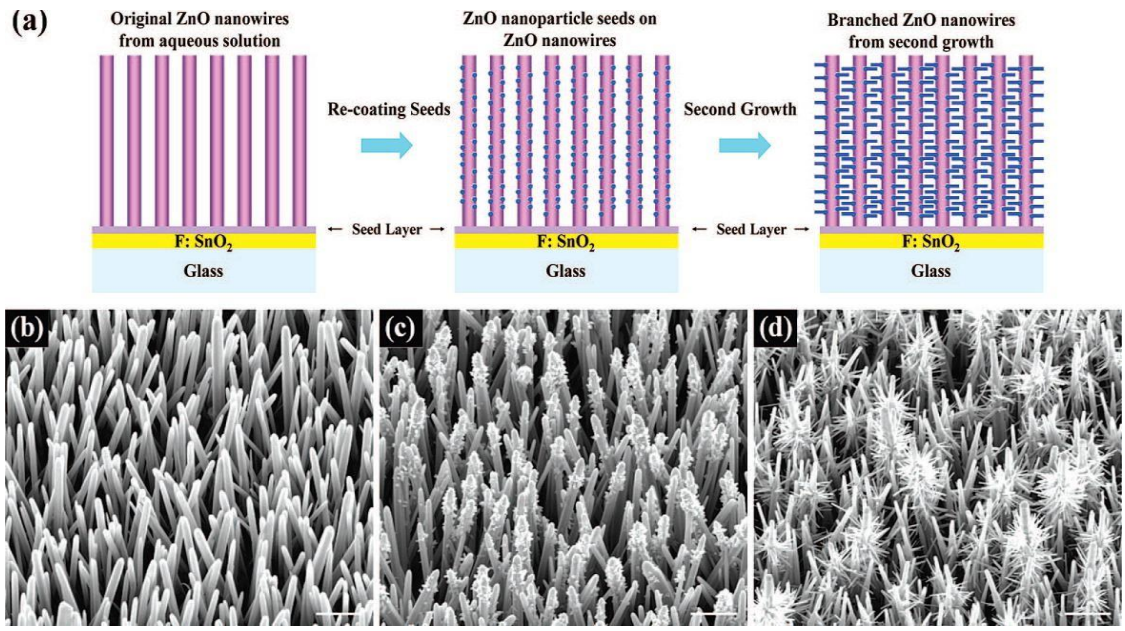

Figure 8. 4. (a) The schematic growth process from the primary to the branched ZnO nanowires, (b) before and (c) after recoating ZnO nanoparticles seed layer, and (d) the final branched ZnO nanowires obtained from the second hydrothermal growth; scale bar, 1 μm. Reprinted with permission from (Cheng, Chiu et al. 2008).

Despite multi-step self-assembly with multi-discontinuous processes have been broadly employed in the synthesis of hierarchical ZnO structures, it seems that some restrictions could not be avoided such as time-consuming reaction and limitation for large-scale production. To solve such problems, multi-step self-assembly completed in one-pot reaction has been adopted for effective growth of 3D complex ZnO nanostructures. Lu et al. (Lu, Xue 2011) has used such procedure to build ZnO 3D superstructures, in which the growth assembly process was driven by forming robust and stable gas/liquid interface between Oxygen stemming from the decomposition of H_2O_2 and dimethyl sulfoxide (DMSO) organic solvent.

Primarily, the microspheres were assembled from ZnO nanorod chunks, and then the 3D superstructure was fabricated via the connection within those microspheres side-by-side in a secondary assembly procedure. A simple low temperature water bath method and without any catalysts-assisted have been used to synthesize homobranched ZnO nano/microstructure. Such nano/microstructure contain a shuttle-like nano/microrod backbone that was surrounded by six radial oriented branches (Figure 8. 5) (Fang, Lv et al. 2015).

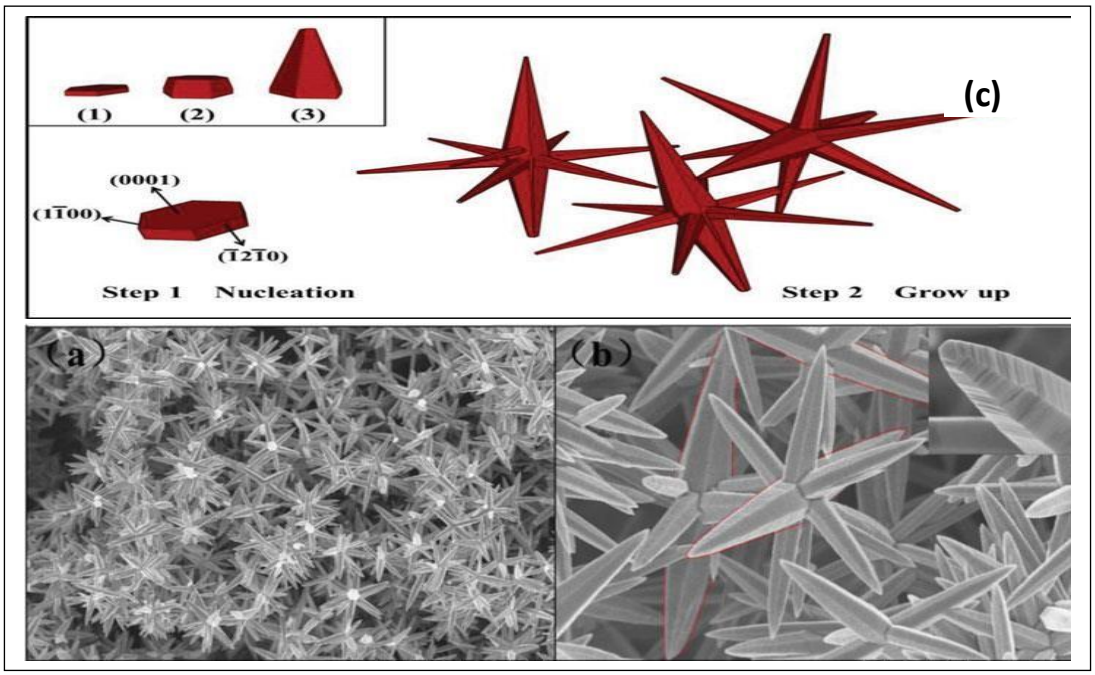

Figure 8. 5. SEM images of multibranched ZnO nano/microstructure with (a) low, (b) high magnifications. (c) Schematic illustration of the growth process. Reprinted with permission from (Fang, Lv et al. 2015).

8. 2. 2. Template-assisted Synthesis

Compared with traditional synthetic methods, the template-assisted fabrication method can efficiently control the morphology and structure of nanomaterials and have the advantages of a good reproducibility during the synthesis process. They have been most widely developed for preparing hollow, porous, and bio-inspired structures, etc. (Liu, Goebl et al. 2013). Usually, the synthesis process involves the growth of desired structures on hard templates, such as polymer microspheres, carbon fibre, porous membrane, plastic foam, which can be removed by chemical etching or thermal decomposition, or soft templates, such as emulsion micelles and even bubbles(Liu, Wang et al. 2015).

The ZnO hollow structures can be formed in various interesting morphologies, such as hollow spheres with core-shell or yolk-shell. Dilger et al. (Dilger, Wessig et al. 2014) employed SiO_2 hard templates to fabricate yolk-shell and hollow ZnO spheres by gas phase treatment at different temperatures. In another case, Sinha et al. (Sinha, Basu et al. 2010) used soft templates as water bubbles to modify the hydrothermal growth of ZnO hollow spheroids under tungsten light irradiation. Porous hierarchical ZnO nanostructures are a material of interest due to the large active surface areas, especially the three-dimensionally-ordered macroporous (3DOM) nanostructures (Stein, Li et al. 2007). Wang et al. (Wang, Tian et al. 2016) used PMMA microspheres as templates via a one-step colloidal crystal templating (CCT) process to assist the formation of In-doped ZnO 3DOM structures (Figure 8. 6).

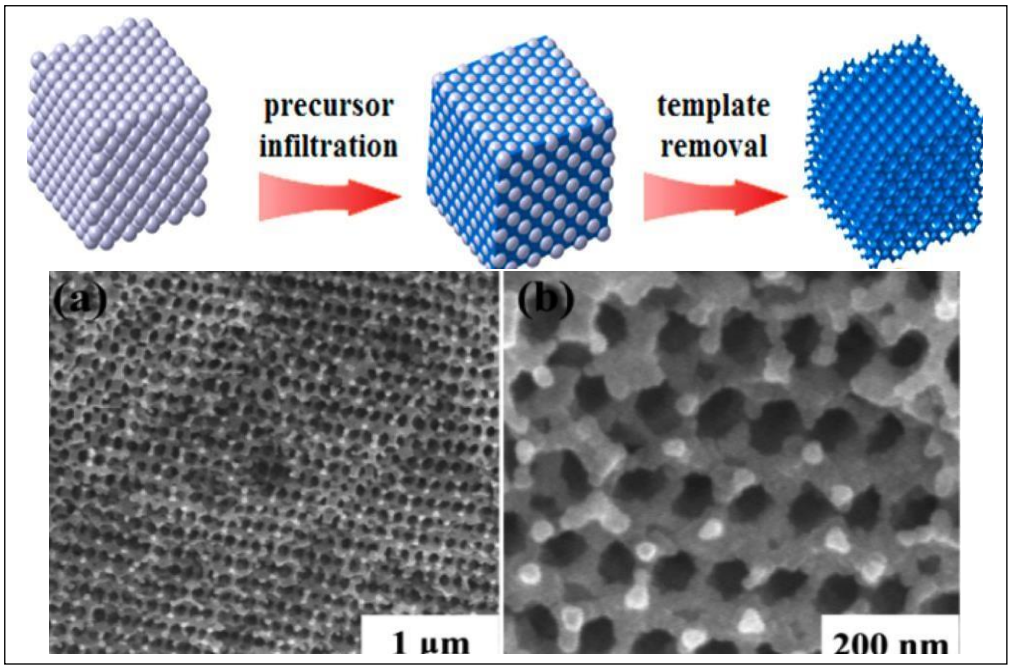

Figure 8. 6. A schematic illustration of the experimental procedure and SEM images of (3DOM) In-ZnO structures (a, b) (Wang, Tian et al. 2016).

Another interesting ZnO hierarchical structure inspired by nature have been developed by using natural butterfly wings as templates (Figure 8. 7). The biomorphic 3D ZnO periodic structures maintained the microstructural features of the original butterfly wing scales' morphology down to the micrometre level and it may be facile for photocatalytic applications (Zhang, Zhang et al. 2006). Besides, layer-layer hierarchical structures (Li, Yin et al. 2011), binding peptides (Limo, Ramasamy et al. 2015), flower-like, spindle- like, sword-like, umbellar-like, prism-like (Wang, Zhang et al. 2011, Wu, Chen et al. 2008) , and other interesting architectural (Stan, Munteanu et al. 2015) can also be produced by template-assisted approaches.

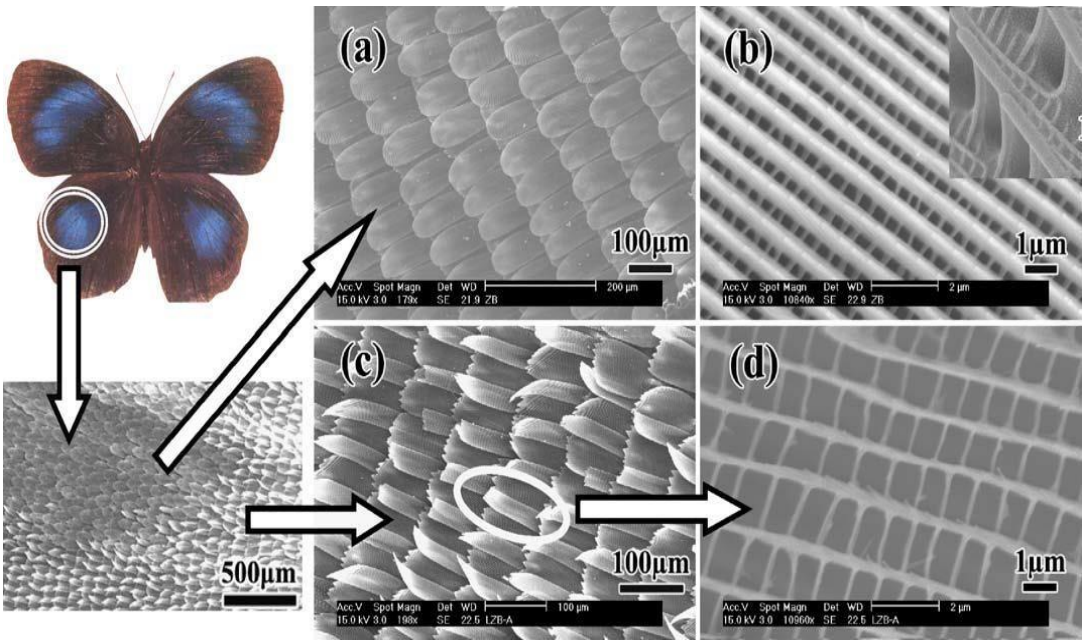

Figure 8. 7. Nature photograph and FESEM images of wing scales template. (a) Details of metallic blue scales; (b) high-magnification image of metallic blue scales. Inset: inclined view of the ridges; (c) details of dark brown scales; (d) high-magnification image of dark brown scales. Reprinted with permission from (Zhang, Zhang et al. 2006).

8. 2. 3. Template-Free Self-Organization

Despite template-assisted processes having been widely employed in the synthesis of 3D ZnO complexes, some typical drawbacks such as long reaction durations, expensive templates, and lack of control on the morphology through removing the templates could limit the efficiency of the process (Kudo, Miseki 2009). To deal with such problems, effective and efficient template-free approaches such as template-free self-organization have been developed to fabricate different 3D-complex nanostructures (Yan, Ouyang et al. 2010).

Wang et al. (Wang, Du et al. 2013) grown hierarchical hollow ZnO microspheres via a one-pot template-free hydrothermal synthesis and interestingly found that the hollowness of these microspheres could be tailored by adjusting the concentration of zinc source (Figure 8. 8). Using a similar approach, hierarchical ZnO hollow spheres consisting of nanoparticles were prepared by a microwave-assisted solvothermal method (Zhao, Qi 2012).

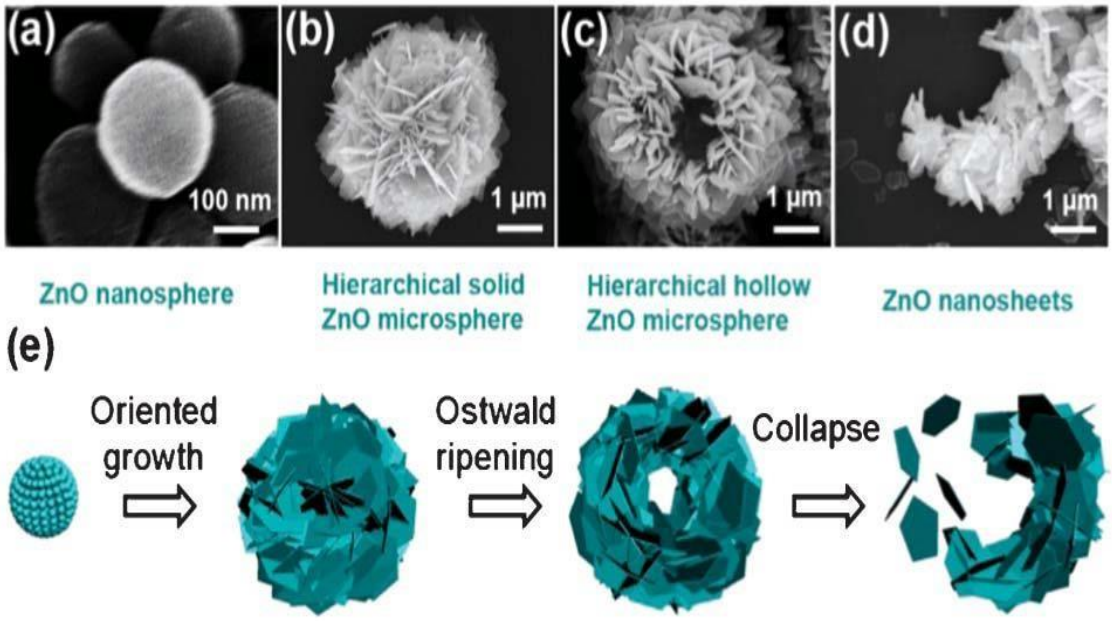

Figure 8. 8. SEM images of the morphology evolution at different reaction times (a–d). (e) A schematic illustration of the growth process of the hollow ZnO microspheres. Reprinted with permission from (Wang, Du et al. 2013).

Highly crystallized and uniformed hierarchical ZnO structures consisting of interconnected monocrystalline nanosheets can be fabricated in a template-free aqueous solution system under sonochemical treatment at room temperature (Shi, Zhu et al. 2013). The fabrication of the hierarchical structures is interpreted using a new mechanism based on oriented attachment and reconstruction.

In the disequilibrium growth system, thicker, porous, and coarse crystallized ZnO sheets were first obtained via oriented attachment of small-sized nanocrystals. After reconstruction, ultrathin, integrated, and monocrystalline nanosheets were produced (Figure 8. 9).

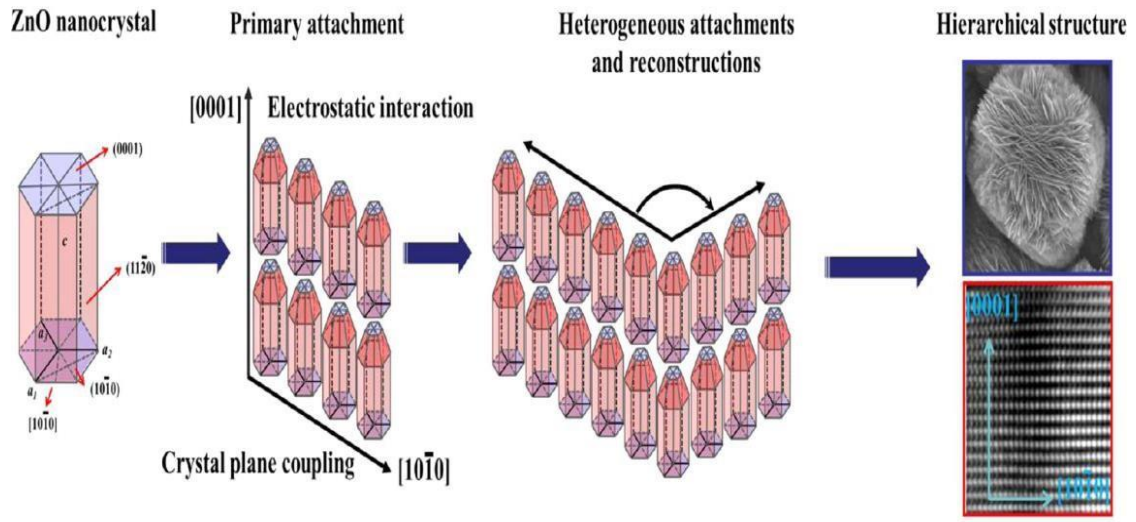

Figure 8. 9. Schematic Diagram of Formation of ZnO Nanosheets and Hierarchical Structure via Oriented Attachment of Small- Sized Nanocrystals and Reconstruction. Reprinted with permission from (Shi, Zhu et al. 2013).

Using a similar strategy, different hierarchical ZnO structures, such as flower-like (Krishnapriya, Praneetha et al. 2016), comb-like (Xu, Wu et al. 2012), twin-sphere (Li, Gong et al. 2013), hyperbranched array (Wu, Feng et al. 2014), hexagonal-pyramid-like microcrystals (Yang, Sun et al. 2010) could also be constructed. Pachauri et al. (Pachauri, Kern et al. 2010) reported various hierarchical structures, including flower-like, viscous- fingers-like and rolling-pin-like, using nanoplatelets as basic building blocks under a simple low-temperature chemical bath-assisted synthesis route.

The morphology of those 3D complex structures could be controlled by adjusting the pH (Chetia, Ansari et al. 2016) or the concentration of precursors (Desai, Sartale 2015). ZnO hierarchical structures with tunable morphology were synthesized by a facile additive-free solution- based method. The supersaturation (S) was adjusted in the range of 1.26 to 3.51 by changing the dilution ratio or the $[OH^-]/[Zn^{2+}]$ ratio (Wang, Hou et al. 2014). The nanoscale building blocks of the hierarchical structures transformed from nanorods-based ($S \leq 1.54$) to nanosheets-based ($1.95 \leq S \leq 2.64$) and, finally, to nanoparticles-based ($S \geq 3.00$) (Figure 8. 10).

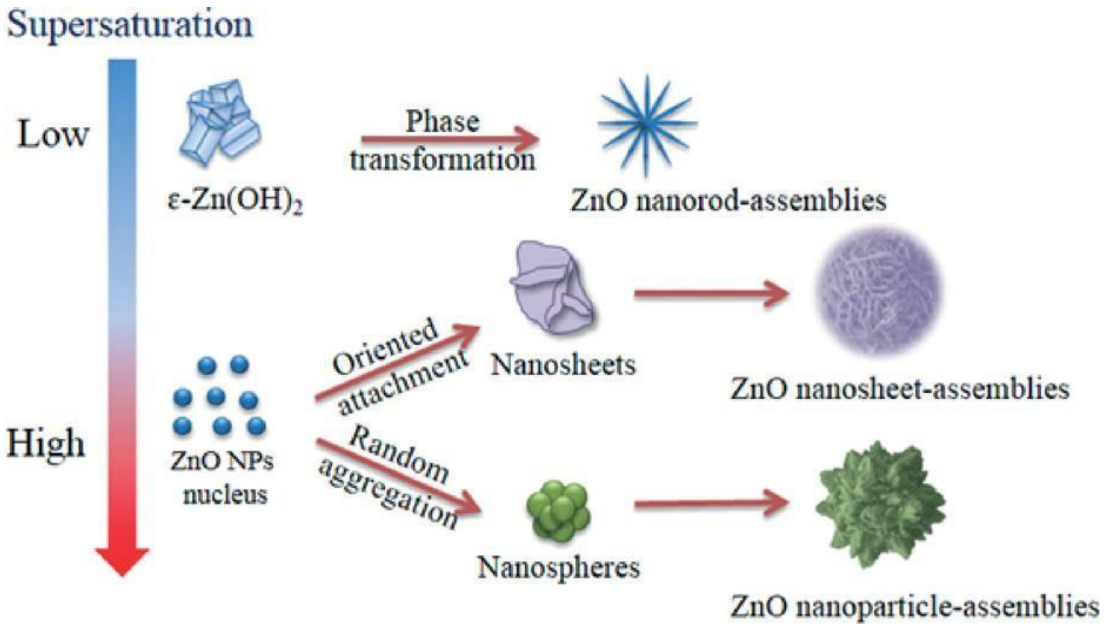

Figure 8. 10. Schematic illustration for the growth mechanisms of ZnO hierarchical structures. Reprinted with permission from (Wang, Hou et al. 2014).

8. 2. 4. Precursor or Self-Templating Methods

Precursor or self-templating route is another typical template-free method that includes the formation of precursors containing certain hierarchical structures followed by the calcination of the precursors to produce the final structures. Different 3D ZnO nanostructures have been fabricated by using zinc-containing inorganic salts with a certain hierarchical morphology. For example, mesoporous hierarchical ZnO nanostructures can be constructed by using a layered basic zinc carbonate (LBZC)-containing multi-layered structure as the precursor (Yang, Im et al. 2011). A PEG -mediated organic–inorganic interface cooperative self-construction route applied to achieve the self-assembly of $Zn_5(CO_3)_2(OH)_6$ nanosheets into novel flower-like 3D superstructures, then the 3D structures composed of nanosheets transformed into porous ZnO nanosheet-based hierarchical structures without morphology change (Liu, Li et al. 2011).

Wang et al. (Wang, Liu et al. 2012) fabricated flower-like ZnO nanosheets with porous structure through annealing the zinc hydroxide carbonate precursor, which was obtained by a one-pot hydrothermal process. A three-dimensional hierarchical porous ZnO with a tubular structure has been prepared by calcining a tubular hierarchical hydrozincite precursor (Fan, Tang et al. 2015). 3D hierarchical porous ZnO have been synthesized by a two-step process (Fan, Tang et al. 2015). Firstly, a simple precipitation self-template method has been used to prepare a precursor of hydrozincite with tubular hierarchical structure composed of nanosheets, and then 3D hierarchical porous ZnO were constructed by calcining the precursor at 300 °C.

8. 3. Synthesis of branched ZnO NFs

Branched NFs are 3D nanoscale structures that comprise of a main nanoflower "trunk" and branches. Currently, a such branched architecture of ZnO nanostructure has provided a wide surface area and shown better performance in optoelectronics, photocatalysis, photovoltaics applications (Xia, Wang et al. 2016). Such 3D morphology is particularly advantageous in (DSSC) system as it enables electrons to travel through a short and direct conduction pathway, due to the unique design of 3D ZnO nanostructures has closer spacing between the nanowires, leading to higher short-circuit currents for electron transfer, which can significantly reduce the electron recombination (McCune, Zhang et al. 2012).

The growth of branched NFs was carried out in tow steps, the first one was the growth of ZnO nanoflower by solution-based method to act as a main backbone. This step included applying catalytic seeding of ZnO nanoparticles to assist the growth of ZnO nanoflower. In the next step, secondary branches were grown by recoating the seed solution directly along these backbones. We have chosen to use the forced seeding method as it is straightforward and effective way to grow the following branches. In addition, since the synthesis of branched ZnO NFs is a complicated and time-consuming process, it was decided to use ZnO nanoparticles seed solution for its simplicity and low experimental budget compared to sputtering deposition of Au seed layer.

8. 3. 1. Experimental details

8. 3. 1. 1. Synthesis of ZnO NFs

ZnO nanoparticles with particle size less than 50 nm were used to prepare the seed solution. Briefly, 7mM ZnO nanoparticles was dissolved in 20 ml of ethanol and then the mixture was vigorously stirred at room temperature for 15 min to form a homogenous solution. Next, the seed solution was spin-coated onto Si substrate at 3000 rpm for 30 s. ZnO NFs were subsequently grown from these seeds by hydrothermal growth process. An equimolar aqueous solution (3 mM) of Zinc Nitrate Hexahydrate ($Zn(NO_3)_2.6H_2O$) and HexamethylTetramine (HMTA) ($C_6H_{12}N_4$) were used as precursors and the growth was then carried out in a convection oven at 70 ^{0}C for 24 hrs. All precursors/solvents were purchased from Sigma-Aldrich with purity of 99%. Later, the grown ZnO NFs were thoroughly rinsed with (DI) and dried naturally.

8. 3. 1. 2 Synthesis of branched ZnO NFs

The next step was to grow nanowire branches on the nanoflower trunk, so another coating solution was made by dissolving 40 ml of 5mM zinc acetate dihydrate ($C_4H_6O_4Zn \cdot 2H_2O$) in methanol at 60 °C under vigorous stirring. This solution was recoated on the main NFs by modified seeding technique called forced seeding approach (Sun, Li et al. 2014). In this technique, the seed solution was first heated above the boiling point of methanol on a hot plate and subsequently the boiling mixture was drop casted on the cold substrate containing the main NFs. The seed particles were forced to be attached on the backbone of nanoflower when solution dry out and then the coated NFs were rinsed with ethanol and heated to 350 °C for 30 min. After the heating step, a fresh nutrient solution was utilized to grow the branches on ZnO NFs. The XRD.

morphologies and dimensions of branched ZnO NFs were characterized using SEM and their phases were analysed using XRD.

8. 3. 2. Result and discussion

The growth mechanism of the branched ZnO NFs is demonstrated in Figure 8. 11 and their counterparts are shown by SEM images in Figure 8. 12. Non-branched nanowires were grown perpendicularly on ZnO-seeded silicon substrate.

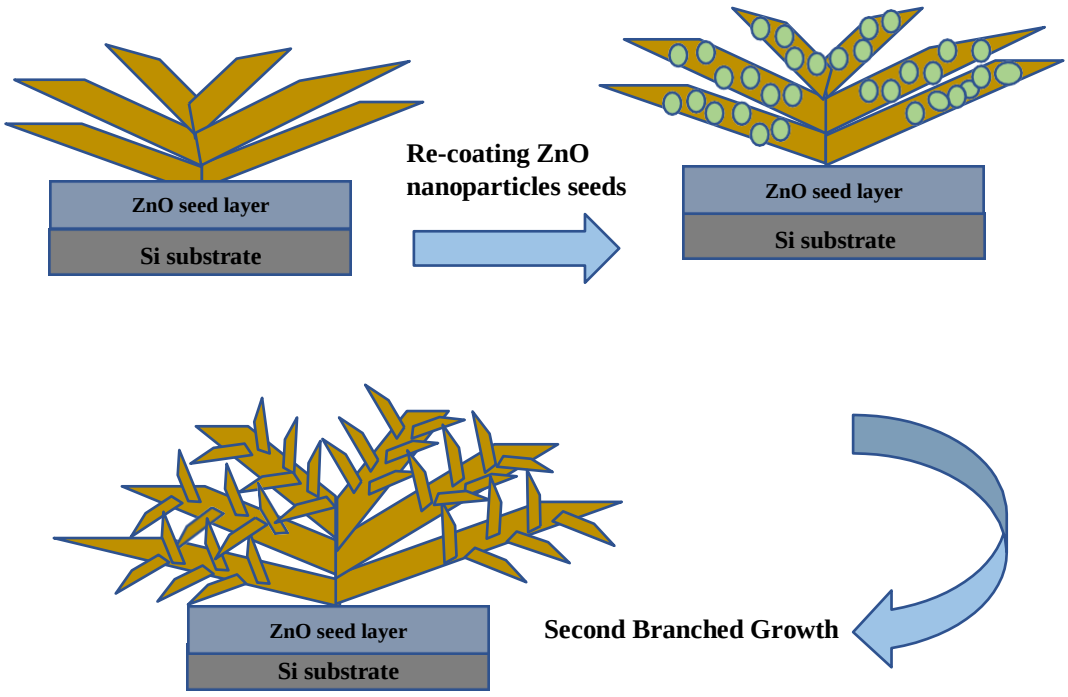

Figure 8. 11. The schematic synthesis process from the main ZnO NFs to the branched ZnO NFs.

As the seeding mixture was drop-casted onto the previously grown ZnO NFs, it is more likely to adhere on the sidewalls of the trunk to assist the next branched synthesis.

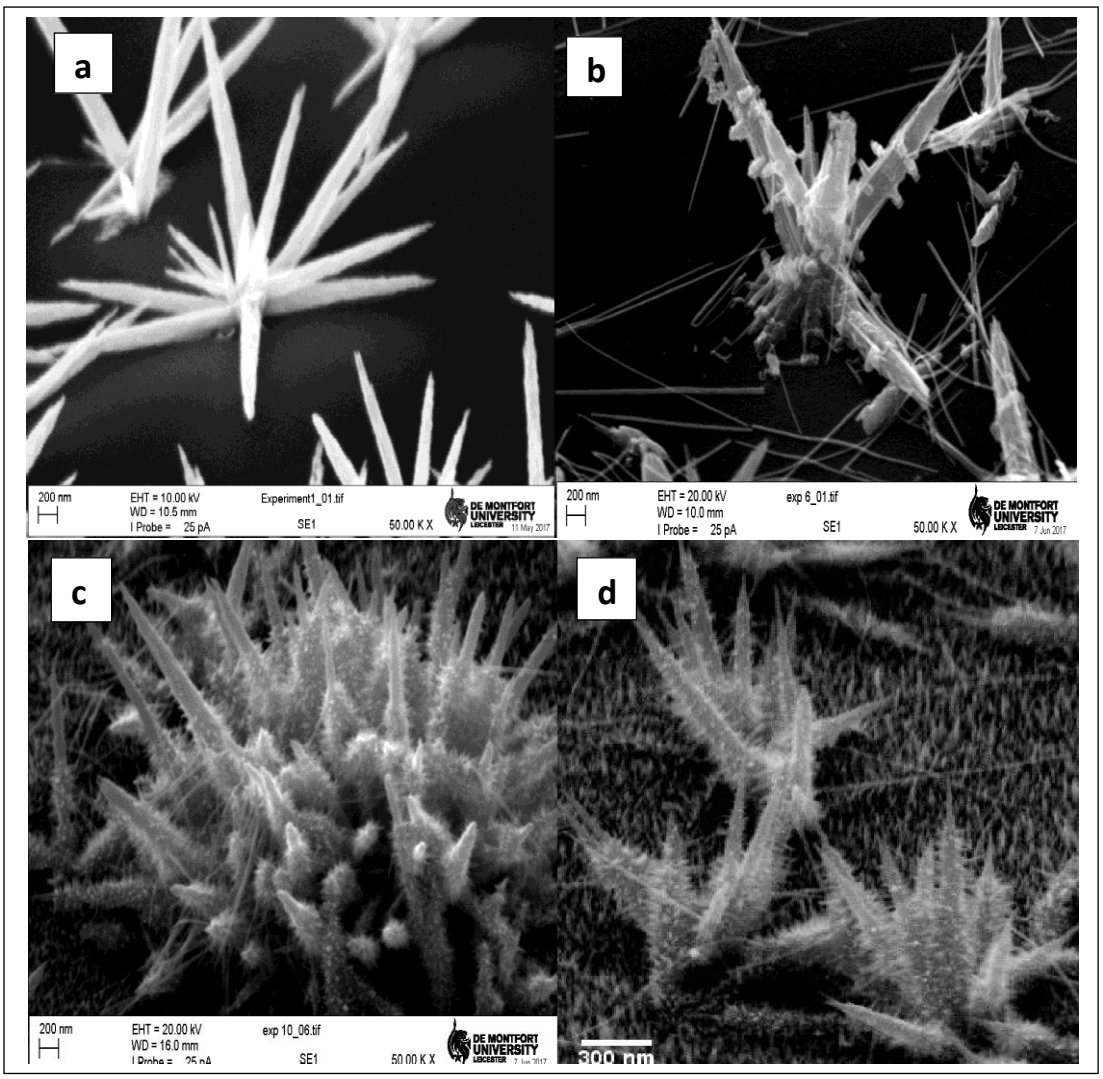

Figure 8. 12. SEM images of (a) Bare ZnO NFs. (b) ZnO NFs coated by a seed solution. (c) and (d) Branched ZnO NFs at low and high magnifications.

After the recoating of ZnO seed solution on the hydrothermally grown NFs, small crystalline particles were attached to serve as a nucleation sites for the secondary branched growth. These secondary branched nanowires were not generated from the main backbone NFs but from the ZnO seed nanoparticles in the c axis direction of single crystal wurtzite structure (Ko, Lee et al. 2011). The diameter and length of the main flowers and branches are determined by Image J package, the backbone NFs have an average length of 1-1.5 µm and

diameter of 100-150 nm. While the average length and diameter of small branches were ≈ 60 nm and ≈ 20 nm respectively. Branch length can be controlled by the experimental parameters such as, growth time, growth temperature and reagent concentration.

During the recoating step of nanoflower trunk by the forced seeding technique, it was observed that heating the substrate containing ZnO NFs and drop casting the seed solution do not lead to produce the branches. This could be attributed to the reason that, due to ZnO nanoparticles randomly distributed on a hot substrate surface it is more likely to be adsorbed by ZnO nucleation layer and start growing wires on a substrate and not attaching on the side walls of nanoflower. In contrast, the branches successfully grown on the nanoflower trunk when the seed solution was heated and drop casted on the substrate at room temperature. That is presumably because of ZnO nanoparticles could first attach on the side walls of the nanoflower and initiate the branches growth. However, there was still a lack of uniformity of subsequently grown branches which may attributed to the uncontrolled forced coating process as seed particles inconsistently disturbed in all spaces on the substrate.

In addition, it was clearly observed that some of the seed particles were settled down between ZnO NFs then, these particles will randomly introduce new nanowires when the hydrothermal growth step was performed to produce the branches as can be seen in the SEM image in Figure 8. 12. Therefore, the uncontrolled growth of seed particles that randomly spread out between the main trunk can significantly affect the morphology of ZnO NFs and restrict their performance in various applications.

8. 3. 3. Growth mechanisms of ZnO NFs

In the present work, the synthesis of ZnO NFs was performed without introducing shape agents, such as surfactants, additives or dopants, in the reaction system. However, HMTA was used which may act as structure directing agent by significantly promoting the axial growth of ZnO non-polar facets and suppressing the radial growth along these planes (Parize, Garnier et al. 2016). The non-polar surfaces of ZnO crystal neutrally comprise of Zn^{2+} and O^{2-} ions. The restriction of the progression of these surfaces could be achieved by different physicochemical interactions, such as the development of covalent and hydrogen bonding or surface-adsorbates electrostatic interactions (Parize, Garnier et al. 2016). The anisotropic growth of ZnO nanostructures arises from the variation in the surface free energy between the [10 1 0] and the [0 0 0 1] ZnO faces. The [1 0 1 0] surface is neutral; hence it has a lower surface energy than the charged [0 0 0 1] surface (McPeak, Le et al. 2011). The driving force of the Crystal growth is to reduce the free energy of the high-energy surfaces (0 0 0 1), leading to an anisotropic growth of ZnO crystal along the c axis.

The whole growth process of NFs is mainly classified into two stages: crystal nucleation and crystal growth. The hydrothermal growth process is mostly driven by the supersaturation conditions which significantly depend on the amount of Zn^{2+} and OH^- ions available in the aqueous solution during the growth process. As the hydrothermal reaction proceeded, the variation in the ratio of Zn^{2+} and OH^- ions can change the growth rates along ZnO surfaces, therefore different morphologies will be grown. Under thermodynamic control, HMTA dissolve to produce ammonia which reacts with water to produce OH^-.

Then under intermolecular absorption forces Zn complexes that serve as growth units generate by the interaction between $Zn(OH)_2$ and OH^-. At the initial stage, a high concentration of growth units is sufficient to combine into ZnO nucleus of the seed layer and dehydrate to produce ZnO crystals at several positions of the interface surface, therefore a different size of ZnO NFs grow anisotropically on the substrate surface. A possible explanation for the size-variation of NFs is that the concentration of growth units is much higher than that of the ZnO nuclei, many of these growth units can directly accumulate to the surface of each single ZnO nucleus and then each growth unit initiates a single crystal which subsequently develops to form a wurtzite structured with tapered tip wire. As a result, a large-sized ZnO nanoflower with multi-wires grown from the same nucleation site forms (Figure 8. 13). With the reaction proceeding, the ions concentration and their activity in the hydrothermal solution gradually decline, so small amount of growth units can connect with ZnO nucleus, resulting in formation of a small ZnO nanoflower with a few numbers of wires.

The aqueous chemistry of reagents and the time-dependent nature of the hydrothermal growth process strongly guide the synthesis of ZnO structure. Depending on the physiochemical interactions at different supersaturation levels of the reaction, different dimension and/or morphologies can grow, e.g. the diameter of the ZnO nanowires was relatively uniform near the base of the wire as the reaction proceeded the diameter becomes narrower leading to the formation of the tapered tip wires.

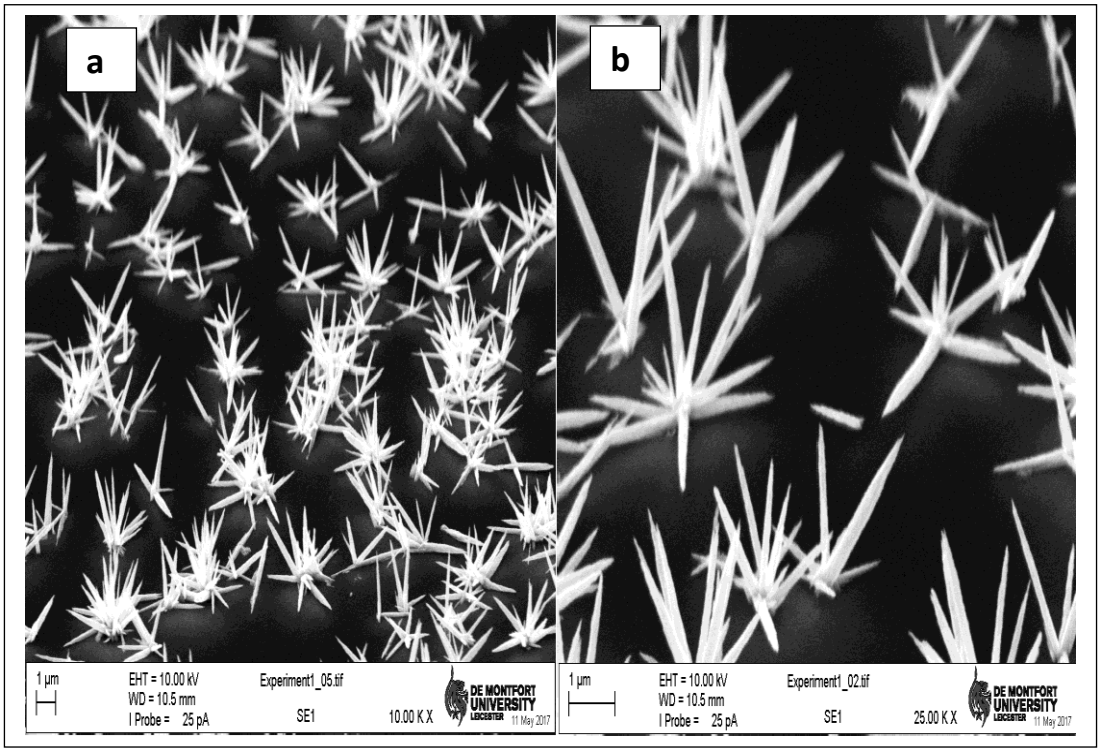

Figure 8. 13. (a) Low magnification and (b) high magnification SEM image of the ZnO NFs obtained by solution-based process.

The crystal structure of ZnO NFs was investigated by XRD analysis (Figure 8. 14), it displayed peaks matching to ZnO hexagonal wurtzite (100), (002), (100) and (103) phases which were well-indexed with the JCPDS No. 36-1451 (Bel Hadj Tahar, Bel Hadj Tahar et al. 2008). Apart from silicon peak (211), the XRD pattern further proves the absence of other impurities or secondary phases other than ZnO peaks. The peaks corresponding to (100), (002), and (110) planes were weak, while the (103) plane had the most

intense and narrowest peak. The preferred (103) peak indicates that the NFs are well crystallized and grow in the [103] direction and its intensity is 1248 au, which further confirms the high quality of the crystalline structure.

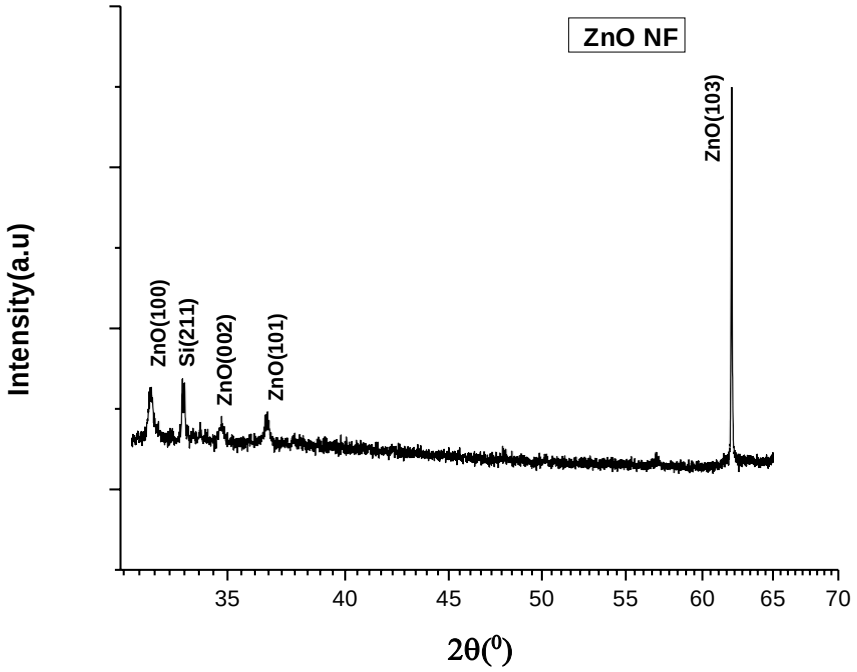

Figure 8. 14. XRD pattern of ZnO NFs synthesized by solution-based method.

In contrast, to the previously reported ZnO nanowire diffraction pattern (chapters 5 and 6), in which (100), (002), and (101) peaks were comparatively dominant. In the fabrication process of those results Au catalyst was deposited onto a Si substrate by RF sputtering to serve as a seed layer consequently, the nanowires showed the [002] orientation. While, here ZnO nanoparticles were deposited onto a Si substrate using spin-coating method hence [103] oriented ZnO nanoflower arrays were observed. The preferential orientation has been observed by several authors studying the fabrication of ZnO nanostructures by different

methods (Yong, Xian et al. 2013, Eranna 2011). It could indicate that the preferred orientation in NFs dependent upon the type of catalyst layer and the deposition methods used (Serrano, Arana et al. 2017). In addition, this result of selectively oriented NFs may confirm a correlation between the ZnO morphology and its preferred orientation.

In summary, (3D) NFs and branched NFs of ZnO were grown on silicon substrate using simple and low-cost solution growth method incorporating seed ZnO nanoparticles deposition. A modified forced seeding technique was applied to form the branched ZnO NFs. Based on a review of literature and the observations of the current work, the proposed growth mechanism was interpreted. The XRD profile reveals high crystalline and well aligned ZnO NFs along [103] orientation which indicates that the NFs are selectively oriented. Such 3D flower structure terminated by branches, could potentially exploit in future nanoscale devices and applications.

As it was mentioned earlier the main aim of this thesis is to investigate the potential feasibility of ZnO nanostructures to act as biomolecules-delivery tools. Therefore, in the following chapter all outcomes obtained through the framework of the thesis were integrated for cellular investigation to study the potential application of ZnO nanostructures as a gene delivery platform in different expression systems.

References

BEL HADJ TAHAR, N., BEL HADJ TAHAR, R., BEN SALAH, A. and SAVALL, A., 2008. Effects of Individual Layer Thickness on the Microstructure and Optoelectronic Properties of Sol–Gel-Derived ZnO Thin Films. *Journal of the American Ceramic Society,* **91**(3), pp. 846-851.

CHENG, B., LE, Y., CAI, W. and YU, J., 2011. Synthesis of hierarchical Ni (OH) 2 and NiO nanosheets and their adsorption kinetics and isotherms to Congo red in water. *Journal of hazardous materials,* **185**(2), pp. 889-897.

CHENG, H., CHIU, W., LEE, C., TSAI, S. and HSIEH, W., 2008. Formation of branched ZnO nanowires from solvothermal method and dye-sensitized solar cells applications. *The Journal of Physical Chemistry C,* **112**(42), pp. 16359-16364.

CHETIA, T.R., ANSARI, M.S. and QURESHI, M., 2016. Rational design of hierarchical ZnO superstructures for efficient charge transfer: mechanistic and photovoltaic studies of hollow, mesoporous, cage-like nanostructures with compacted 1D building blocks. *Physical Chemistry Chemical Physics,* **18**(7), pp. 5344-5357.

DESAI, M.A. and SARTALE, S., 2015. Facile soft solution route to engineer hierarchical morphologies of ZnO nanostructures. *Crystal Growth & Design,* **15**(10), pp. 4813-4820.

DILGER, S., WESSIG, M., WAGNER, M.R., REPARAZ, J.S., SOTOMAYOR TORRES, C.M., QIJUN, L., DEKORSY, T. and POLARZ, S., 2014. Nanoarchitecture Effects on Persistent Room Temperature

Photoconductivity and Thermal Conductivity in Ceramic Semiconductors: Mesoporous, Yolk–Shell, and Hollow ZnO Spheres. *Crystal Growth & Design,* **14**(9), pp. 4593-4601.

ERANNA, G., 2011. *Metal oxide nanostructures as gas sensing devices.* CRC Press.

FAN, F., TANG, P., WANG, Y., FENG, Y., CHEN, A., LUO, R. and LI, D., 2015. Facile synthesis and gas sensing properties of tubular hierarchical ZnO self-assembled by porous nanosheets. *Sensors and Actuators B: Chemical,* **215**, pp. 231-240.

FANG, F., LV, S., FANG, X., ZHAO, H., LI, J., CHU, X., WEI, Z., FANG, D. and WANG, X., 2015. Growth Mechanism and Properties of Multibranched ZnO Nano/Microstructure. *Integrated Ferroelectrics,* **164**(1), pp. 60-66.

HANNON, J., KODAMBAKA, S., ROSS, F. and TROMP, R., 2006. The influence of the surface migration of gold on the growth of silicon nanowires. *Nature,* **440**(7080), pp. 69-71.

HATA, K., FUTABA, D.N., MIZUNO, K., NAMAI, T., YUMURA, M. and IIJIMA, S., 2004. Water-assisted highly efficient synthesis of impurity-free single-walled carbon nanotubes. *Science (New York, N.Y.),* **306**(5700), pp. 1362-1364.

KO, S.H., LEE, D., KANG, H.W., NAM, K.H., YEO, J.Y., HONG, S.J., GRIGOROPOULOS, C.P. and SUNG, H.J., 2011. Nanoforest of hydrothermally grown hierarchical ZnO nanowires for a high efficiency dye-sensitized solar cell. *Nano letters,* **11**(2), pp. 666-671.

KRISHNAPRIYA, R., PRANEETHA, S. and MURUGAN, A.V., 2016. Investigation of the effect of reaction parameters on the microwave-assisted hydrothermal synthesis of hierarchical jasmine-flower-like ZnO nanostructures for dye-sensitized solar cells. *New Journal of Chemistry,* **40**(6), pp. 5080-5089.

KUDO, A. and MISEKI, Y., 2009. Heterogeneous photocatalyst materials for water splitting. *Chemical Society Reviews,* **38**(1), pp. 253-278.

LAO, J.Y., WEN, J.G. and REN, Z.F., 2002. Hierarchical ZnO nanostructures. *Nano Letters,* **2**(11), pp. 1287-1291.

LI, C.C., YIN, X.M., LI, Q.H. and WANG, T.H., 2011. Enhanced gas sensing properties of ZnO/SnO 2 hierarchical architectures by glucose-induced attachment. *CrystEngComm,* **13**(5), pp. 1557-1563.

LI, F., GONG, F., XIAO, Y., ZHANG, A., ZHAO, J., FANG, S. and JIA, D., 2013. ZnO twin-spheres exposed in±(001) facets: stepwise self-assembly growth and anisotropic blue emission. *ACS nano,* **7**(12), pp. 10482-10491.

LIMO, M.J., RAMASAMY, R. and PERRY, C.C., 2015. ZnO binding peptides: smart versatile tools for controlled modification of ZnO growth mechanism and morphology. *Chemistry of Materials,* **27**(6), pp. 1950-1960.

LIU, G., WANG, T., ZHANG, H., MENG, X., HAO, D., CHANG, K., LI, P., KAKO, T. and YE, J., 2015. Nature-Inspired Environmental “Phosphorylation” Boosts Photocatalytic H2 Production over Carbon Nitride Nanosheets under Visible-Light Irradiation. *Angewandte Chemie,* **127**(46), pp. 13765-13769.

LIU, S., LI, C., YU, J. and XIANG, Q., 2011. Improved visible-light photocatalytic activity of porous carbon self-doped ZnO nanosheet-assembled flowers. *CrystEngComm,* **13**(7), pp. 2533-2541.

LIU, Y., GOEBL, J. and YIN, Y., 2013. Templated synthesis of nanostructured materials. *Chemical Society Reviews,* **42**(7), pp. 2610-2653.

LU, P. and XUE, D., 2011. ZnO 3D-Superstructures via Two-Step Assembly at Gas/Liquid Interface. *Nanoscience and Nanotechnology Letters,* **3**(3), pp. 429-433.

MAITI, S., PAL, S. and CHATTOPADHYAY, K.K., 2015. Recent advances in low temperature, solution processed morphology tailored ZnO nanoarchitectures for electron emission and photocatalysis applications. *CrystEngComm,* **17**(48), pp. 9264-9295.

MCCUNE, M., ZHANG, W. and DENG, Y., 2012. High efficiency dye-sensitized solar cells based on three-dimensional multilayered ZnO nanowire arrays with “caterpillar-like” structure. *Nano letters,* **12**(7), pp. 3656-3662.

MCPEAK, K.M., LE, T.P., BRITTON, N.G., NICKOLOV, Z.S., ELABD, Y.A. and BAXTER, J.B., 2011. Chemical bath deposition of ZnO nanowires at near-neutral pH conditions without hexamethylenetetramine (HMTA): understanding the role of HMTA in ZnO nanowire growth. *Langmuir,* **27**(7), pp. 3672-3677.

PACHAURI, V., KERN, K. and BALASUBRAMANIAN, K., 2010. Template-free self-assembly of hierarchical ZnO structures from nanoscale building blocks. *Chemical Physics Letters,* **498**(4), pp. 317-322.

PARIZE, R., GARNIER, J., CHAIX-PLUCHERY, O., VERRIER, C., APPERT, E. and CONSONNI, V., 2016. Effects of hexamethylenetetramine on the nucleation and radial growth of ZnO nanowires by chemical bath deposition. *The Journal of Physical Chemistry C,* **120**(9), pp. 5242-5250.

SERRANO, A., ARANA, A., GALDÁMEZ, A., DUTT, A., MONROY, B., GÜELL, F. and SANTANA, G., 2017. Effect of the seed layer on the growth and orientation of the ZnO nanowires: Consequence on structural and optical properties. *Vacuum,* .

SHI, Y., ZHU, C., WANG, L., ZHAO, C., LI, W., FUNG, K.K., MA, T., HAGFELDT, A. and WANG, N., 2013. Ultrarapid sonochemical synthesis of ZnO hierarchical structures: from fundamental research to high efficiencies up to 6.42% for quasi-solid dye-sensitized solar cells. *Chemistry of Materials,* **25**(6), pp. 1000-1012.

SINHA, A.K., BASU, M., PRADHAN, M., SARKAR, S. and PAL, T., 2010. Fabrication of Large-Scale Hierarchical ZnO Hollow Spheroids for Hydrophobicity and Photocatalysis. *Chemistry–A European Journal,* **16**(26), pp. 7865-7874.

STAN, A., MUNTEANU, C., MUSUC, A.M., BIRJEGA, R., ENE, R., IANCULESCU, A., RAUT, I., JECU, L., DONI, M.B. and ANGHEL, E.M., 2015. A general, eco-friendly synthesis procedure of self-assembled ZnO-based materials with multifunctional properties. *Dalton Transactions,* **44**(17), pp. 7844-7853.

STEIN, A., LI, F. and DENNY, N.R., 2007. Morphological control in colloidal crystal templating of inverse opals, hierarchical structures, and shaped particles. *Chemistry of Materials,* **20**(3), pp. 649-666.

SUN, X., LI, Q., JIANG, J. and MAO, Y., 2014. Morphology-tunable synthesis of ZnO nanoforest and its photoelectrochemical performance. *Nanoscale,* **6**(15), pp. 8769-8780.

WANG, D., DU, S., ZHOU, X., WANG, B., MA, J., SUN, P., SUN, Y. and LU, G., 2013. Template-free synthesis and gas sensing properties of hierarchical hollow ZnO microspheres. *CrystEngComm,* **15**(37), pp. 7438-7442.

WANG, D. and LIEBER, C.M., 2003. Inorganic materials: nanocrystals branch out. *Nature materials,* **2**(6), pp. 355-356.

WANG, J., HOU, S., ZHANG, L., CHEN, J. and XIANG, L., 2014. Ultra-rapid formation of ZnO hierarchical structures from dilution-induced supersaturated solutions. *CrystEngComm,* **16**(30), pp. 7115-7123.

WANG, X., ZHANG, Q., WAN, Q., DAI, G., ZHOU, C. and ZOU, B., 2011. Controllable ZnO architectures by ethanolamine-assisted hydrothermal reaction for enhanced photocatalytic activity. *The Journal of Physical Chemistry C,* **115**(6), pp. 2769-2775.

WANG, X., LIU, W., LIU, J., WANG, F., KONG, J., QIU, S., HE, C. and LUAN, L., 2012. Synthesis of nestlike ZnO hierarchically porous structures and analysis of their gas sensing properties. *ACS applied materials & interfaces,* **4**(2), pp. 817-825.

WANG, Z., TIAN, Z., HAN, D. and GU, F., 2016. Highly sensitive and selective ethanol sensor fabricated with in-doped 3DOM ZnO. *ACS applied materials & interfaces,* **8**(8), pp. 5466-5474.

WANG, Z.L. and ZHOU, W., 2011. *Three-dimensional Nanoarchitectures: Designing Next-generation Devices.* Springer.

WU, Q., CHEN, X., ZHANG, P., HAN, Y., CHEN, X., YAN, Y. and LI, S., 2008. Amino acid-assisted synthesis of ZnO hierarchical architectures and their novel photocatalytic activities. *Crystal Growth and Design,* **8**(8), pp. 3010-3018.

WU, W., FENG, H., RAO, H., XU, Y., KUANG, D. and SU, C., 2014. Maximizing omnidirectional light harvesting in metal oxide hyperbranched array architectures. *Nature communications,* **5**.

XIA, Y., WANG, J., CHEN, R., ZHOU, D. and XIANG, L., 2016. A Review on the Fabrication of Hierarchical ZnO Nanostructures for Photocatalysis Application. *Crystals,* **6**(11), pp. 148.

XU, F., DAI, M., LU, Y. and SUN, L., 2010. Hierarchical ZnO nanowire–nanosheet architectures for high power conversion efficiency in dye-sensitized solar cells. *The Journal of Physical Chemistry C,* **114**(6), pp. 2776-2782.

XU, X., WU, M., ASORO, M., FERREIRA, P. and FAN, D., 2012. One-step hydrothermal synthesis of comb-like ZnO nanostructures. *Crystal growth & design,* **12**(10), pp. 4829-4833.

YAN, S.C., OUYANG, S.X., GAO, J., YANG, M., FENG, J.Y., FAN, X.X., WAN, L.J., LI, Z.S., YE, J.H. and ZHOU, Y., 2010. A Room-Temperature Reactive-Template Route to Mesoporous ZnGa2O4 with Improved Photocatalytic Activity in Reduction of CO2. *Angewandte Chemie,* **122**(36), pp. 6544-6548.

YANG, M., SUN, K. and KOTOV, N.A., 2010. Formation and assembly–disassembly processes of ZnO hexagonal pyramids driven by dipolar and excluded volume interactions. *Journal of the American Chemical Society,* **132**(6), pp. 1860-1872.

YANG, S.J., IM, J.H., KIM, T., LEE, K. and PARK, C.R., 2011. MOF-derived ZnO and ZnO@ C composites with high photocatalytic activity and adsorption capacity. *Journal of hazardous materials,* **186**(1), pp. 376-382.

YONG, Z., XIAN, C., LIGUANG, F., LIANFANG, Y., HUIHUI, L. and YUEFEI, G., 2013. Effects of Annealing on the Structural and Photoluminescent Properties of Ag-Doped ZnO Nanowires Prepared by Ion Implantation. *Plasma Science and Technology,* **15**(8), pp. 817.

ZHANG, T., DONG, W., KEETER-BREWER, M., KONAR, S., NJABON, R.N. and TIAN, Z.R., 2006. Site-specific nucleation and growth kinetics in hierarchical nanosyntheses of branched ZnO crystallites. *Journal of the American Chemical Society,* **128**(33), pp. 10960-10968.

ZHANG, W., ZHANG, D., FAN, T., DING, J., GUO, Q. and OGAWA, H., 2006. Morphosynthesis of hierarchical ZnO replica using butterfly wing scales as templates. *Microporous and mesoporous materials,* **92**(1), pp. 227-233.

ZHAO, X. and QI, L., 2012. Rapid microwave-assisted synthesis of hierarchical ZnO hollow spheres and their application in Cr (VI) removal. *Nanotechnology,* **23**(23), pp. 235604.

Chapter 9

ZnO Nanostructures for Gene Delivery Applications

9. 1. Introduction

The evolution of sophisticated new experimental methods and tools of nanotechnology has been exploited in cell biology research for a number of applications. The dimensions of semiconductor nanowires are smaller than that of cells, and hence the nanowires can act as a probe tip to pierce and disturb the function of the cell membrane. Such a benefit of nanowires allows them to be an applicable system for sensing and engineering cells with minimum perturbation (Rahong, Yasui et al. 2016). Furthermore, nanowires can be utilized as devices which are capable of recording and stimulating the variations of electrical and chemical signals in living cells and tissues (Rahong, Yasui et al. 2016).

Promising studies have been reported that ZnO nanostructures are an effective platform to accelerate different biological processes, eventually resulting in the generation of new living tissue useful for organ repair (Laurenti, Cauda 2017). In this work, the aim is to demonstrate Proof of concept (POC) studies to discover how efficient ZnO nanostructures could be on the transformation process of the yeast cells. This an early stage of studies will show the feasibility of the potential application of ZnO nanomaterials as a gene-delivery tool to transfer foreign DNA to the host cells for expressing different proteins. This evidence for proof of concept will allow to involve more complex expression system like mammalian cells.

In the current chapter, the potential applications of ZnO nanostructures as a gene delivery/-tissue engineering tool in different expression systems is illustrated. In addition, a comparative study between various heterologous expression systems (yeast cells / Chinese hamster ovary (CHO)) for expressing of cytochromes 2D6, pMax GFP and P450 is discussed. Also, Limitations of the expression systems are discussed and possibilities to enhance the expression productivity are suggested.

9. 2. Yeast expression system

Enormous attention has been paid for Yeast *Saccharomyces cerevisiae* (baker's yeast), due to its role as a powerful eukaryotic species to investigate basic biological procedures such as aging (Bitterman, Medvedik et al. 2003), transport of mRNA proteins (Müller, Heuck et al. 2007), the cell division cycle (Breeden 2003), etc. In addition, yeast was widely used as a means for pharmaceutical (Menacho-Marquez, Murguia 2007), virus (Galao, Scheller et al. 2007), and ecotoxicology (Teixeira, Duque et al. 2007) studies. It also acts as a model organism to investigate cancer diseases (Yuen, Montpetit et al. 2005).

Furthermore, yeast has served as an effective host organism to synthesize recombinant pharmaceutical proteins (Porro, Sauer et al. 2005) Because of its intrinsic tolerance of low pH values and high concentrations of sugar and ethanol, i.e., properties that minimise the possibility of contamination in fermented products. Moreover, its resistance to inhibitors present in biomass hydrolysates and ability to be grown to high density enable it to be extensively involved in physiology, biochemistry, genetic engineering and fermentation technologies.

All these features make yeast a cost-effective and powerful substitute tool to express CYP450 proteins compared to mammalian expression platform (Pandey, Shin et al. 2016). It was also shown that CYP450 spectra can easily be demonstrated in the microsomes extracted from whole cell preparation (Johnston, Huang et al. 2008). The CYP450 mainly acts as oxidative catalyst in the metabolism of several endogenous and exogenous substances. CYP450 also participates in production of different hormones and affects hormone-related cancers, therefore it plays a critical role in anticancer drugs and treatment (Mittal, Tulsyan et al. 2015). Commonly, Yeast was extensively used for heterologous expression of mammalian CYP450 enzymes and has been shown to be productive for expressing different eukaryotic proteins (Nasser, Pooja et al. 2003). An expression of foreign proteins in yeast was first reported by Ohkawa et al (Çelik, Çalık 2012), while an expression of mammalian CYP450 proteins in the yeast was first studied by Oeda et al (Oeda, SAKAKI et al. 1985). They produced active CYP1A1 protein by using recombinant CYP1A1 gene and the yeast endogenous NADPH-P450 reductase gene (Oeda, SAKAKI et al. 1985). In comparison to bacterial cell culture, the yeast cell effects a cellular structure similar to mammalian cells, as it contains endoplasmic reticular (microsomal) membranes to which CYP450 proteins can be anchored (Hauri, Schweizer 1997). It is believed that to obtain high catalytic activity of mammalian CYP450 in the yeast heterologous expression platform, it is necessary to co-express mammalian P450 reductase and a mammalian CYP450 as the host yeast endogenous reductase combines poorly with mammalian CYP450 (Pompon, Louerat et al. 1996).

It is difficult to express various mammalian P450s in yeast a heterologous expression platform, however this obstacle can be dealt with by redesigning the DNA sequences to maximize the chance of high protein expression. Episomal and integrated vectors have been successfully employed for efficient cloning and expression of various genes in yeast. Different promotors include constructive and inducible have been also used for gene expression in yeast e.g. gene overexpression can be obtained by adding a strong promoter upstream of the gene of interest which can boost the expression level (Nevoigt 2008).

9. 2. 3. Materials and methods

9. 2. 3. 1. Preparation L-B Agar for growing bacteria cells

A plasmid is a circular non-chromosomal segment of DNA that exists in some bacteria. Biologists can manipulate in an Eppendorf tube and introduce these synthetic plasmids into bacteria. These artificial plasmids are used as a vector to replicate or express the gene or DNA sequences of interest that have been inserted into the plasmids. Plasmids are introduced into bacteria through a process called transformation. Although bacteria transformation is far from 100% efficient antibiotic selection can be used to select for the cells carrying the plasmid of interest. It is very efficient since bacteria replicate plasmid DNA before each cell division and since some plasmids are present in several copies per cell, a simple overnight culture of bacteria can yield vast number of plasmid DNA molecules, for this reason, bacteria cells can serve as a factory for making a large amount of plasmid DNA and the DNA sequences of interest (Rosano, Ceccarelli 2014).

L-B Agar Liquid media is the most widely used rich medium that contains nutrients required for the culture and growth of individual bacteria colonies. One of these nutrients is agar which is solidifying agent can form a gel that bacteria are unable to digest but can grow on it. In general, to prepare a one litre gel mixture 25 g of L-B agar powder has to be measured out. Here, 5 g of L-B broth powder was measured and added to 200 ml of sterile water, the bottle then was swirled to form a colloid solution. It is important to do not make the seal air-tight as it can cause cracking during the sterilization process. Next, the bottle was labelled by autoclave tape which darkens indicating the solution has been at 121^0 C for over 20 minutes in the autoclave under pressure.

Finally, L-B agar colloid was placed in the autoclave and autoclaved to 121^0 C under 20 psi for 30 minutes. The high pressure is necessary to enhance the sterilisation process at elevated temperatures. Once the autoclave cycle is complete, L-B agar media was cooled down prior to adding 100 μg/ml; of ampicillin to it. The agar bottle then was swirled to insure homogeneous distribution of the ampicillin throughout the L-B agar. The addition of an antibiotic resistance gene on a plasmid enables scientists to easily separate bacteria including that plasmid from bacteria that do not include it by artificial selection (i.e. growing the bacteria in the presence of the antibiotic of interest) (Lodish, Berk et al. 2000).

9. 2. 3. 2. Streak out bacteria cells

The streak plate process is a pure culture technique that allows an isolation of the desired colonies form contaminants. To streak bacteria cells, first the appropriate number of plates were labelled by the date, the including culture medium, the identity of bacteria cells (E. coli strain DH 5 α) and the antibiotic (ampicillin 100ug/ml). Approximately 20 ml of molten agar was gently poured into each sterile plate and then allowed them to solidify (nearly 10-15 minutes) on the bench. Next, the poured plates were inverted (so that the agar side of the plate base is above, and the lid is down) in the incubator room at 37^0 C for 10 minutes. The streaking process was started by sterilizing a wire loop in flame until glowing red then allowed it to fully cool by standing for a few seconds. Next the sterile loop was dipped into the overnight microbial culture and picked up a loopful of bacteria cells.

These bacteria gently spread back and forth across the surface of the labelled plate. During the streaking process, many bacteria fall off from the loop and land on the agar surface by making a uniform smear with the inoculum at the edge of the plate. After finishing the first phase, the loops were sterilized to kill microorganisms and carry out the next phase by making streaks away from the original inoculums. Since there is thinning of inoculum through repeating streaking motion, isolated colonies are formed at ideal streak point where the spreading has separated the individuals of bacteria cells at positions where they can make single colonies. After streaking, the plate was incubated overnight at 37^0 C. In the incubation process, the microbial organisms multiply and assemble to produce colonies which can be clearly seen by naked eye.

9. 2. 3. 3. Isolation of Plasmid DNA

During different cloning methods it is essential to transfer the gene of interest from one plasmid to another through a process known as transformation. In order to extract plasmid DNA from bacteria, biologists use a plasmid isolation kit, it is also known as a plasmid miniprep kit which consists of a variety of buffers and columns that bind to the plasmid DNA to purify it. There are different methodologies for extracting plasmid DNA from bacteria culture, these methodologies are ranging from commercial purification kits provided by manufactures such as QIAGEN or via crude methodology such as alkaline lysis protocols.

Here, these two protocols were applied for the purification of plasmid DNA. Each method is demonstrated in the following subsections. Initially, the bacterial cell culture has to grow, so approximately 200 ml of L-B broth media was mixed with 200 µl of ampicillin to maintain a selection. Then, nearly 10 ml of L-B broth medium containing the selective antibiotics was transferred to autoclave vessels that were labelled with the appropriate details. Next, a single colony of freshly streaked selective plate cultures were picked up by flamed loop and dipped into sterile vessels containing the broth and ampicillin. The vessels were incubated overnight at 37^0 C with vigorous shaking (approximately 220 rpm).

9. 2. 3. 3. 1. Extraction of plasmid DNA by the alkaline lysis

The protocol to carry out the experiment was adapted from Molecular Cloning (Sambrook, Russell 2001). It began with an overnight liquid culture of transformed bacteria carrying the desired plasmid. First, 1.5 ml sterile Eppendorf tubes were twice filled with the overnight culture. The Eppendorf tubes were placed in a microfuge with the hinge facing out so that the pellet will always be located on the hinge side wall nearby the bottom. A spin for 1 minute at a speed of 8000 rpm was applied to produce a pellet of the bacterial cells of interest. The supernatant was discarded, at this stage it was required to add extra culture media and spin again if a small pellet was produced which indicates a poor culture growth. The pellet was resuspended in 100 µl of solution 1 and at this point it was important to ensure the cells were entirely resuspended to avoid forming insoluble clumps at the next lysis step. Then, 200 µl of solution 2 was added and gently mixed until the solution becomes almost clear.

The neutralisation step was performed by adding 150 µl of solution 3, the bacterial lysate was allowed to precipitate on ice for 10 minutes. Then, a spin at 13000 rpm for 5 minutes was performed. The supernatant was transferred to a fresh tube without disturbing the pellet. To precipitate the plasmid DNA, approximately one volume of room temperature isopropanol was added to the supernatant. The supernatant was centrifuged at speed of 10000 rpm for 10 minutes, then it was carefully decanted. The DNA pellet was washed with 1 ml of 70 % ethanol and centrifuged again at speed of 10000 rpm for 10 minutes. The supernatant was gently decanted without disturbing the pellet and dried in air for 5-10 minutes.

Finally, the DNA pellet was re-dissolved in an appropriate volume of deionised water (45-50 µl) and stored at -20^0 C. Table 9. 1 demonstrates all reagents which were used in the alkaline lysis protocol. Solutions 1 and 3 were stored at 4^0 C, while solution 2 was stored at room temperature.

Table 9. 1. All reagents used in the alkaline lysis protocol.

Solution 1	Solution 2	Solution 3
Glucose 50 mM	1% SDS (sodium dodecylsulphate)	5M potassium acetate (KAc)
Tris 25 mM (PH 8)		
EDTA 10 mM (PH 8)	0.2 N NaOH (sodium hydroxide)	Glacial acetic acid

9. 2. 3. 3. 2. Extraction of plasmid DNA by Qiagen

The Qiagen protocol was also performed to extract plasmid DNA of interest from bacterial cultures. This methodology is usually based on the modified alkaline lysis process and comprised of three main steps: (1) preparation of bacterial lysate to break down the cells and release the plasmid DNA, (2) binding the plasmid DNA to the silica membrane through a spin column, (3) washing and elution of plasmid DNA to get pristine, high-quality DNA (Qiagen plasmid purification handbook 2005).

The process initiated with an overnight media culture of transformed bacteria carrying plasmid DNA of interest. First, 2 ml of bacterial liquid media was transferred into a sterile micro-centrifuge tube and then centrifugated at 13.000 rpm for 1 min.

The supernatant was decanted and 250 µl of P1 buffer (50 mM Tris-HCl, 10 mM EDTA, PH 8) was added to the resuspend pellet which contains 'lyse blue reagent' and 100 µg/ml of RNaseA. The suspension cell culture was resuspended entirely by vortexing until the cell pellet was homogenized. 250 µL of lysis buffer P2 (200 mM NaHO,1% SDS) was added to lyse the cell suspension and mixed gently by inverting the tube 6 times. Next, 350 µL of neutralization buffer P3 (3 mM potassium acetate PH 5.5) was added to precipitate cellular debris but leave the plasmid DNA in solution, and then the tube was inverted 4 times to ensure the cell suspension was well mixed.

The tube was centrifuged for 10 min at 13.000 rpm to separate the solid precipitate which will be discarded from the liquid supernatant. The supernatant containing the plasmid DNA was passed through a QIA spin column containing a silica membrane which was placed on a micro centrifuge tube and centrifuged for 1 min at 13.000 rpm. At this step, the plasmid DNA becomes bound to the silica membrane at the bottom of the spin column while the rest of the supernatant was passed through the column and discarded. The column was then washed by adding 750 µL of PE wash buffer (2 mM Tris-HCl, PH 8 and 20 mM NaCl) to remove any remaining contaminants and centrifuged for 1 min at 13.000 rpm. Finally, the column was placed on a fresh sterile 1.5 micro-centrifuge tube and the plasmid DNA was eluted into another micro-centrifuge tube by adding 50 µL of an elution buffer EB (10 mM Tris-HCl, 1 mM EDTA PH 8.5) to the centre of the column and centrifuging for 1 min at 13.000 rpm and the eluted plasmid DNA was stored at -20^0 C.

9. 2. 3. 4. Determination of DNA Concentration and Purity by Ultraviolet Spectrophotometry

After plasmid DNA extraction, it is essential to identify its concentration and purity which can be obtained by measuring the absorption of UV light. The UV absorption of a specific DNA depends on its base composition, as DNA's have different base compositions, the peak absorbances will also be different. The plasmid DNA concentration was quantified by measuring UV absorption at wavelength of 260 nm. DNA absorbs light at 260 nm and protein absorbs light more strongly at 280 nm, therefore the ratio between the absorbance at wavelengths of 260 nm and 280 nm (A260/A280) was used to evaluate DNA purity. The range of ratio is usually between 1.7 and 2 and Pure DNA should have a ratio of approximately 1.8. For a 1-cm pathlength, the optical density (i.e. absorbance) at 260 nm equal to 1.0 is roughly equivalent to 50 µg/mL double-stranded DNA (dsDNA) and 33 µg/mL single-stranded DNA (ssDNA). The NanoDrop automatically measures concentration and records it as ng/µl (1 ng/µl =1 µg/ml) by the relation:

$$\text{Concentration} = 50\ \mu g/mL \times A260 \times \text{dilution factor}$$

Here, a clean quartz cuvette (path length 1 cm) containing 1 ml of water was set as blank. Another quartz cuvette (path length 1 cm) contained 2 µL of plasmid DNA that was extracted by both the alkaline lysis protocol and Qiagen kit and 1 ml of sterile water. The absorption was measured at 260 nm and 280 nm using ultraviolet Spectrophotometer. The levels of DNA are more accurate in the Qiagen prepared DNA, DNA produced via the crude methodology tend to have more contaminant RNA and hence this is why the levels of DNA are higher

Table 9. 2. The concentration and purity of DNA extracted by both Crude and Qiagen protocols.

Sample	Concentration (ug/ml)	Purity (A260/A280) Ratio
BAA 14-Q	490.8	0.985
AL 1A2-Q	58.7	1.42
BZ 54-Q	555	1.92
2D6-Q	53.8	1.31
AL 1A2-C	911.8×4	2.13
2D6-C	969.4×2	2.13
BZ 30-C	826.3	1.83
BZ 49-C	118.1	1.83
BZ 73-C	871.8	1.92
2D6 71-C	251.5	1.63
BZ 21-C	905.3	1.92
BZ 48-C	27.1	1.67

9. 2. 3. 5. Preparation YPD Agar media for growing yeast Saccharomyces Cerevisiae cells

Yeast can easily grow on a medium comprising only dextrose and salts but to make the cells growth faster it is essential to add a protein source such as peptone and yeast cell extract hydrolysates. Yeast extract supplies trace elements and vitamins like B-complex which stimulate cell growth. YPD Agar also includes agar as the solidifying agent and glucose as carbohydrate source. Here, roughly 2.5 g of glucose, 2.5 g of yeast extract, 1.6 g of peptone, and 5 g of Agar molecular genetics powder were measured and added to 250 ml of sterile water, the bottle then was swirled to form colloid. Next, we labelled the bottle by autoclave tape and replaced in the autoclave which was set to 121^0 C under 20 psi for 35 minutes.

9. 2. 3. 6. Streak out yeast cells

To streak yeast cells out, first the appropriate number of plates was labelled by the date, the including culture medium, the identity of yeast cells. An approximately 20 ml of YPD Agar was gently poured into each sterile plate and then allowed them to solidify. Next, the poured plates were inverted (so that the agar side of the plate base is above, and the lid is down) in the incubator room at 37^0 C for 10 minutes. The streaking process was started by sterilizing a wire loop in flame until glowing red then allowed it to fully cool by standing for a few seconds. Next the sterile loop was dipped into the yeast media culture and picked up a loopful of yeast cells. These cells were gently spread back and forth across the surface of the labelled plate.

After finishing the first streak, the loop was sterilized to kill microorganisms and make streaks away from the original inoculums. Since there is thinning of inoculum through repeating streaking motion, isolated colonies are formed at ideal streak point where the spreading has separated the individuals of yeast cells at positions where they can make single colonies. After streaking, the plate was incubated for 3 days at the appropriate temperature of 37^0 C for growing the yeast cells.

9. 2. 3. 7. Yeast cell transformation by ZnO NFs

After the growth of the yeast cell, another different media was prepared for transformation process. This media is also known as selective-minimum media (SMM) which was contained 6.7 g of Yeast nitro base and 2 % glucose mixed with 250 ml of pure water and autoclaved at 37^0 C. one colony of yeast cell was picked up and mixed with 2ml of (SMM) and incubated for overnight at 37^0 C with vigorous shaking (approximately 220 rpm). NFs and flat Si wafer were first washed by 10 ml of sterile water. They were soaked into 35 ml of 70% absolute ethanol for 30 min and then allowed to dry naturally in the hood. A 5 µl and 10 µl of plasmid 2D6-Q (53.8 Ng/ml) was pipetted on the top of NFs and Si and left for 1 h to completely dry on NFs and bare Si wafer (see Figure 9. 1). In the next step, 1.5 ml of the overnight cell culture was passed into a sterile micro-centrifuge tube and centrifuged at 16.000 rpm for 2.5 min. The supernatant was decanted and resuspend pellet was washed by selective- minimum media and centrifuged at 16.000 rpm for 2.5 min. After disposing the supernatant, the pellet was washed twice by 100 µl of PBS buffer to remove the remnants of the culture media, (as it may interfere with the transformation process) and centrifuged at 16.000 rpm for 2.5 min.

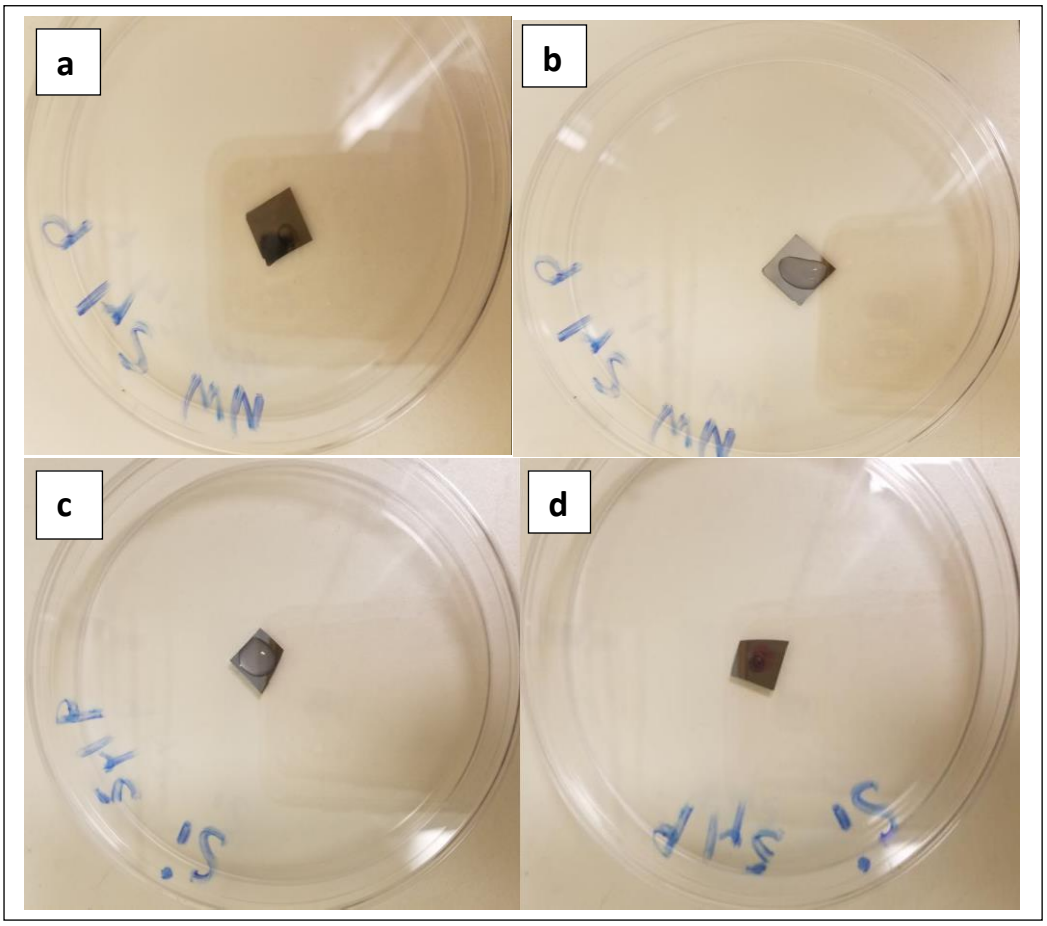

Figure 9. 1. Photographs showing the drop casting of cytochrome 2D6 on the top of (a, b) ZnO NFs and (c, d) flat Si wafer.

Pellet was again resuspended into 500 µl of PBS buffer; and then 50 µl of the cells was dropped onto the surface of NFs and bare Si wafer and left for 1 h inside the hood. At this step, if the cells were dehydrated a small amount of PBS buffer should be added. For washing away the cells from the NFs and Si wafer, another selective agar media (SD-agar) was prepared. The media contained 1.7 g of yeast nitro base, 5 g of both agar and 2 % glucose mixed with 250 ml of pure water. In addition, approximately 8.3 ml of three essential cellular compounds include Adenine, Histidine and Tryptophan were added to give cells the ability to produce protein of interest.

The cells were washed up by dropping 100 µl of SD-agar media onto NFs and Si wafer and leaving for 1 min to allow cells to disperse. Finally, the cells were collected and distributed on SD-agar plates and then incubated at 30 ^{0}C.

After 3 days, the SD-agar plates were checked but no obvious transformed cells were observed. Figure 9. 2 illustrates SEM images of the attached yeast cells on the top of ZnO NFs. One potential explanation for the failure of cell transformation could be that during the physical attachment of ZnO NFs with yeast cells, severe cell damage has occurred to the cell membrane leading to release of intracellular components and eventually the death of yeast cell (Oprea, Andronescu et al. 2014). Another reason could be drawn based on SEM images that the size of some yeast cells was too large which could hinder the NFs ability to penetrate the nuclear membrane to deliver the plasmid inside the cell nucleus where the machinery that will turn DNA plasmid into protein. Further, some reports were shown that the nuclear membrane was not penetrated by any nanostructures because the membrane folds in a complicated way to prevent the NFs from the nucleus interior (Persson, Køble r et al. 2013).

Even though these NFs provide a large surface area which could promote the NFs-cell interactions, the dimensions of NFs are much smaller than the typical size of yeast *saccharomyces cerevisiae* cells that would minimize the chance of the nucleus interaction with the NFs (Mendes 2013). Based on the phase of growth, the sizes of yeast cells change from strain to strain. They are typically spherical and have a diameter of 5-10 µm (Wollman, Leake 2015). It can be clearly seen from SEM data that the NFs were robust, and they did not break when they were in contact with the cells.

Identifying whether or not the cell membrane is penetrated by the nanostructures is a very crucial issue to help understanding which geometry of nanostructure can be used as biomolecule delivery platform.

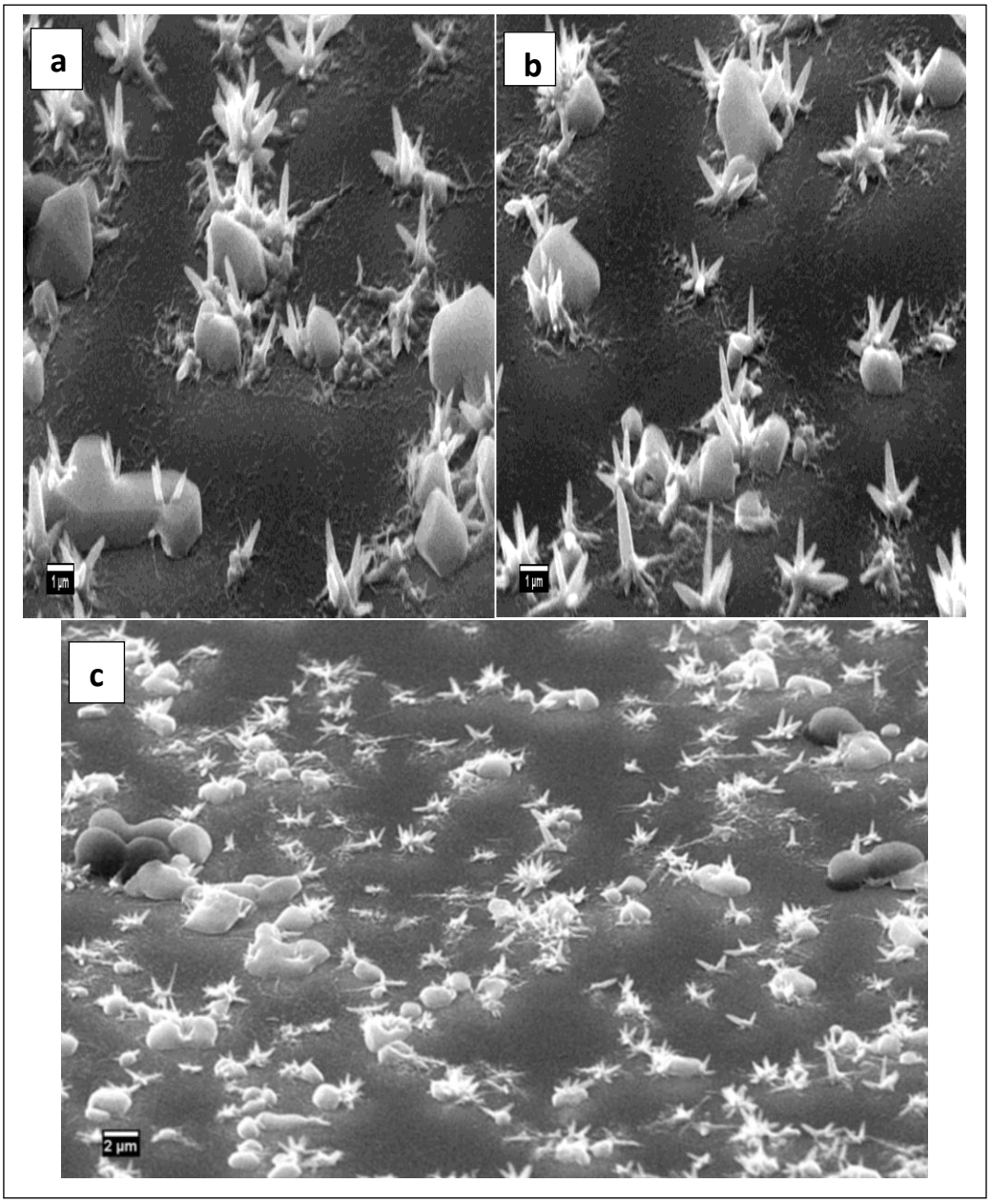

Figure 9. 2. High magnification (a, b), Low magnification (c) SEM images of the attached yeast cells on the top of ZnO NFs.

According to these findings, the transformation of yeast cells did not take place, a possible cause of which was that the cells could be contaminated by the NFs. Therefore, it was essential to extremely clean the nanostructured materials before culturing with the yeast cells as well as to examine the robustness of the nanomaterial during microbiological processing.

In addition, to investigate the interfacial interactions of nanostructured surfaces with the yeast cell walls we changed the settling mechanism of the NFs-yeast cell system by placing the NFs on SD-agar plates containing yeast cells. It was anticipated that this would help assessing the effect of physical attachment of the nano-yeast interface before starting with more a complex system such as mammalian cells; the key point is to increase the chance of cells being transformed by ensuring the DNA plasmid is thoroughly delivered into organisms with a thick cell wall like yeast cells, especially *Saccharomyces cerevisiae*, which are a preferred design organism to investigate intracellular interactions. In the following subsection, it is demonstrated the effect of the intensive cleaning procedure on the NFs structural integrity as well as the effect of different culturing conditions on the Nano-cell interface interactions.

9. 2. 3. 8. Cleaning procedure of ZnO NFs and their culture with yeast cells

NFs were first soaked in sterile water for 3hrs, water was changed after each hour. They were then soaked into 70% absolute ethanol for 4 hrs with regular changing of ethanol at 1hr intervals and lastly kept in the hood for overnight to dry naturally. 75ng of DNA plasmid (pyes2/2D6-105.7ng/µl) was transferred to the top of NFs and then allowed to dry completely in air for an hour. The overnight cell culture was counted by diluting 20 µl of overnight culture with 480 µl of SMM media and counting using haemocytometer, and the concentration of yeast cells were $5.85x10^5$ cells/ml. For transformation, two methods were applied; in the first one the NFs were placed onto the 20µl liquid culture of yeast cells while in the second method the NFs were placed directly on the top of monolayer of yeast agar-plate.

After incubation time of an hour, NFs were taken away from both liquid culture and agar plate and allowed to dry to be imaged by SEM. The cells were collected and plated on to SD agar plates containing amino acids and then incubated at 30 ^{0}C. After 3 days, the SD-agar plates were checked but they were contaminated so cell transformations did not take place. In order to address the physical contact of the yeast cells and nanostructured materials, the NFs were prepared for SEM differently. Some NFs were taken directly from both the yeast agar plate and yeast liquid culture, while others were rinsed with SMM media after taking from agar plates and liquid media. It was clearly obvious the NFs were entirely buried by the high cell density of yeast culture on the agar plate (Figure 9. 3).

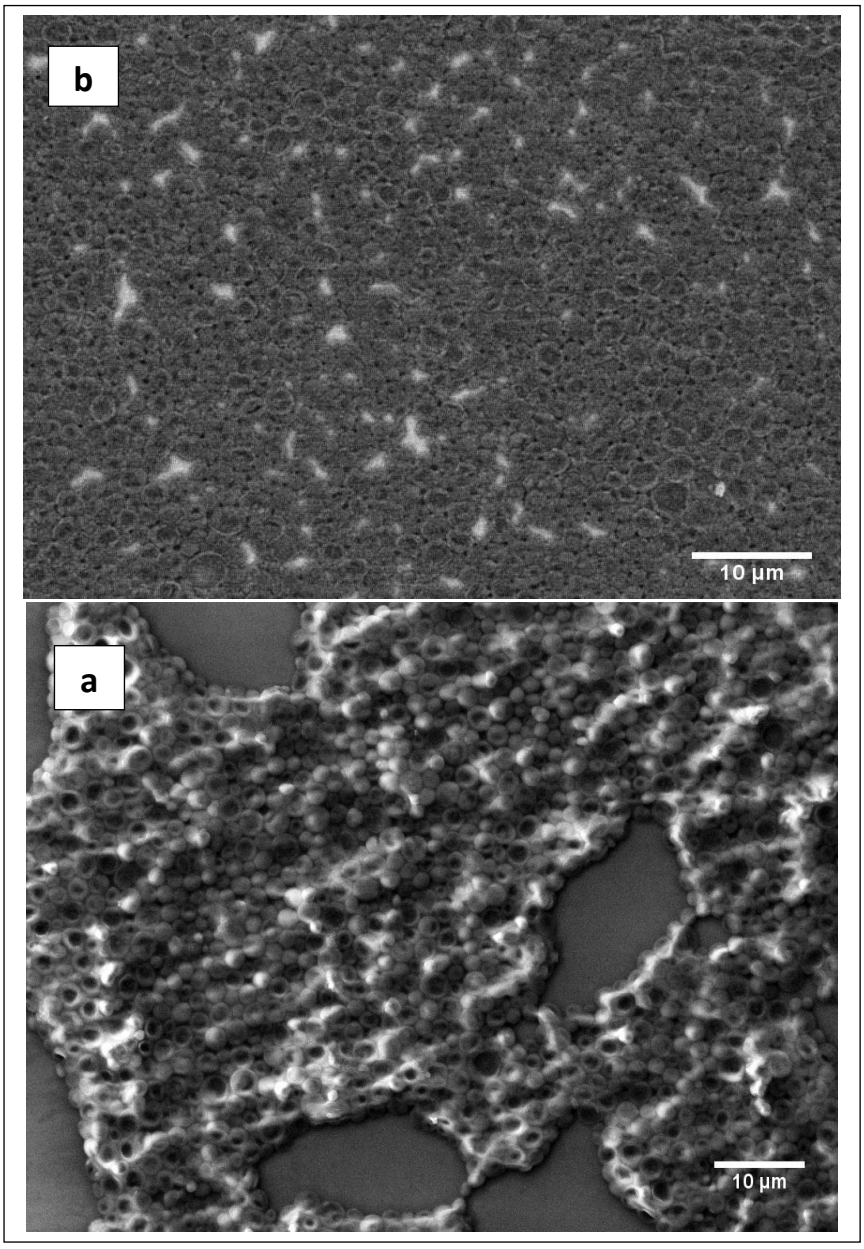

Figure 9. 3. SEM images of the attached yeast cells on the top of Nanoflower taken directly from the agar plates (a) without washing with (SMM) media, (b) washing with (SMM) media.

However, the SEM image of NFs that were taken immediately from the yeast liquid culture without rinsing with (SMM) media showed low-densely NFs (Figure 9. 4. (b)). These wires were extremely affected by the intensive clean procedure, they were broken and floated on the substrate surface. The NFs completely disappeared on the samples treated with (SMM) media, as they were swept away by overflowing liquid (Figure 9. 4. (a)).

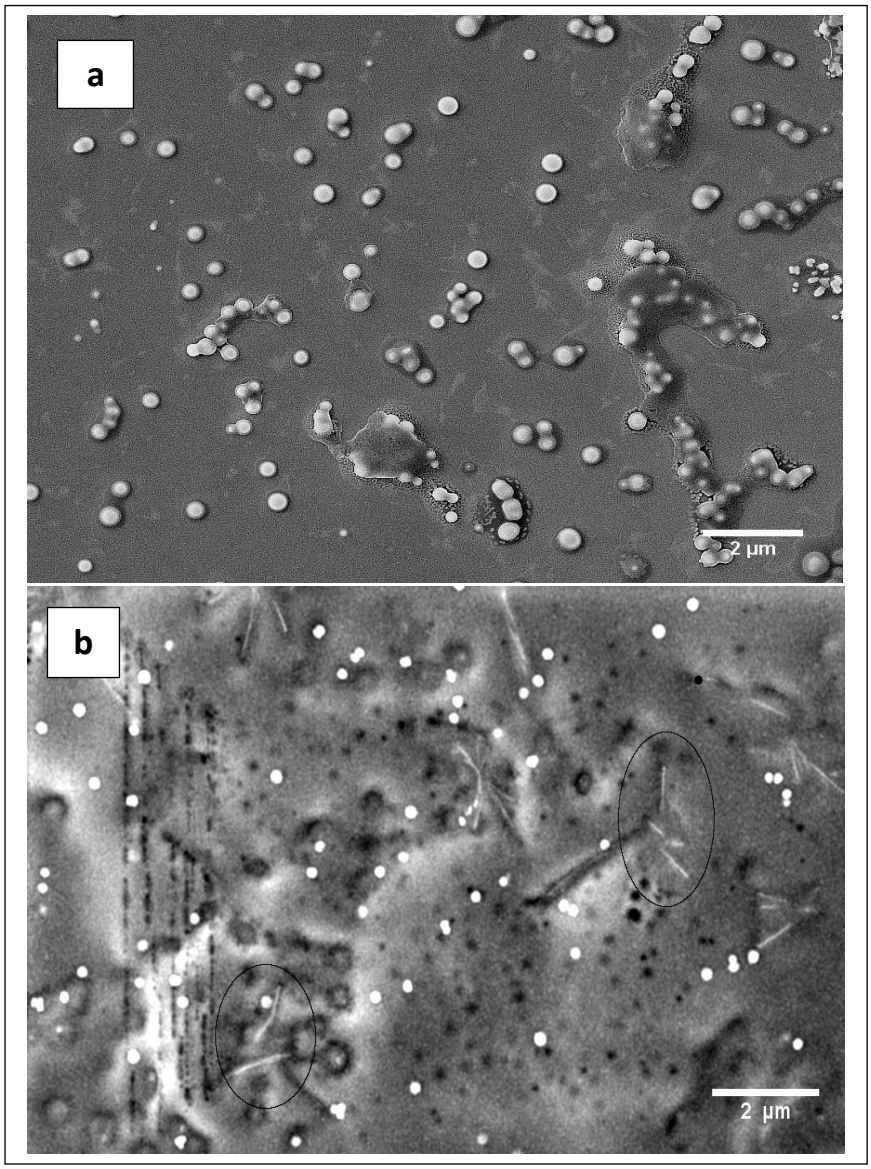

Figure 9. 4. SEM images of the attached yeast cells on the top of NFs taken directly from the yeast liquid culture (a) washing with (SMM) media, (b) without washing with (SMM) media; the collapsed NFs indicated by black circles.

Based on these insights gained from SEM, it seems that processing the NFs with fluids or culture media for a long time leads to their removal, which gives a potential cause of not succeeding of yeast transformation process. Regarding the clean treatment of NFs, it seems that washing once by sterile water and soaking in 70% absolute ethanol for 15 min is the better way to keep the nanoflower sturdy and durable. In terms of the nanoflower-cell interactions, it appeared that placing NFs on the yeast agar plates was not appropriate as the dense growth of yeast cells on the agar plate concealed the NFs. Whilst, the liquid culture media of yeast cells was more applicable in showing how cells incorporated with these NFs (see Figure 9. 2). These results should aid in our comprehending of the tenets of nanomaterial capacity under intensive biological treatment and asset in developing effective and functional Nano-bio delivery platform.

9. 3. Mammalian expression system

A mammalian expression platform has been used for transient and stable expression of different genes (Khan 2013). Mammalian cells, and preferably, human cells, are ideal to express human proteins because they do not undergo the obstacles that exist in the other eukaryotic platforms which are mainly related to post-translational modifications (Khan 2013). The gene expression in mammalian cells requires an appropriate cell line and applicable vectors that can serve as a tool to transfer the gene of interest into several cell lines which are used for transfection process (Khan 2013).

Despite the vast utilizing of mammalian cells to express many heterologous proteins, this expression system has its drawbacks such as high-cost, complexity, as well as the potentiality of infection by animal viruses is fairly high (Khan 2013). The most broadly used mammalian cells to produce CYP450 proteins are (CHO) cells, human hepatic HePG2 cells, V79 Chinese hamster lung cells, NIH3T3 human fibroblast cells, lymphoblast cells (Khan 2013).

9. 3. 1. Transfection of CHO cells

Passaging the cells is used to elongate the lifetime or extend the cells number in the culture media by transferring some or all cells from a previous culture to fresh growth medium. Before starting the protocol, the fluency of cell culture was determined and flask over 50% confluent were split into more flasks. First, the spent cell medium was removed from the flask by using a sterilized pipette and then washed with 5 ml PBS buffer to remove all traces of serum, calcium, and magnesium. After discarding the wash solution, approximately 5 ml of trypsin solution was added to break down proteins and dissociate adherent cells. The culture flask was incubated at 37^0 C for 4 min and then the cell culture was observed under the microscope for detachment. When more than 90% of the cells have detached, 10 ml of complete medium was added. All contents were transferred to 25 ml universal and spun at 1000 rpm for 3 min to pellet cells. The medium was discarded and then the tube was gently flicked to loosen the cell pellets. Next, 10 ml of complete growth medium was added and mixed well to ensure a formation of homogenous solution of single cells. 4 ml of this cell suspension was transferred to a fresh tube with adding 25 ml of complete growth medium. The cell suspension was incubated to be ready for use.

9. 3. 2. Culturing CHO cells with ZnO NFs

ZnO NFs were soaked in 70% ethanol for 15 min, and then dried on air in the hood. Two different concentrations (10 µl, 15 µl) of plasmid pMax-GFP (0.5µg/µl) was pipetted on the top of NFs and left to dry in air. Media was removed from overnight CHO culture and then NFs were placed face down on the cell monolayers and incubated at 37^0 C for 3 hrs.

The NFs were removed from plates and washed by 20 µl of trypsin to release any attached cells. These cells were transferred into a fresh plate and 100 µl of PBS media was added. 100 µl of PBS media was added to the original plate which was not treated by trypsin. The plates were incubated at 37^0 C and then imaged using fluorescence microscope after 5 days. It was observed from FM images the CHO cells were not shown green fluorescence as pMax-GFP proteins were not expressed. Despite the cells being pierced by NFs (see Figure 9. 6), they were shown to survive after 5 days of culture. However, the density of cell and its shape were clearly affected by adding trypsin, as trypsin-treated cells were detached from the surface of culture plate and their density declined. Conversely, the surface morphology of cells that not treated with trypsin was different as the cells remained adhered and spread with rounded- shape (Figure 9. 5).

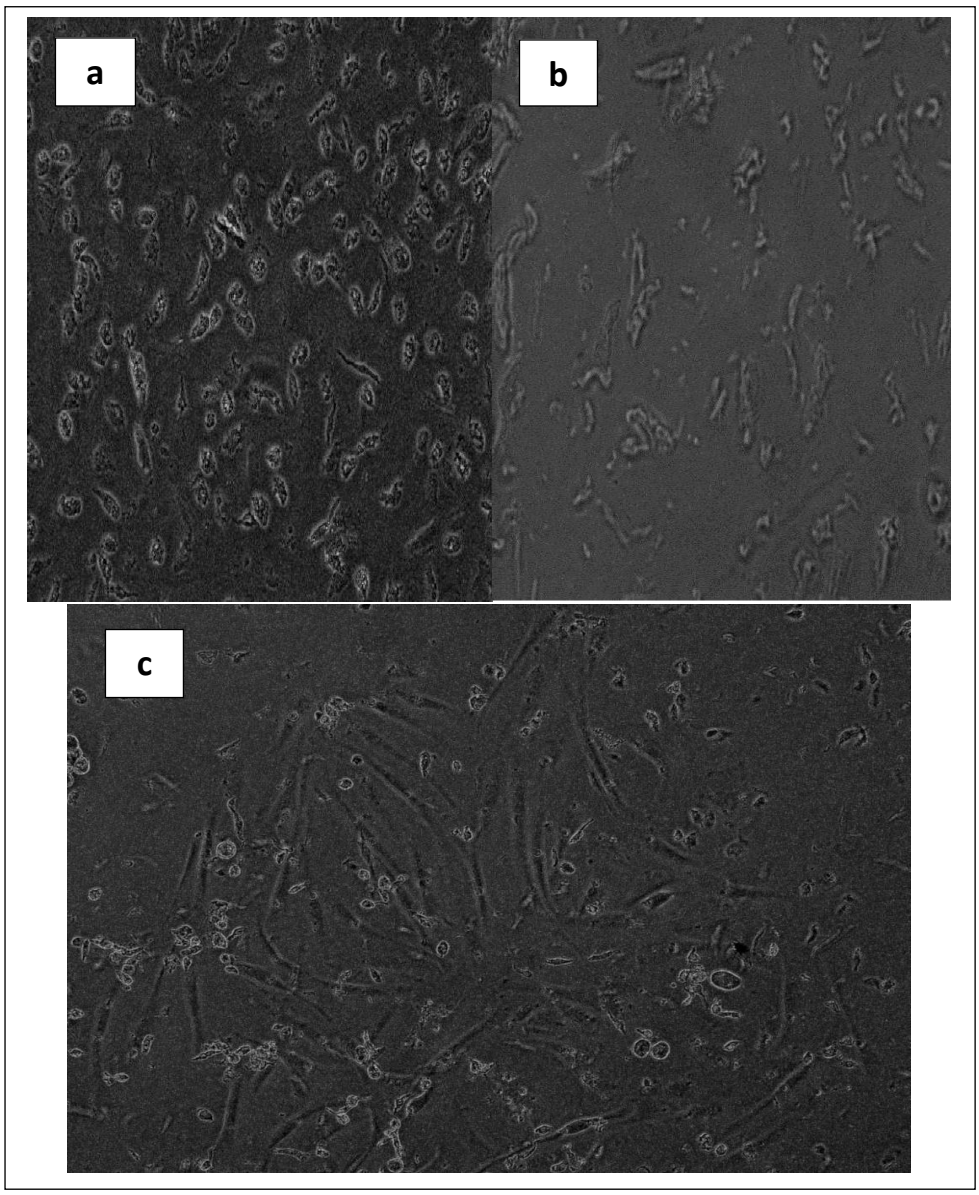

Figure 9. 5. White-light imaging of FM for CHO cells immediately after NFs culture condition (a) non-trypsinized, (b) trypsinized, (c) non-trypsinized after 5 days.

SEM images of interactions of CHO cells with NFs illustrated in figure 9. 6. The initial physical contact between cells and NFs is at the cell membrane wall and it is obvious that NFs were capable to be implanted into cell membrane.

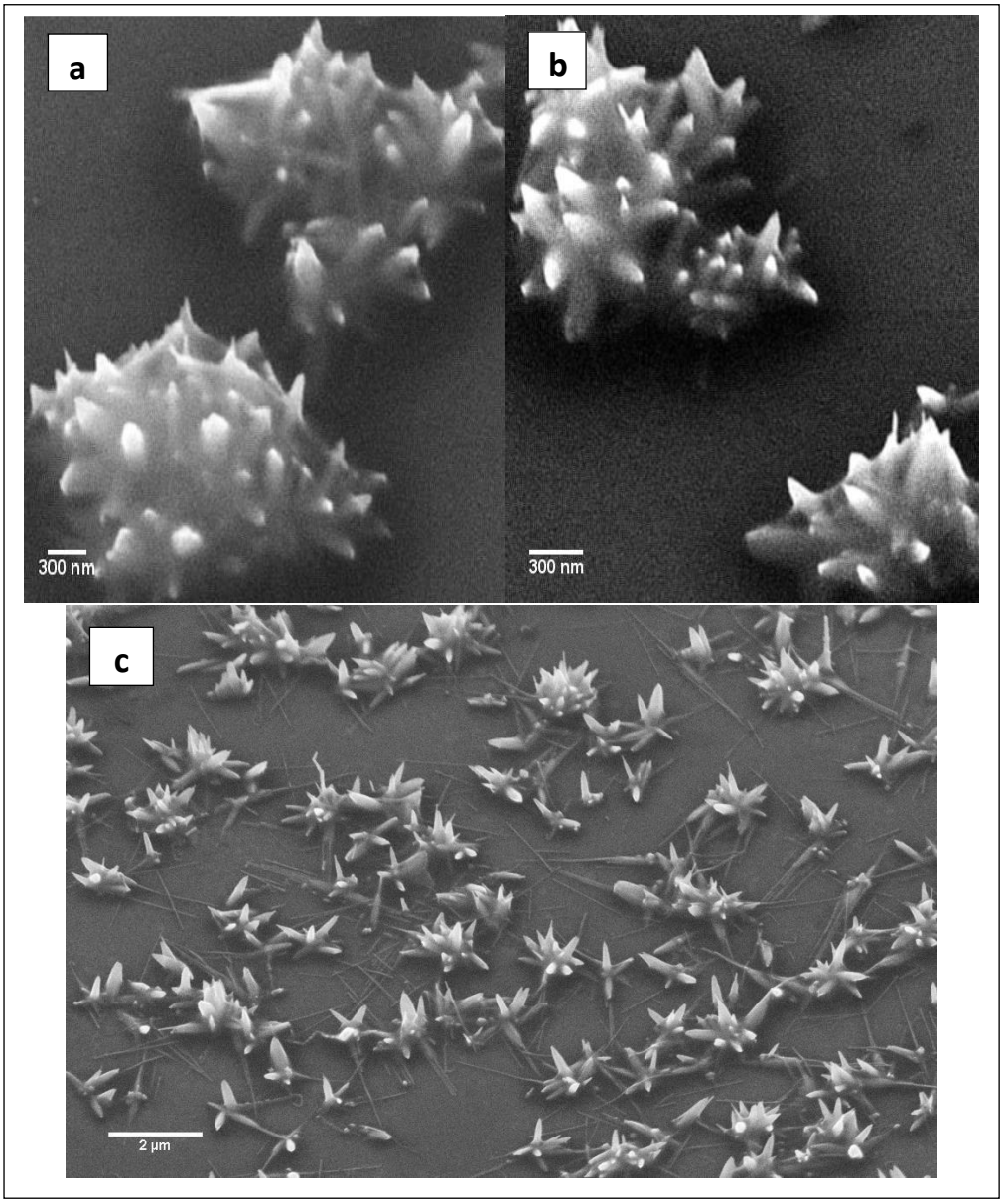

Figure 9. 6. High magnification (a, b), Low magnification (c) SEM images of the cultured CHO cells on the top of NFs substrate.

Although CHO cells were penetrated by NFs, gene was not expressed which raises a question whether the NFs getting through the cells were certainly gaining efficient access to their cytosol. The nanoflower–membrane entry in the range of the nanoflower diameter (50–100 nm) which is in the same size of receptor-mediated endocytosis (Prinz 2015). The cell membrane engulfed the NFs, which could result in uncompleting endocytosis. Another potential explanation for the unsuccessful transfection is that cell components were catastrophically damaged by the NF interaction leading to cell death.

At this point, it was necessary to decipher the impact of the nanomaterial geometry and density for this type of interaction. In the following section, CHO cells were cultured on different nanoarrays geometry to help understanding the effects of the array morphology on cell–nanoarrays interactions.

9. 3. 3. Effect of ZnO morphology on the process of gene delivery

The shape of ZnO nanostructures is another valuable aspect that influences their functionality and performance. To gain a better understanding on the impact of the physical surface topography of nanotexture in determining the cell-substrate interactions, different morphologies of ZnO nanomaterials, including densely packed NFs with average length of 800 nm and diameter of 200 nm, and densely packed nanocolumns with average length of 1.7 µm and diameter of 400 nm (see Figure 9. 7) were fabricated through solution-based process; and examined for introducing cellular molecules into host mammalian cells.

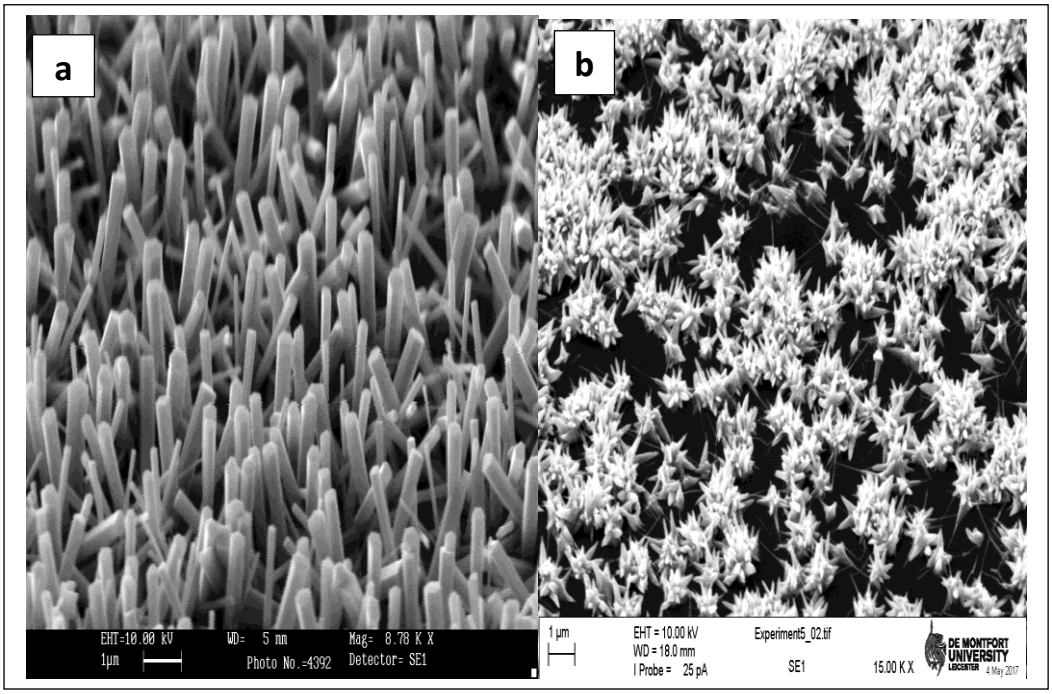

Figure 9. 7. SEM images of ZnO (a) nanocolumns (b) NFs. Scale bar is 1 µm.

All samples were soaked in 70% ethanol for 15 min, and then dried naturally in the hood. 10 µl of plasmid pMax-GFP (0.5µg/µl) were pipetted on the top surface of nanostructures and kept for drying. CHO cells were trypsinized and resuspended in 5ml of complete media. For counting the cells, 200 µl of CHO cell was diluted with 200 µl of trypan blue and then counted by haemocytometer. Two different concentration ($1x10^5$,$2x10^5$) of cells were used and then nanostructures were placed face down on the cell monolayers and incubated at 37^0 C for 2 hrs. After incubation, culture media was transferred to 6 well plates and 2ml of complete media was added. Nanowires were transferred to another 6 well plates and washed by 2ml of complete media. After monitoring CHO cells using FM, no green fluorescent proteins were expressed.

However, after 24 hrs of culturing the shape of cells cultured on the two nanostructures was different. On the nanocolumn arrays, cells exhibited a rounded morphology with a much larger size (Figure 9. 8).

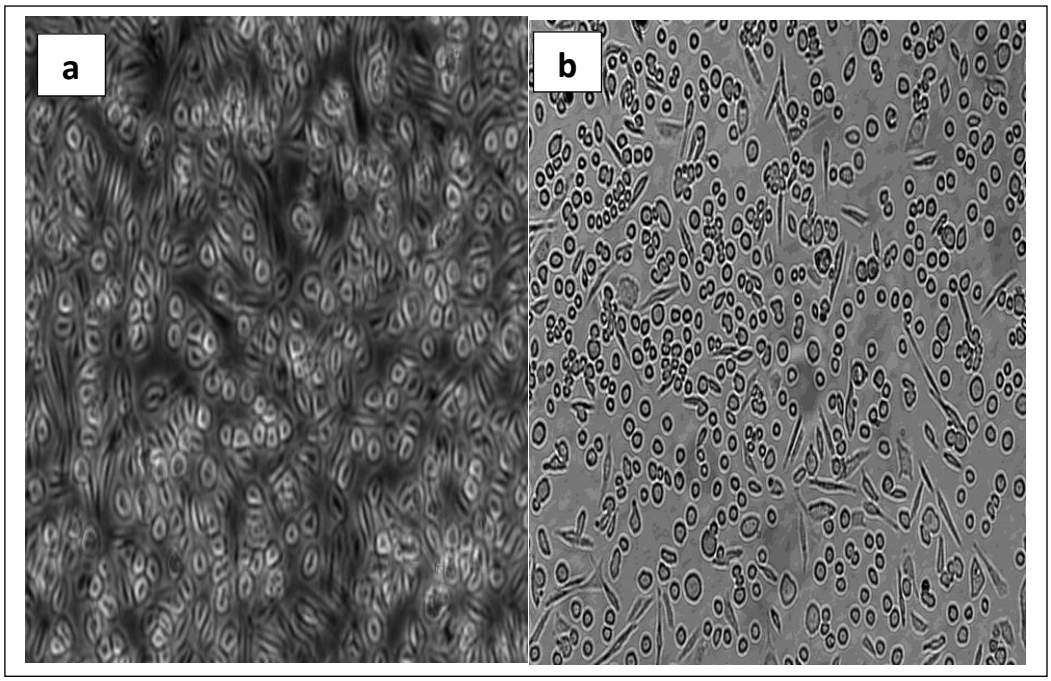

Figure 9. 8. Cell cultured with ZnO nanocolumns (a) after 24hrs, (b) after 72hrs.

In contrast, cells that cultured on the NFs structures expanded well and showed elongated shape and reduced size (Figure 9. 9). After 72 hrs, most viewable cells had a rounded morphology. One explanation of the variation of cell shape could be due to contact with the nanocolumns not causing excessive stress to the cell, resulting in viable systems. In contrast to the NFs where cells are challenged by the sharp tips of the NFs which make them lined up into elongated patterns to avoid piercing by these tips.

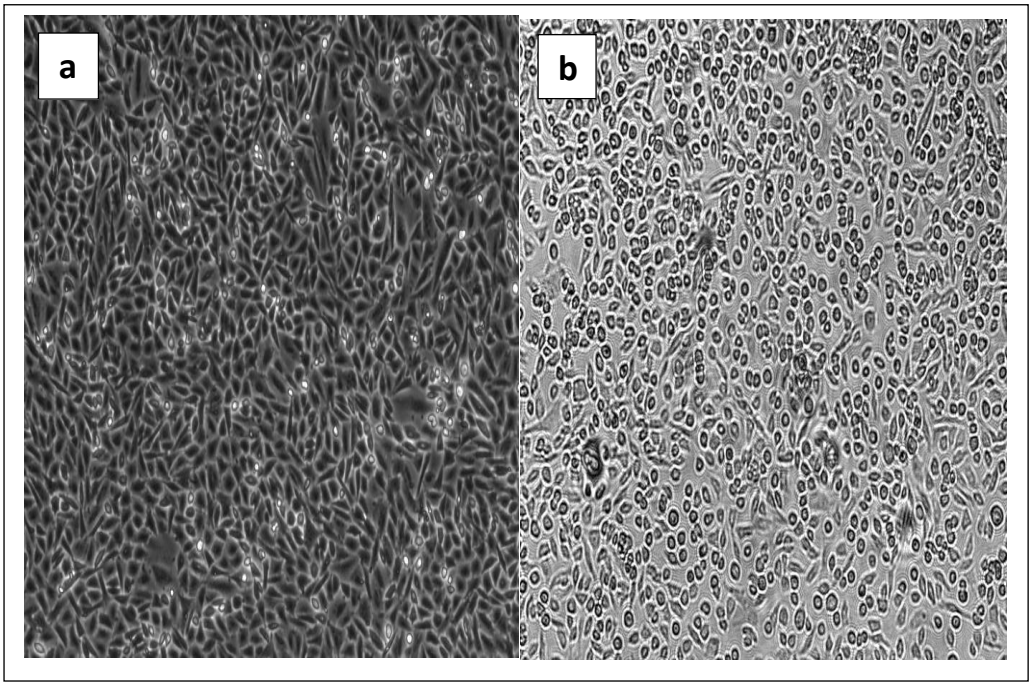

Figure 9. 9. Cell cultured with highly dense ZnO NFs (a) after 24hrs, (b) after 72hrs.

Based on these observations, it seems that same cell line behaves differently on various types of nanostructure morphology which indicates the significance of the topographical features of nanomaterials on the interactions of the Nano-cell interface. Tilted SEM images of the cultured CHO cells on the top of ZnO nanocolumns and NFs are illustrated in figures (9. 10 & 9. 11) respectively.

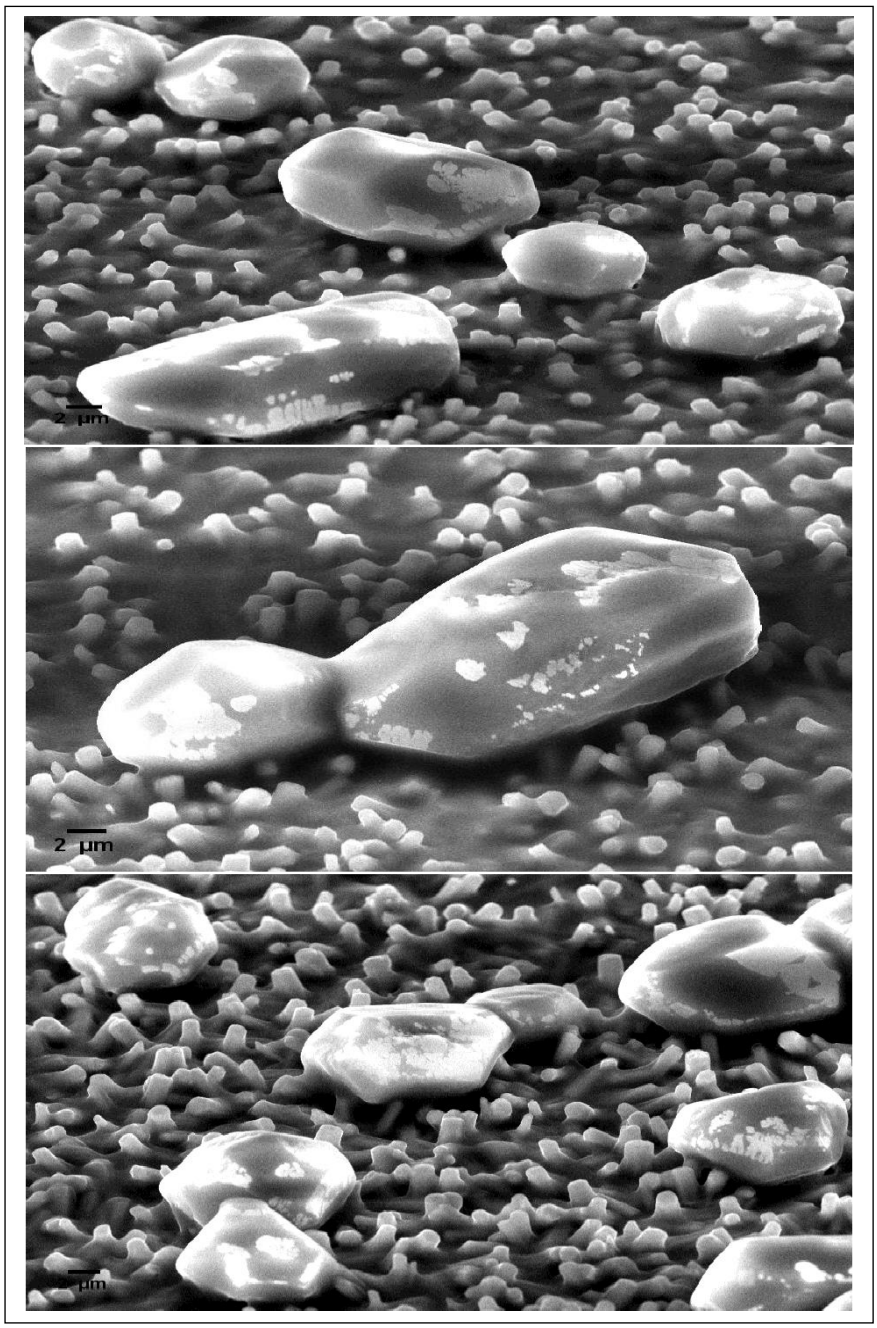

Figure 9. 10. Tilted-high magnification SEM images of the cultured CHO cells on the top of ZnO nanocolumns.

Based on these images, it was seemed that nanostructures morphology highly affects the penetration mechanism as the physical contact of the cells on the 2D nanocolumn surfaces was lower compared to their attachments on the 3D NFs.

As it can be seen from figure (9.10) that closed packed 2D nanocolumns may inhibit the cell to reach the substrate surface by suspending them on the top surface of nanocolumns where the cell wall may not undergo deformation or stretching induced by the topographical nanotextures. Therefore, the nanocolumns access into cells' interiors will be limited, such observations are in accordance with FM data where the CHO cells maintain a rounded shape because of not being stretching by the nanotextures.

They are also in good agreement with literature report, as it was demonstrated that close-packed nanoarrays geometry provides higher density a "bed of nails" effect where the cells lay on the bed of nanoarrays (Xie, Xu et al. 2013). In this case, the penetration mechanism is driven by the gravitational force, which is distributed among those higher density nanocolumns, reducing the pressure on the cell membrane, therefore, penetration would not be possible.

In contrast, 3D flower-shaped structure seemed to provide a wider contact region with the cells through its multibranched geometry where the cells could easily interact and wrap around the NFs. Therefore, the cell membrane can suffer from large-scale deformations and hence penetration process would be more likely to take place (Figure 9. 11).

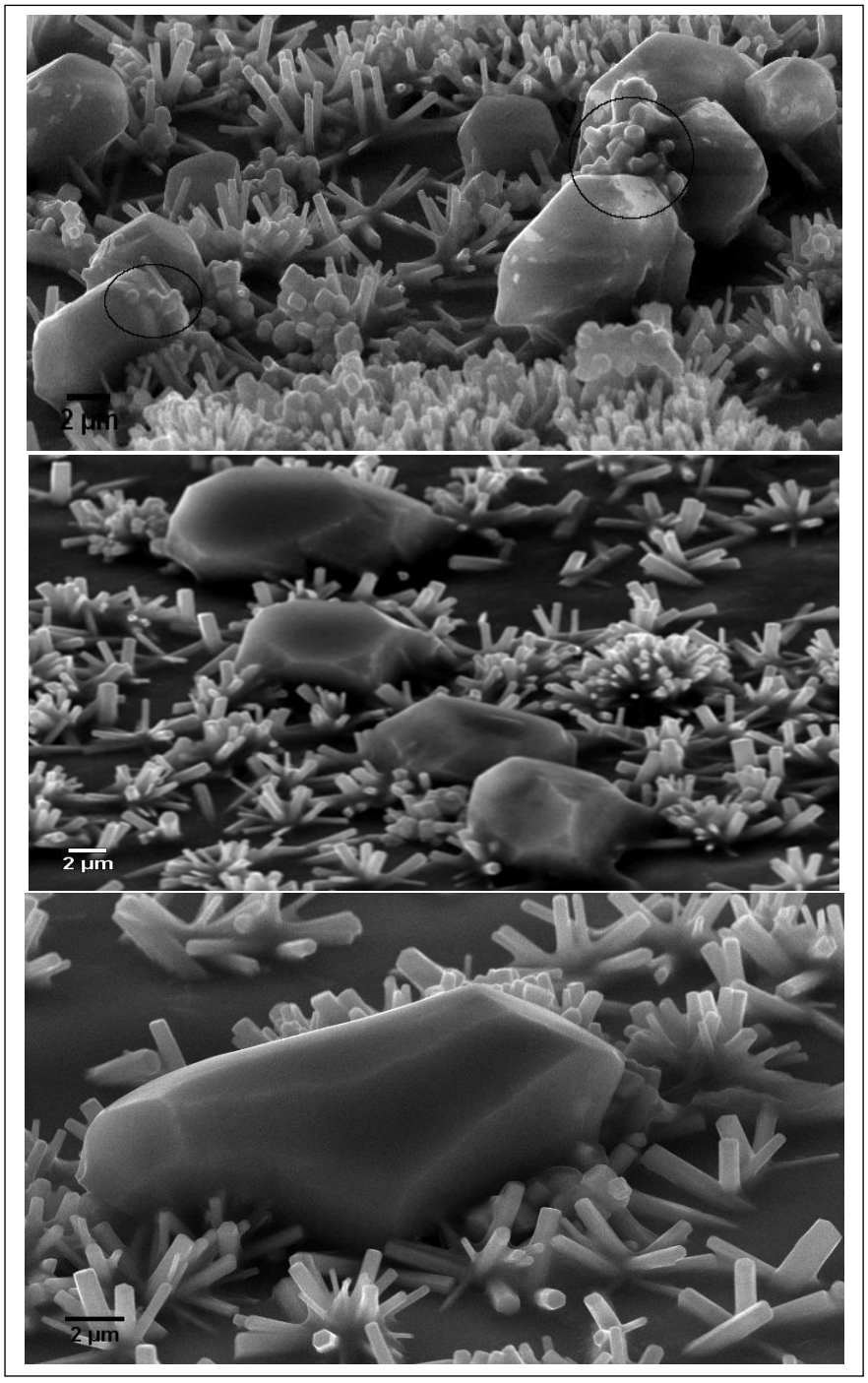

Figure 9. 11. Tilted-high magnification SEM images of the cultured CHO cells on the top of ZnO NFs.

In addition, our data suggest that the density of nanostructures is a significant factor as a low-density nanostructure is more effective in achieving a wide-ranging interaction in the Nano-bio interface. In this case, cells can reach to the substrate surface where a significant perturbation effect on the cell membrane can be generated by inducing adhesion forces between cell and nanostructures which promote penetration mechanism (Qi, Yi et al. 2008).

9. 4. Conclusion

A proof of concept study was illustrated to investigate the practicability of ZnO nanomaterials as potential gene-delivery platform to transfer foreign DNA to different cell lines. In the first stage of the study, yeast *saccharomyces cerevisiae* cells were used as a host organism to express proteins of interest. Even though the cell did not transform, an essential information based on SEM images was gathered about the Nano-cell interactions. We suggest that the large size of yeast *saccharomyces cerevisiae* cell compared to nanostructures as one possible obstacle that hinder the nanostructures ability for cellular interior to deliver the plasmid DNA to the cell nucleus. In addition, as contamination may have been an issue, it was necessary to discover the effect of intensive biological treatment on the nanomaterial's robustness and reproducibility before culturing with the cells. We found that the nanostructures being in contact with fluids or culture media for a long-time result in their breakage and/or removal. Therefore, it is suggested that washing once by sterile water and soaking in 70% absolute ethanol for 15 min is an improved method to maintain the robustness and durability necessary for such investigations.

Furthermore, the cell settling mechanism on the nanostructures was investigated to assess the interfacial interactions of the Nano-cell system under different culturing conditions. It was found that placing nanostructures onto liquid culture of yeast *saccharomyces cerevisiae* cells was more practicable than settling them on the top of monolayer of yeast agar-plate. As cell culture media exhibited clearly the Nano-cell interactions while the thick growth of the cells on the agar plate completely concealed the nanomaterials.

The second stage of study was dealt with (CHO) cells as a gene expression platform for producing pMax-GFP proteins. Based on SEM micrographs, it was obvious that NFs were able to be implanted into cell membrane. However, protein was not produced which raises a question whether the NFs getting through the cells were certainly having access to their cytosol. We suggest that cell being enmeshed or embedded within many sharp tips of nanoflower is one potential cause of the unsuccessful transfection as these pointed ends of flower could generate extreme damage into the cell membrane. According to this consequence, it was important to investigate if the morphology of ZnO nanostructures matters. It was found that same cell line (CHO) interacts differently with two varied types of nanostructure geometry. On the nanocolumn arrays, cells showed a rounded shape with a much larger size whereas on the NFs, cells shrank in size and exhibited elongated structure which indicates the importance of the morphological characteristics of nanotextures on the interactions of the Nano-cell interface. These findings should help in our understanding of the tenets of Nano-cell interactions and asset in developing effective and functional nanostructures-assisted biomolecule delivery platform.

References

BITTERMAN, K.J., MEDVEDIK, O. and SINCLAIR, D.A., 2003. Longevity regulation in Saccharomyces cerevisiae: linking metabolism, genome stability, and heterochromatin. *Microbiology and molecular biology reviews: MMBR,* **67**(3), pp. 376-99, table of contents.

BREEDEN, L.L., 2003. Periodic transcription: a cycle within a cycle. *Current Biology,* **13**(1), pp. R31-R38.

ÇELIK, E. and ÇALIK, P., 2012. Production of recombinant proteins by yeast cells. *Biotechnology Advances,* **30**(5), pp. 1108-1118.

GALAO, R.P., SCHELLER, N., ALVES-RODRIGUES, I., BREINIG, T., MEYERHANS, A. and DÍEZ, J., 2007. Saccharomyces cerevisiae: a versatile eukaryotic system in virology. *Microbial Cell Factories,* **6**(1), pp. 32.

HAURI, H. and SCHWEIZER, A., 1997. The ER–Golgi membrane system: compartmental organization and protein traffic. *Comprehensive Physiology,*.

JOHNSTON, W.A., HUANG, W., DE VOSS, J.J., HAYES, M.A. and GILLAM, E.M., 2008. Quantitative whole-cell cytochrome P450 measurement suitable for high throughput application. *Journal of biomolecular screening,* **13**(2), pp. 135-141.

KHAN, K.H., 2013. Gene expression in Mammalian cells and its applications. *Advanced pharmaceutical bulletin,* **3**(2), pp. 257-263.

LAURENTI, M. and CAUDA, V., 2017. ZnO Nanostructures for Tissue Engineering Applications. *Nanomaterials,* **7**(11), pp. 374.

LODISH, H., BERK, A., ZIPURSKY, S.L., MATSUDAIRA, P., BALTIMORE, D. and DARNELL, J., 2000. Molecular cell biology 4th edition. *National Center for Biotechnology Information, Bookshelf,* .

MENACHO-MARQUEZ, M. and MURGUIA, J., 2007. Yeast on drugs: Saccharomyces cerevisiae as a tool for anticancer drug research. *Clinical and Translational Oncology,* **9**(4), pp. 221-228.

MENDES, P.M., 2013. Cellular nanotechnology: making biological interfaces smarter. *Chemical Society Reviews,* **42**(24), pp. 9207-9218.

MITTAL, B., TULSYAN, S., KUMAR, S., MITTAL, R.D. and AGARWAL, G., 2015. Cytochrome P450 in cancer susceptibility and treatment. *Advances in clinical chemistry.* Elsevier, pp. 77-139.

MÜLLER, M., HEUCK, A. and NIESSING, D., 2007. Directional mRNA transport in eukaryotes: lessons from yeast. *Cellular and molecular life sciences,* **64**(2), pp. 171-180.

NASSER, M., POOJA, V., ABDIN, M. and JAIN, S., 2003. Evaluation of yeast as an expression system.

NEVOIGT, E., 2008. Progress in metabolic engineering of Saccharomyces cerevisiae. *Microbiology and molecular biology reviews : MMBR,* **72**(3), pp. 379-412.

OEDA, K., SAKAKI, T. and OHKAWA, H., 1985. Expression of rat liver cytochrome P-450MC cDNA in Saccharomyces cerevisiae. *Dna,* **4**(3), pp. 203-210.

OPREA, O., ANDRONESCU, E., FICAI, D., FICAI, A., N OKTAR, F. and YETMEZ, M., 2014. ZnO applications and challenges. *Current Organic Chemistry,* **18**(2), pp. 192-203.

PANDEY, A., SHIN, K., PATTERSON, R.E., LIU, X. and RAINEY, J.K., 2016. Current strategies for protein production and purification enabling membrane protein structural biology. *Biochemistry and Cell Biology,* **94**(6), pp. 507-527.

PERSSON, H., KØBLER, C., MØLHAVE, K., SAMUELSON, L., TEGENFELDT, J.O., OREDSSON, S. and PRINZ, C.N., 2013. Fibroblasts cultured on nanowires exhibit low motility, impaired cell division, and DNA damage. *Small,* **9**(23), pp. 4006-4016.

POMPON, D., LOUERAT, B., BRONINE, A. and URBAN, P., 1996. [6] Yeast expression of animal and plant P450s in optimized redox environments. *Methods in enzymology.* Elsevier, pp. 51-64.

PORRO, D., SAUER, M., BRANDUARDI, P. and MATTANOVICH, D., 2005. Recombinant protein production in yeasts. *Molecular biotechnology,* **31**(3), pp. 245-259.

PRINZ, C.N., 2015. Interactions between semiconductor nanowires and living cells. *Journal of Physics: Condensed Matter,* **27**(23), pp. 233103.

QI, S., YI, C., JI, S., FONG, C. and YANG, M., 2008. Cell adhesion and spreading behavior on vertically aligned silicon nanowire arrays. *ACS applied materials & interfaces,* **1**(1), pp. 30-34.

RAHONG, S., YASUI, T., KAJI, N. and BABA, Y., 2016. Recent developments in nanowires for bio-applications from molecular to cellular levels. *Lab on a Chip,* **16**(7), pp. 1126-1138.

ROSANO, G.L. and CECCARELLI, E.A., 2014. Recombinant protein expression in Escherichia coli: advances and challenges. *Frontiers in microbiology,* **5**, pp. 172.

SAMBROOK, J. and RUSSELL, D.W., 2001. Molecular cloning: a laboratory manual. 2001.

TEIXEIRA, M.C., DUQUE, P. and SÁ-CORREIA, I., 2007. Environmental genomics: mechanistic insights into toxicity of and resistance to the herbicide 2, 4-D. *Trends in biotechnology,* **25**(8), pp. 363-370.

WOLLMAN, A.J. and LEAKE, M.C., 2015. Millisecond single-molecule localization microscopy combined with convolution analysis and automated image segmentation to determine protein concentrations in complexly structured, functional cells, one cell at a time. *Faraday discussions,* **184**, pp. 401-424.

XIE, X., XU, A.M., ANGLE, M.R., TAYEBI, N., VERMA, P. and MELOSH, N.A., 2013. Mechanical model of vertical nanowire cell penetration. *Nano letters,* **13**(12), pp. 6002-6008.

YUEN, K.W., MONTPETIT, B. and HIETER, P., 2005. The kinetochore and cancer: what's the connection? *Current opinion in cell biology,* **17**(6), pp. 576-582.

Chapter 10

Conclusions and Future scope

In this chapter, the conclusion of the research conducted in the thesis is introduced and also future scope based on the findings gathered in the framework of this study is suggested.

10. 1. Conclusions

This thesis was dedicated towards the synthesis of different nanostructured ZnO materials for their functionality in the cellular interfacing system to deliver biomolecules through biological organism. The focus was to develop capable platform materials through rational control over design and synthesis to comprehend exceptional structural and functional intricacy in nanostructure building blocks.

A systematic modification statistical analysis of the impact of various reaction conditions on the crystal morphology of hydrothermally synthesized ZnO nanostructures was demonstrated. It was found that to produce uniformly sized and consistently distributed ZnO nanoneedles, a low precursor concentration associated with low processing temperature are preferential. While, uniformly distributed and well-aligned hexagonal nanowires were grown at high ratio of Zn $(NO_3)_2$ and HMTA combined with low growth temperature. The crystal structure and phase purity of nanostructured materials were analysed via SEM, and XRD.

XRD pattern showed that they were a single crystalline wurtzite structures with a preferential growth orientation along c-axis.

The effect of RF sputtered gold layer on the fabrication of bespoke ZnO nanostructures was also investigated. The physical properties of this nucleation/intermediary layer under different annealing conditions were studied as well as the structural topology of subsequently grown ZnO nanowires on these layers was investigated. Based on the measurement of XRD lattice constant and FWHM data, it was observed the crystallite size of the gold thin layer was significantly dependent on annealing temperature, where elevated temperatures resulted in larger crystallite size, reduced lattice strain and improved crystallinity. Moreover, it was found that not only the annealing temperature but also the nature of adsorbate gases affects both gold thin layer and the structural characteristics of solution processed ZnO nanostructures. The underlying mechanism behind the contributory of the gold catalytic activity in the growth of ZnO nanostructures was suggested.

Integration the fabrication process of nanostructures with a consistent control over their locations is necessary to accomplish the promising outcome of potential applications. A step towards the control of ZnO nanomaterial sites was taken by employing template-assisted colloidal self- assembled crystal layers of PS spheres on the substrate surface to produce a long sequence of periodic arrangements. Such lithographic patterning technique enabled good control on the nanowire positions and acceptable quality ZnO nanoarrays with well arrangement over a large scale on Si substrate was achieved.

Due to complexity in morphology and high surface areas, the formation of (3-D) complex ZnO nanomaterials with a precisely controlled size and shape is demanding and highly challenging in materials science and nanoscale devices. (2-D) nanoneedles and (3-D) NFs that produced in the earlier stage of this thesis were assembled to help building nanostructured 3D complex architectures. Template-free multi-step sequential solution phase synthesis approach was used to fabricate (3-D) multibranched NFs of ZnO. A modified forced seeding technique was straightforward and effective way to grow the secondary branches along the main backbone. Based on SEM observations, the proposed growth mechanism was explained. The XRD profile showed high crystalline and well aligned NFs along [103] orientation. Such a result indicates the favourite orientation in ZnO NFs dependent upon the nature of catalyst layer and the deposition techniques used which may confirm a correlation between the ZnO morphology and its preferred orientation.

Finally, a proof of concept study of the potential feasibility of ZnO nanomaterial was further highlighted through its integration with different cell lines to serve as biomolecules-delivery tools. Even though the transformation process did not take place into yeast *saccharomyces cerevisiae* cells and (CHO) cells, an essential information based on SEM and FM images was gathered about the nanostructure-biosystem interface. Due to the large size of yeast *saccharomyces cerevisiae* cell compared to nanostructures it was important to investigate the cell settling mechanism of these cells on the nanostructures to assess the interfacial interactions of the Nano-cell system under different culturing conditions.

It was observed that placing

nanostructures onto liquid cell culture was more practicable than settling them on the top of monolayer of cell agar-plate. Moreover, the impact of intensive biological treatment on the nanomaterials robustness and reproducibility was addressed. We found that processing the nanostructures with fluids or culture media for a long-time resulted in their removal. Therefore, we suggest that washing once by sterile water and soaking in 70% absolute ethanol for 15 min is the applicable approach to maintain the robustness and durability of the nanomaterials.

In addition, it was clearly observed from SEM data of (CHO) cells that cell being enmeshed or embedded within many pointed ends of nanoflower which could create extreme damage into the cell membrane. Therefore, the effect of the morphological characteristics of nanotextures on the interactions of the Nano-cell interface was studied. Based on FM images, it was observed that same cell line (CHO) interacts differently with two varied types of nanostructure geometry.

10. 2. Future Scope

In the framework of this thesis, an assortment of ZnO nanostructures was fabricated, including (1-D) and (3-D) structures using low-temperature solution-processing techniques. They are more reaction parameters involved in the growth process need further investigations which would possibly enhance the quality of the final products. Various characterisation methods were applied to get better understanding on the structural and functional properties of ZnO nanostructure. However, more detailed study using other high resolutions tools might add to or reinforce the research outcomes.

Especially, TEM analysis needs to be performed to obtain better insight into the crystalline nature of the synthesized ZnO nanostructures. Due to limited facilities and time, this has not been carried out as a part of this PhD project and will be considered in the future work.

An interesting correlation between the annealing atmosphere and the aspect ratio of nanostructured ZnO materials was found especially those were annealed in oxygen ambient. Therefore, in-depth investigations with regard to annealing samples in oxidation atmosphere, following by hydrothermally growth could reveal more information about the important function of the catalyst gold layer in the hydrothermal growth process. In addition, in situ TEM analysis under real-growth condition could reveal better insight into the coalescence and nucleation of gold nanoparticles that caused such irregularly shaped large islands across the surface area.

Even though the growth of (3-D) ZnO complexes structure was demonstrated, there was a lack of controlling the secondary branches growth on the side walls of the nanoflower which affected its uniformity and distribution over the substrate surface. It would be valuable research to suggest a precisely controlled coating method to overcome the random distribution of ZnO seed particles and produce highly crystallized and uniformed hierarchical ZnO structures.

Although, an effort for controlling the nanostructured material sites was carried out using self-assembled close-packed crystals of polystyrene spheres. Further optimizations still needed to obtain defect-free patterns over large surface area so that well-aligned and consistently distributed nanoarrays across the sample could be achieved.

One of the most important findings of this thesis was the demonstration of the applicability of ZnO nanostructures as potential biomolecule delivery platform. However, it was an initial proof of concept study and there are a plenty of parameters need to be considered and studied in more details. One of the most important issue is the interface between the nanostructures and cells which is very complicated and affects by many underlying chemical and physiological processing parameters related both to the cells and nanostructured materials. Therefore, it is crucial to understand how the nanostructures penetrate the cell membrane and what the mechanism of cells to attach or interact with these structures. Further in-depth efforts required to be devoted which could open new vistas and unlock the full potential for these materials as efficient nanostructure- assisted cellular delivery system.

Cells cultured on various nanostructures are influenced to some degrees by their morphology so, performing systematic experimentations using different shapes and dimensions of nanomaterials on various cell lines may enhance our insight on how nanomaterials and cell interact. In addition to the topographical and structural impact of nanotextures, hydrophobic/hydrophilic properties of the nanostructured surface could play another critical role on the Nano-cell interactions. Moreover, chemical and physical characteristics related to mammalian cell structure and function (e.g. cell motility, the cell membrane composition, cytoplasm, nucleus, mitochondria) need to be addressed and high-resolution imaging techniques are required to simultaneously monitor cells under the conditions of culturing with nanostructures. Such an analysis should aid in assessing the convoluted mechanism underlying the Nano-cellular system and enabling the envision and design of an applicable nanostructures-assisted biomolecule delivery platform.

In addition, it is critical to understand the correlation between the ZnO nanostructure morphology and the mammalian cell size (e.g. length, diameter, density). Additionally, culture conditions (e.g., nutrient depletion and/or waste accumulation) can affect the growth phases of the mammalian cells.

This research work is at a nascent phase and there were a number of challenges in progressing the optimisation work. Therefore, we have only scratched the surface of ZnO nanostructure capability and demonstrated that these nanomaterials are a true platform to ultimately drive the future technology. Hence, its integration with different disciplines and expertise in electrochemistry, solid-state physics, material science, and biology would offer the opportunity of a future generation of highly rapid, sensitive, stable, selective and novel applications.

Appendices

Appendix A

The optimization growth of ZnO nanowires guided by statistically designed experiments

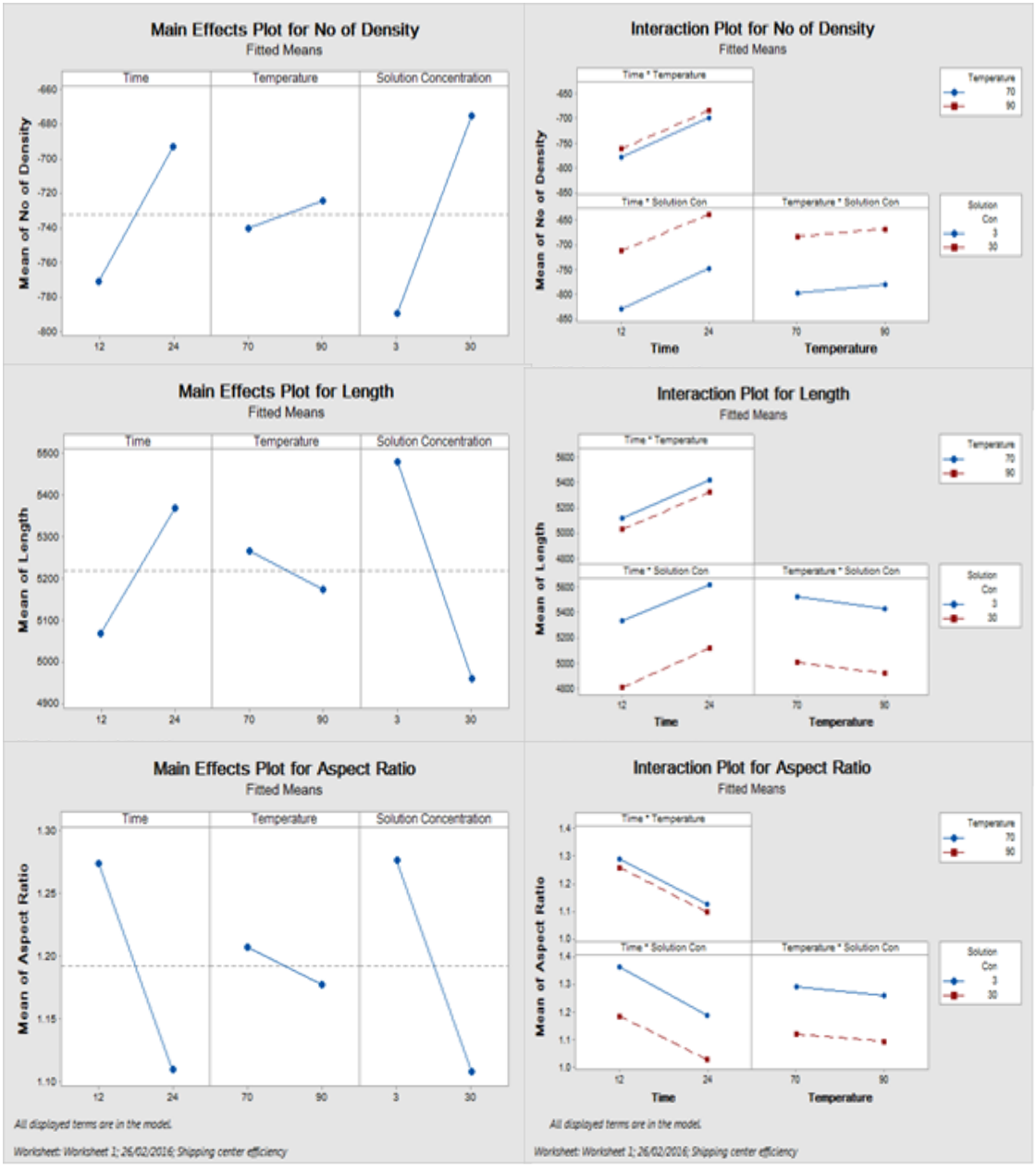

Figure 5. 13. The main effect and interaction effect of the reaction parameters of the first stage.

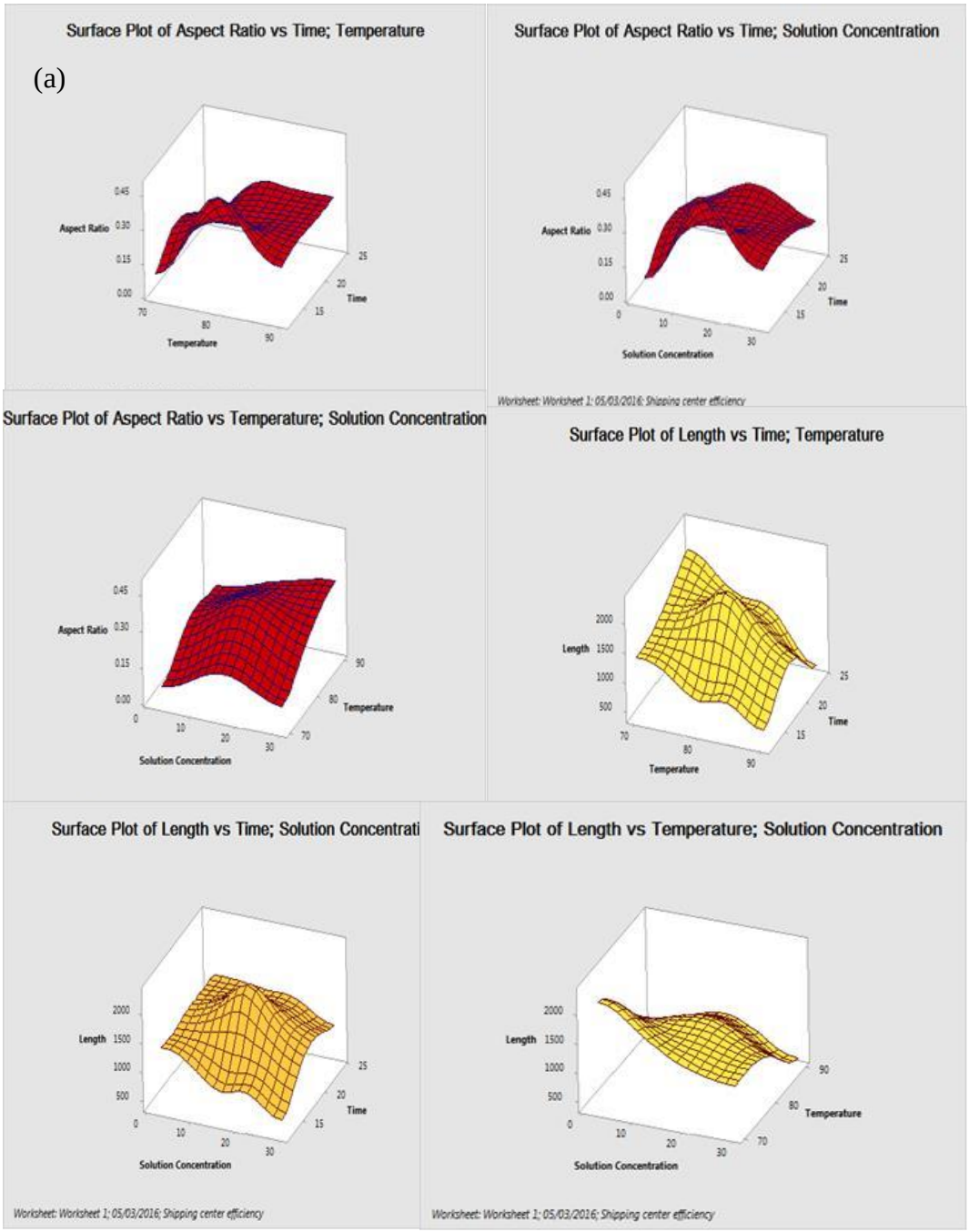

Figure 5. 14. (a) 3D surface plots of the length and aspect ratio of ZnO nanowires (stage 1).

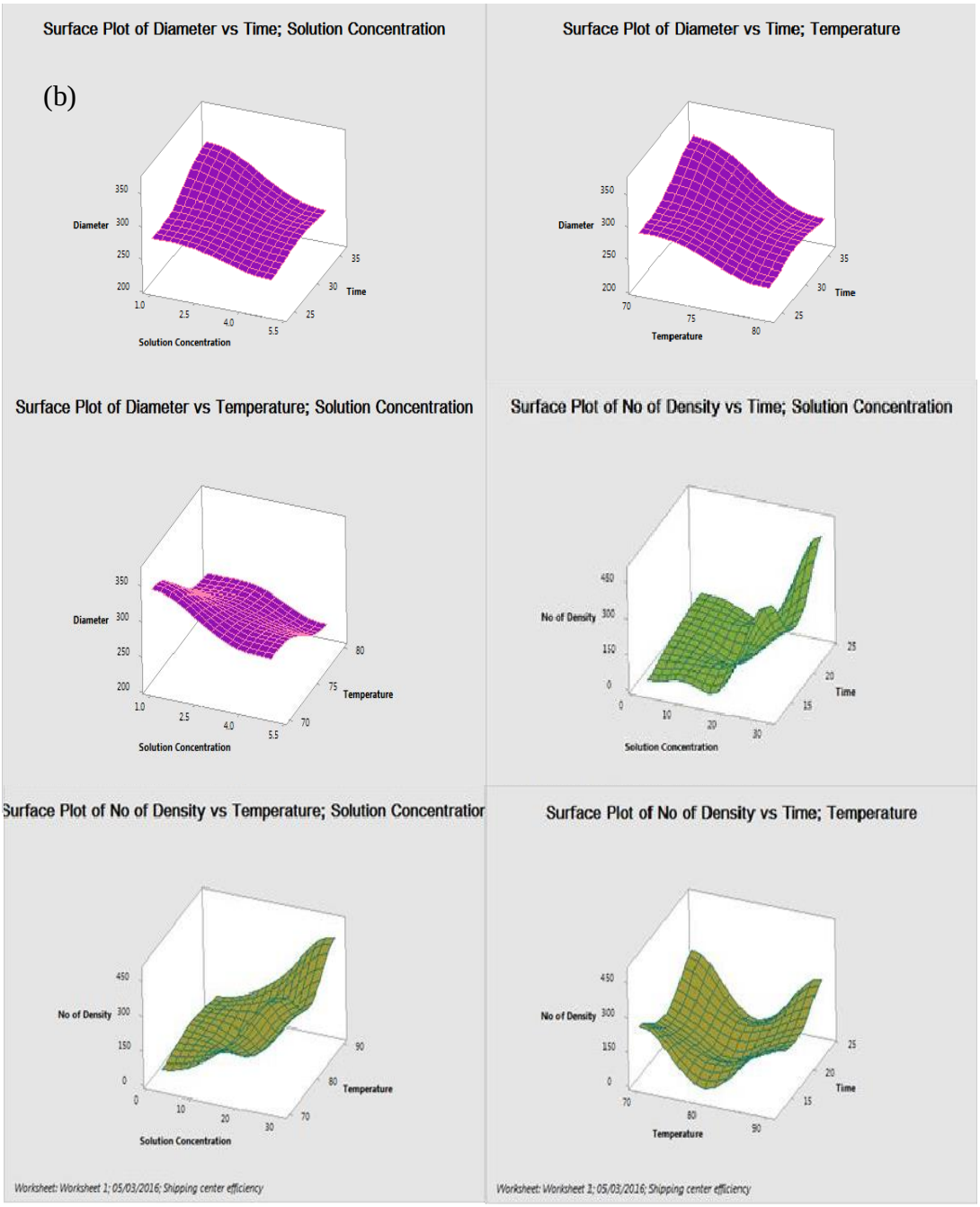

Figure 5. 14. (b) 3D surface plots of a number of density of ZnO nanowires and their diameter (stage 1).

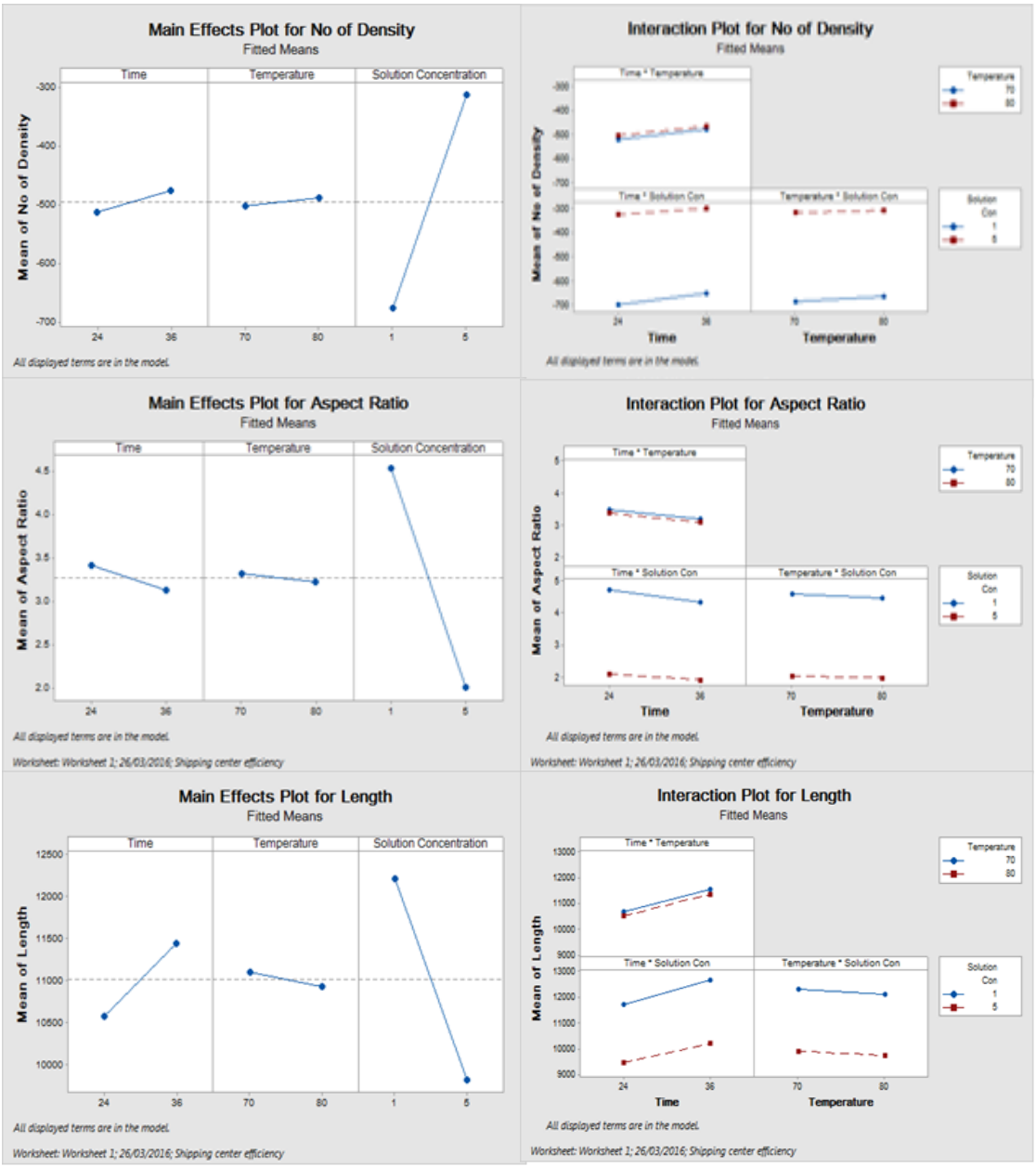

Figure 5. 15. The main effect and interaction effect of the reaction parameters of the second stage.

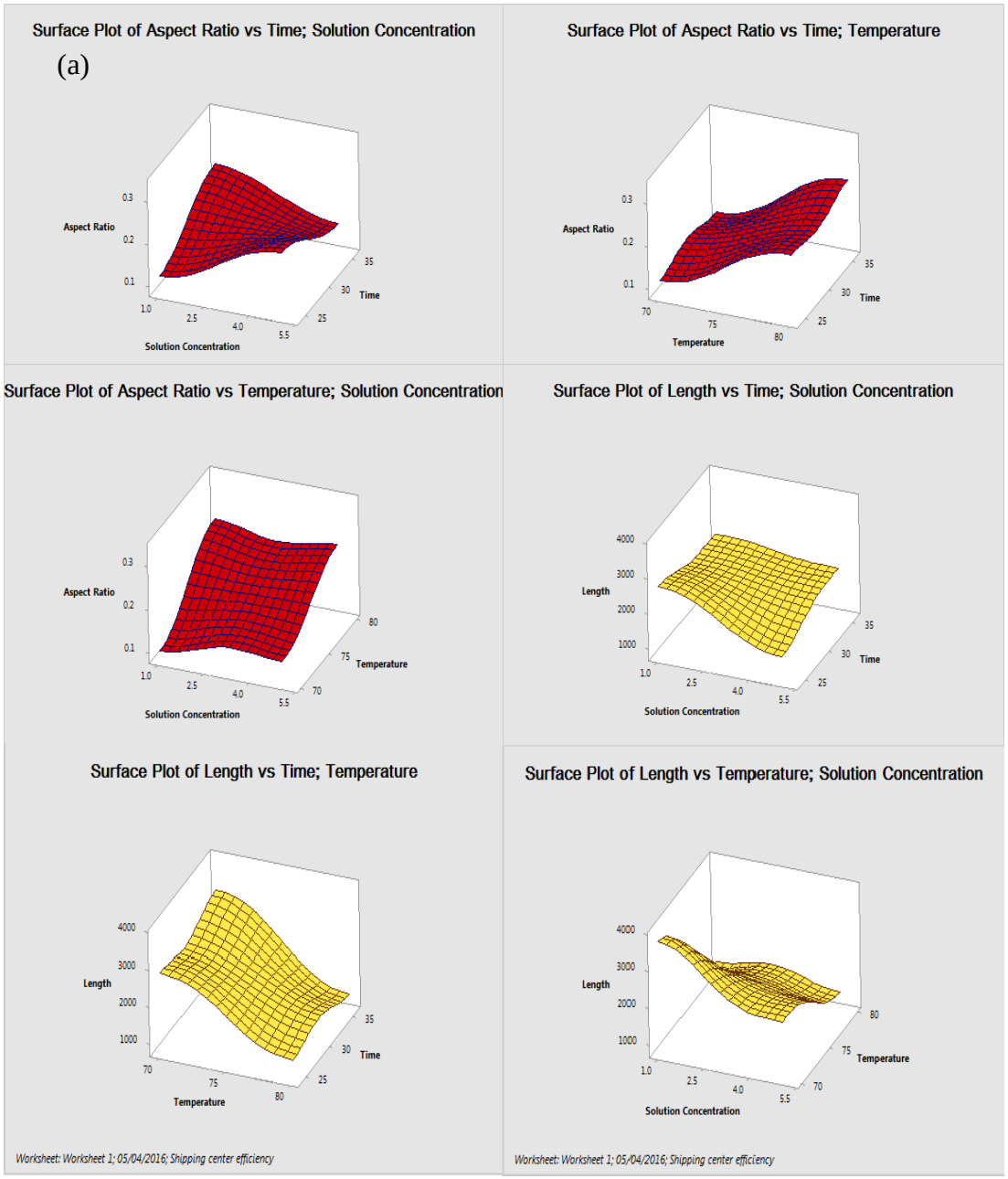

Figure 5. 16. (a) 3D surface plots of the length and aspect ratio of ZnO nanowires (stage 2).

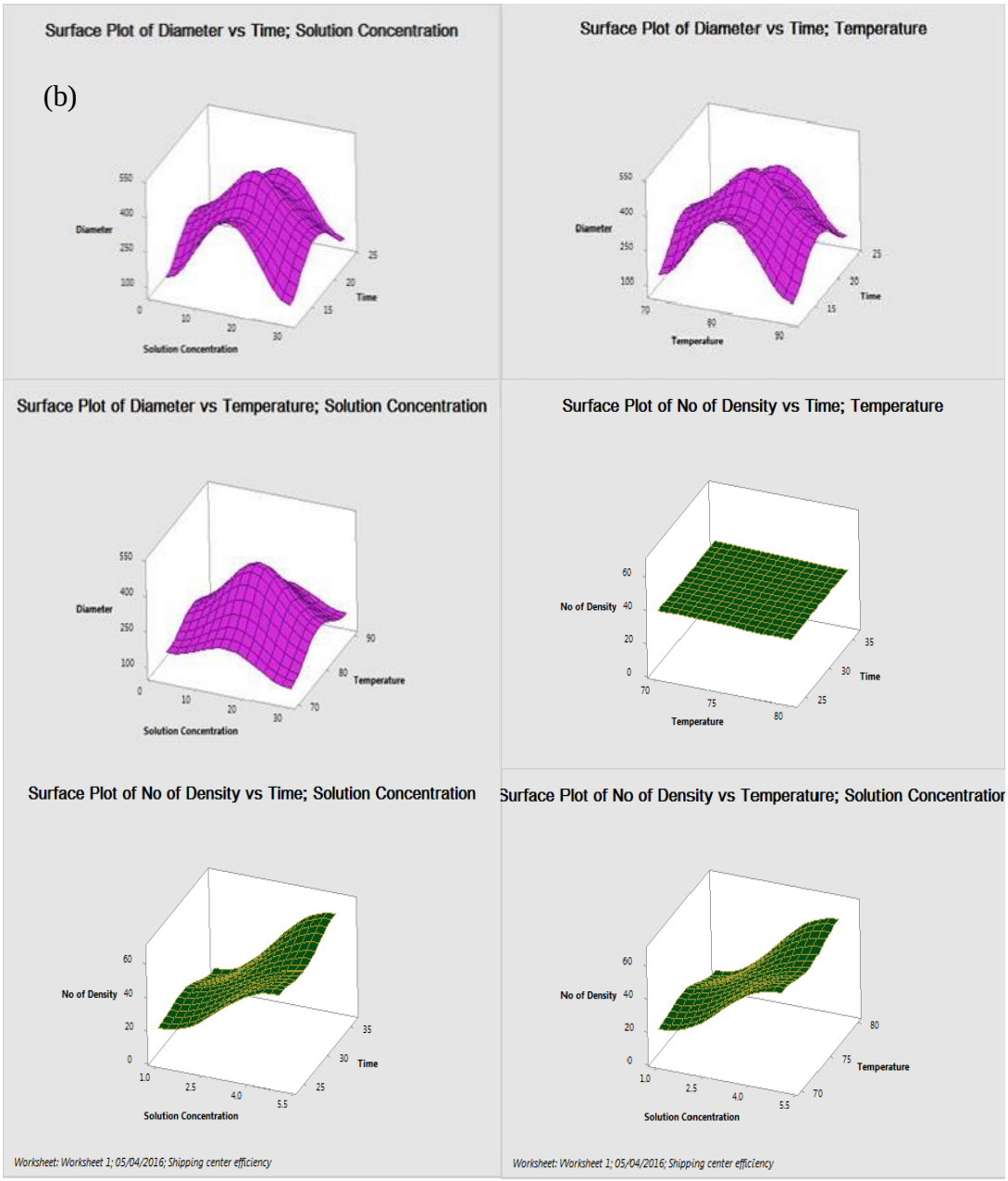

Figure 5. 16. (b) 3D surface plots of a number of density of ZnO nanowires and their diameter (stage 2).

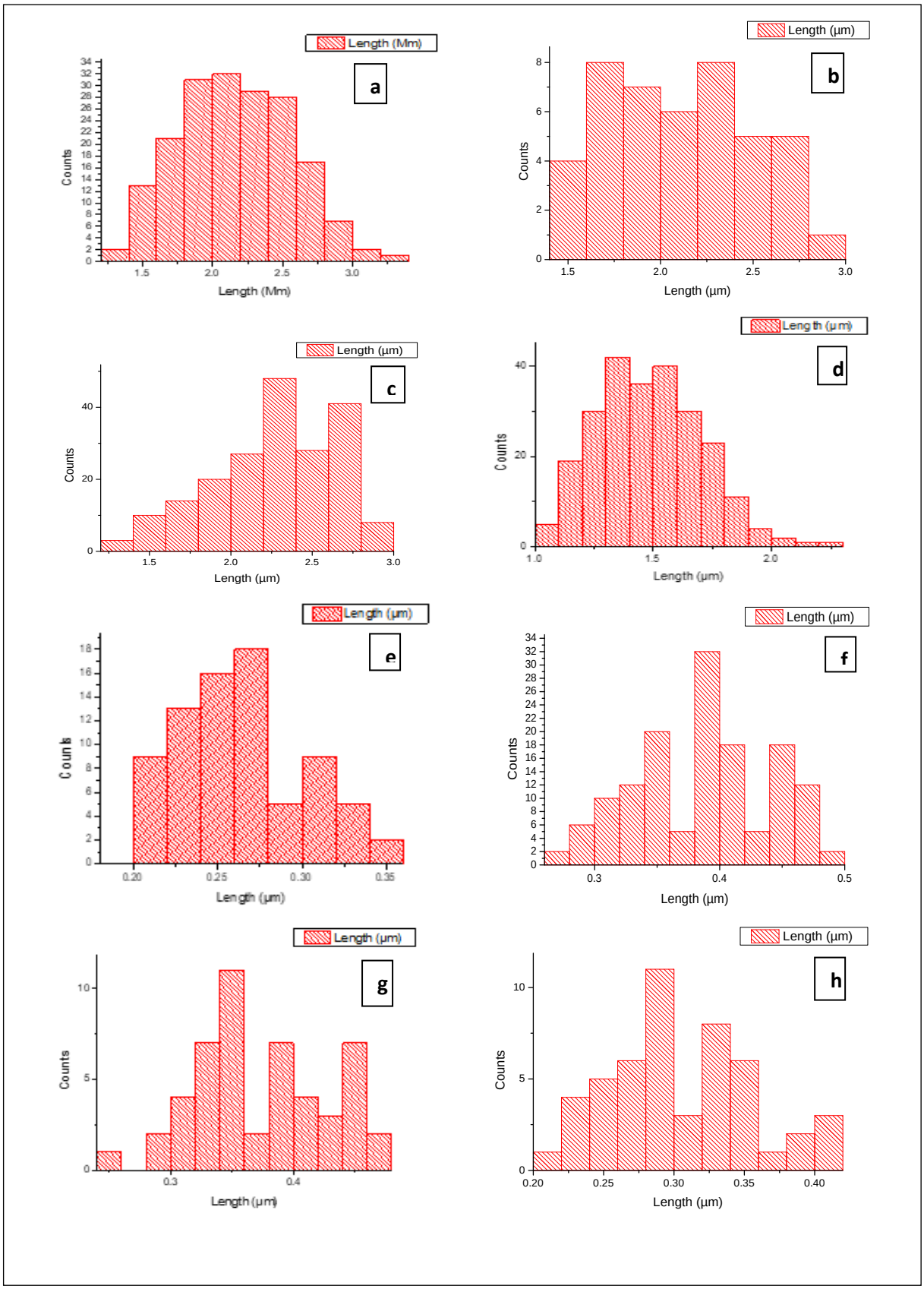

Figure 5. 17. (a) Controlling the morphology of ZnO nanostructures based on the growth conditions in the first stage; (a) at 3 mM, 70 ^{0}C, 24hrs. (b) at 3 mM, 70 ^{0}C, 12hrs. (c) at 30

mM, 70 ^{0}C ,12hrs. (d) at 30 mM, 70 ^{0}C ,24hrs (e) at 30 mM, 90 ^{0}C, 12hrs. (f) at 30 mM, 90 ^{0}C, 24hrs. (g) at 3 mM, 90 ^{0}C ,12hrs. (h) at 3 mM, 90 ^{0}C ,24hrs.Histogram summaries the average length of ZnO nanostructures.

Table 5. 4. Descriptive statistics of the average length of ZnO nanostructures (first stage).

Run order	Mean Length (µm)	Standard Deviation	Minimum Length (µm)	Median Length (µm)	Maximum Length (µm)
a	2.16284	0.39935	1.24	2.15	3.24
b	2.13023	0.37937	1.52	2.115	2.88
c	1.48168	0.218	1.03	1.47	2.25
d	2.27824	0.3816	1.33	2.3	2.95
e	0.38486	0.05438	0.27	0.38	0.49
f	0.25883	0.03576	0.2	0.26	0.34
g	0.3706	0.05211	0.25	0.355	0.46
h	0.3032	0.04808	0.22	0.3	0.4

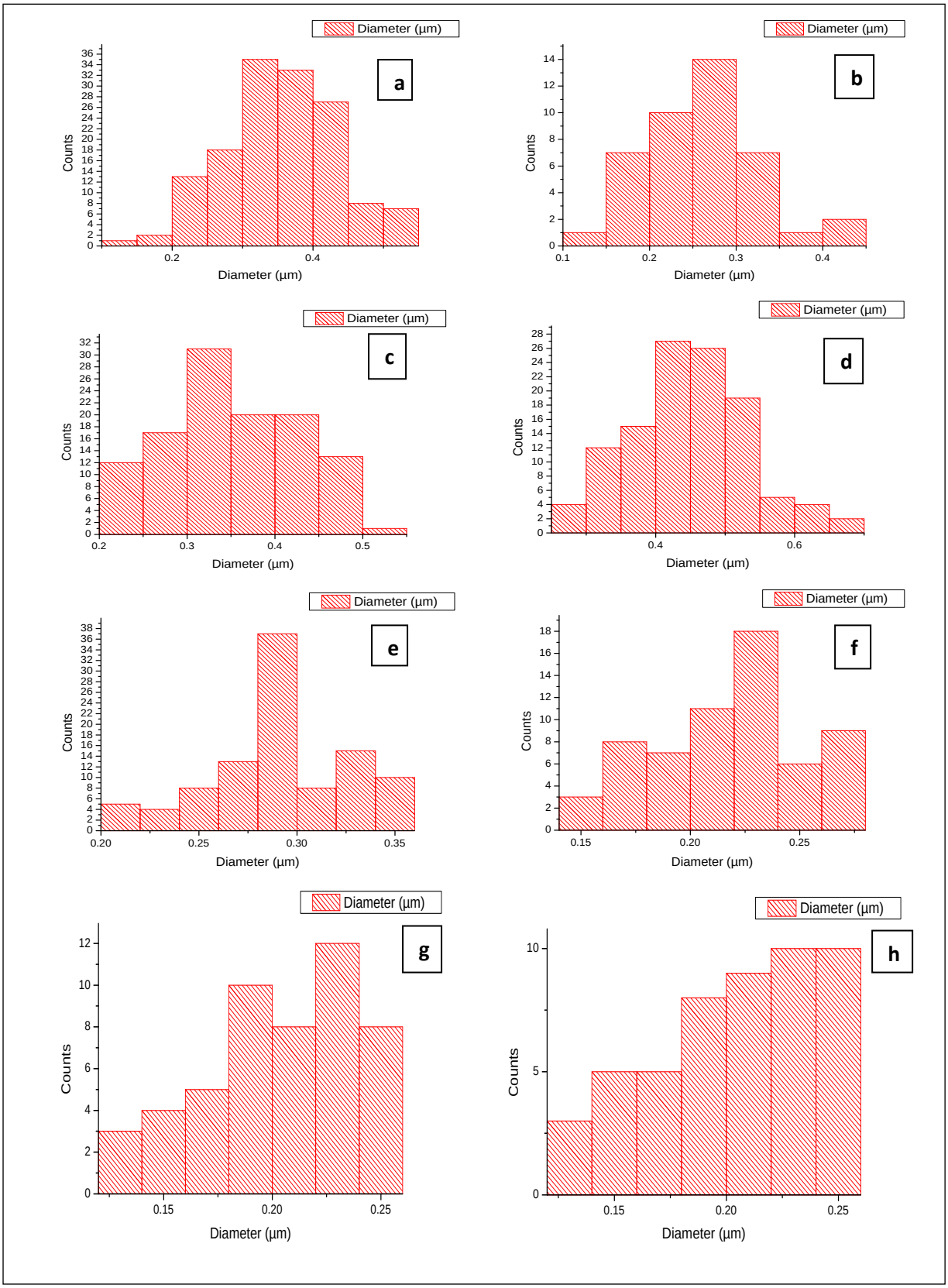

Figure 5. 17. (b) Controlling the morphology of ZnO nanostructures based on the growth conditions in the first stage; (a) at 3 mM, 70 ^{0}C, 24hrs. (b) at 3 mM, 70 ^{0}C, 12hrs. (c) at 30

mM, 70 ^{0}C ,12hrs. (d) at 30 mM, 70 ^{0}C ,24hrs (e) at 30 mM, 90 ^{0}C, 12hrs. (f) at 30 mM, 90 ^{0}C, 24hrs. (g) at 3 mM, 90 ^{0}C ,12hrs. (h) at 3 mM, 90 ^{0}C ,24hrs. Histogram summaries the average diameter of ZnO nanostructures.

Table 5. 5. Descriptive statistics of the average diameter of ZnO nanostructures (first stage).

Run order	Mean diameter (μm)	Standard Deviation	Minimum diameter (μm)	Median diameter (μm)	Maximum diameter (μm)
a	0.35729	0.07565	0.15	0.36	0.54
b	0.26786	0.06311	0.15	0.26	0.4
c	0.35342	0.06837	0.22	0.35	0.54
d	0.44579	0.08138	0.29	0.435	0.67
e	0.2913	0.03389	0.22	0.29	0.35
f	0.21823	0.03272	0.15	0.23	0.27
g	0.2006	0.03449	0.13	0.2	0.25
h	0.1998	0.0356	0.13	0.2	0.25

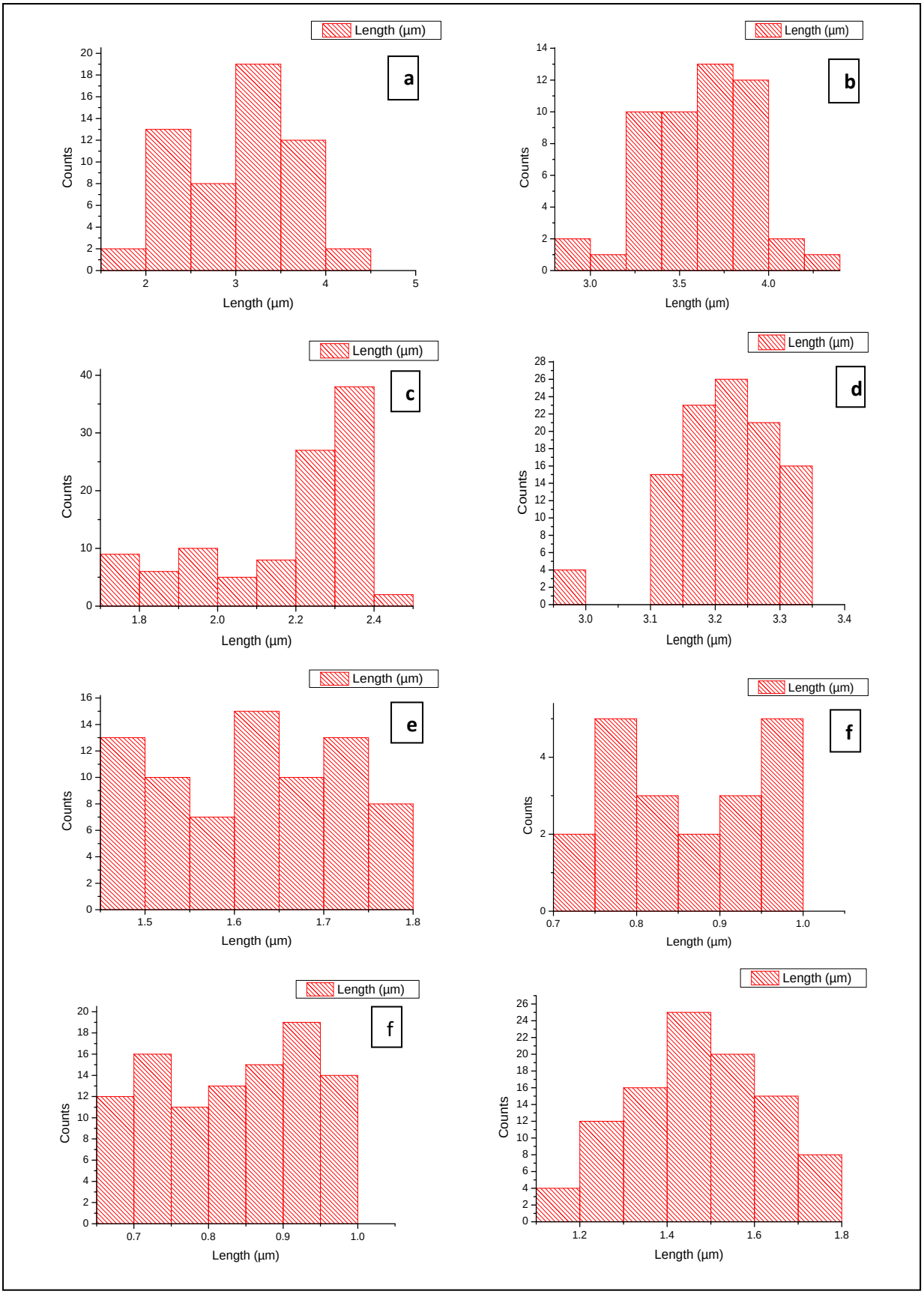

Figure 5. 18. (a) Controlling the morphology of ZnO nanostructures based on the growth conditions in the second stage; (a) at 1 mM, 70 ^{0}C, 24h. (b) at 1 mM, 70 ^{0}C, 36h. (c) at 5

mM, 70 ^{0}C ,24h. (d) at 5 mM, 70 ^{0}C ,36h. (e) at 1 mM, 80 ^{0}C, 24h. (f) at 1 mM, 80 ^{0}C, 36h. (g) at 5 mM, 80 ^{0}C ,24h. (h) at 5 mM, 80 ^{0}C ,36h. Histogram summaries the average length of ZnO nanostructures.

Table 5. 6. Descriptive statistics of the average length of ZnO nanostructures (second stage).

Run order	Mean Length (µm)	Standard Deviation	Minimum Length (µm)	Median Length (µm)	Maximum Length (µm)
a	3.02429	0.61563	1.9	3.05	4.47
b	3.63275	0.2877	3	3.65	4.38
c	2.19371	0.20121	1.75	2.28	2.41
d	3.22057	0.08036	3	3.22	3.35
e	1.63	0.09852	1.48	1.645	1.78
f	0.8715	0.09051	0.75	0.86	1
g	0.8386	0.10004	0.67	0.84	1
h	1.4794	0.15383	1.14	1.48	1.75

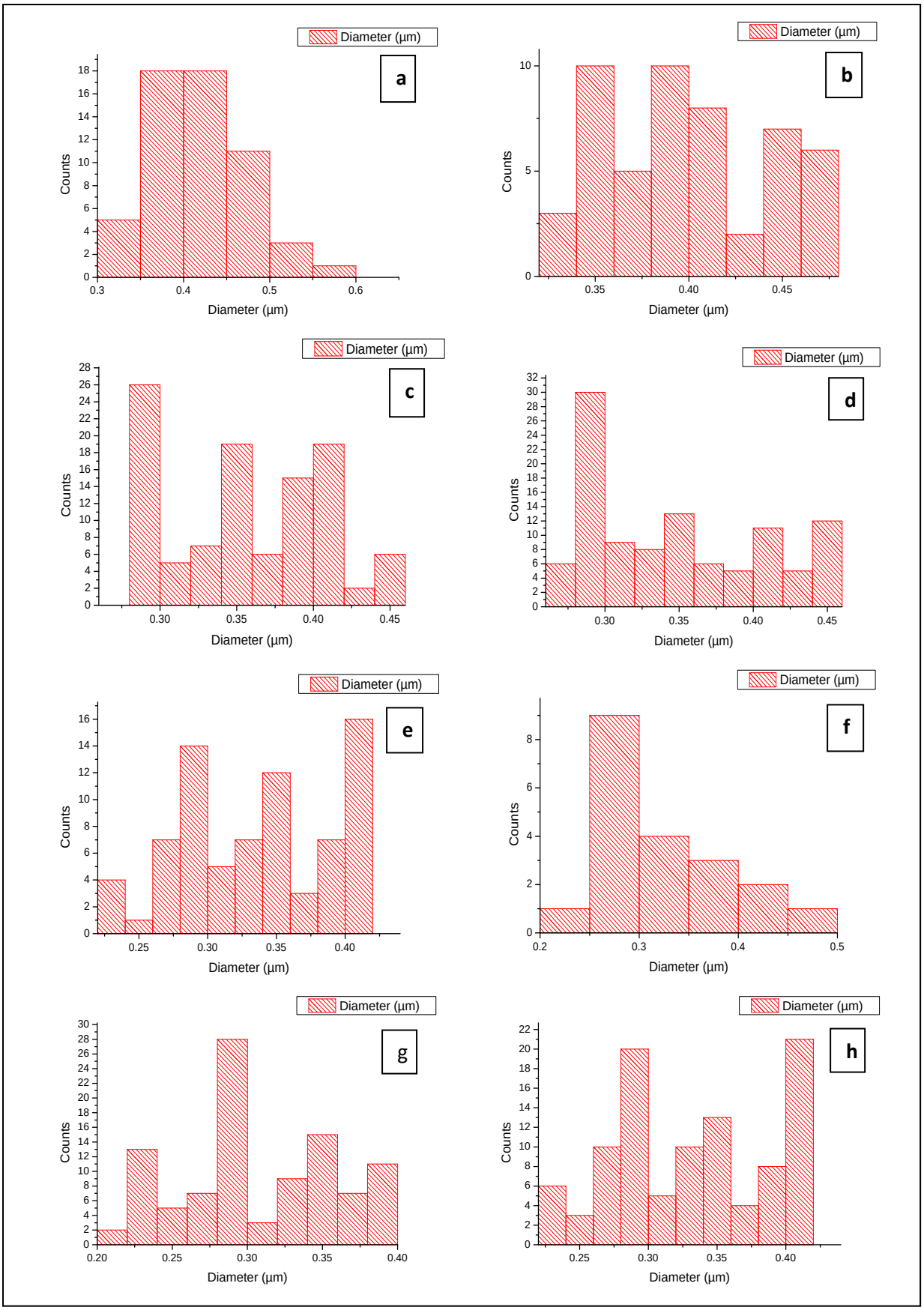

Figure 5. 18. (b) Controlling the morphology of ZnO nanostructures based on the growth conditions in the second stage; (a) at 1 mM, 70 ^{0}C, 24h. (b) at 1 mM, 70 ^{0}C, 36h. (c) at 5

mM, 70 ^{0}C ,24h. (d) at 5 mM, 70 ^{0}C ,36h. (e) at 1 mM, 80 ^{0}C, 24h. (f) at 1 mM, 80 ^{0}C, 36h. (g) at 5 mM, 80 ^{0}C ,24h. (h) at 5 mM, 80 ^{0}C ,36h. Histogram summaries the average diameter of ZnO nanostructures.

Table 5. 7. Descriptive statistics of the average diameter of ZnO nanostructures (second stage).

Run order	Mean diameter (µm)	Standard Deviation	Minimum diameter (µm)	Median diameter (µm)	Maximum diameter (µm)
a	0.42946	0.05452	0.35	0.43	0.6
b	0.39765	0.0432	0.33	0.39	0.47
c	0.35638	0.05048	0.28	0.36	0.44
d	0.34752	0.05919	0.27	0.33	0.45
e	0.33645	0.05484	0.24	0.335	0.42
f	0.327	0.05732	0.25	0.315	0.45
g	0.3073	0.04917	0.22	0.3	0.39
h	0.3318	0.05716	0.23	0.33	0.42

Appendix B

Figure and image permissions

Title: Atomistic Mechanisms of ZnO Aggregation from Ethanolic Solution: Ion Association, Proton Transfer, and Self-Organization

Author: Agnieszka Kawska, Patrick Duchstein, Oliver Hochrein, et al

Publication: Nano Letters

Publisher: American Chemical Society

Date: Aug 1, 2008

PERMISSION/LICENSE IS GRANTED FOR YOUR ORDER AT NO CHARGE

This type of permission/license, instead of the standard Terms & Conditions, is sent to you because no fee is being charged for your order. Please note the following:

- Permission is granted for your request in both print and electronic formats, and translations.
- If figures and/or tables were requested, they may be adapted or used in part.
- Please print this page for your records and send a copy of it to your publisher/graduate school.
- Appropriate credit for the requested material should be given as follows: "Reprinted (adapted) with permission from (COMPLETE REFERENCE CITATION). Copyright (YEAR) American Chemical Society." Insert appropriate information in place of the capitalized words.
- One-time permission is granted only for the use specified in your request. No additional uses are granted (such as derivative works or other editions). For any other uses, please submit a new request.

Title: Shape and Size Effects of ZnO Nanocrystals on Photocatalytic Activity

Author: Anna Mclaren, Teresa Valdes-Solis, Guoqiang Li, et al

Publication: Journal of the American Chemical Society

Publisher: American Chemical Society

Date: Sep 1, 2009

Title: Site-Specific Nucleation and Growth Kinetics in Hierarchical Nanosyntheses of Branched ZnO Crystallites

Author: Tierui Zhang, Wenjun Dong, Mary Keeter-Brewer, et al

Publication: Journal of the American Chemical Society

Publisher: American Chemical Society

Date: Aug 1, 2006

Title: Hierarchical ZnO Nanowire–Nanosheet Architectures for High Power Conversion Efficiency in Dye-Sensitized Solar Cells

Author: Feng Xu, Min Dai, Yinong Lu, et al

Publication: The Journal of Physical Chemistry C

Publisher: American Chemical Society

Date: Feb 1, 2010

Title: Formation of Branched ZnO Nanowires from Solvothermal Method and Dye-Sensitized Solar Cells Applications

Author: Hsin-Ming Cheng, Wei-Hao Chiu, Chia-Hua Lee, et al

Publication: The Journal of Physical Chemistry C

Publisher: American Chemical Society

Date: Oct 1, 2008

Title: Highly Sensitive and Selective Ethanol Sensor Fabricated with In-Doped 3DOM ZnO

Author: Zhihua Wang, Ziwei Tian, Dongmei Han, et al

Publication: Applied Materials

Publisher: American Chemical Society

Date: Mar 1, 2016

Title: Epitaxy of Vertical ZnO Nanorod Arrays on Highly (001)-Oriented ZnO Seed Monolayer by a Hydrothermal Route

Author: Weibing Wu, Guangda Hu, Shougang Cui, et al

Publication: Crystal Growth and Design

Publisher: American Chemical Society

Date: Nov 1, 2008

additional uses are granted (such as derivative works or other editions). For any other uses, please submit a new request.

Title: Ultrarapid Sonochemical Synthesis of ZnO Hierarchical Structures: From Fundamental Research to High Efficiencies up to 6.42% for Quasi-Solid Dye-Sensitized Solar Cells

Author: Yantao Shi, Chao Zhu, Lin Wang, et al

Publication: Chemistry of Materials

Publisher: American Chemical Society

Date: Mar 1, 2013

PERMISSION/LICENSE IS GRANTED FOR YOUR ORDER AT NO CHARGE

This type of permission/license, instead of the standard Terms & Conditions, is sent to you because no fee is being charged for your order. Please note the following:

- Permission is granted for your request in both print and electronic formats, and translations.
- If figures and/or tables were requested, they may be adapted or used in part.
- Please print this page for your records and send a copy of it to your publisher/graduate school.
- Appropriate credit for the requested material should be given as follows: "Reprinted (adapted) with permission from (COMPLETE REFERENCE CITATION). Copyright (YEAR) American Chemical Society." Insert appropriate information in place of the capitalized words.

- One-time permission is granted only for the use specified in your request. No additional uses are granted (such as derivative works or other editions). For any other uses, please submit a new request.

Title: Biomimetic Arrays of Oriented Helical ZnO Nanorods and Columns

Author: Zhengrong R. Tian, James A. Voigt, Jun Liu, et al

Publication: Journal of the American Chemical Society

Publisher: American Chemical Society

Date: Nov 1, 2002

PERMISSION/LICENSE IS GRANTED FOR YOUR ORDER AT NO CHARGE

This type of permission/license, instead of the standard Terms & Conditions, is sent to you because no fee is being charged for your order. Please note the following:

- Permission is granted for your request in both print and electronic formats, and translations.
- If figures and/or tables were requested, they may be adapted or used in part.
- Please print this page for your records and send a copy of it to your publisher/graduate school.
- Appropriate credit for the requested material should be given as follows: "Reprinted (adapted) with permission from (COMPLETE REFERENCE CITATION). Copyright (YEAR) American Chemical Society." Insert appropriate information in place of the capitalized words.
- One-time permission is granted only for the use specified in your request. No

additional uses are granted (such as derivative works or other editions). For any other uses, please submit a new request.

Title: Growth Mechanism and Properties of Multibranched ZnO Nano/Microstructure

Author: Fang Fang, , Shanshan Lv, et al

Publication: Integrated Ferroelectrics

Publisher: Taylor & Francis

Date: Jul 24, 2015

Rights managed by Taylor & Francis

Thesis/Dissertation Reuse Request

Taylor & Francis is pleased to offer reuses of its content for a thesis or dissertation free of charge contingent on resubmission of permission request if work is published.

Title: Biofunctional ZnO Nanorod Arrays Grown on Flexible Substrates

Author: Ting-Yu Liu, Hung-Chou Liao, Chin-Ching Lin, et al

Publication: Langmuir

Publisher: American Chemical Society

Date: Jun 1, 2006

PERMISSION/LICENSE IS GRANTED FOR YOUR ORDER AT NO CHARGE

This type of permission/license, instead of the standard Terms & Conditions, is sent to you because no fee is being charged for your order. Please note the following:

- Permission is granted for your request in both print and electronic formats, and translations.
- If figures and/or tables were requested, they may be adapted or used in part.
- Please print this page for your records and send a copy of it to your publisher/graduate school.
- Appropriate credit for the requested material should be given as follows: "Reprinted (adapted) with permission from (COMPLETE REFERENCE CITATION). Copyright (YEAR) American Chemical Society." Insert appropriate information in place of the capitalized words.
- One-time permission is granted only for the use specified in your request. No additional uses are granted (such as derivative works or other editions). For any other uses, please submit a new request.

Order Date	Article Title	Publication	Type Of Use	Order Status	Order Number
25-Apr-2019	Morphosynthesis of hierarchical ZnO replica using butterfly wing scales as templates	Microporous and Mesoporous Materials	reuse in a thesis/dissertation	Completed	4576100576983
25-Apr-2019	pH-dependent growth of zinc oxide nanorods	Journal of Crystal Growth	reuse in a thesis/dissertation	Completed	4575850722888
25-Apr-2019	Effects of Preparation Conditions on the Growth of ZnO Nanorod Arrays Using Aqueous Solution Method	International Journal of Applied Ceramic Technology	Dissertation/Thesis	Completed	4575831410328
25-Apr-2019	Effects of Preparation Conditions on the Growth of ZnO Nanorod Arrays Using Aqueous Solution Method	International Journal of Applied Ceramic Technology	Dissertation/Thesis	Completed	4575830737423

Appendix C

List of Acronyms

3DOM……Three Dimensionally Ordered Macroporous

AFM……Atomic Force Microscopy

ALD……Atomic Layer Deposition

CCT……Colloidal Crystal Templating

CHO……Chinese hamster ovary

CTAB……Cetyltrimethylammonium Bromide

CVD……Chemical Vapor Deposition

DI……Deionized Water

DMSO……Dimethyl Sulfoxide

DNA……Deoxyribonucleic Acid

DSSC……Dye-Sensitized Solar Cell

EBID……Electron Beam Induced Deposition

EBL……Electron Beam Lithography

EDA……Ethylenediamine

Ems……Electron Microscopes

EUVL……Extreme Ultraviolet Lithography

FET……Field Effect Transistor

FM……Fluorescence Microscopy

FWHM……Full Width Half Maximum

HMTA……hexamethylenetetramine

IBL……Ion Beam Lithography

IEP……Isoelectric Point

JCPDS……Joint Committee on Powder Diffraction Standards

LBZC……..Layered Basic Zinc Carbonate

LED……Light Emitting Diodes

LPCVD……Low Pressure Chemical Vapour Deposition

MEA……..Monoethanolamine

MOCVD……Metal Organic Chemical Vapor Deposition

NC-AFM……..Non-contact Atomic Force Microscopy

NIL……Nanoimprint Lithography

NFs……Nanoflowers

NSL ……Nanosphere lithography

PDMS……..Polydimethylsiloxane

PE……Pulse Electrodeposition

PECVD……Plasma-enhanced Chemical Vapour Deposition

PEG……..Polyethylene Glycol

PEI……Polyethyleneimine

PET……Polyethylene Terephthalate

PL……Photoluminescence

PLAD……Pulsed Laser Ablation Deposition

PMMA……..Polymethyl Methacrylate

PSS……Poly Sodium Styrenesulfonate

PVA……Polyvinyl Alcohol

PVD……Physical Vapor Deposition

PVP……Poly Vinylpyrrolidone

RF……Radio Frequency

SCE……..Saturated Calomel Electrode

SDS……Sodium Dodecyl Sulfate

SEM……Scanning Electron Microscopy

SMM……Selective-Minimum Media

SPL……Scanning Probes Lithography

TEOS……Tetraethoxysilane

TPU……Thermoplastic Polyurethane

UV……Ultra-Violet

VLS……Vapour Liquid Solid

W-H……Williamson Hall

XRD……X-ray Diffraction

XRL……X-ray lithography

ZnO……Zinc Oxide